Chapter 1

Introduction

1.1   DNA

Deoxyribonucleic acid (DNA) is central to all forms of life - it is a unique genetic blueprint present in every cell of an organism, from single celled simple life forms to immensely complex ones such as humans. The structure of DNA[1] allows the genetic code to be both replicated during cell division and expressed in protein molecules, through the central dogma of molecular biology, first outlined by Crick in 1958 and re-stated in 1970[2], which defines the flow of information through different polymer molecules. The process of *transcription* transfers genetic information encoded as DNA to the messenger molecule ribonucleic acid (RNA), before *translation* results in the information from RNA being expressed in protein molecules that carry out cellular functions. The process of DNA *replication* ensures the hereditary information remains unchanged as it is copied and transmitted millions of times during an organism's lifetime (*Figure 1.1*).
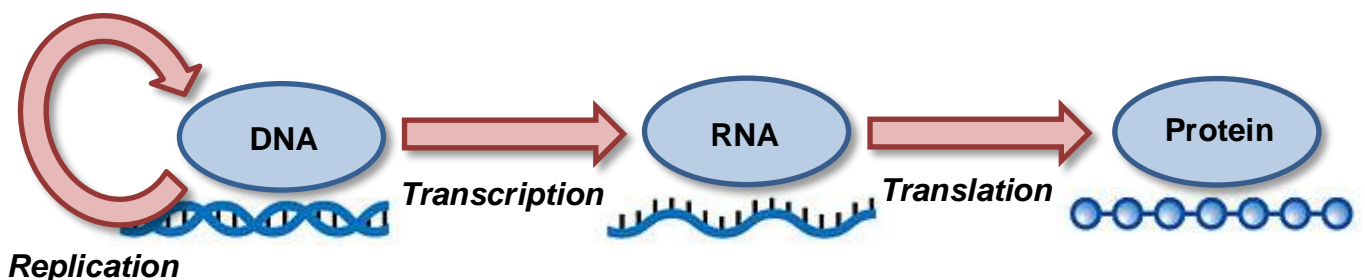
Figure 1.1 - The central dogma of molecular biology

1.1.1   Structure

The primary structure of DNA is a single stranded polymer chain made up of the four nucleotide monomer units. A nucleotide is made up from a phosphate group, a sugar and a nitrogen-containing entity called a base. There are four different bases, two are purine derivatives, adenine (A) and guanine (G), and two are pyrimidine derivatives, cytosine (C) and thymine (T) (*Figure 1.2*).
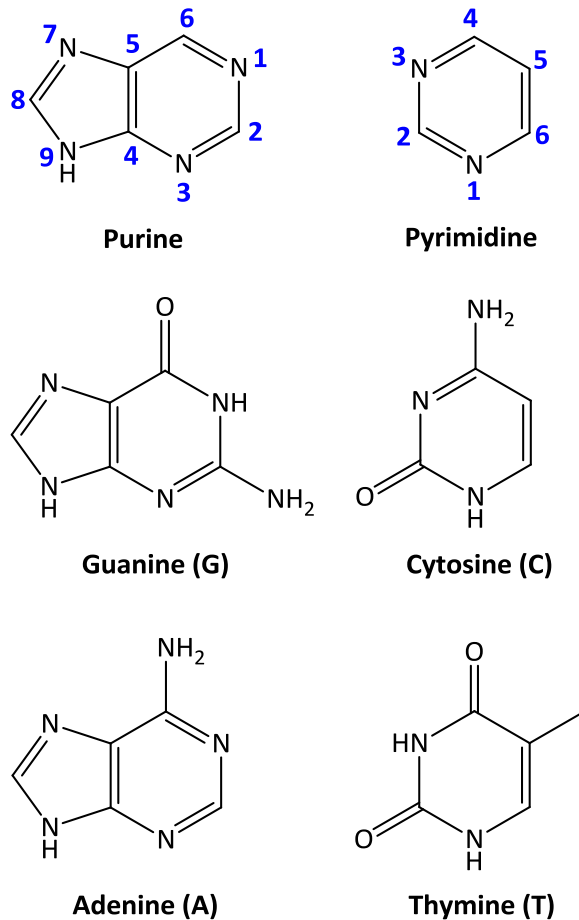
Figure 1.2 - Purine and Pyrimidine bases

The sugar in DNA is deoxyribose, a ribose unit lacking the oxygen usually attached to the 2' carbon atom. When one of the four bases is attached to a sugar via a glycosidic linkage, from the N9 (purine) or N1 (pyrimidine) of the base to the 1' carbon of the sugar, a nucleoside is formed; such as deoxyadenosine in the case of the adenine base. A phosphate group attached to the sugar, on the 5' carbon, completes the monomer to make a nucleotide. These nucleotides can be linked through phosphodiester bonds between the sugar and the phosphate groups to become DNA. The 5' carbon and 3' carbon ends of the sugar give rise to directionality for the bases in a single strand, which are always written in the 5'-to-3' direction; also the direction of assembly *in vivo* as the polymerase attaches new nucleotides to the 3' hydroxyl group (*Figure 1.3*).
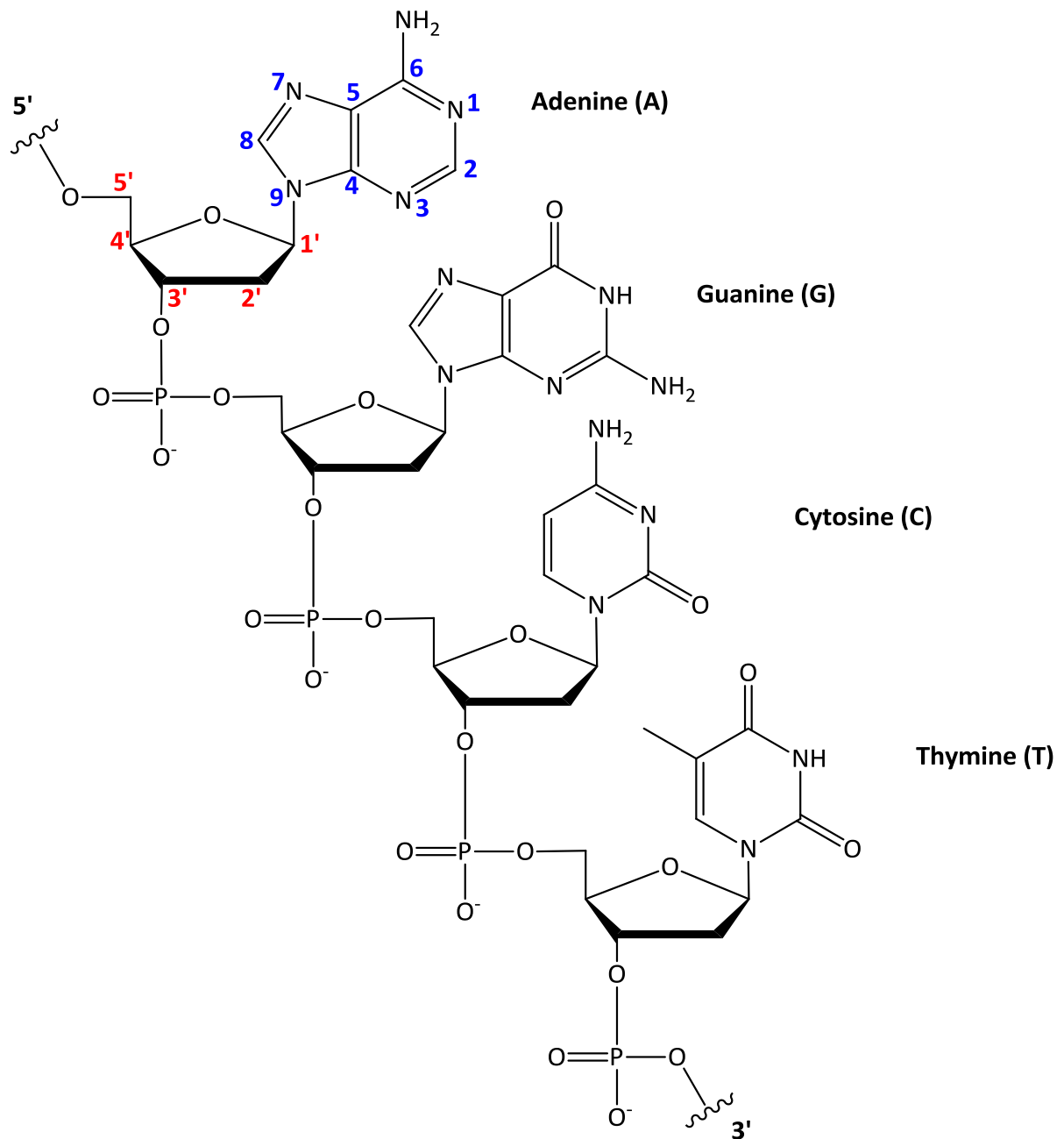
Figure 1.3 - Chemical structure of single stranded DNA for the sequence AGCT (hydrogen atoms omitted for clarity, labelling convention included on the first nucleotide)

The key to all of DNA's remarkable functions are the specific interactions between the bases G-C and A-T through hydrogen bonding, known as complementary base pairing, when two single strands run anti-parallel to each other (*Figure 1.4*). The two sugar-phosphate backbones are held apart at a constant distance throughout the molecule because of the two base pairings having the same width. This leads to the secondary structure of DNA,

which allows the bases to be packed in the most energetically favourable way in the interior and leaves the negatively charged backbone exposed on the outside.[3] The packing is most efficient when the backbones twist around one another, resulting in one complete turn every ten base pairs to give the classical double helix depiction of DNA - two polynucleotide chains held together by the hydrogen bonded base pairs that are perpendicular to a central axis around which the backbones twist (*Figure 1.4*).
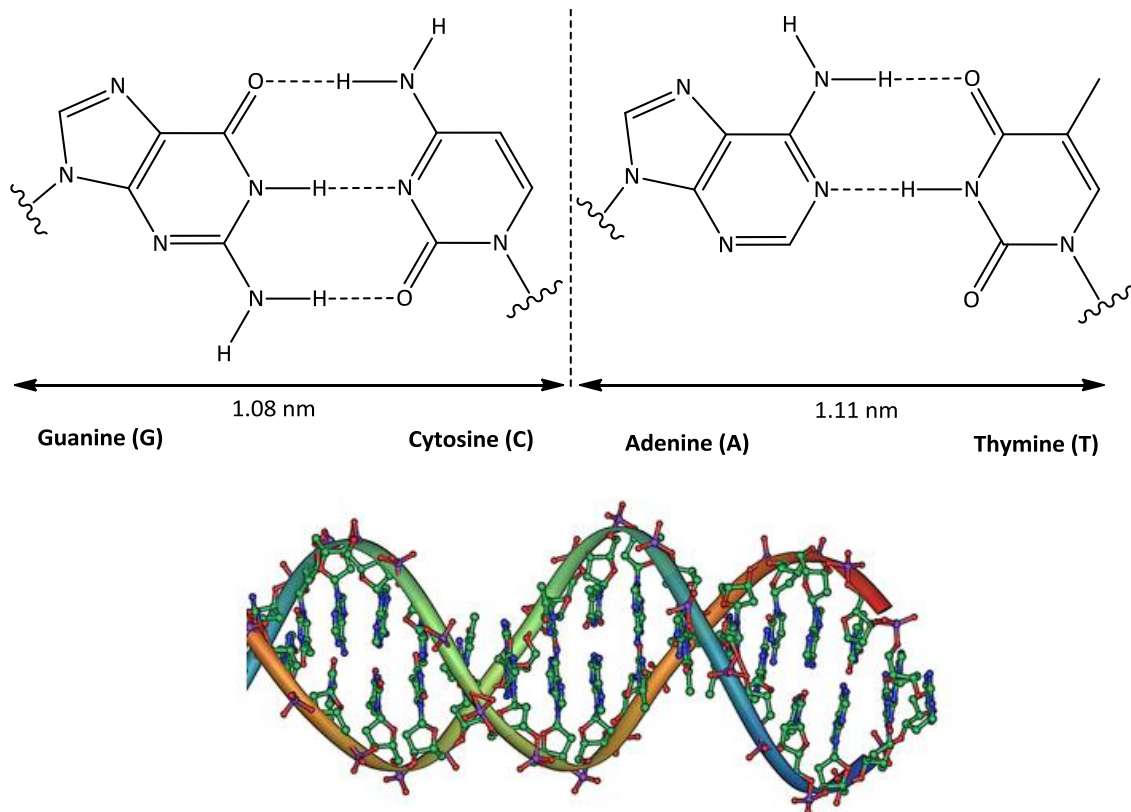
Figure 1.4 – Above: Complementary base pairing. Below: Double helical DNA representation

Adjacent base pairs are offset by a rotation of 36º and spaced 0.34 nm apart, which gives a repeating structure of ten base pairs in one 360º rotation over a 3.4 nm distance, and allows sufficient overlap of the planar surfaces for a stacking interaction that further stabilises the helix.[4] The bases also twist slightly in the plane of the base pair (5º to 25º between two bases in a pair) to increase the packing efficiency further, although as purines occupy the centre of the double helix, when there is an alternating purine-pyrimidine sequences they overlap with purines in the opposite strand and cause steric hindrance, but purine-purine and pyrimidine-pyrimidine sequences have no such clashes.[5]

Once the secondary structure of DNA was discovered by Watson and Crick in 1953[1] it was immediately clear from the nature of the complementary base pairing that DNA can be used as a template to copy itself. This involves the double strand being reversibly unzipped by cellular machinery (the enzyme DNA helicase) to allow free nucleotides to partner each single strand and form two copies of the original double helix. This elucidated the mechanism of DNA replication and ultimately the relay of genetic information.

1.1.2   Conformations

There are 3 major conformations of DNA found in vitro – A, B and Z. Which conformation is adopted depends on two variations of the nucleotides sugar entity, which in turn determines how the base is directed relative to that sugar (*Figure 1.5*).
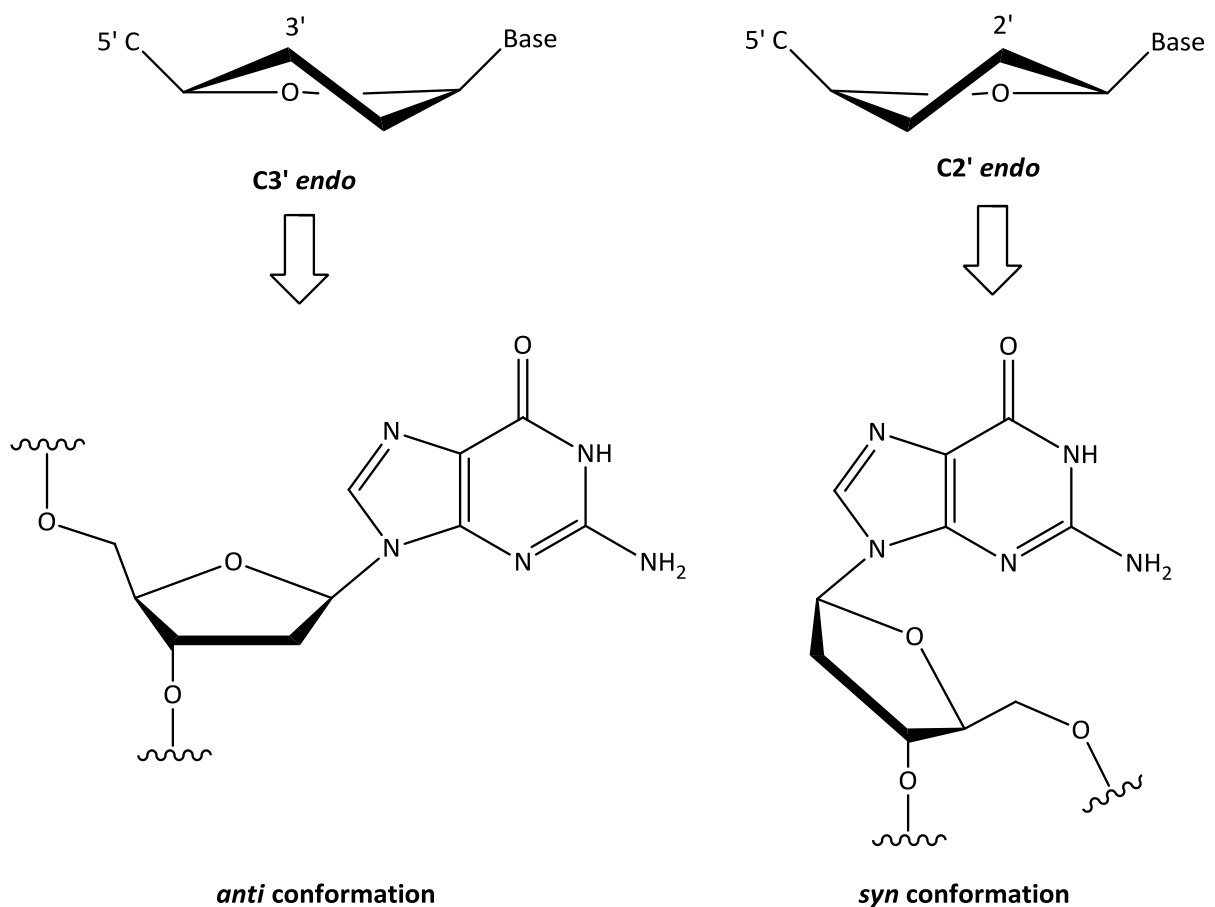

Figure 1.5 - C3' and C2' *endo* conformations of the deoxyribose sugar

The two sugar conformations are determined by which of the carbon atoms are directed upwards in an 'endo' position, either the 3' or 2' carbon, which lead to the *anti* and *syn* conformations, respectively, of the corresponding nucleoside. In the syn conformation, if the position of the base is maintained, for a planar base pair, it is the direction of the sugar phosphate backbone which is distorted from the most commonly observed classical double helix conformation of B-DNA. The 3 conformations of DNA and some of their properties are shown in *Figure 1.6*.[4]
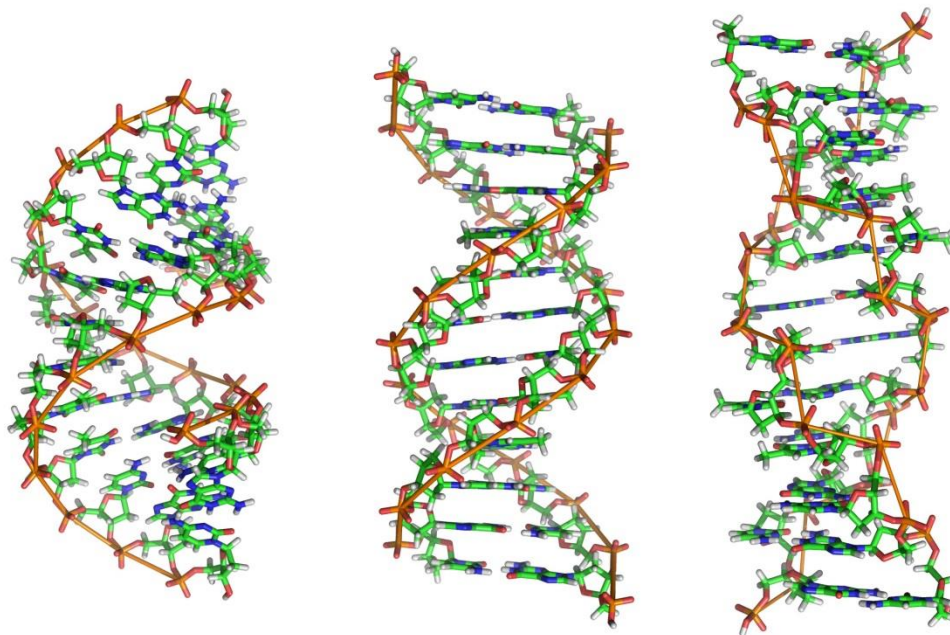
Parameter	A-DNA	B-DNA	Z-DNA
Helix sense	Right	Right	Left
Residues per turn	11.0	10.5	11.6
Axial rise	2.6 Å	3.4 Å	3.7 Å
Helix pitch	28 Å	36 Å	45 Å
Rotation per residue	33˚	36˚	-9˚, -51˚
Diameter of helix	23 Å	20 Å	18 Å
Sugar pucker:			
A, T, C	C3' *endo, anti*	C2' *endo, anti*	C2' *endo, anti*
G	C3' *endo, anti*	C2' *endo, anti*	C3' *endo, syn*
Major groove	Narrow, deep	Wide, deep	Flattened
Minor groove	Wide, shallow	Narrow, deep	Narrow, deep

Figure 1.6 - From left to right A-DNA, B-DNA and Z-DNA, and a table of parameters[4].

The environmental factors that determine which of the conformations is adopted include relative humidity, the amount of salt retained and the cation species that are present. For example the most commonly occurring form, B-DNA, has a high level of hydration around the structure.[4]

All of the conformations have strands running anti-parallel and A- and B-DNA are both right-handed helices with the glycosidic link in the *anti*-conformation, so appear similar, but A-DNA is wide and compact with bases displaced from the centre of the axis, whereas B-DNA is narrow and elongated with the bases perpendicular to the axis. The preference for the A-DNA conformation arises in dehydrated conditions which is often the case in samples prepared for crystallographic studies. Using the hydrophilicity of base pairs as a key factor, accurate sequence based methods to predict the adoption of A- versus B-DNA have been determined.[6]

Z-DNA is strikingly different because it is a left-handed helix and is the most elongated. It is most likely to form with long guanine and cytosine containing sequences. There is a distinctive zigzag in the backbone due to an alternating *syn* and *anti* conformation of guanine and cytosine that causes an inversion in the direction of the backbone; producing a repeating structure of only two base pairs (purine plus pyrimidine)[4]. A large body of work has been carried out looking into the occurrence and importance of Z-DNA *in vivo*[7] but to date almost all the DNA in cells and aqueous solution has been found to be in the B-DNA form, therefore this is the most relevant conformation for research on DNA interactions.

1.1.3   The Major and Minor Groove

An important feature of the secondary structure of DNA is the major and minor groove - these are the areas between the phosphodiester backbones that are exposed as an external surface of molecule and have a chemical composition unique to the sequence. The width of the grooves depends on the conformation of DNA. In B-DNA the major groove, as the name suggests, is wider (12 Å) than the minor groove (6 Å). The asymmetrical groove width arises from the glycosidic linkage being off-centre of the base-pair, which results in the two backbones twisting around the base pairs more on one side (*Figure 1.7*).
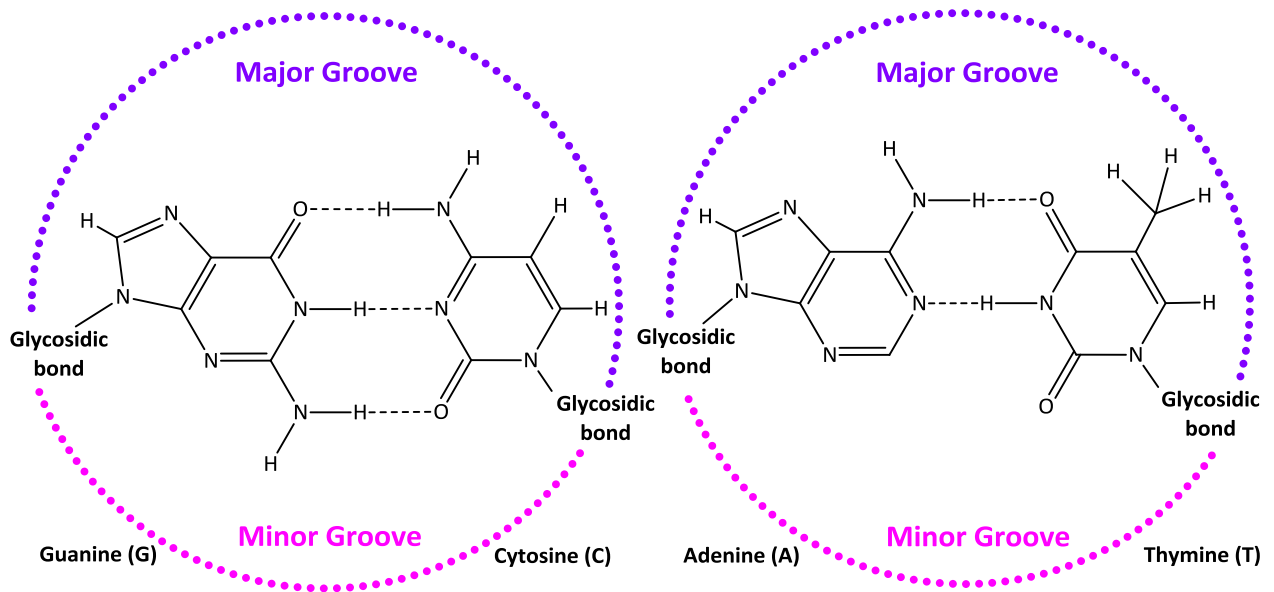
Figure 1.7 - Major and minor groove relative to the two base pairs

As neither base pair is symmetrical there are four combinations of bases that consist of different chemical environments with different hydrogen bonding abilities, through a pattern of donors and acceptors along with the non-hydrogen bonding lone hydrogen atoms, and on thymine, the steric contribution of a methyl group. These contributions to the surface form a pattern for each of the four base pair combinations and give a secondary code to supplement the primary base pair sequence, with the major groove offering four different patterns, but the minor groove having only two combinations, as the pattern is repeated when each of C-G and A-T are reversed. This information can be used by proteins and other biomolecules to read the DNA sequences without needing to unwind the double helix; generally through the major groove as this is definitively unique for different sequences.

1.1.4   Cellular DNA

In the cellular environment the amount of DNA is too great to simply exist as a double helix and it undergoes a remarkable packaging process to give the whole genome in highly-condensed portions of unbroken DNA, known as chromosomes, contained within the nucleus, a sub-cellular compartment with its own membrane. To put the task into

perspective, if all of the double helices in a human cell were laid end to end they would reach 2 meters, yet the nucleus is only 6 μm in diameter.[3]

The complex of DNA and associated proteins that exists in the nucleus of a cell is known as chromatin and is made up of several organisational tiers. Firstly, DNA wound around histone proteins forms nucleosome core particles which with an unwound linker region of DNA make a nucleosome, continuing in series to give the "beads on a string" model (*Figure 1.8*).[8]
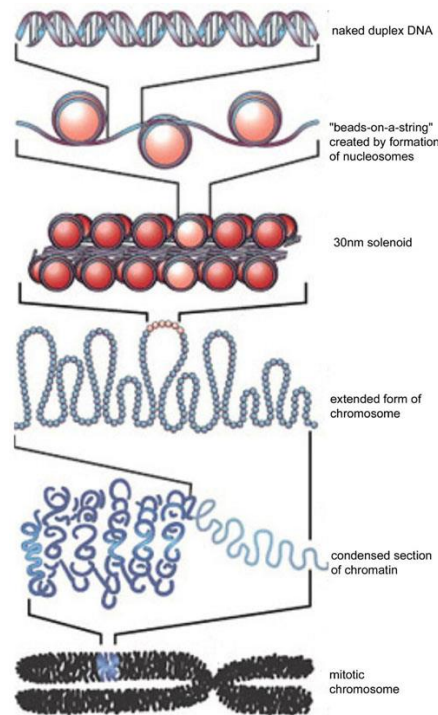
Figure 1.8 – The formation of chromosomes from duplex DNA[8]

This assembly results in a length of chromatin approximately one third of the initial length, which is then packed on top of each other to make a fiber 30 nm in diameter, with the exact architecture not definitively determined but thought to be of a zig-zag form. This 30 nm wide chromatin fiber of packed nucleosomes, however, would still be 0.1 cm in length, so the chromatin is folded into a series of loops and coils and then, during cell division, is formed into the chromosomes often seen in microscopy images.[3]

Chromatin can generally be described as either tightly condensed heterochromatin or lightly condensed euchromatin. Heterochromatin can commonly be seen forming structural regions of the chromosomes or as an example of genes switched off from expression by being inaccessible to transcription and translation processes. Euchromatin is often more

actively involved in transcription and generally has a higher concentration of genes than regions of heterochromatin.[9]

In addition to the chromatin found in the nucleus, mitochondrial DNA also exists in the membrane-bound organelle responsible for energy production in the cell. This DNA, however, is not only a separate genome but rather than packaged into chromosomes, is present in a closed circular double helix form. The presence of this is an important consideration when thinking of direct molecular targeting of DNA within a cell, as the nuclear and mitochondrial forms that are present could offer different binding affinities and outcomes upon interference.[3] In the studies within this thesis, however, molecular photophysical properties offer visualisation of DNA targeting to elucidate this possibility.

1.2   Binding Modes

Many molecules ranging from small organics to vast protein structures can bind to DNA and this can occur both irreversibly and reversibly through several different binding modes. As DNA is responsible for all cellular functions it is a very important target for a massive range of therapeutics, and understanding the interactions that are possible is therefore a vital field of research.

1.2.1   Irreversible Binding

Irreversible (covalent) binding can occur on the backbone, sugar residue or base, resulting in the formation of a covalent bond. There can be one or more covalent bonds from the molecule to DNA formed, and in the case of multiple bonds they can either be on the same strand (intrastrand) or bridge across two strands (interstrand). When the structure of DNA is sufficiently modified to disrupt the reading of the DNA code then transcription is the main process affected, which results in modified gene expression or cell death.

In therapeutic terms, this type of interaction covers the most successful treatment to date for a variety of cancers – cisplatin (diamminedichloroplatinum) and its derivatives.[10] This class of molecule binds specifically to the N7 of guanine or adenine, across two strands, to form intrastrand crosslinks which significantly alters the shape of the helix (*Figure 1.9*).[11]
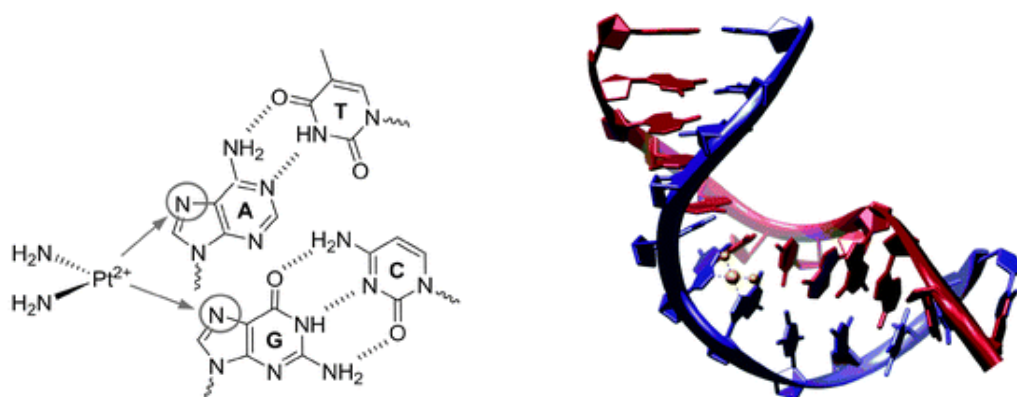

Figure 1.9 – The irreversible binding mode of cisplatin with 2D NMR solution structure of DNA binding through a GpG intrastrand crosslink[11] (PDB 1A84)

1.2.2   Reversible Binding

Molecules can also bind to DNA through weaker non-covalent interactions, collectively known as reversible binding, of which there are three main modes - electrostatic binding, groove binding and intercalation.[12]

1.2.2.1   Electrostatic Binding

Electrostatic binding to DNA is the simplest of the reversible binding modes and relies on a non-specific electrostatic attraction between a cationic species and the negatively charged polyanionic phosphodiester backbone of DNA. The cationic species can be simple monovalent cations or larger polyatomic species, for example, organic species containing amine groups such as spermidine (*Figure 1.10*).
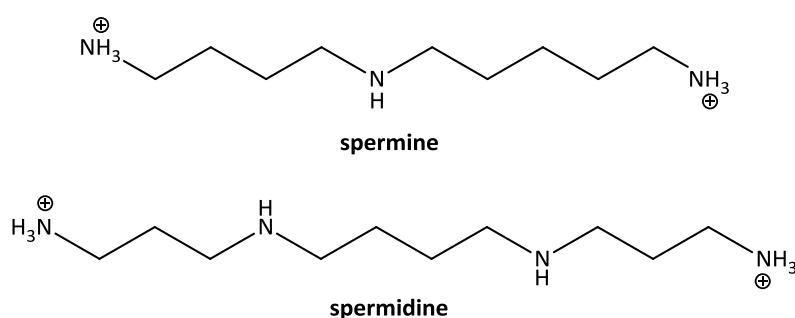
Figure 1.10 - Cationic species suitable for electrostatic binding to DNA

The backbone of DNA is polyanionic therefore to remain stable in solution it must undergo an effect known as counter-ion condensation. First described by Manning's theory in 1969, this states that counter-ions will condense onto the polyion until the charge density on the polyion is reduced below a certain critical value.[13] It is termed condensation as the counter-ions form a cloud rather than be associated to specific sites, with the ions retaining their inner hydration sphere and being allowed to move along the sugar phosphate backbone.[13] If the salt concentration of the solution is diluted the condensed ions will remain constant per phosphate charge on the backbone.[13] The uncondensed mobile anions are then treated in the Debye-Hückel approximation. The main effect of DNA condensation is an increase in the

melting temperature, T_m, the temperature at which the double stranded helix unwinds into two separate single strands.[5]

Counter-ion condensation also becomes an important effect for the other two reversible interactions of groove binding and intercalation. The release of these counter-ions when displaced by the binding molecules is entropically favoured and can count towards the overall free energy of the binding.[5]

1.2.2.2   Groove Binding

Groove binding can occur in either the minor or major groove and relies on a combination of reversible van der Waals, hydrophobic or hydrogen bonding interactions. Molecules can show high sequence specificity due to the interaction with the edges of the base pairs that make up the inside of the grooves surface, and are usually specific to either the minor or major groove as there is a distinct difference in width and chemical environment.[5] In general, groove binders are more sequence specific than intercalators because they can cover many base pairs.[5]

Groove binders such as the well-studied molecule netropsin do not usually elongate the helix as the molecules bind.[14] Although this molecule has been shown to widen the minor groove and bend the helix slightly as it binds, neither structural change unwinds or elongates the helix.[15] In fact, these changes make only a subtle difference to the structure of DNA and it remains essentially unperturbed in B-DNA form.[16]

The mechanism of groove binding can be likened to the enzyme-substrate lock and key model. Groove binders are often positively charged so with the counter-ion condensation effect there will be a displacement of counter ions as the charge density of DNA is decreased upon binding, which is an entropically favourable contribution to the overall free energy.[5]

Minor groove binders often consist of aromatic rings with flexible linkages to allow an adjustable curvature in the molecule for an isohelical fit into the groove, maximising contact for van der Waals interactions. An example of specificity for the minor groove being increased is in adenine rich sequences which have an increased propeller twist that causes a narrowing of the minor groove, thus enhancing van der Waals contacts and producing more

favourable binding.[5] In contrast, in the C-G base pair the C2 amine group on guanine projects out into the minor groove edge as it hydrogen bonds with the C2 carbonyl of cytosine, therefore disfavouring minor groove binding for C-G rich sequences.[5] This, however, can be overcome if the molecule is capable of forming hydrogen bonds with the guanine C2 amine group.

DAPI (4',6-diamidino-2-phenylindone) is a another minor groove binder that can be used as a fluorescent stain for live or fixed cells with a high binding affinity for A-T rich regions of DNA.[17] Another commonly used stain for nucleic acids is Hoechst 33258, which is also a minor groove binder as can be seen from the crystal structure (*Figure 1.11*).[18]
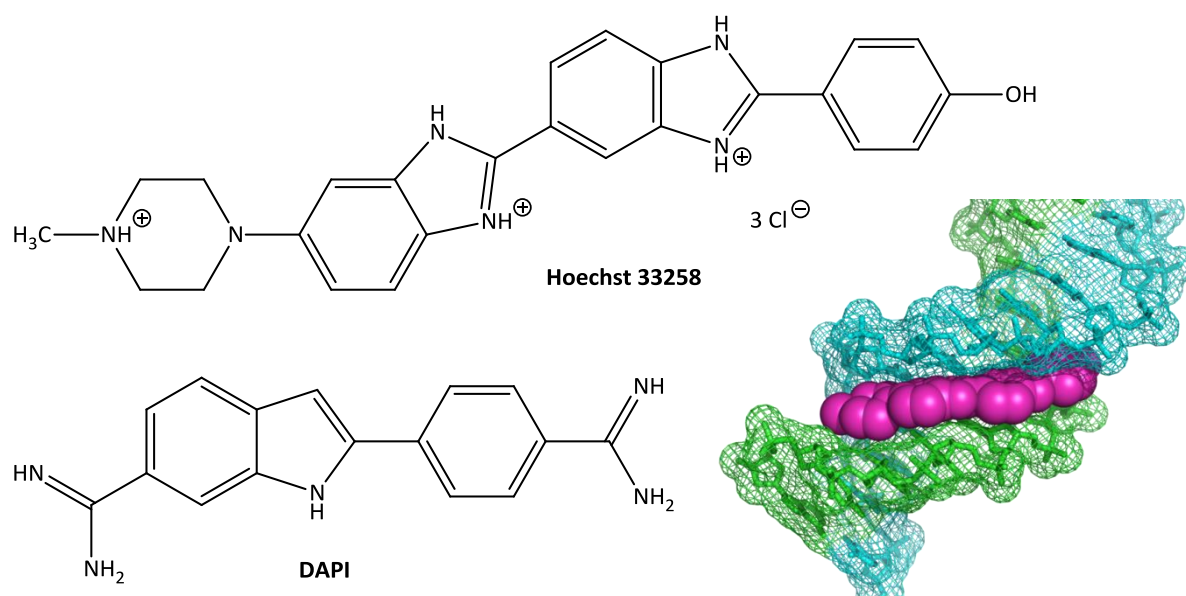
Figure 1.11 – DAPI and Hoechst 33258 with crystal structure of DNA binding[18] (PDB 264D)

The major groove can offer even more sequence specificity than the minor groove because it has a greater number of variables in the pattern of different hydrogen bonding interactions i.e. for each base pair there are four different areas rather than three, and there is no symmetry in the pattern so four unique combinations, rather than two for the minor groove where the hydrogen bonding pattern has symmetry in each base pair. This results in many protein binding interactions where the function of the protein is highly specific to the sequence of DNA.[5]

1.2.2.3   Intercalation

Ligand intercalation is the insertion of a molecule into double stranded DNA, with an associated extension of the helix as the base pairs either side of the insertion site open up to accommodate the additional planar molecule, first proposed by Lerman in 1961.[19–21] The first evidence for intercalation was found through investigations of acridine complexes when bound to DNA and the effects this had on DNA viscometry and sedimentation. It was concluded that acridine complexes intercalated between adjacent nucleotide pair layers by extension and unwinding of the deoxyribose-phosphate backbone (*Figure 1.12*).[19]

R = H   Acridine
R = NH$_2$ Proflavine
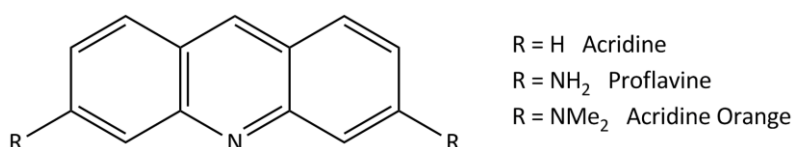R = NMe$_2$ Acridine Orange

Figure 1.12 - Chemical structure of the intercalators acridine, proflavine and acridine orange

Intercalators usually consist of an extended, electron deficient, planar aromatic ring system, with two or more six-membered rings forming a platform similar to a DNA base pair.[5] The intercalator has an associated van der Waals thickness that has to be accommodated in the intercalation site, which from a planar aromatic system usually results in an extension of the helix by 3.4Å.[22] This unwinds the helix at the site of intercalation and although only reducing the degree of rotation between the immediate base pairs sandwiching the intercalator by a small amount, this then has a knock on effect seen throughout the whole structure, so it is the cumulative modification of the helical twist in all of the affected base pairs that is measured for the unwinding angle.[5]

Since its identification in the 1960's, the interaction has been intensively studied, with the changes that occur upon intercalation summarised in three steps: unwinding and lengthening of the DNA helix, electronic interaction of the intercalators within the helix, and rigidity and orientation of the intercalator.[22] The electronic interaction is stabilised in the helix by π-π stacking and dipole-dipole interactions, and with substantial structural overlap of the base pairs and intercalator it is then held rigidly in place and orientated with the planar moiety perpendicular to the helical axis for the final step.[22] From these three steps it

can be deduced that corresponding experimental criteria are to be fulfilled to confirm intercalation – evaluation of structural changes to DNA, indication of an electronic interaction and demonstration of molecular orientation or rigidity.[22]

For the first criterion, macromolecular effects on the structure of DNA must be investigated, such as changes in the solution viscosity of bulk DNA or sedimentation coefficient, as originally used by Lerman.[19] Also, a downfield shift in the ^{31}P spectrum of the phosphodiester backbone can be observed.[23] For the second criterion, hypochromism and a shift to longer wavelength of the transition for the intercalated chromophore can be observed[24], along with emission enhancements if the molecule is capable of luminescence, showing a change in electronic structure of the excited state.[22] From the ^{1}H spectrum there should also be an upfield shift in the aromatic protons of the intercalator observed; due to the ring currents of the stacked aromatic bases.[25] For the final criterion, the bound orientation of the molecule relative to the helical axis can be detected by dichroic techniques or luminescence polarisation which will also establish the time over which there is rigid binding.[22,26]

Whilst indicating intercalation, not all of the investigations mentioned above can reliably differentiate from groove binding. The criteria for defining the difference between those two binding modes has been well documented and the techniques originally concluded to definitively differentiate between them were viscometry and fluorescence contact energy transfer measurements, but not other fluorescent techniques.[16] The first technique uses the substantial change in the DNA structure after intercalation rather than the unperturbed B-DNA form upon groove binding, and the second relies on the interaction of intercalators with base pairs.[16] The fluorescence contact energy transfer, however, has since been found to occur in some cases of groove binding so is viewed with great caution as a differentiator. This leaves viscometry measurements as the only truly exclusive indication of intercalation.[27] Another more recent technique used after this debate is Scanning Probe Microscopy, SPM, which measures the length of plasmid DNA in the presence and absence of DNA binders and therefore detects the lengthening of the helix from intercalation.[28] These techniques are all aside from conclusive atomically resolved crystallographic determination, an option employed in an ideal situation where a suitable crystal is obtained. As more intercalative molecules were investigated, with an expansion away from completely intercalative molecules to those containing merely functional domains or

regions, a review by Long and Barton highlighted that total molecular shape and function are of importance, particularly in systems with multiple binding modes and domains.[22] The importance of such structural considerations was demonstrated in studies into intercalation of metalloporphyrins containing metals that were either capable or incapable of axial ligation[29], an investigation of the effects of molecular twist on non-fused aromatic rings[30], and a comparison of (bi-pyridyl)platinum(II) and bis(pyridine)platinum(II) species to demonstrate the need for ligand planarity.[31]

As the significance of intercalative molecules grew, the specific structural aromatic requirements of the intercalating moiety were investigated by Sartorius *et al.* with 38 different structures.[32] It was concluded from this study, primarily using NMR, that single phenyl rings do not intercalate either as benzene or with additional charged side chains.[32] Two fused rings when unmodified (naphthalene) or with neutral side chains do not intercalate either, but when the naphthalene core has a charged side chain, it becomes an intercalator, and for three fused rings and higher there is intercalation even in their unmodified neutral form (*Figure 1.13*).[32]
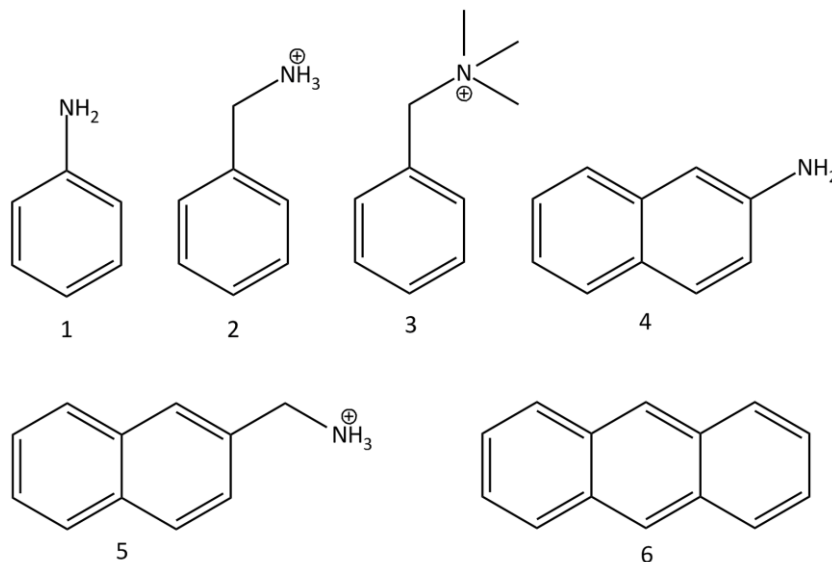

Figure 1.13 - Aromatic requirements for intercalation - 1-4 do *not* intercalate, 5-6 do intercalate

The most important use of intercalators is as a therapeutic against a variety of diseases including cancer. A widely used class of intercalating drugs are anthracyclines which are

antibiotics obtained from the *Streptomyces* bacteria, for example the therapeutic daunomycin (also known as daunorubicin) in the treatment of a variety of cancers by inhibiting DNA replication and RNA transcription (*Figure 1.14*).[33,34]
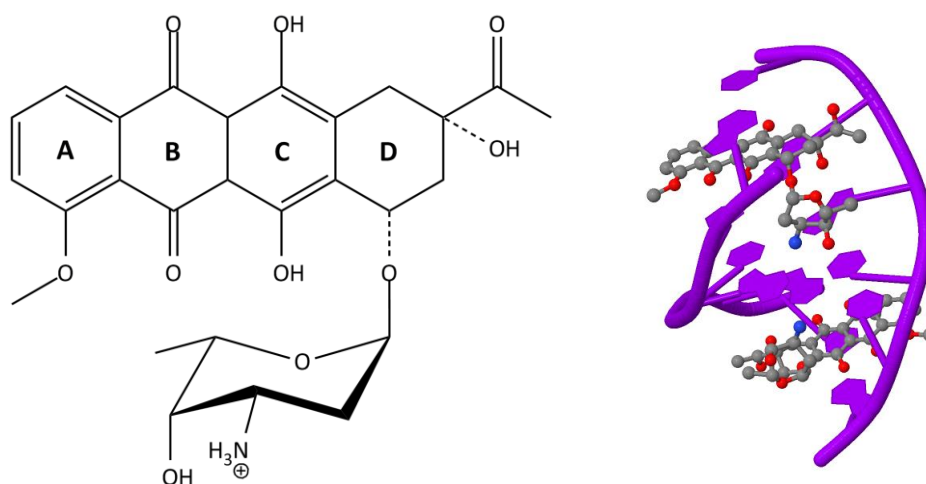

Figure 1.14 – Chemical structure of daunomycin and crystal structure complexed to d(CGTACG) DNA[35] (PDB 1DA0)

The crystal structure of daunomycin bound to DNA, specifically the sequence d(CGTACG), has been resolved to show the exact binding orientation and an intercalation preference for insertion in-between adjacent C-G base-pairs flanked by A-T pairs, as predicted.[36–38] The exact orientation is with the long axis of the four fused rings almost perpendicular to the base pair axis, with the central two rings (B and C) nestled in the cavity between base pairs but the methoxy substituted ring (A) protruding into the major groove and the amino sugar protruding into the minor groove (*Figure 1.14*).[35]

The preference for insertion in-between G-C base pairs arises from the hydrogen bonds from the hydroxyl group on ring A donating to guanine N3 and being an acceptor for the guanine N2 amino group. Also, ring A and the amino sugar change their conformation as binding occurs to ensure a tight fit of the sugar into the minor groove, which is stabilised by two bridging water molecules between this group and the DNA. There is also stabilisation in the major groove by a hydrated sodium ion coordinated to the guanine N7 and the two carbonyl oxygen's of daunomycin ring B with a distorted octahedral geometry.[34]

1.2.2.4　　Mechanism of Intercalation

The mechanism of intercalation is described as an 'induced fit' rather than the contrasting 'lock and key' of groove binding.[39,40] This mechanism requires three distinct steps of varying thermodynamic favourability.[39] The first is the separation of DNA to form the site of intercalation: an energetically unfavourable conformational change as it unwinds the DNA and increases the phosphate spacing, although entropically favourable as this lengthening reduces the charge density of the backbone and releases condensed counter-ions. The intercalator must then move from the bulk solution to the site and as the planar aromatic moieties are hydrophobic it can be referred to as the 'hydrophobic transfer process', the main energetic driving force behind intercalation. This is due to more entropic favourability as DNA-bound water molecules, previously in a well ordered hydration layer, are released, as well as positively charged intercalators then facilitating the additional release of condensed counter ions. Finally the non-covalent interactions between the molecule and DNA are established, which involves a combination of hydrophobic effect, reduction of columbic repulsion, van der Waals interactions, π-stacking and hydrogen bonding. Chaires described how these mechanistic steps contributed to the overall free binding energy using *Equation 1.1*.[39] The experimentally observed binding free energy is defined as ΔG$_{obs}$ and related to the binding association constant (K) by the standard Gibbs relationship seen in *Equation 1.2*.

The contributions to the binding free energy are defined as follows:

ΔG_{conf} = conformational changes in DNA structure and drug

ΔG_{t+r} = losses in translational and rotational degrees of freedom

ΔG_{hyd} = hydrophobic transfer of drug from solution into its binding site

ΔG_{pe} = polyelectrolyte contribution from released counter-ions

ΔG_{mol} = formation of non-covalent interactions

$$\Delta G_{obs} = \Delta G_{conf} + \Delta G_{t+r} + \Delta G_{hyd} + \Delta G_{pe} + \Delta G_{mol}$$

Equation 1.1 - Contributions to the overall binding free energy

$$\Delta G_{obs} = -RTlnK$$

Equation 1.2 – The standard Gibbs relationship where R = gas constant and T = temperature

1.2.2.5 **Bisintercalation**

As with many therapeutic molecules, the successful outcome from treatment with the intercalator daunomycin can be jeopardised by resistant cell lines. One interesting attempt to overcome resistance to daunomycin was to bind two of the drug molecules together to increase the binding affinity to DNA.[41–45] Bis-daunomycin was designed from a consideration of the crystallographic information obtained on daunomycin bound to hexanucleotides in a 2:1 ratio of drug to DNA duplex. This showed that one molecule intercalated at either end of the nucleotide, with the daunosamine moieties pointing inwards towards each other, revealing a logical link up between the two amino sugars: the reactive NH_2 substituents which face each other with a separation of less than 7Å.[41] In turn the crystal structure of the designed new molecule complexed to DNA was obtained to support the experimental data and confirm its bis-intercalation, with the para-xylene linker clearly seen to occupy the minor groove (*Figure 1.16*).[45]
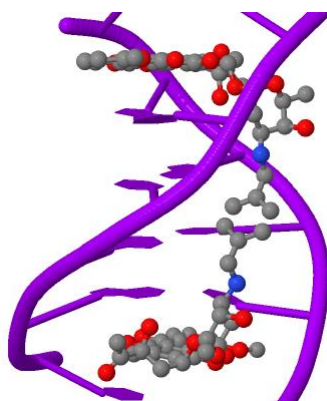

Figure 1.16 – Crystal Structure of DNA-bisdaunomycin complex[45] (PDB 1AGL)

The concept of bisintercalators possessing stronger affinity comes from the theory of binding constants being the product of multiplication. Theoretically the binding free energy of the bisintercalator is equal to the addition of the two monomers (*Equation 1.3*).[41]

$$\Delta G_{bis} = \Delta G_{mono} + \Delta G_{mono}$$

Equation 1.3 - The relationship between mono and bisintercalator binding free energies[41]

However as to the relationship between ΔG and K is logarithmic (*Equation 1.2*) this means the binding affinity of the bisintercalator is the square of the monointercalator
This theoretical relationship was experimentally observed as techniques, including differential scanning calorimetry, revealed ultratight binding with a binding constant of 3.1 x 10^{11} M^{-1} at 20 °C.[42]
Another theoretical advantage of bisintercalation is that sequence specificity should be increased as, for example, in the case of daunomycin the molecule now spans six base pairs rather than three. This site size is equal to the cleavage site for some restriction enzymes so there is potential for binding specificities analogous to these enzymes.[41] The preferential binding site was found to be the expected sequence (G/C)(G/C)(A/T)(A/T)(G/C)(G/C) with no preference for unique di-, tri- or tetra-nucleotide sequences.[43]

1.3   Metal Complexes and DNA

As studies into interactions with DNA continued and the range of small organic molecules capable of a variety of interactions expanded, attention was turned to transition metal complexes. This avenue of investigation is not immediately obvious as in nature transition metals are almost exclusively only found in the coordination sites of large proteins and cofactors, with the cell generally employing organic moieties for the binding and recognition of DNA.[46] The advantages offered by metal centred systems, however, is that they are modular system with set geometries making a scaffold of functional ligands, and in addition a whole spectrum of photophysical and electrochemical properties.[46] Although this project explores the non-covalent interactions of metal complexes and the effects they have, a related field of study is already well developed. The covalent interactions of metal complexes with DNA was started by the revolutionary discovery of the anticancer drug cisplatin.[10]

1.3.1   Irreversibly Binding Metal Complexes

The field of irreversibly bound metal-DNA complexes all started with a serendipitous discovery of cisplatin's biological activity in 1965.[10] With the continued development of this remarkably successful class of compounds came exploration into other metals, notably ruthenium.[47–51] Osmium and iridium complexes have also been investigated with positive therapeutic outcomes from irreversible binding with DNA.[52–55]

1.3.1.1   Cisplatin and Derivatives

Rarely in science has there been such a significant and successful outcome from an unintentional discovery as that of cisplatin. The success story started with the work of Rosenberg investigating the possible effects of electromagnetic radiation on the division of mammalian and bacterial cells.[10] In the case of *Escherichia coli* supposedly inert platinum electrodes were included in the growth chamber and when a current was applied, the

outcome was bacteria filaments that grew to three hundred times the expected length of the usual short rods.[10] It was found that the electrolysis products from these electrodes that were the cause of the effects observed with two active products being formed – the neutral platinum(II) species *cis*-diamminedichloroplatinum(II), now known as cisplatin, and a platinum(IV) analogue *cis*-diamminetetrachloroplatinum(IV) (*Figure 1.17*).[10]

cis-diamminedichloroplatinum(II)   *cis*-diamminetetrachloroplatinum(IV)
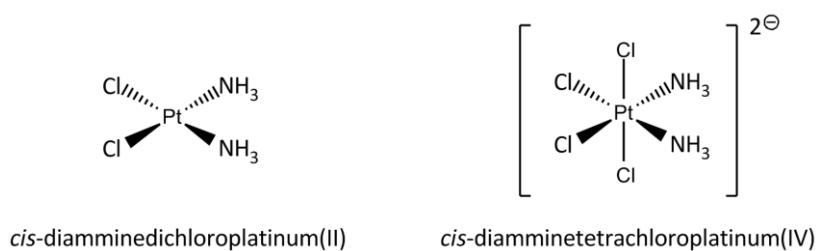
Figure 1.17 - The two active electrolysis products of the platinum electrodes

In contrast to the *cis* isomers, the *trans* isomer was found to be much less active.[10] This active species was not a novel compound but one first synthesised in 1885 and known as Peyrone's chloride. In 1968, only three years after Rosenberg's discovery, cisplatin was administered intraperitoneally to mice carrying a tumour and marked tumour regression was observed. After more confirmatory *in vivo* tests, in 1971 the first patients were treated to complete a remarkably quick turnaround from 'on the bench' discovery to the admission to humans in clinical trials. These trials culminated in US Food and Drug Administration (FDA) approval in 1978 to conclude the success story of anti-cancer treatment that is now used throughout the whole world.

The mode of action of cisplatin centres on the formation of intrastrand crosslinks in DNA double helices. The first step in this process is the aquation of one of the labile chloride ligands, which occurs at chloride concentrations less than 100 mM, as found in cells.[56] The aqua ligand is then easily displaced to allow covalent binding to one of the DNA bases, which in most cases has been found to be the N7 of guanine.[57] The second chloride can then undergo aquation and form another covalent bond to an adjacent guanine on the same strand to form an intrastrand GpG 1,2 crosslink (60-65%) or in some cases adenine for an intrastrand ApG 1,2 crosslink (20-25%); with small proportions seen to bridge across a base in-between the two covalent linkages or bridge across two strands for an interstrand crosslink.[57] These adducts result in the DNA bending and unwinding but the pathway from

these DNA-distorting-adducts to the usual outcome of apoptotic cell death is still debated.[10] It is thought that as well as the adducts impeding cellular processes such as replication and transcription they can be recognised by cellular proteins which in turn activates downstream signalling leading to apoptosis (programmed cell death).[58] Targeting DNA has proved such a successful strategy in cancer treatments because rapidly proliferating cells of the tumour environment are preferentially targeted as they require high rates of DNA replication. Induced apoptosis is then a successful outcome as the apoptosed cells can be taken up by macrophages.

The success of cisplatin is not without drawbacks – namely a very high toxicity and the possibility of resistance either intrinsically or acquired throughout treatment. Toxicity towards the kidneys and gastrointestinal tract is particularly apparent, as a consequence the search began for an alternative that retained anti-cancer activity yet lessened toxic side effects. The design principle pursued to achieve this goal was to replace the chlorides of cisplatin with a more stable leaving group, leading to clinical trials of carboplatin (*cis*-diammine-[1,1-cyclobutanedicarboxylato]platinum(II) (*Figure 1.18*) which proved the hypothesis correct, as the compound negated the nephrotoxicity and reduced the other side effect toxixcities.[59] It was shown that only the kinetics of DNA binding differed with a much slower aquation of carboplatin requiring thirty-forty times the dosage of cisplatin to achieve equivalent binding to DNA, but once bound exactly the same adducts were formed, resulting in the same cytotoxicity.[60] Carboplatin was granted FDA approval in 1989 and in most countries replaced cisplatin regimes as an equivalent treatment, for example in several randomised clinical trials ovarian cancer survival rates are the same.[61]

With one problem of cisplatin significantly reduced, attentions were focused on the other major drawback of intrinsic or acquired resistance. This resistance can be broken down into two categories – the prevention of cisplatin forming DNA adducts and the mechanisms used to counteract or remove the DNA adducts once they have been formed.[10]

The first category covers the cellular uptake and any removal thereafter from the cytoplasm before association with the DNA occurs. The uptake of cisplatin is governed by molecular characteristics, for example its high polarity means its passive entry into cells is relatively slow and is dependent on factors such as salt concentrations and pH, for passive diffusion. However, it has been shown that the plasma membrane transporter copper transporter-1 (CTR1) is also used in its cellular uptake.[62] This is key to many cases of acquired resistance as

exposure to cisplatin, or copper, can lead to downregulation of this transporter; which mediates internalisation by macropinocytosis followed by proteasomal degradation.[63] As well as the uptake of the drug, efflux out of the cell must be considered. There is now evidence that the same efflux proteins involved in copper transport can also be responsible for exporting cisplatin.[64] A final factor prior to DNA binding is reactivity in the cytoplasm with thiol-containing species that act to detoxify the cell.[10] For example the tripeptide glutathione as well as metallothioneins are rich in the sulfur-containing amino acids cysteine and methionine for which platinum has a high binding affinity.[65,66] Binding of cisplatin to glutathione may also be mediated by glutathione-S-transferase (GST). The reactions catalysed by this enzyme makes the compound more anionic and readily removable from the cell via the ATP-dependant glutathione S-conjugate export (GS-X) pump[67], with one study showing an increased level of GST in the resistant cell lines versus the sensitive cell lines.[68]

The second category of resistance involves processing of cisplatin-DNA adducts. This is usually through an increased capacity to repair the DNA by the removal of the cisplatin adducts. Although this can occur through four different pathways, that involving nucleotide excision repair (NER) is known to be the major mechanism.[69] NER has been shown to have a significant effect as when the expression of one of the key endonuclease proteins ERCC1 (excision-repair-cross-complementing-1) involved in NER is reduced by interfering RNA molecules (containing a complementary code to the sequence of the gene) there is an increased sensitivity to cisplatin with less NER of cisplatin-DNA adducts.[70] Another post-adduct mechanism of resistance is increased tolerance to mismatch repair (MMR). Despite being one of the pathways in repairing adducts, it is postulated that when the associated proteins recognise the adducts several unsuccessful repair cycles are undertaken before an apoptotic response is initiated therefore loss of this mechanism results in less apoptosis.[71] Also there can be an enhancement in replicative bypass in which DNA polymerases overlook the cisplatin adducts.[72] Finally, expression of apoptotic signalling pathways may be reduced through protein mediation.[10]

The elucidation of some of these resistance mechanisms prompted a new wave of synthesis of cisplatin derivatives with goals of increased uptake, decreased cytoplasm reactivity and efflux, and reduced tolerance of DNA-adducts once formed.[10] Alongside these objectives, which are synthesis-based, came alternative tactics outside of the drug itself - such as

improved delivery, co-administration with pharmacological modulators of resistance mechanisms, and combination therapies with molecularly targeted drugs - but these are outside the scope of this review. Out of all of the numerous platinum complexes synthesised and trialled in this new drive for an improved therapeutic, only oxaliplatin that has so far gained approval, but as this overcomes significant cisplatin resistance, it is a valuable addition to the clinical armoury (*Figure 1.18*).
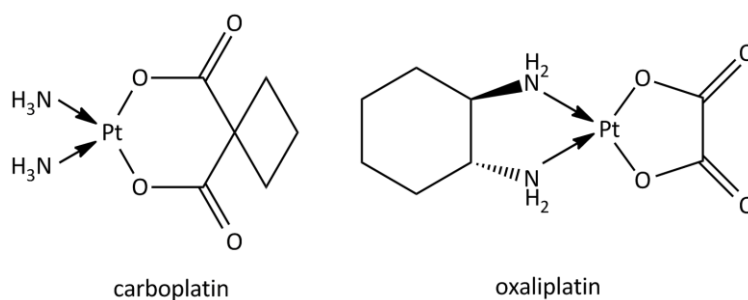

carboplatin   oxaliplatin

Figure 1.18 – The first two cisplatin derivatives to gain clinical approval

The activity of oxaliplatin (1R,2R-diaminocyclohexane oxalate-platinum(II)) was reported in 1978 when a series of compounds with the three possible isomers of the diaminocyclohexane carrier ligand (stable groups that remain coordinated to the platinum throughout binding rather than acting as a leaving group for aquation) were tested.[73] Not only was oxaliplatin active but it has since been shown to overcome some cisplatin resistance, with one of the key findings being that at high concentrations there was no longer a dependence on CTR1 for cellular accumulation which has been shown to be a factor in the resistance against the previous two platinum complexes.[74] Also, although the adduct formed is mainly GpG intrastrand crosslinks they are still structurally different to those formed by cisplatin or carboplatin. This is thought to circumvent some of the post-binding resistance as there is more destabilisation of the helix, and the diaminocyclohexane ligand is directed into the major groove of DNA which could prevent the binding of repair proteins.[75] It was found in clinical trials to be most effective in combination with other drugs (the thymidylate synthase inhibitor 5-flourouracil). It is particularly effective against colorectal cancers after showing improvements in treatment of cases which were insensitive to the previous platins[76] and was granted US FDA approval in 2002.

Further developments in platinum therapeutics have been made recently with the compound satraplatin, a product of the continued collaboration between Johnson Matthey PLC and the Institute of Cancer Research after the development of carboplatin.[10] Satraplatin (bis-acetato-ammine-dichloro-cyclohexylamine platinum(IV) (*Figure 1.19*) is an orally active compound (cisplatin, carboplatin and oxaliplatin are delivered intravenously) designed to have a toxicity profile of carboplatin. It showed similar activity to cisplatin and carboplatin treatments[77], with circumvention of acquired cisplatin resistance mechanisms involving reduced transport[78], and is under consideration for approval.

Picoplatin, *cis*-amminedichloro-2-methylpyridine platinum(II), (*Figure 1.19*) is another compound to come out of the same collaboration, with the design principle of steric bulk around the platinum to make the cytoplasmic reactivity with the thiol-containing species less favourable and therefore reduce the associated inactivity and efflux out of the cell.[79] Although demonstrating promising *in vitro* activity and reaching phase III clinical trials for small cell lung cancer it has since failed to improve on the response of existing treatments.[80]
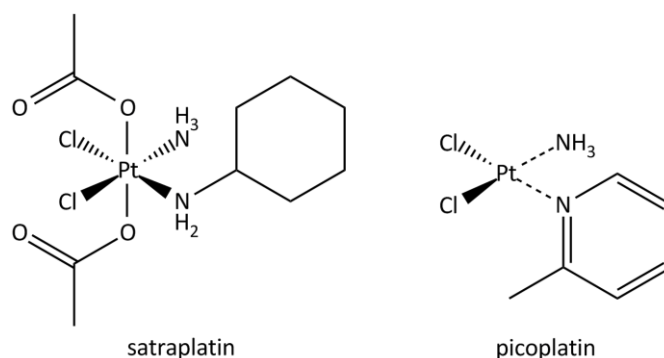

satraplatin   picoplatin

Figure 1.19 - Recently trialled platinum therapeutics

To put the success of the approved therapeutics into context, there are, in total, the three previously mentioned complexes plus three used exclusively in Japan, Korea and China respectively. A further fourteen compounds to date have entered clinical trials but failed to progress.[81]

1.3.1.2   Other Transition Metal Centres

Aside from irreversible binding to DNA by platinum complexes, other metal centres can bind to DNA to offer similar therapeutic actions. This field of research aims to further improve on the drawbacks of current platinum therapeutics by expanding the range of treatable cancers, overcoming intrinsic and acquired resistance which can still prevail, and alleviating the often severe side effects.[50]

Ruthenium has been extensively studied as substitution kinetics, for Ru^{II} and Ru^{III} species, are similar to platinum(II).[50] The first sign of antitumor ruthenium properties was found with the inorganic dye ruthenium red in the 1970's[82], followed by a study of the complexes *fac*-[RuCl$_3$(NH$_3$)$_3$] and *cis*-[RuCl$_2$(NH$_3$)$_4$]Cl in the 1980's[83], which showed promising antitumor activity but were limited as drugs by their solubility.[84]

A large amount of research has been carried out with Ru^{II} half-sandwich arene compounds with the general formula [(η^6-arene)Ru(YZ)(X)] where YZ is a bidentate chelating ligand and X is a good leaving group such as chloride (*Figure 1.20*).[50]
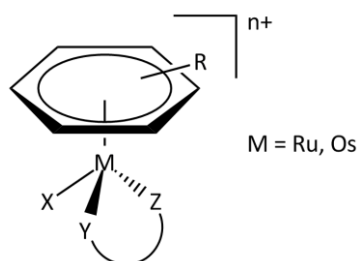

Figure 1.20 - General structure of 'piano-stool' complexes

These compounds are often referred to as 'piano-stool' complexes and offer flexibility in their design by modification of each of the components (arene, YZ or X) to alter the thermodynamic and kinetic properties.[50] As well as single covalent bond formation from the site of the leaving group to the N7 of Guanine, there can also be intercalation by the arene component and finally hydrogen bonding from the chelating ligand to the C^6=O of Guanine.[85] This unique binding mode causes unusual distortions that differ from cisplatin. Interestingly, in a study with an ovarian cancer cell line, the area of the arene has been shown to correlate with its antitumor activity.[86] It is believed that, like cisplatin complexes,

the aqua species is formed when the chloride concentration drops from 100 μM in the intracellular regions to 4 μM in the cell nucleus, as the compound reaches its target.[87]

Another class of ruthenium compounds found to have antitumor activity contain the arylazopyridine ligands (azpy) with the general formula $[Ru(azpy)_2Cl_2]$.[88] These compounds have several isomers of varying cytotoxicity and DFT calculations have helped rationalise these differences based on the intercalative ability of each isoform (*Figure 1.21*).[89]
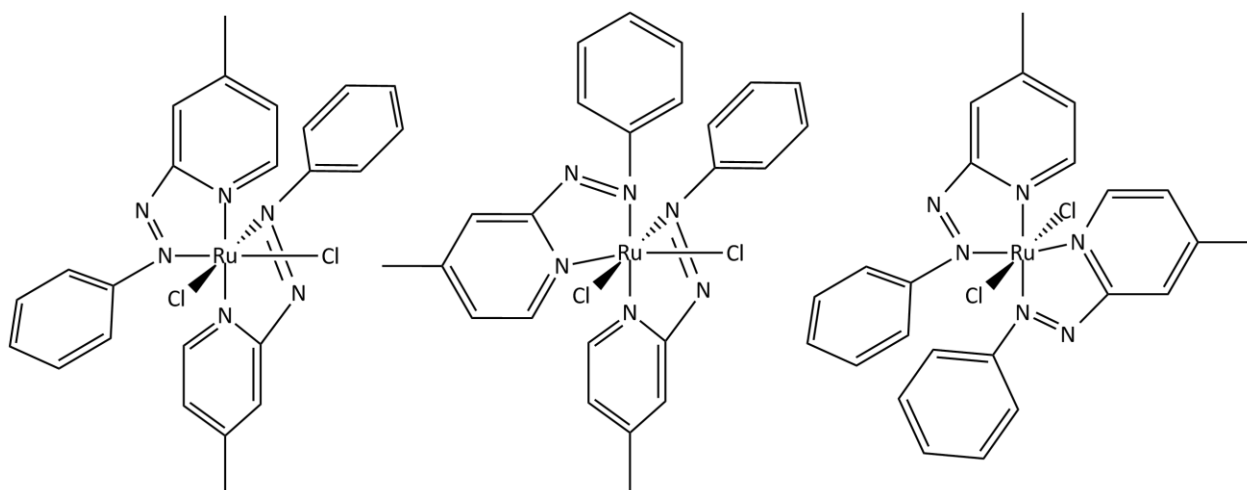

Figure 1.21 - From L-R α-, β- and γ-$[Ru(azpy)_2Cl_2]$

A similar bisazopyridine ligand has been used to bridge a dinuclear ruthenium complex with the formula $[Ru_2Cl_4L_2]$ that has shown *in vitro* antitumor properties.[90]

Metal complexes including more ruthenium species capable of antitumor activity, have been comprehensively covered in the review of non-platinum metallopharmaceuticals by Clarke *et al.*[84]

Another metal centre that has been studied more recently is osmium. Although similar to ruthenium it was overlooked due to the toxicity of OsO_4 and the substitutionally inert nature of Os^{II} or Os^{III} compounds compared to their ruthenium analogues.[50] Fine tuning of the ligands for thermodynamic and kinetic properties, however, has led to osmium complexes of the 'piano stool' general structure (*Figure 1.20*) with cytotoxicity's comparable to cisplatin and carboplatin.[91] These complexes are thought to bind to DNA in the same way as the ruthenium analogues with a combination of irreversible guanine N7 covalent linkage, arene intercalation and hydrogen bonds, although interestingly they have been found to

unwind the DNA strands, in contrast to cisplatin lesions which only bend the helix, and also do not show cross-resistance with cisplatin.[92]

Collaborative work between Sadler and McGowan looked into both ruthenium and osmium piano stool complexes where isomerism in the amide linkage (as the YZ component in *Figure 1.20*) changed the anticancer activity.[93] In this study when the ligand was bound to the metal through two nitrogen atoms (Y,Z = N,N in Figure), rapid binding of the complex to guanine occurred and several derivatives showed cytotoxic activity. When the ligands were bound through nitrogen and oxygen (Y,Z = N,O), however, the complex did not bind to guanine and subsequently had no cytotoxic effects. Following on from the correlation between ligand binding mode and cytotoxicity, ruthenium and iridium complexes of the piano stool architecture were investigated with a variety of ligands to give (N,N), (N,O) and (O,O) ligand binding modes, with a trend in anticancer activity observed of which the (N,O) species were the most toxic.[94] More recently, McGowan and co-workers have completed a comprehensive study into the anticancer activity of a library of ruthenium and iridium complexes featuring β–ketoenamine ligands, with results showing the complexes induce single strand DNA breaks and cause cell death by apoptosis in a variety of cancerous cell lines.[95]

1.3.2   Non-Classical Therapeutics

The compounds discussed so far all fall into the category of classical chemotherapeutics with the aim being the formation of DNA lesions. All of these genotoxic systems form non-repairable cisplatin-style lesions in the double helix and exploit the fast replication and mitotic processes of malignant cells to enhance these effects. A non-conventional target in comparison are the proteins and enzymes involved in tumor metabolism, with metal complexes again providing some promising interactions in a relatively new field of study.[50] These include gold(I) phosphine complexes that act as inhibitors to some mitochondrial enzymes found in elevated levels in the tumor environment.[96,97] Gold(III) is isoelectronic and isostructural with Pt(II) so analogues to the platin species were soon tried but were found to be unstable and susceptible to reduction to metallic gold under physiological conditions.[98] This low stability, however, has been improved upon with gold(III) porphyrin complexes that

show cytotoxicity *in vitro* and *in vivo* greater than cisplatin and without cross-resistance.[99] Other metals featured in non-classical therapeutic complexes include gallium[100], ruthenium[101] and cobalt[102].

Recent developments have seen two ruthenium compounds show particularly suitable therapeutic activity enter ongoing clinical trials: *trans*-[RuCl$_4$(DMSO)(Im)](ImH) (where DMSO = dimethyl sulfoxide and Im = imidazole), known as NAMI-A[48], and [RuCl$_4$(Ind)]IndH (where Ind = Indazole), referred to as KP1019 (*Figure 1.22*).[103]
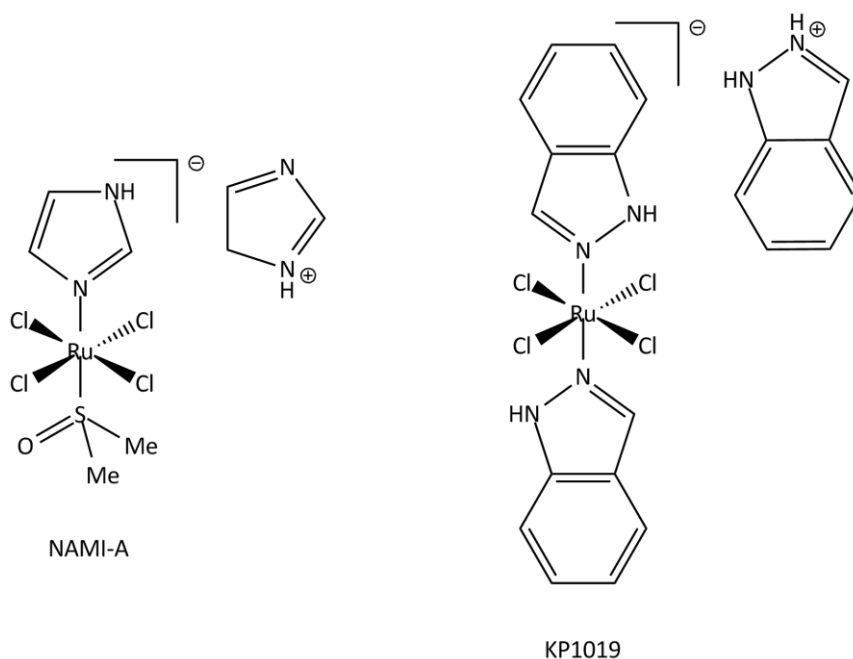

NAMI-A

KP1019

Figure 1.22 - The two ruthenium therapeutics in clinical trials

NAMI-A has a different mode of activity to existing platinum therapeutics as it shows anti-metastatic activity, that is the prevention of tumours spreading.[48,103] Some reports have focused on the interaction of these two compounds with differing cell components to DNA, in the case of NAMI-A modifying cell invasion and metastasis and for KP1019 promoting apoptosis through the mitochondrial pathway, differentiating them from cisplatin and giving them the non-classical label.[104] In the preclinical studies, however, interactions of KP1019 with DNA were established through electrophoretic analysis which revealed the ability to untwist and bend DNA – a likely cause for the cytotoxic action.[103]

Ru^{III} compounds like NAMI-A and KP1019 are also thought to act as prodrugs and undergo reduction to the more reactive Ru^{II} species *in vivo*. Prodrugs are derivatives that are transformed into the desired active form *in vivo*, for example by photoactivation, redox activity or ligand substitution.[50] This approach was theorised to be effective for Ru^{III} compounds as during delivery to the tumour there should be minimal non-target biomolecular interactions; therefore avoiding deactivation and side effect toxicities. Once in the tumour environment, however, reduction to the corresponding Ru^{II} species can occur due to the reductive tumour environment – a result of high glutathione concentration, high pH, and an insufficient blood supply to rapidly dividing cells lowering the O_2 concentration.

1.3.3 Reversibly Binding Metal Complexes

Along with the many metal complexes that irreversibly bind to DNA, there is also a whole class of reversibly bound complexes that have been explored for their therapeutic properties, with most interest focusing on the intercalating species. There are some important characteristics shared by non-covalent metal complexes which include them being kinetically inert, a requirement for stability. Most are d^6 octahedral or d^8 square planar, usually a rigid structure is held in place to maximise recognition with DNA, and finally preparation is often designed to incorporate photophysical or photochemical properties that are of great use in probing or affecting the chemistry.[46]

Photoactivation in particular offers the advantage of exclusively treating the local area of the tumor and avoiding side effects elsewhere in healthy tissue, with photodynamic therapy (PDT) currently used in the clinic to treat readily accessible tumors with the appropriate nontoxic photosensitizers.[105] The limitation of this approach is accessibility of the light stimuli to the diseased tissue, and the requirement that the sensitizer needs to be activated by light between 650 nm and 900 nm; longer wavelengths are not energetic enough for activation, and shorter wavelengths are too energetic and can cause to much off-target damage.[50]

A typical mechanism for PDT involves a porphyrin-based system becoming photo-excited and transferring energy to ground state triplet oxygen ($^3O_2$) to generate the highly reactive singlet oxygen species ($^1O_2$), which damages the DNA and leads to cell death. It must be

remembered that tumor environments are often deficient in oxygen (hypoxic) so this method is not always viable. Metal-bound porphyrins can have a positive effect on the tumor-localizing properties and there are several molecules in clinical trials.[106]

1.3.3.1   Metallo-Intercalators

As the interest in intercalation grew and the field expanded as described in section 1.2.5, attention soon turned to metallo-intercalators, defined as metal-centred complexes with one or more intercalating ligands (*Figure 1.23*).
The intercalating ligand acts in the same way as a small organic intercalating molecule, unwinding the DNA to enable π-stacking between two base pairs. Once bound the intercalating ligand secures the complex in place and governs where the ancillary ligands are directed in relation to the double helix.[46] The binding affinity of the complex has been shown to have a positive correlation with an increase in the area of the intercalating ligand as the non-covalent interactions with the base pairs are enhanced.[12]
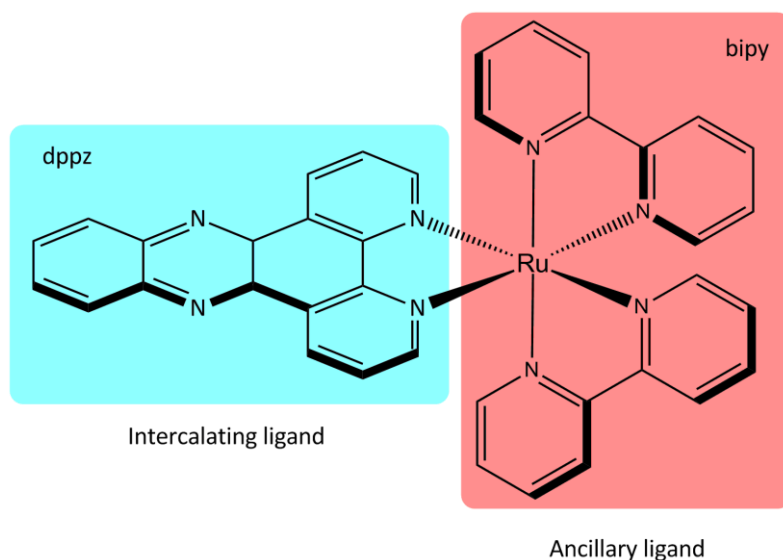

Figure 1.23 – Δ-[Ru(bipy)$_2$(dppz)]$^{2+}$ showing the general structure of a metallo-intercalator
(bipy = 2,2'-bipyridine and dppz = dipyrido[3,2-a:2',3'-c]phenazine)

The first work to show metal complexes binding to DNA via intercalation was carried out by Lippard *et al*. with square planar platinum(II) complexes, originally with terpyridine ligands

in 1974 which was soon after confirmed with X-ray diffraction patterns.[107,108] This was followed by DNA binding studies with other planar heterocyclic ligands attached to the platinum and investigation into effects such as ionic strength on these systems binding properties.[109]

Three-dimensional structures were then investigated in the 1980s at first by Barton *et al.* using the octahedral geometry of zinc(II) with phenanthroline (phen) ligands in a tris-phen complex, which showed a stereoselective preference for the DNA binding of one enantiomer over the other, and was labelled as partial insertion between the base pairs.[110] This stereospecific DNA binding was then shown with the analogous ruthenium tris-phen complex, initially stated as an intercalator (*Figure 1.24*).[111,112]
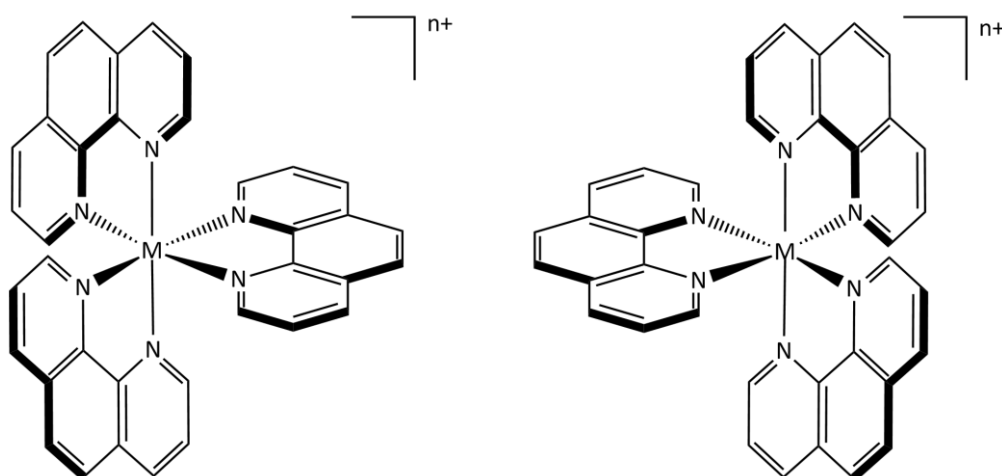

Figure 1.24 - The two enantiomers of [M(phen)$_3$]$^{n+}$ - Λ on the left and Δ on the right (M = metal centre, n+ = charge on the metal complex)

The ruthenium systems were chosen both for their kinetically inert characteristics of the low spin d^6 systems and intense metal to ligand charge transfer (MLCT) band in the visible region, and this tris-phen complex has been thoroughly discussed since the first studies which concluded it was interacting with DNA through intercalation.[112] This intercalation was proposed to be the same binding mode for both enantiomers although favoured for the Δ-enantiomer where the orientation of the non-intercalating ligands matched the right handed helical groove, whereas a lower affinity for the Λ-enantiomer was attributed to the phosphate backbone restricting access, due to the steric clash with the ligands in this conformation, and therefore preventing full intercalation.[113] This was concluded from

hypochromic shifts - although these were less pronounced than for other species - and fluorescence quenching experiments which were proposed to indicate intercalation when compared with complexes bound by electrostatic interactions.[112] Following on from this however, it was proposed that two binding modes exist – intercalation and surface binding – with the rates of quenching for both enantiomers still slower than free $[Ru(phen)_3]^{2+}$ and the Δ-enantiomer still binding by intercalation, but the Λ-enantiomer instead bound to the surface in a different way with the ancillary ligands following the contours of the groove and displacing the intercalating ligand away from the helix, therefore exposing it to the quencher.[114] ^{1}H NMR studies were then used to show these modes of binding were consistent.[115]

This, however, was contradicted by the findings of Hiort *et al*. in 1990 which from circular dichroism (CD) and linear dichroism (LD) spectroscopy proposed each enantiomer had its own binding mode in the major groove, with different stereospecific geometries from steric and coulombic factors, but neither interacted through intercalation.[116] It was at this time that the criteria for intercalation (discussed in section 1.2.5) established by Lerman were addressed by Chaires *et al.* by comparing the viscometry measurements for $[Ru(phen)_3]^{2+}$ with the known intercalator ethidium bromide which lengthens the DNA helix to increase the viscosity, and the known groove binder Hoechst 33258 which leaves the DNA helix, and viscosity, unperturbed. Neither enantiomer was found to increase the viscosity and therefore was not intercalating in the classical way, with the Λ-enantiomer appearing similar to Hoechst 33258 and the Δ-enantiomer giving a decrease in viscosity – suggested to be due to a partial intercalation acting as a wedge to produce a static bend in the helix.[117] The binding affinities were also investigated and found to be relatively weak which supported a electrostatic binding mode.[117] Other spectroscopic and physical techniques were then used to confirm two single individual binding modes.[118] Coury *et al*. have also used scanning force microscopy (SFM) to show a lack of intercalation into DNA as there was no increase in length compared with the elongation induced by the control ethidium bromide.[28]

In a further twist, DNA saturation with regard to binding of the two enantiomers was looked into by Rodger *et al*. in 1999 using spectroscopic techniques and computer modelling to outline three binding modes: partially inserted with a single phenanthroline ligand parallel to the base pairs in the major groove, slotted with one ligand in the minor groove or minor facial with two ligands in the minor groove.[119] This study concluded that, at all mixing ratios,

the partially inserted mode is favoured for the Λ-[Ru(phen)$_3$]$^{2+}$, but with Δ-[Ru(phen)$_3$]$^{2+}$ the minor facial mode is favoured at low concentrations in contrast to the slotting mode at high concentrations with some partial insertion also occurring.[119]

1.3.3.2 The Molecular Light Switch Effect

Metallo-intercalators are capable of probing the structure of DNA without directly interacting with it, due to the reversible binding mode and the complex being coordinately saturated and substitutionally inert which prevents the formation of covalent linkages, along with the photophysical and photochemical properties of the complex that can be employed. The molecular light switch effect utilises these properties when a transition from one environment to another leads to luminescence where there was previously none, that is the light is 'switched on' in the new environment. This effect is related to solvachromic luminescence when a chemical substance can change colour due to a change in solvent polarity, but with the intensity of the emission being the significant variable observed. A typical example of a light switch complex is [Ru(bipy)$_2$dppz]$^{2+}$ (*Figure 1.26*).[120]
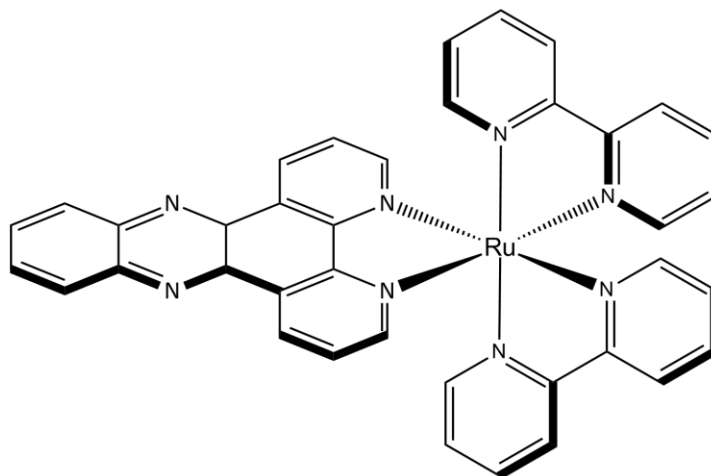

Figure 1.26 - The molecular light switch complex [(bipy)$_2$Ru(dppz)]$^{2+}$

The light switch effect occurs when excited by the suitable wavelength of light, there is a charge transfer of an electron from an orbital predominantly metal in character to an orbital predominantly ligand in character, known as a metal to ligand charge transfer (MLCT). In the

case of $[(bipy)_2Ru(dppz)]^{2+}$, exciting the complex results in emissive or non-emissive deactivation depending on the solvent environment. In aqueous solution there is no luminescence as the excited state is non-emissively deactivated through water molecules hydrogen bonding with the endocyclic nitrogen atoms of the intercalating ligand, but in organic solvents, a solvachromic luminescence is observed as an emissive deactivation occurs in the absence of these interactions.

In complexes with equivalent ligands, such as $[Ru(bipy)_3]^{2+}$, rapid hopping of the electron between ligands occurs, and there is a transient symmetrical charge separation in the excited state. The reason for the directional excitation occurring onto the dppz ligand in $[(bipy)_2Ru(dppz)]^{2+}$ is that the electron charge transfer favours the stronger electron accepting ligand stabilised by the nitrogen atoms of dppz. The properties of the $[(bipy)_2Ru(dppz)]^{2+}$ complex can be said to consist of two electronically independent parts – a $[Ru(bipy)_3]^{2+}$-like chromophore and a phenazine electron acceptor.[121–123]

These molecular light switch complexes were first investigated as a DNA probe by Barton, *et al*.[120,124] When this light switch mechanism is transferred to DNA binding, there is non-emissive deactivation of the excited state when the complex is free in aqueous solution, but emissive deactivation is observed when the complex is bound to DNA. This emission is a result of the excited state being protected in-between the base pairs from the surrounding water molecules; with this degree of protection reflected in the extent of the molecular light switch effect.[124] In addition, it was shown there is differentiation between A-, B- and Z-DNA in the emission spectra.[120] The two enantiomers of the complex were then investigated by Hiort, *et al.* and it was shown that each has two distinctive excited state lifetimes that seemed related to two different binding modes of the complex.[125] One mode has the complex intercalating from the minor groove to direct the metal-dppz axis perpendicular to the base pairs, with the other mode having the metal-dppz axis aligned along the base pair axis.[125] The perpendicular binding mode has both nitrogen atoms intercalated into the base pair stack and protected from the external solvent to give a long lived excited state, whereas the latter binding mode, that can be called side on, leaves one of the phenazine nitrogen atoms accessible by water as it points into the major groove, which results in some quenching of the excited state although still much slower compared with the compound free in solution.[125]

The exact mode of intercalation was debated and in further studies intercalation from the major groove was disproved in favour of a minor groove entry, with no room for the two different orientations and the bi-exponential decay could be attributed instead to a loading effect.[126] It was also found that there was preferential binding to d(AT) regions of both calf thymus DNA (CT-DNA) and a modified T-4 DNA which has major groove steric hindrance on the cytosine bases.[127]

Many more metallo-intercalators have been made with a range of transition metal centres, including rhenium and platinum complexes with a dppz or similar intercalating ligand, as reviewed by Metcalfe *et al*.[128]

1.3.3.3 Metallo-Insertors

Metallo-insertion is a variation on metallo-intercalation where a planar aromatic ligand inserts in-between the base pairs, but rather than unwinding and extending the DNA helix, a single base pair is ejected to accommodate the new planar ligand and replace the π-stacking interactions.[46]

1.3.3.4 Hetero-Metallic Complexes

Focusing on ruthenium-platinum complexes, some of the first work done with relevance to this project was that of Sahai, *et al.* in 1986 when they prepared a hetero-oligionuclear complex containing one ruthenium and three platinum centres bridged by a quinoxaline ligand.[129] In the 1990's more heterometallic complexes were made with a mixed metal bimetallic complex of the form $[(bipy)_2Ru(BL)PtCl_2]^{2+}$ (where BL = bridging ligand) was synthesised with a 2,3-bis(2-pyridyl)pyrazine (2,3-dpp) bridge by Yam, *et al*.[130] This was followed by work from Brewer, *et al*. with bridging ligands of 2,3-bis(2-pyridyl)quinoxaline (dpq) and bis(2-pyridyl)benzoquinoxaline (dpb) (*Figure 1.27*).[131] Subsequent work focused on the DNA interactions of these complexes where it was suggested a non-covalent interaction of the cisplatin type was the mode of binding.[132]
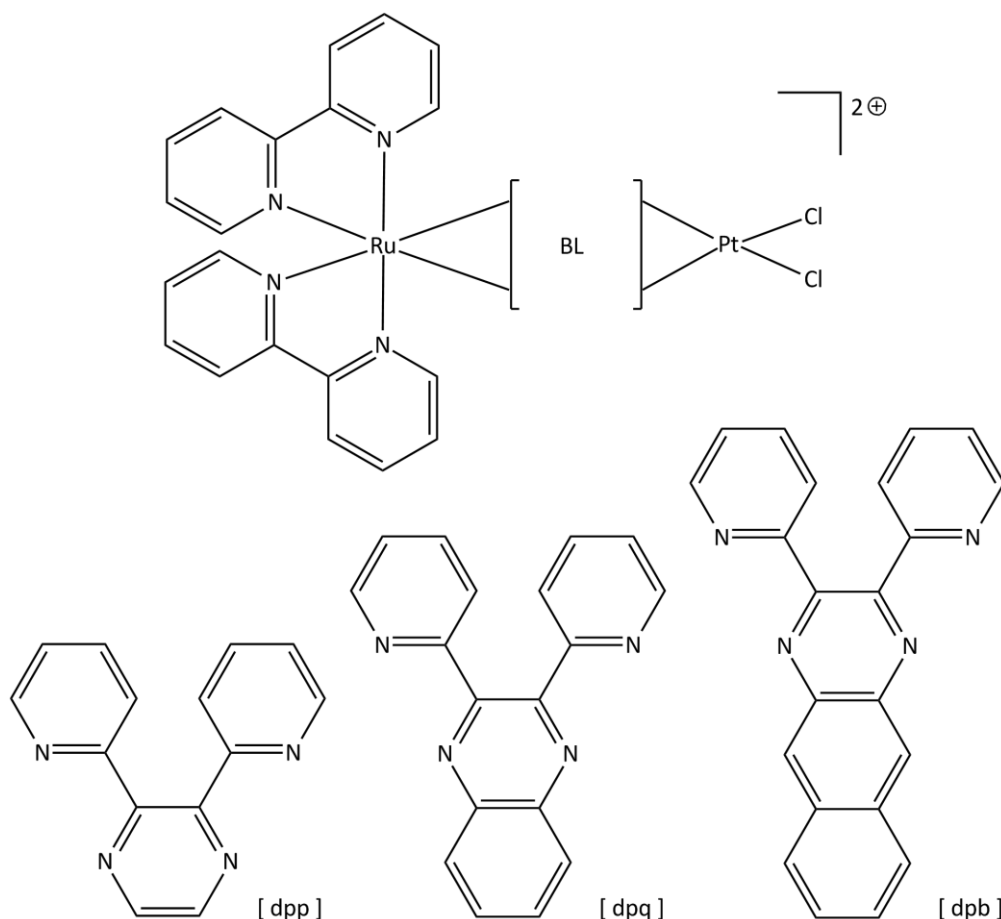
Figure 1.27 - Bimetallic ruthenium-platinum complex with bridging ligands dpp, dpq and dpb

Further studies carried out by Brewer, *et al*. with the same three bridging ligands (dpp, dpq, dpb) but 2,2':6',2''- terpyridine (tpy) ancillary ligands produced a series of compounds that were shown to feature tunable charge transfer bands based on the stability of the π* orbitals on the bridging ligand; and substantial DNA binding for all three.[133] In another study a series was investigated with the bridging ligand remaining dpp but the ancillary ligands varied, and this showed further tunability of the photophysical properties in the ruthenium-platinum system.[134]

An alternative design principle of a more flexible linker between metal centres has also been investigated. One study by Schilden *et al*. in 2004 involved a ruthenium-platinum bimetallic linked by a diethyleneglycol unit, of the form [(tpy)Ru(dtdeg)PtCl]$^{3+}$ (dtdeg = bis[4'-(2,2':6',2''-terpyridyl)]-diethyleneglycol ether), which was shown to non-covalently bind to 9-ethylguanine.[135] This was based on the hypothesis that the ruthenium moiety displayed the known polypyridyl-ruthenium non-covalent DNA binding and increasing the affinity for

its target by the 2+ charge, combined with the already cytotoxic platinum compound [Pt(tpy)Cl]Cl.2H$_2$O.[107,136,137]

Another ruthenium-platinum complex of interest was synthesised by Haga, *et al*. in 2006 with a dual linker tethered to the PtCl$_2$ unit by each reactive amine end to form a metallocycle that associated with CT-DNA and also displayed visible-light-induced scission of (supercoiled Pbr322) DNA.[138]

Bimetallic combinations other than ruthenium-platinum have also been used in the search for new therapeutics. For example, by tethering a reactive PtCl$_2$ unit to a known mismatch-specific rhodium-centred metallo-intercalator, Barton, *et al*; directed the cisplatin moiety to preferentially react with mismatched DNA.[139] The rhodium precursor of this molecule has been shown to target thermodynamically destabilised mismatched sites in DNA with a hit-rate of 80%, and interestingly cleaves the DNA backbone upon photoactivation.[140]

This research into therapeutic heterometallic complexes forms the basis for my work in synthesising ruthenium-platinum and ruthenium-rhenium complexes.

1.4   Cytotoxicity

A cytotoxic compound is one that can cause damage to living cells, and cytotoxicity can be described as the degree to which an agent has a specific destructive action on certain cells. The fate of cells exposed to a cytotoxic compound can vary – apoptosis often being the dominant mechanism but nonapoptotic mechanisms such as oncosis, autophagy, mitotic catastrophe and senescence can also have a role in cell death from treatment with conventional chemotherapeutic agents, with the three relevant routes to this project described herein.[141]

It must be noted that whilst the three routes of apoptosis, oncosis and autophagy are all modes of cell death, one often misunderstood term is necrosis, which should be considered as the post-mortem cellular changes that occur *after* cell death that restore an equilibrium with a cell's environment and is thus applicable to both the apoptosis and oncosis.[142–144] Despite the descriptions provided by, for example, Majno *et al*[142] and Trump *et al*[143], and a summary in a specialized 2012 review on oncosis by Weerasinghe *et al*[144], confusion in the literature between oncosis and necrosis is still apparent. For example, the 2003 review paper by Proskuryakov *et al*[145] – which seeks to describe the differences between apoptosis and necrosis – appears to confuse necrotic pathways with oncosis. The review concludes that necrosis itself is an alternative programmed cell death mechanism with outcomes that lead to very different consequences for the organism affected. Nonetheless, despite this confusion in the literature, there are clearly modes of cell death that can be incontrovertibly labelled as apoptosis or oncosis (*Figure 1.28*).
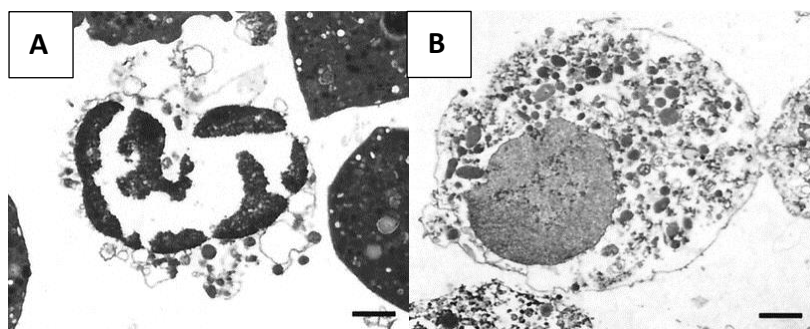

Figure 1.28 – Electron micrographs of polymorphonuclear leukocytes (PNMs) undergoing apoptosis (**A**) and oncosis (**B**)[146]

1.4.1   Apoptosis

Apoptosis is often referred to as programmed cell death (PCD) and follows a well ordered and defined series of cellular events. Although observations had been made for many decades previously, the term 'apoptosis' and the definition of the distinct morphological changes in cells in physiological conditions were introduced by Kerr *et al* in 1972.[147] The structural changes during apoptosis initially involve cell shrinkage and nuclei condensation followed by nuclear fragmentation and separation of the protruding sections on the cell surface formed during the reduction in size. This gives a multitude of membrane bound fragments, known as apoptotic bodies, containing compacted but chemically and structurally intact organelles and varying nuclear matter. These apoptotic bodies are then phagocytosed by other cells – broken down at first by internally contained enzymes (autolysis) followed by lysosomal enzyme degradation – to give lysosomal residual bodies.[142] Much work has since been carried out to gain a deeper understanding of this process which - as reviewed recently by Fuchs and Steller - is essential to normal development processes such as homeostasis, and is involved in both the causation and combatting of disease.[148] The developmental role of apoptosis is particularly apparent during the focal elimination of cells in embryonic development, which is the controlled removal of cells for example to fashion limbs and develop initially webbed hands and feet into defined digits.[149]

A key discovery for the mechanism behind PCD came from genetic studies in the nematode *C. elegans* identifying specific genes which acted to initiate the program of cell suicide.[150,151] From these genetic studies the machinery behind cell death was found to be a family of cysteine proteases referred to as caspases (cysteinyl aspartate-specific proteinases) which mediate proteolytic cleavage in dying cells and one of which, caspase 3, can be identified by Western blotting as an apoptosis marker.[152,153]

There are two signalling pathways for apoptosis – the intrinsic mitochondria-mediated or extrinsic extracellular-mediated pathway – although once activated the same caspase facilitated mechanism proceeds.[141,154] For the intrinsic pathway, stress signals such as DNA damage or high levels of reactive oxygen species (ROS) are responsible for activation, as well as viral infection or activation of oncogenes. On the other hand, the extrinsic pathway is activated as a result of extracellular ligands binding to plasma membrane receptors.[141]

1.4.2   Oncosis

Oncosis is a cellular reaction to injury, causing cell death through a different pathway to that of apoptosis and is not commonly implicated in developmental processes. Oncosis has a very different morphologically to apoptosis as, in contrast to the steps described above, cells swell, there is collapse of the plasma membrane, and then they are rapidly lysed, with a resulting efflux of cell remnants into the extracellular space which can potentially induce a problematic inflammatory response.[144]

Oncosis can be induced by inhibition of cellular energy production, imbalance of intracellular calcium flux, generation of ROS, or activation of nonapoptotic proteases - events which are all linked and can enhance the activation with multiple triggers.[141] One biochemical characteristic in the lead-up to oncosis, but not apoptosis, is the initial rapid decrease in intracellular ATP. This oncosis-inducing interference with ATP synthesis deactivates Na^+, Ca^+-ATPase in the cell membrane which causes an increased intracellular concentration of K^+ and Cl^- ions and prompts an influx of water and Ca^{2+} ions – resulting in the cell swelling observed as the first morphological change.[144]

1.4.3   Autophagy

Autophagy is the term used to describe pathways that result in cytoplasmic materials being delivered to the lysosome in animal cells for enzymatic degradation and - in contrast to apoptosis and necrosis - does not necessarily have to result in cell death.[155] It is an adaptive process that occurs under certain metabolic stresses or from developmental triggers, and results in intracellular protein and organelle degradation, via formation of a double membraned encapsulation of cytoplasmic contents, called an autophagosome, which then fuses with a lysosome for degradation.[141]

Under normal physiological conditions autophagy occurs at basal levels for the turnover of cell components but excessive autophagy can result in cell death, for example it has been recently shown to be responsible for joint destruction in rheumatoid arthritis.[156]

Dysfunctional autophagy pathways have also been implicated in tumorigenesis with studies

showing a gene, *Beclin 1,* responsible for autophagosome formation to be deleted in various sporadic human carcinomas.[157]

The induction of autophagy can be investigated through the expression of the marker for autophagosome formation - the microtubule associated protein-1 light chain 3B (LC3B). Western blot analyses can show LC3B-I and LC3B-II, the former being the cystolic form that through lipidation is converted to LC3B-II to allow it to associate with autophagic vessels.[158]

1.5 Metal Complex Fluorescence Microscopy

The visualisation of cells is key to understanding many cellular processes and whilst this field was started with organic DNA-binding molecules, the advantages of various metal complexes have become apparent with recent advances overcoming some of the main disadvantages of traditional organic dyes such as low water solubility, high toxicity and photo bleaching.[159] Imaging with metal complexes, on the other hand, offers the advantages including the MLCT excitation occurring in the visible region, having a high Stokes shift, and possessing chemical and photostability.[160]

1.5.1 Related Ruthenium Complex Studies

One of the recent advances in live cell imaging with metal complexes came from the Gill, *et al.* in the Thomas group with the binuclear ruthenium complex $[((L)_2Ru)_2(tpphz)]^{4+}$, where L is either of the ancillary ligands bipyridine (bipy) or phenanthroline (phen) (*Figure 1.29*).[160]
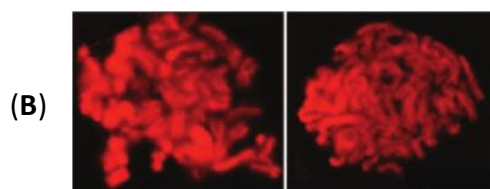

RuRu (bipy)

(A)

RuRu (phen)
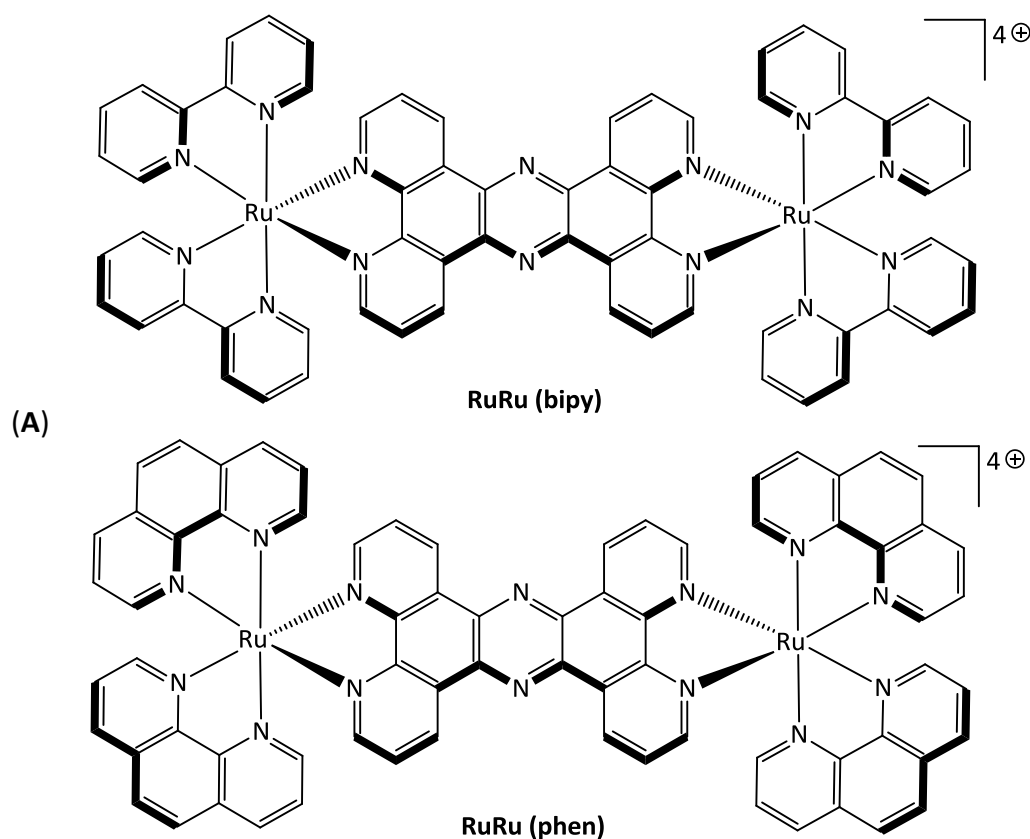
Figure 1.29 – (**A**) The complexes [((L)$_2$Ru)$_2$(tpphz)]$^{4+}$ (L = bipy or phen) used by Gill, *et al*.
(**B**) Live cell imaging of chromosomal DNA in the MCF-7 human breast cancer cell line

The phenanthroline complex [((phen)$_2$Ru)$_2$(tpphz)]$^{4+}$overcame previous metal complex membrane permeability limitations for efficient cellular uptake where the favourable properties of the MLCT excitation allowed for high resolution nuclear imaging, seen in *Figure 1.29* with the example of mitotic chromosomal DNA in cells of the human breast adenocarcinoma cell line MCF-7.[160]

Other dinuclear complexes studied in the Thomas group for cellular imaging applications include iridium-ruthenium species with bipyridine and phenanthroline ancillary ligands, which can be cyclometalated in the case of the iridium, as featured in a recent publication by Wragg, *et al*.[161] Many studies of metal complex microscopy have used the strategy of increasing lipophilicity to enhance passive diffusion, but this approach can produce systems that deviate from intended targets and bind to alternative, more lipophilic intracellular targets such as membrane structures and the endoplasmic reticulum.[162]

Another interesting ruthenium complex studied in the Thomas group which has imaging applications through MLCT excitation is [(phen)$_2$Ru(tpphz)]$^{2+}$ (*Figure 1.30*).[163]
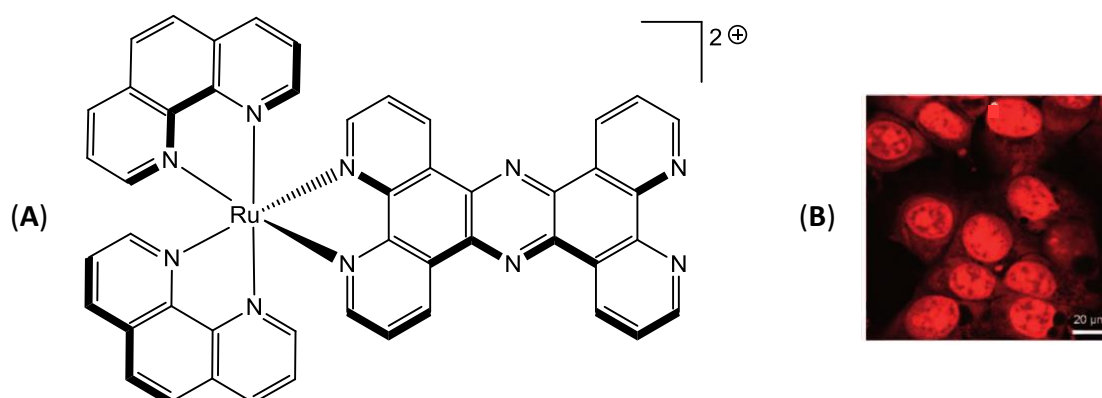

Figure 1.30 – (**A**) The metallo-intercalator [(phen)$_2$Ru(tpphz)]$^{2+}$ (**B**) Fixed cell staining of the MCF-7 human breast cancer cell line

This mononuclear [(phen)$_2$Ru(tpphz)]$^{2+}$ complex has shown, after efficient cellular uptake, both effective imaging through MLCT excitation and notable cytotoxic properties. The toxicity is comparable to cisplatin and shows little cross resistance in the cisplatin sensitive/resistant model of the A2780/A2780cis human ovarian carcinoma cell lines, as well as being capable of high resolution nuclear imaging as seen by those obtained by Gill, *et al*. (*Figure 1.30*).[163] This is an example of a theranostic compound – an agent that has both diagnostic and therapeutic properties – and forms the basis of this PhD research which synthesises several derivatives of [(phen)$_2$Ru(tpphz)]$^{2+}$and explores their cytotoxicity, with the aid of cellular imaging.

1.7 References

1. Watson, J. & Crick, F. Molecular structure of nucleic acids: a structure for deoxyribose nucleic acid. *Nature* **171,** 737–738 (1953).
2. Crick, F. Central dogma of molecular biology. *Nature* **227,** 561–563 (1970).
3. Alberts, B. *et al. Molecular biology of the cell*. (Garland Science, 2008).
4. Belmont, P., Constant, J. F. & Demeunynck, M. Nucleic acid conformation diversity: from structure to function and regulation. *Chem. Soc. Rev.* **30,** 70–81 (2001).
5. Blackburn, G. M., Gait, M. J., Loakes, D. & Williams, D. M. *Nucleic acids in chemistry and biology*. (2006).
6. Basham, B., Schroth, G. P. & Ho, P. S. An A-DNA triplet code: thermodynamic rules for predicting A- and B-DNA. *Proc. Natl. Acad. Sci. U. S. A.* **92,** 6464–8 (1995).
7. Rich, A. & Herbert, A. The Biology of Left-handed Z-DNA. *J. Biol. Chem.* **271,** 11595–11598 (1996).
8. Felsenfeld, G. & Groudine, M. Controlling the double helix. *Nature* **421,** 448–453 (2003).
9. Oberdoerffer, P. & Sinclair, D. a. The role of nuclear architecture in genomic instability and ageing. *Nat. Rev. Mol. Cell Biol.* **8,** 692–702 (2007).
10. Kelland, L. The resurgence of platinum-based cancer chemotherapy. *Nat. Rev. Cancer* **7,** 573–84 (2007).
11. Gelasco, A. & Lippard, S. J. NMR solution structure of a DNA dodecamer duplex containing a cis-diammineplatinum(II) d(GpG) intrastrand cross-link, the major adduct of the anticancer drug cisplatin. *Biochemistry* **37,** 9230–9239 (1998).
12. Erkkila, K. E., Odom, D. T. & Barton, J. K. Recognition and reaction of metallointercalators with DNA. *Chem. Rev.* **99,** 2777–96 (1999).
13. Manning, G. S. Limiting Laws and Counterion Condensation in Polyelectrolyte Solutions I. Colligative Properties. *J. Chem. Phys.* **51,** 924 (1969).
14. Finlay, A., Hochstein, F., Sobin, B. & Murphy, F. Netropsin, a new antibiotic produced by a Streptomyces. *J. Am. Chem. Soc.* **73,** 341–343 (1951).
15. Kopka, M. L., Yoon, C., Goodsell, D., Pjura, P. & Dickerson, R. E. Binding of an antitumor drug to DNA. *J. Mol. Biol.* **183,** 553–563 (1985).
16. Suh, D. & Chaires, J. B. Criteria for the mode of binding of DNA binding agents. *Bioorg. Med. Chem.* **3,** 723–8 (1995).
17. Kapuscinski, J. DAPI: a DNA-Specific Fluorescent Probe. *Biotech. Histochem.* **70,** 220–233 (1995).
18. Vega, M. C. *et al.* Three-dimensional crystal structure of the A-tract DNA dodecamer d(CGCAAATTTGCG) complexed with the minor-groove-binding drug Hoechst 33258. *Eur. J. Biochem.* **222,** 721–6 (1994).
19. Lerman, L. S. Structural considerations in the interaction of DNA and acridines. *J. Mol. Biol.* **3,** 18–30 (1961).
20. Luzzati, V., Masson, F. & Lerman, L. S. Interaction of DNA and proflavine: A small-angle X-ray scattering study. *J. Mol. Biol.* **3,** 634–639 (1961).
21. Lerman, L. The structure of the DNA-acridine complex. *Proc. Natl. Acad. Sci. USA* **49,** 94–102 (1963).
22. Long, E. & Barton, J. On demonstrating DNA intercalation. *Acc. Chem. Res.* **23,** 271–

273 (1990).

23. Patel, D. J., Shapiro, L. & Hare, D. DNA and RNA: NMR studies of conformations and dynamics in solution. *Q. Rev. Biophys.* **20,** 35–112 (1987).

24. Dougherty, G. & Pigram, W. J. Spectroscopic analysis of drug-nucleic acid interactions. *CRC Crit. Rev. Biochem.* **12,** 103–32 (1982).

25. Patel, D. Nuclear magnetic resonance studies of drug-nucleic acid interactions at the synthetic DNA level in solution. *Acc. Chem. Res.* **12,** 118–125 (1979).

26. Monnot, M., Mauffret, O., Lescot, E. & Fermandjian, S. Probing intercalation and conformational effects of the anticancer drug 2-methyl-9-hydroxyellipticinium acetate in DNA fragments with circular dichroism. *Eur. J. Biochem.* **204,** 1035–9 (1992).

27. Hyun, K. M., Choi, S. D., Lee, S. & Kim, S. K. Can energy transfer be an indicator for DNA intercalation? *Biochim. Biophys. Acta* **1334,** 312–6 (1997).

28. Coury, J., Anderson, J., McFail-Isom, L., Williams, L. & Bottomley, L. Scanning force microscopy of small ligand-nucleic acid complexes: tris(o-phenanthroline) ruthenium(II) as a test for a new assay. *J. Am. Chem. Soc.* **119,** 3792–3796 (1997).

29. Geacintov, N. E., Ibanez, V., Rougee, M. & Bensasson, R. V. Orientation and linear dichroism characteristics of porphyrin-DNA complexes. *Biochemistry* **26,** 3087–92 (1987).

30. Wilson, W. *et al.* Binding of unfused aromatic cations to DNA. The influence of molecular twist on intercalation. *J. Am. Chem. Soc.* **110,** 8292–8299 (1988).

31. Lippard, S. J. Platinum complexes: probes of polynucleotide structure and antitumor drugs. *Acc. Chem. Res.* **11,** 211–217 (1978).

32. Sartorius, J. & Schneider, H. Intercalation mechanisms with ds-DNA: binding modes and energy contributions with benzene, naphthalene, quinoline and indole derivatives including some antimalarials. *J. Chem. Soc. Perkin Trans. 2* 2319–2327 (1997).

33. Marco, A. Di, Silvestrini, R., Marco, S. Di & Dasdia, T. Inhibiting effect of the new cytotoxic antibiotic daunomycin on nucleic acids and mitotic activity of HeLa cells. *J. Cell Biol.* **27,** 545–550 (1965).

34. Wang, A. H., Ughetto, G., Quigley, G. J. & Rich, A. Interactions between an anthracycline antibiotic and DNA: molecular structure of daunomycin complexed to d(CpGpTpApCpG) at 1.2-A resolution. *Biochemistry* **26,** 1152–63 (1987).

35. Moore, M., Hunter, W., D'Estaintot, B. L. & Kennardt, O. DNA-drug interactions: The Crystal Structure of d(CGATCG) Complexed with Daunomycin. *J. Mol. Biol.* **206,** 693–705 (1989).

36. Chaires, J. B., Dattagupta, N. & Crothers, D. M. Studies on interaction of anthracycline antibiotics and deoxyribonucleic acid: equilibrium binding studies on interaction of daunomycin with deoxyribonucleic acid. *Biochemistry* **21,** 3933–40 (1982).

37. Chaires, J., Fox, K., Herrera, J., Britt, M. & Waring, M. Site and sequence specificity of the daunomycin-DNA interaction. *Biochemistry* **26,** 8227–8236 (1987).

38. Chaires, J., Herrera, J. & Waring, M. Preferential binding of daunomycin to 5'TACG and 5'TAGC sequences revealed by footprinting titration experiments. *Biochemistry* **29,** 6145–6153 (1990).

39. Chaires, J. Energetics of drug–DNA interactions. *Biopolymers* 201–215 (1997).

40. Chaires, J. B. A thermodynamic signature for drug-DNA binding mode. *Arch. Biochem. Biophys.* **453,** 26–31 (2006).

41. Chaires, J. B. *et al.* Structure-based design of a new bisintercalating anthracycline antibiotic. *J. Med. Chem.* **40,** 261–266 (1997).

42. Leng, F., Priebe, W. & Chaires, J. Ultratight DNA binding of a new bisintercalating anthracycline antibiotic. *Biochemistry* **37,** 1743–1753 (1998).

43. Fox, K., Webster, R. & Phelps, R. Sequence selective binding of bis-daunorubicin WP631 to DNA. *Eur. J. Biochem.* **271,** 3556–3566 (2004).

44. Robinson, H., Priebe, W., Chaires, J. & Wang, A. Binding of two novel bisdaunorubicins to DNA studied by NMR spectroscopy. *Biochemistry* **36,** 8663–8670 (1997).

45. Hu, G. G. *et al.* Structure of a DNA-bisdaunomycin complex. *Biochemistry* **36,** 5940–5946 (1997).

46. Zeglis, B. M., Pierre, V. C. & Barton, J. K. Metallo-intercalators and metallo-insertors. *Chem. Commun. (Camb).* **7345,** 4565–79 (2007).

47. Sava, G. *et al.* Influence of chemical stability on the activity of the antimetastasis ruthenium compound NAMI-A. *Eur. J. Cancer* **38,** 427–35 (2002).

48. Sava, G. *et al.* Dual Action of NAMI-A in Inhibition of Solid Tumor Metastasis Selective Targeting of Metastatic Cells and Binding to Collagen. *Clin. Cancer Res.* **9,** 1898–1905 (2003).

49. Pizarro, A. M. & Sadler, P. J. Unusual DNA binding modes for metal anticancer complexes. *Biochimie* **91,** 1198–211 (2009).

50. van Rijt, S. H. & Sadler, P. J. Current applications and future potential for bioinorganic chemistry in the development of anticancer drugs. *Drug Discov. Today* **14,** 1089–97 (2009).

51. Ang, W. H., Casini, A., Sava, G. & Dyson, P. J. Organometallic ruthenium-based antitumor compounds with novel modes of action. *J. Organomet. Chem.* **696,** 989–998 (2011).

52. van Rijt, S. H., Mukherjee, A., Pizarro, A. M. & Sadler, P. J. Cytotoxicity, hydrophobicity, uptake, and distribution of osmium(II) anticancer complexes in ovarian cancer cells. *J. Med. Chem.* **53,** 840–9 (2010).

53. Rijt, S. H. Van, Kostrhunova, H., Brabec, V. & Sadler, P. J. Functionalization of osmium arene anticancer complexes with (poly)arginine: effect on cellular uptake, internalization, and cytotoxicity. *Bioconjug. Chem.* **22,** 218–226 (2011).

54. Liu, Z. *et al.* Organometallic half-sandwich iridium anticancer complexes. *J. Med. Chem.* **54,** 3011–26 (2011).

55. Liu, Z. *et al.* Contrasting reactivity and cancer cell cytotoxicity of isoelectronic organometallic iridium(III) complexes. *Inorg. Chem.* **50,** 5777–83 (2011).

56. Davies, M. S., Berners-Price, S. J. & Hambley, T. W. Rates of platination of -AG- and -GA- containing double-stranded oligonucleotides: effect of chloride concentration. *J. Inorg. Biochem.* **79,** 167–72 (2000).

57. Fichtinger-Schepman, A. M., van der Veer, J. L., den Hartog, J. H., Lohman, P. H. & Reedijk, J. Adducts of the antitumor drug cis-diamminedichloroplatinum(II) with DNA: formation, identification, and quantitation. *Biochemistry* **24,** 707–13 (1985).

58. Chaney, S. G. *et al.* Protein interactions with platinum-DNA adducts: from structure to function. *J. Inorg. Biochem.* **98,** 1551–9 (2004).

59. Harrap, K. Preclinical studies identifying carboplatin as a viable cisplatin alternative. *Cancer Treat. Rev.* **12,** 21–33 (1985).

60. Knox, R., Friedlos, F., Lydall, D. & Roberts, J. Mechanism of Cytotoxicity of Anticancer Platinum Drugs: Evidence that cis-diamminedichloroplatinum(II) and cis-diammine-

(1,1-cyclobutanedicarboxylato)platinum(II) Differ Only in the Kinetics of Their Interaction with DNA. *Cancer Res.* **46,** 1972–1979 (1986).

61.   Ovarian, A. *et al.* Chemotherapy in advanced ovarian cancer: four systematic meta-analyses of individual patient data from 37 randomized trials. *Br. J. Cancer* **78,** 1479–1487 (1998).

62.   Ishida, S., Lee, J., Thiele, D. J. & Herskowitz, I. Uptake of the anticancer drug cisplatin mediated by the copper transporter Ctr1 in yeast and mammals. *Proc. Natl. Acad. Sci. U. S. A.* **99,** 14298–302 (2002).

63.   Holzer, A. K. & Howell, S. B. The internalization and degradation of human copper transporter 1 following cisplatin exposure. *Cancer Res.* **66,** 10944–52 (2006).

64.   Safaei, R., Otani, S., Larson, B. J., Rasmussen, M. L. & Howell, S. B. Transport of Cisplatin by the Copper Efflux Transporter ATP7B. **73,** 461–468 (2008).

65.   Mistry, P., Kelland, L. R., Abel, G., Sidhar, S. & Harrap, K. R. The relationships between glutathione, glutathione-S-transferase and cytotoxicity of platinum drugs and melphalan in eight human ovarian carcinoma cell lines. *Br. J. Cancer* **64,** 215–20 (1991).

66.   Bogojeski, J., Petrović, B. & Bugarčić, Ž. in *Chronic Lymphocytic Leuk.* **16,** 339–366 (2012).

67.   Ishikawa, T. The ATP-dependent glutathione S-conjugate export pump. *Trends Biochem. Sci.* **17,** 463–8 (1992).

68.   Lewis, a D. *et al.* Glutathione S-transferase isoenzymes in human tumours and tumour derived cell lines. *Br. J. Cancer* **60,** 327–31 (1989).

69.   Johnson, S. W. *et al.* Relationship between Platinum-DNA Adduct Formation and Removal and Cisplatin Cytotoxicity in Cisplatin-sensitive and -resistant Human Ovarian Cancer Cells Relationship between Platinum-DNA Adduct Formation and Removal and Cisplatin Cytotoxicity in Cisplat. *Cancer Res.* **54,** 5911–5916 (1994).

70.   Liu, Y.-P. *et al.* The effects of ERCC1 expression levels on the chemosensitivity of gastric cancer cells to platinum agents and survival in gastric cancer patients treated with oxaliplatin-based adjuvant chemotherapy. *Oncol. Lett.* **5,** 935–942 (2013).

71.   Fink, D., Nebel, S., Aebi, S., Zheng, H. & Cenni, B. The role of DNA mismatch repair in platinum drug resistance. *Cancer Res.* 4881–4886 (1996).

72.   Albertella, M. R., Green, C. M., Lehmann, A. R. & O'Connor, M. J. A role for polymerase eta in the cellular tolerance to cisplatin-induced damage. *Cancer Res.* **65,** 9799–806 (2005).

73.   Kidani, Y., Inagaki, K. & Iigo, M. Antitumor activity of 1, 2-diaminocyclohexaneplatinum complexes against sarcoma-180 ascites form. *J. Med. Chem.* **21,** 1315–1318 (1978).

74.   Holzer, A., Manorek, G. & Howell, S. Contribution of the major copper influx transporter CTR1 to the cellular accumulation of cisplatin, carboplatin, and oxaliplatin. *Mol. Pharmacol.* **70,** 1390–1394 (2006).

75.   Kasparkova, J., Vojtiskova, M., Natile, G. & Brabec, V. Unique properties of DNA interstrand cross-links of antitumor oxaliplatin and the effect of chirality of the carrier ligand. *Chem. A Eur. J.* **14,** 1330–41 (2008).

76.   Giacchetti, S. & Perpoint, B. Phase III multicenter randomized trial of oxaliplatin added to chronomodulated fluorouracil–leucovorin as first-line treatment of metastatic colorectal cancer. *J. Clin. Oncol.* **18,** 136–147 (2000).

77.   Kelland, L., Abel, G. & McKeage, M. Preclinical antitumor evaluation of bis-acetato-

ammine-dichloro-cyclohexylamine platinum (IV): an orally active platinum drug. *Cancer Res.* 2581–2586 (1993).

78. Sharp, S. Y., Rogers, P. M. & Kelland, L. R. Transport of cisplatin and bis-acetato-ammine-dichlorocyclohexylamine Platinum(IV) (JM216) in human ovarian carcinoma cell lines: identification of a plasma membrane protein associated with cisplatin resistance. *Clin. Cancer Res.* **1,** 981–9 (1995).

79. Holford, J. In vitro circumvention of cisplatin resistance by the novel sterically hindered platinum complex AMD473. *Br. J. Cancer* **77,** 366–373 (1998).

80. Hamilton, G. & Olszewski, U. Picoplatin pharmacokinetics and chemotherapy of non-small cell lung cancer. *Expert Opin. Drug Metab. Toxicol.* **9,** 1381–1390 (2013).

81. Wheate, N. J., Walker, S., Craig, G. E. & Oun, R. The status of platinum anticancer drugs in the clinic and in clinical trials. *Dalton Trans.* **39,** 8113–27 (2010).

82. Rudolph, R. Electron microscopy demonstration of sulphurated acid mucopolysaccharides in canine mast cell tumors, using barium chloride and ruthenium red, together with comments on the classification and differentiation of tumor cells. *Arch. Exp. Vet.* **25,** 925–935 (1971).

83. Clarke, M. J., Sigel, H. & Sigel, A. in *Met. Ions Biol. Syst.* 231–283 (Marcel Dekker, 1980).

84. Clarke, M. J., Zhu, F. & Frasca, D. R. Non-platinum chemotherapeutic metallopharmaceuticals. *Chem. Rev.* **99,** 2511–34 (1999).

85. Chen, H. *et al.* Organometallic ruthenium(II) diamine anticancer complexes: arene-nucleobase stacking and stereospecific hydrogen-bonding in guanine adducts. *J. Am. Chem. Soc.* **124,** 3064–82 (2002).

86. Aird, R., Cummings, J. & Ritchie, A. In vitro and in vivo activity and cross resistance profiles of novel ruthenium (II) organometallic arene complexes in human ovarian cancer. *Br. J. Cancer* **86,** 1652–1657 (2002).

87. Wang, F. *et al.* Kinetics of aquation and anation of ruthenium(II) arene anticancer complexes, acidity and X-ray structures of aqua adducts. *Chem. A Eur. J.* **9,** 5810–20 (2003).

88. Hotze, A. C. G. *et al.* Structure-dependent in vitro cytotoxicity of the isomeric complexes [Ru(L)2Cl2] (L= o-tolylazopyridine and 4-methyl-2-phenylazopyridine) in comparison to [Ru(azpy)2Cl2]. *J. Biol. Inorg. Chem.* **9,** 354–64 (2004).

89. Chen, J. C., Li, J., Qian, L. & Zheng, K. C. Electronic structures and SARs of the isomeric complexes α-, β-, γ- [Ru(mazpy)2Cl2] with different antitumor activities. *J. Mol. Struct. THEOCHEM* **728,** 93–101 (2005).

90. Hotze, A. C. G., Kariuki, B. M. & Hannon, M. J. Dinuclear double-stranded metallosupramolecular ruthenium complexes: potential anticancer drugs. *Angew. Chem. Int. Ed. Engl.* **45,** 4839–42 (2006).

91. Peacock, A. F. a & Sadler, P. J. Medicinal organometallic chemistry: designing metal arene complexes as anticancer agents. *Chem. Asian J.* **3,** 1890–9 (2008).

92. Kostrhunova, H. *et al.* DNA interactions of monofunctional organometallic osmium(II) antitumor complexes in cell-free media. *J. Med. Chem.* **51,** 3635–43 (2008).

93. van Rijt, S. H. *et al.* Amide linkage isomerism as an activity switch for organometallic osmium and ruthenium anticancer complexes. *J. Med. Chem.* **52,** 7753–7764 (2009).

94. Lucas, S. J. *et al.* Synthesis of iridium and ruthenium complexes with (N,N), (N,O) and (O,O) coordinating bidentate ligands as potential anti-cancer agents. *Dalt. Trans.* **41,** 13800 (2012).

95. Lord, R. M. *et al.* Hypoxia-Sensitive Metal β-Ketoiminato Complexes Showing Induced Single-Strand DNA Breaks and Cancer Cell Death by Apoptosis. *J. Med. Chem.* **58,** 4940–4953 (2015).

96. Barnard, P. J. & Berners-Price, S. J. Targeting the mitochondrial cell death pathway with gold compounds. *Coord. Chem. Rev.* **251,** 1889–1902 (2007).

97. Powis, G. & Kirkpatrick, D. L. Thioredoxin signaling as a target for cancer therapy. *Curr. Opin. Pharmacol.* **7,** 392–7 (2007).

98. Shaw, C. Gold-based therapeutic agents. *Chem. Rev.* **99,** 2589–2600 (1999).

99. Che, C.-M. *et al.* Gold(III) porphyrins as a new class of anticancer drugs: cytotoxicity, DNA binding and induction of apoptosis in human cervix epitheloid cancer cells. *Chem. Commun. (Camb).* 1718–9 (2003).

100. Zanias, S. *et al.* Synthesis, Structure, and Antiproliferative Activity of Three Gallium(III) Azole Complexes. *Bioinorg. Chem. Appl.* **2010,** (2010).

101. Meggers, E. *et al.* Exploring Chemical Space with Organometallics: Ruthenium Complexes as Protein Kinase Inhibitors. *Synlett* **2007,** 1177–1189 (2007).

102. Ott, I. *et al.* Antitumor-active cobalt-alkyne complexes derived from acetylsalicylic acid: studies on the mode of drug action. *J. Med. Chem.* **48,** 622–9 (2005).

103. Hartinger, C. G. *et al.* From bench to bedside--preclinical and early clinical development of the anticancer agent indazolium trans-[tetrachlorobis(1H-indazole)ruthenate(III)] (KP1019 or FFC14A). *J. Inorg. Biochem.* **100,** 891–904 (2006).

104. Bergamo, A. & Sava, G. Ruthenium anticancer compounds: myths and realities of the emerging metal-based drugs. *Dalton Trans.* **40,** 7817–7823 (2011).

105. Dougherty, T. J. *et al.* Photodynamic Therapy. *J. Natl. Cancer Inst.* **90,** 889–905 (1998).

106. Detty, M., Gibson, S. & Wagner, S. Current clinical and preclinical photosensitizers for use in photodynamic therapy. *J. Med. Chem.* **47,** 3897–3915 (2004).

107. Lippard, S. J., Jenette, K., Varsiliades, H. & Bauer, W. Metallointercalation Reagents. 2-Hydroxyethanethiolato (2,2′,2″-terpyridyl) platinum(II) Monocation Binds Strongly to DNA By Intercalation. *Proc. Natl. Acad. Sci. USA* **71,** 3839–3843 (1974).

108. Bond, P., Langridge, R., Jenette, K. & Lippard, S. J. X-ray fiber diffraction evidence for neighbor exclusion binding of a platinum metallointercalation reagent to DNA. *Proc. Natl. Acad. Sci. U. S. A.* **72,** 4825–4829 (1975).

109. Howe-Grant, M. & Lippard, S. J. Binding of platinum(II) intercalation reagents to deoxyribnonucleic acid. Dependence on base-pair composition, nature of the intercalator, and ionic strength. *Biochemistry* **18,** 5762–9 (1979).

110. Barton, J., Dannenberg, J. & Raphael, A. Enantiomeric selectivity in binding tris (phenanthroline) zinc (II) to DNA. *J. Am. Chem. Soc.* **104,** 4967–4969 (1982).

111. Yamagishi, A. Evidence for stereospecific binding of tris (1, 10-phenanthroline)-ruthenium (II) to DNA is provided by electronic dichroism. *J. Chem. Soc., Chem. Commun.* 572–573 (1983).

112. Barton, J., Danishefsky, A. & Goldberg, J. Tris (phenanthroline) ruthenium (II): stereoselectivity in binding to DNA. *J. Am. Chem. Soc.* **106,** 2172–2176 (1984).

113. Kumar, C., Barton, J. & Turro, N. Photophysics of ruthenium complexes bound to double helical DNA. *J. Am. Chem. Soc.* **107,** 5518–5523 (1985).

114. Barton, J., Goldberg, J., Kumar, C. & Turro, N. Binding modes and base specificity of tris (phenanthroline) ruthenium (II) enantiomers with nucleic acids: tuning the stereoselectivity. *J. Am. Chem. Soc.* **108,** 2081–2088 (1986).

115. Rehmann, J. P. & Barton, J. K. 1H NMR Studies of Tris (phenanthroline) Metal

Complexes Bound to Oligonucleotides: Characterization of Binding Modes. *Biochemistry* **29,** 1701–1709 (1990).

116. Hiort, C., Norddn, B. & Rodgerf, A. Enantiopreferential DNA Binding of [Ru(II)(1,10-phenanthroline)3]2+ Studied with Linear and Circular Dichroism. *J. Am. Chem. Soc.* **112,** 1971–1982 (1990).

117. Satyanarayana, S., Dabrowiak, J. C. & Chaires, J. B. Neither delta- nor lambda-tris(phenanthroline)ruthenium(II) binds to DNA by classical intercalation. *Biochemistry* **31,** 9319–24 (1992).

118. Satyanarayana, S., Dabrowiak, J. C. & Chaires, J. B. Tris(phenanthroline)ruthenium(II) enantiomer interactions with DNA: mode and specificity of binding. *Biochemistry* **32,** 2573–84 (1993).

119. Coggan, D. Z. M., Haworth, I. S., Bates, P. J., Robinson, A. & Rodger, A. DNA Binding of Ruthenium Tris(1,10-phenanthroline): Evidence for the Dependence of Binding Mode on Metal Complex Concentration. *Inorg. Chem.* **38,** 4486–4497 (1999).

120. Friedman, A., Chambron, J., Sauvage, J., Turro, N. & Barton, J. A molecular light switch for DNA: Ru(bpy)2(dppz)2+. *J. Am. Chem. Soc.* **112,** 4960–4962 (1990).

121. Amouyal, E., Homsi, A., Chambron, J. & Sauvage, J. Synthesis and Study of a Mixed-ligand Ruthenium(II) Complex in Its Ground and Excited States: Bis(2,2'-bi pyridine)(dipyrido[3,2-a:2',3'-c]phenazine- N4N5)ruthenium(II). *J. Chem. Soc. Dalt. Trans.* 1841–1845 (1990).

122. Fees, J., Kaim, W., Matheb, M. W., Krej, M. & Mi, S. Electronic Structure of the 'Molecular Light Switch' [Ru(bpy)2(dppz)]2+ (dppz = Dipyrido[3,2-a:2',3'-c]phenazine). Cyclic Voltammetric, UV/Vis, and EPR/ENDOR Study of Multiply Reduced Complexes and Ligands. *Inorg. Chem.* **32,** 166–174 (1993).

123. Fees, J., Ketterle, M., Klein, A., Fiedler, J. & Kaim, W. Electrochemical, spectroscopic and EPR study of transition metal complexes of dipyrido[3,2-a:2',3'-c]phenazine. *J. Chem. Soc. Dalt. Trans.* 2595–2600 (1999). doi:10.1039/a903417j

124. Jenkins, Y., Friedman, a E., Turro, N. J. & Barton, J. K. Characterization of dipyridophenazine complexes of ruthenium(II): the light switch effect as a function of nucleic acid sequence and conformation. *Biochemistry* **31,** 10809–16 (1992).

125. Hiort, C., Lincoln, P. & Norden, B. DNA Binding of delta- and lamda-[Ru(phen)2DPPZ]2+. *J. Am. Chem. Soc.* **115,** 3448–3454 (1993).

126. Tuite, E., Lincoln, P. & Nordén, B. Photophysical evidence that Δ-and Λ-[Ru(phen)2(dppz)]2+ Intercalate DNA from the minor groove. *J. Am. Chem. Soc.* **119,** 239–240 (1997).

127. Holmlin, R. E., Stemp, E. D. a. & Barton, J. K. Ru(phen)(2)dppz(2+) Luminescence: Dependence on DNA Sequences and Groove-Binding Agents. *Inorg. Chem.* **37,** 29–34 (1998).

128. Metcalfe, C. & Thomas, J. a. Kinetically inert transition metal complexes that reversibly bind to DNA. *Chem. Soc. Rev.* **32,** 215 (2003).

129. Sahai, R. & Rillema, D. A novel hetero-oligomer containing one ruthenium(II) and three platinum(II) metal centres bridged by 2,3-Bis(2-pyridyl)quinoxaline. *J. Chem. Soc. Chem. Commun.* **31,** 1133–1134 (1986).

130. Wing-Wah Yam, V., Wing-Man Lee, V. & Cheung, K.-K. luminescent organometallic ruthenium(II)/platinum(II) binuclear complex and its ruthenium(II)/dichloro-platinum(II) and palladium(II) counterparts. X-Ray Crystal Structure of [Ru(bpy)2(u-2,3-dpp)PtCl2]2+ [2,3-dpp = 2,3-bis(2-pyridyl)pyrazine]. *J. Chem. Soc. Chem. Commun.*

2075–2076 (1994).

131. Milkevitch, M., Brauns, E., Brewer, K. J. & June, R. V. Spectroscopic and Electrochemical Properties of a Series of Mixed-Metal d6,d8 Bimetallic Complexes of the Form [(bpy)2M(BL)PtCl2]2+ (bpy = 2,2'-Bipyridine; BL = dpq (2,3-Bis(2-pyridyl)quinoxaline) or dpb (2,3-Bis(2-pyridyl)- benzoquinoxaline); M = OsII or. *Inorg. Chem.* **35,** 1737–1739 (1996).

132. Milkevitch, M., Storrie, H., Brauns, E., Brewer, K. J. & Shirley, B. W. A New Class of Supramolecular, Mixed-Metal DNA-Binding Agents: The Interaction of Ru(II),Pt(II) and Os(II),Pt(II) Bimetallic Complexes with DNA. *Inorg. Chem.* **36,** 4534–4538 (1997).

133. Williams, R. L., Toft, H. N., Winkel, B. & Brewer, K. J. Synthesis, characterization, and DNA binding properties of a series of Ru, Pt mixed-metal complexes. *Inorg. Chem.* **42,** 4394–400 (2003).

134. Jain, A., Wang, J., Mashack, E. R., Winkel, B. S. J. & Brewer, K. J. Multifunctional DNA interactions of Ru-Pt mixed metal supramolecular complexes with substituted terpyridine ligands. *Inorg. Chem.* **48,** 9077–84 (2009).

135. van der Schilden, K. *et al.* A Highly Flexible Dinuclear Ruthenium(II)-Platinum(II) Complex: Crystal Structure and Binding to 9-ethylguanine. *Angew. Chem. Int. Ed. Engl.* **43,** 5668–70 (2004).

136. Howe-Grant, M., Wu, K. C., Bauer, W. R. & Lippard, S. J. Binding of platinum and palladium metallointercalation reagents and antitumor drugs to closed and open DNAs. *Biochemistry* **15,** 4339–46 (1976).

137. Lowe, G. *et al.* Cytotoxicity of 2,2':6',2"-terpyridineplatinum(II) complexes against human ovarian carcinoma. *J. Med. Chem.* **42,** 3167–74 (1999).

138. Sakai, K. *et al.* A tris(2,2'-bipyridine)ruthenium(II) derivative tethered to a cis-PtCl2(amine)2 moiety: syntheses, spectroscopic properties, and visible-light-induced scission of DNA. *Dalt. Trans.* **2,** 3300 (2006).

139. Petitjean, A. & Barton, J. Tuning the DNA reactivity of cis-platinum: conjugation to a mismatch-specific metallointercalator. *J. Am. Chem. Soc.* **126,** 14728–14729 (2004).

140. Jackson, B., Alekseyev, V. & Barton, J. A versatile mismatch recognition agent: specific cleavage of a plasmid DNA at a single base mispair. *Biochemistry* **38,** 4655–4662 (1999).

141. Ricci, M. & Zong, W. Chemotherapeutic approaches for targeting cell death pathways. *Oncologist* **11,** 342–357 (2006).

142. Majno, G. & Joris, I. Apoptosis, oncosis, and necrosis. An overview of cell death. *Am. J. Pathol.* **146,** 3–15 (1995).

143. Trump, B. F., Berezesky, I. K., Chang, S. H. & Phelps, P. C. The pathways of cell death: oncosis, apoptosis, and necrosis. *Toxicol. Pathol.* **25,** 82–88 (1997).

144. Weerasinghe, P. & Buja, L. M. Oncosis: An important non-apoptotic mode of cell death. *Exp. Mol. Pathol.* **93,** 302–308 (2012).

145. Proskuryakov, S. Y. ., Konoplyannikov, A. G. & Gabai, V. L. Necrosis: a specific form of programmed cell death? *Exp. Cell Res.* **283,** 1–16 (2003).

146. Dacheux, D. *et al.* Pseudomonas aeruginosa Cystic Fibrosis Isolates Induce Rapid, Type III Secretion-Dependent, but ExoU-Independent, Oncosis of Macrophages and Polymorphonuclear Neutrophils. *Infect. Immun.* **68,** 2916–2924 (2000).

147. Kerr, J., Wyllie, A. & Currie, A. Apoptosis: a basic biological phenomenon with wide-ranging implications in tissue kinetics. *Br. J. Cancer* **26,** 239–257 (1972).

148. Fuchs, Y. & Steller, H. Programmed cell death in animal development and disease. *Cell*

147, 742–58 (2011).

149. Lindsten, T. *et al.* The combined functions of proapoptotic Bcl-2 family members bak and bax are essential for normal development of multiple tissues. *Mol. Cell* **6,** 1389–99 (2000).

150. Metzstein, M. M., Stanfield, G. M. & Horvitz, H. R. Genetics of programmed cell death in C. elegans: past, present and future. *Trends Genet.* **14,** 410–6 (1998).

151. Ellis, H. M. & Horvitz, H. R. Genetic control of programmed cell death in the nematode C. elegans. *Cell* **44,** 817–29 (1986).

152. Nicholson, D. & Thornberry, N. Caspases: killer proteases. *Trends Biochem. Sci.* **22,** 299–306 (1997).

153. Porter, a G. & Jänicke, R. U. Emerging roles of caspase-3 in apoptosis. *Cell Death Differ.* **6,** 99–104 (1999).

154. Danial, N. & Korsmeyer, S. Cell death: critical control points. *Cell* **116,** 205–219 (2004).

155. Mizushima, N. & Komatsu, M. Autophagy: renovation of cells and tissues. *Cell* **147,** 728–41 (2011).

156. Lin, N.-Y. *et al.* Autophagy regulates TNFα-mediated joint destruction in experimental arthritis. *Ann. Rheum. Dis.* **72,** 761–8 (2013).

157. Aita, V. M. *et al.* Cloning and genomic organization of beclin 1, a candidate tumor suppressor gene on chromosome 17q21. *Genomics* **59,** 59–65 (1999).

158. Fong, M. Y. *et al.* Withaferin A synergizes the therapeutic effect of doxorubicin through ROS-mediated autophagy in ovarian cancer. *PLoS One* **7,** e42265 (2012).

159. Martin, R. M., Leonhardt, H. & Cardoso, M. C. DNA labeling in living cells. *Cytom. Part A* **67,** 45–52 (2005).

160. Gill, M. R. *et al.* A ruthenium(II) polypyridyl complex for direct imaging of DNA structure in living cells. *Nat. Chem.* **1,** 662–667 (2009).

161. Wragg, A. *et al.* Tuning the Cellular Uptake Properties of Luminescent Heterobimetallic Iridium(III)-Ruthenium(II) DNA Imaging Probes. *Chemistry* **20,** 14004–11 (2014).

162. Gill, M. R. *et al.* Targeting the endoplasmic reticulum with a membrane-interactive luminescent ruthenium(II) polypyridyl complex. *Chem. Sci.* **4,** 4512 (2013).

163. Gill, M. R., Derrat, H., Smythe, C. G. W., Battaglia, G. & Thomas, J. a. Ruthenium(II) metallo-intercalators: DNA imaging and cytotoxicity. *Chembiochem* **12,** 877–80 (2011).

Chapter 2

Synthesis and DNA Binding

2.1 Aims

The initial aim of this project was to synthesise the four complexes **1 – 4** shown in *Figure 2.1*. These polypyridyl ruthenium complexes are structural extensions of the complex Ru(tpphz) **1** which a previous study demonstrated binds to DNA and exhibits cytotoxic activity.[1]
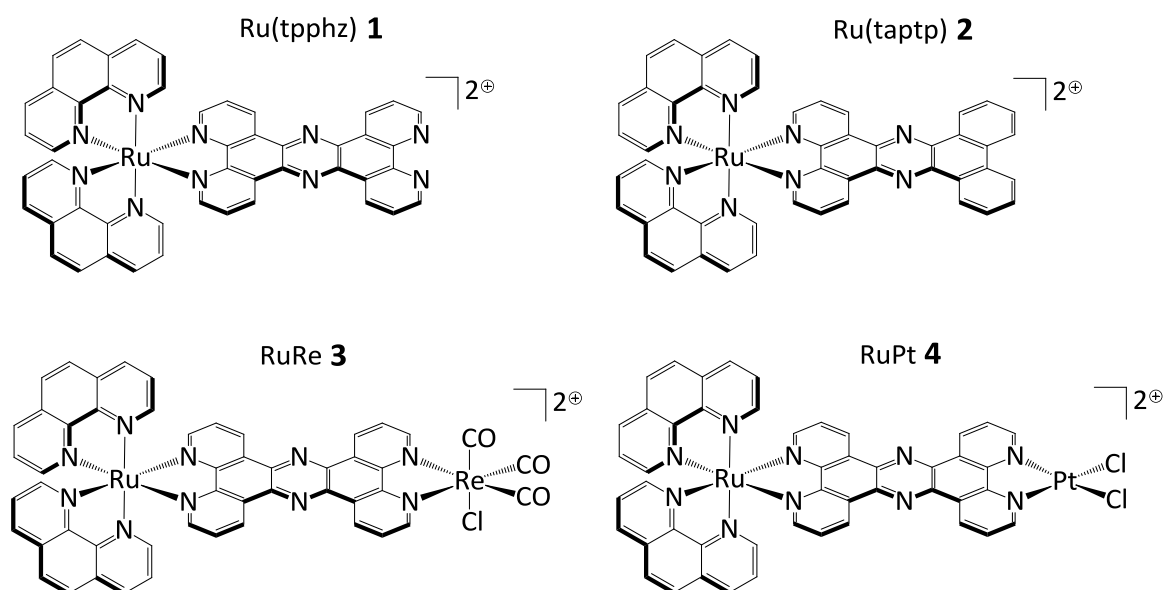

Figure 2.1 – The four target complexes **1 – 4**

2.2   Synthesis

The first synthetic target was the resynthesis of the complex Ru(tpphz) **1**. One conceivable route to this complex involves synthesis of the tetrapyridophenazine ligand (tpphz) followed by an equimolar ratio reaction with the ruthenium polypyridyl unit (phen)$_2$Ru. However, this always yields the dinuclear ruthenium product [{Ru(phen)$_2$}$_2$(tpphz)]$^{4+}$ due to the two equivalent binding sites of tpphz, the lower solubility of the free ligand, and the high stability of the product. An alternative literature route was utilised in the preparation whereby the tpphz ligand is covalently synthesized using a precursor ligand already bound to the ruthenium centre.[2]

First, ruthenium(III) chloride hydrate was coordinated to bidentate phenanthroline ligands to make (phen)$_2$RuCl$_2$. The modified phenanthroline ligand 1,10-phenanthroline-5-6-dione (DPQ) was then synthesised by a literature preparation[3] and coordinated through displacement of the two chlorides in the final bidentate site to yield [Ru(phen)$_2$(DPQ)]$^{2+}$. In a separate synthesis the modified phenanthroline ligand 1,10-phenanthroline-5,6-diamine (phen-diamine) was made from DPQ, *via* the 1-10-phenanthroline-5,6-dioxime intermediate (phen-dioxime).[4] Finally, the [Ru(phen)$_2$(DPQ)]$^{2+}$ complex and phen-diamine were combined in a condensation reaction to form the tpphz ligand already coordinated to ruthenium, and yield [Ru(phen)$_2$(tpphz)]$^{2+}$, **1**. This final reaction was carried out with newly synthesised DPQ complex and phen-diamine and executed under nitrogen with dry solvents as per Schlenk line techniques. This resulted in an orange precipitate that did not require purification by column chromatography; although for small samples of maximum purity column chromatography was employed using an alumina stationary phase and an eluent of acetonitrile that contained an increasing fraction of water/KNO$_3$.

For the complex Ru(taptp) **2**, a different synthetic approach was employed in which the taptp ligand was made first following a literature preparation.[5] This ligand has only one available bidentate binding site so it could then be reacted with [Ru(phen)$_2$Cl$_2$] to displace the two chlorides and form the mononuclear complex [Ru(phen)$_2$(taptp)]$^{2+}$; again the reaction was carried out under Schlenk line conditions and no further purification was required.

The dinuclear complexes RuPt **3** and RuRe **4** both use Ru(tpphz) **1** as the starting material. In the case of RuPt **3** two different platination methods were attempted. First, tetrachloroplatinate, $K_2[PtCl_4]$ was used to make $(DMSO)_2PtCl_2$ which was then reacted with Ru(tpphz) **1**, as a PF_6 salt in acetone. This did not yield the desired product, with unreacted Ru(tpphz) **1** collected as the precipitate. Instead, tetrachloroplatinate was directly reacted with Ru(tpphz) **1** in a methanol/water solvent mixture. This gave a brown precipitate which had the correct M^{1+} peak in the mass spectrum and a downfield shift in the ^1H NMR spectrum for the protons closest to the terminal nitrogen atoms; indicative of deshielding by the additional $PtCl_2$ unit drawing electron density away from those protons.

For the complex RuRe **4**, the starting material of Ru(tpphz) **1** was reacted with pentacarbonyl rhenium(I) chloride, $Re(CO)_5Cl$, in acetonitrile. This yielded an orange product which again had the correct M^{1+} peak in the mass spectrum and a downfield shift in the protons closest to the terminal nitrogen atoms from the deshielding effect of the $Re(CO)_3Cl$ unit drawing electron density.

The overall reaction scheme for complexes **1 – 4** is shown below in *Figure 2.2*. Only the isolated molecules are shown with additional reagents and conditions omitted for clarity (all syntheses contained in *Experimental Section 6.2*).

For all aqueous luminescence and cellular studies the complexes were first converted to their water-soluble chloride salts. This was achieved by anion metathesis where the PF_6 salt was first dissolved in acetone and then tetrabutylammonium chloride was added to exchange the counter ion and thus precipitate the chloride complex (procedure contained in *Experimental Section 6.2.16*).

phen

NO₂

DPQ

tpphz

phen-NO₂

phen-dioxime

RuCl₃.x(H₂O)

(phen)₂RuCl₂

phen-diamine

(phen)Ru(DPQ) (PF₆)₂

RuRu (PF₆)₄

Ru(tpphz) 1 (PF₆)₂

phen-quin

"PtCl₂"

RuPt 4 (PF₆)₂

ReCl(CO)₅

RuRe 3 (PF₆)₂

(taptp)

(phen)₂RuCl₂

Ru(taptp) 2 (PF₆)₂

Figure 2.2 – Overall synthetic route for complexes **1 – 4**

2.3　Luminescence

Since the first demonstration of the DNA light switch effect by Barton, *et al.*[6] with the complex [Ru(bipy)$_2$(dppz)]$^{2+}$, many ruthenium polypyridyl complexes have been shown to have the same property *in vitro*.[7] This effect originates from the metal-to-ligand-charge-transfer (MLCT) of the system - when photo-excited at a specific wavelength a low oxidation state electron rich metal can transfer electron density from its *d*-orbital to a ligands π^* orbital and create a high energy unstable excited state. When free in aqueous solution the excited state is short-lived due to non-radiative decay through the surrounding hydrogen bonds with water molecules. Conversely, if the molecule is bound to DNA (see *Introduction Section 1.2*), it can be protected from the surrounding water molecules in a hydrophobic environment which allows the excited state to decay through a radiative path – usually phosphorescence. This route of excitation to a triplet state and the phosphorescent emission it can then proceed through to return to its singlet ground state are represented in the Jablonski diagram below (*Figure 2.3*).[8]

A = Absorption
ISC = Inter-System Crossing
F = Fluorescence
P = Phosphorescence
S$_0$ = Singlet ground state
S$_1$ = Singlet excited state
T$_1$ = Triplet excited state
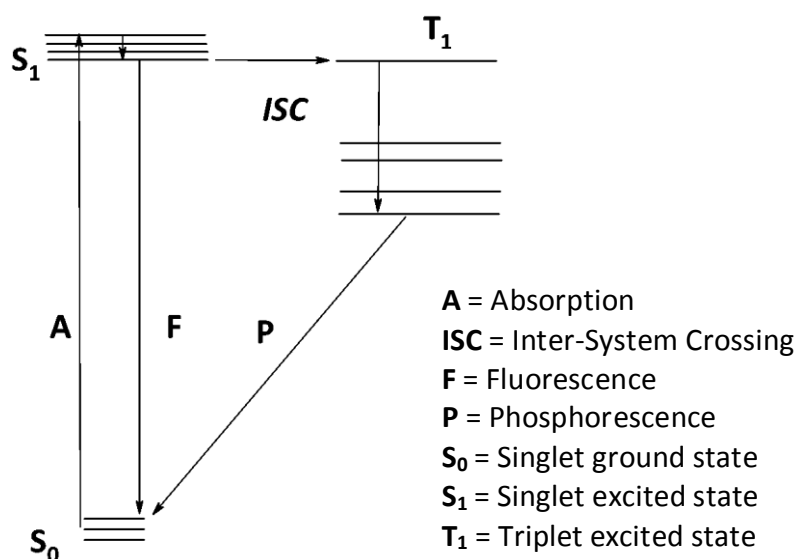
Figure 2.3 – Jablonski diagram of a ^{3}MLCT emission

To confirm the complexes display the DNA light switch effect, an aqueous 1 millimolar solution of solubilised genomic calf thymus DNA (1 mM CT-DNA) was titrated into a solution of the relevant system as an aqueous buffered chloride salt (10 µM, protocol contained in *Experimental Section 6.3*). The sample, contained within a 1 cm path length quartz cuvette, was excited at 440 nm upon each cumulative addition of DNA and the emission spectrum recorded to observe any change in luminescence with the increasing concentration of DNA.

It was already established that mononuclear complex **1** does display the DNA light switch effect and this provided a positive control.[1] Shown below (*Figures 2.4 – 2.7*) are the series of luminescence titrations for complexes **1 – 4**, with the emission seen to increase as the DNA light switch effect occurs until a point of saturation when all available complex is associated with DNA. By plotting ([DNA]/[complex]) versus the fraction bound (gathered from the increasing emission) a binding curve of the complex can be obtained, which emphasizes the point of saturation as a clear plateau in the curve, and these plots follow each of the corresponding luminescence titrations.

To extract the key value of the equilibrium binding constant, K_b, the binding data must be fitted to a Scatchard plot. The most basic form of this is the linear binding isotherm first proposed by Scatchard in 1949 for small molecules binding to isolated protein sites[9] – a relatively simple system that does not account for many overlapping sites in a DNA-ligand system that inevitably deviate from linearity. Many models have been created to fit the non-linear deviation but a popular one for this system, and the one used for this data, is the McGhee and Von Hippel (MVH) model (See *Experimental 6.3.2* for equation used). The parameters of K_b and also the site size occupied by the molecule in number of base pairs, n, could be estimated using the software SigmaPlot 13.0 to fit the binding data to a MVH model, and are included in *Figure 2.8*. The approximation of site size is an indicator of the number of base pairs occupied by the binding of the molecule, and if the value is below 1, insinuates an association of the molecule external to the DNA duplex.
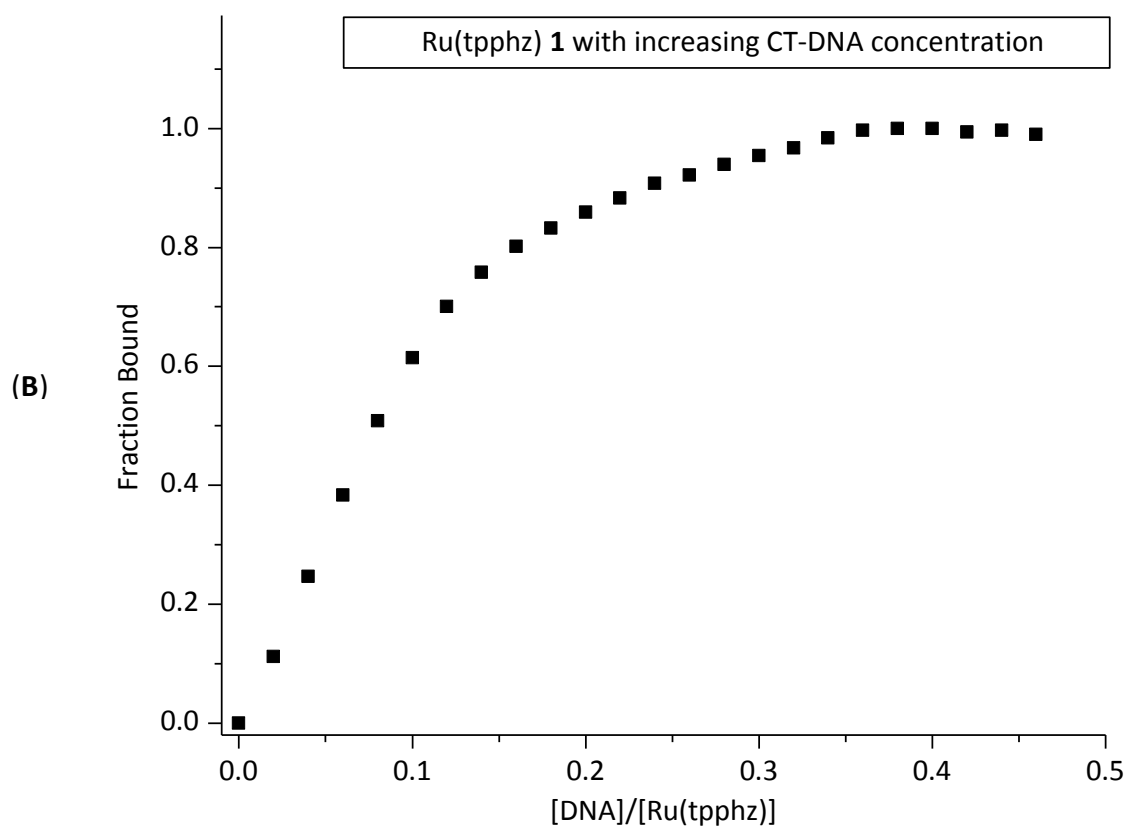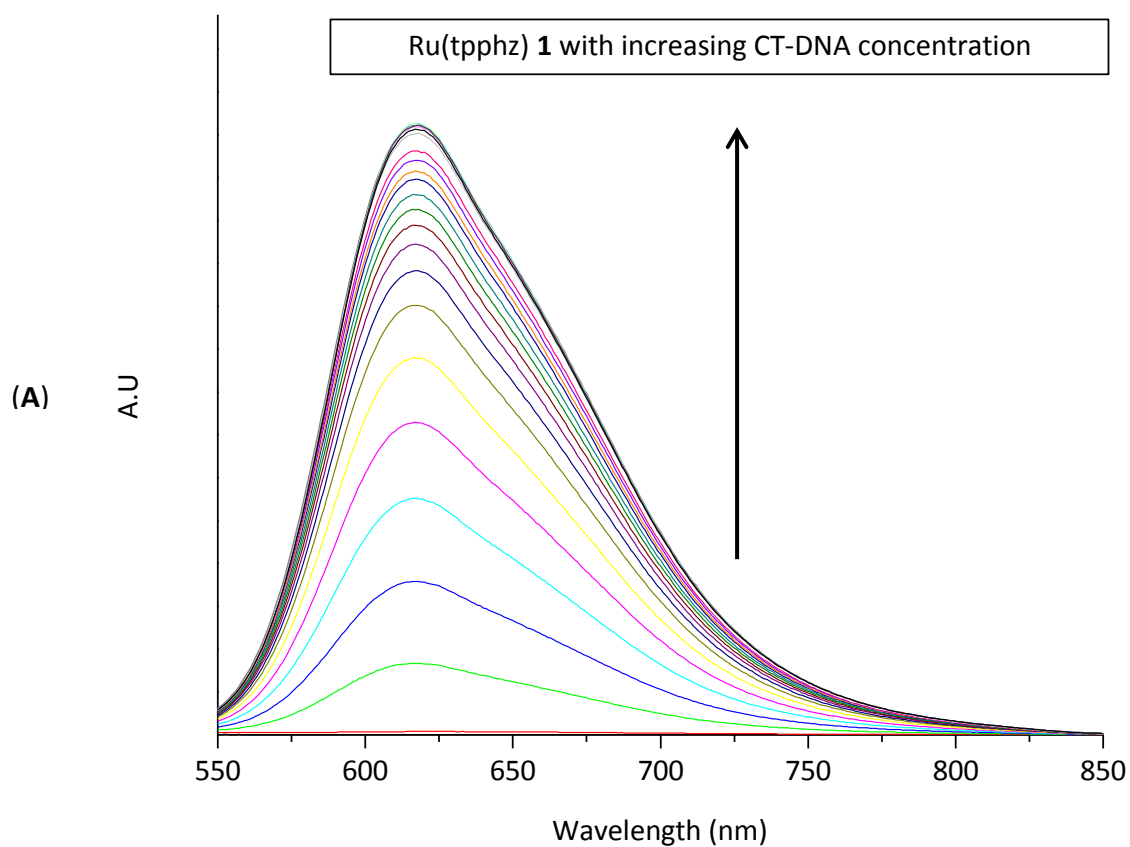
Figure 2.4 – (**A**) Luminescence titration of 10 μM [Ru(tpphz)]Cl$_2$ in aqueous solution (25 mM NaCl, pH 7.4) with increasing additions of 1 mM CT-DNA (**B**) corresponding binding curve
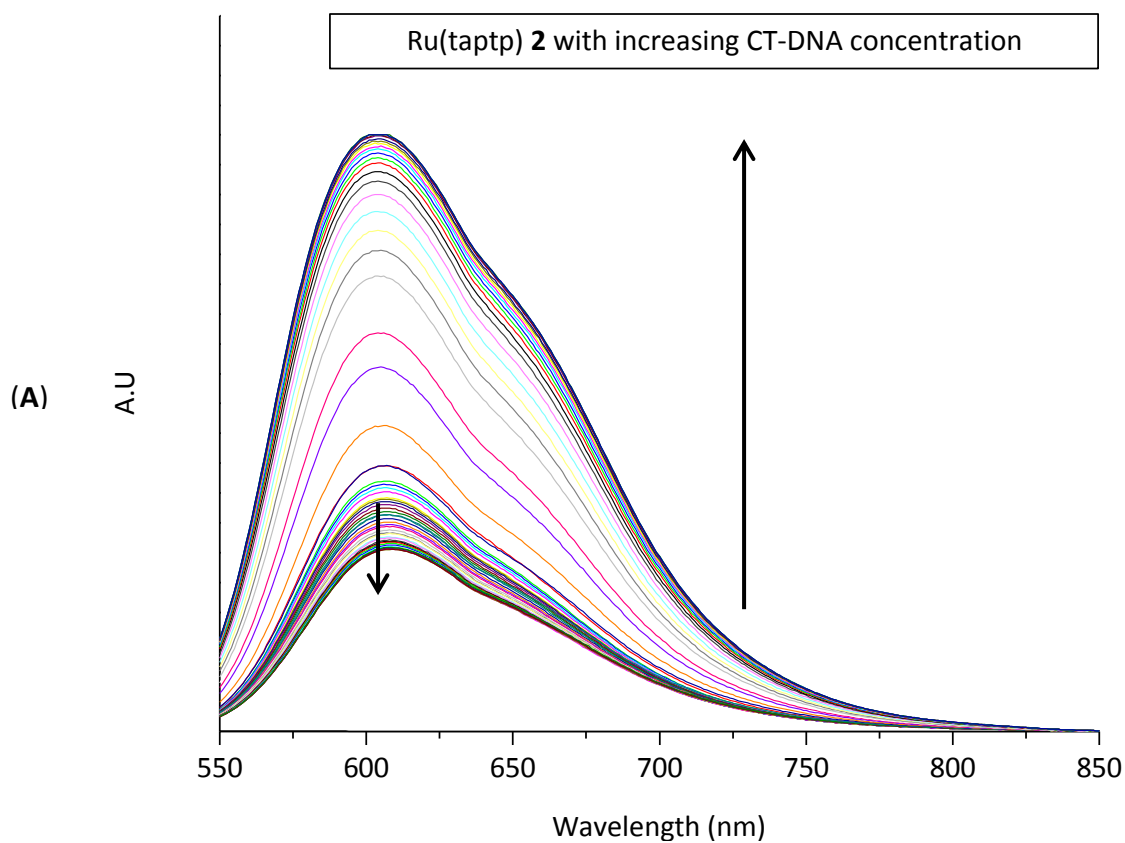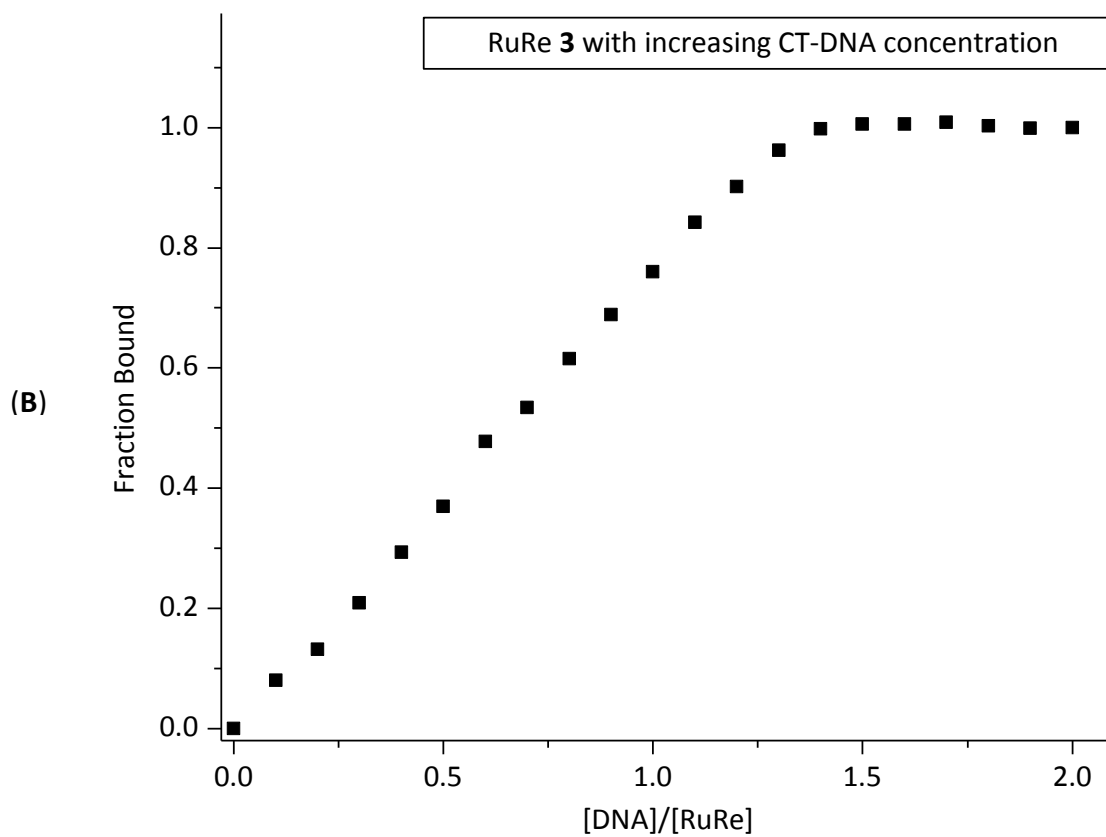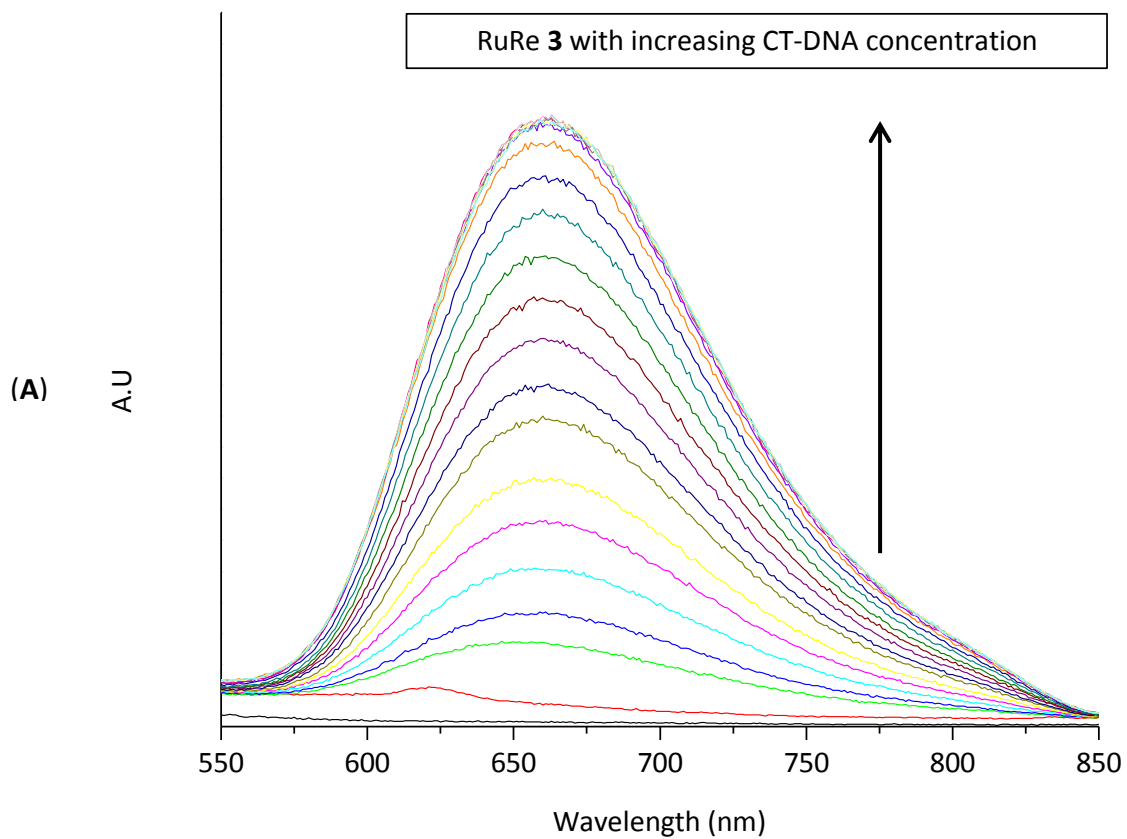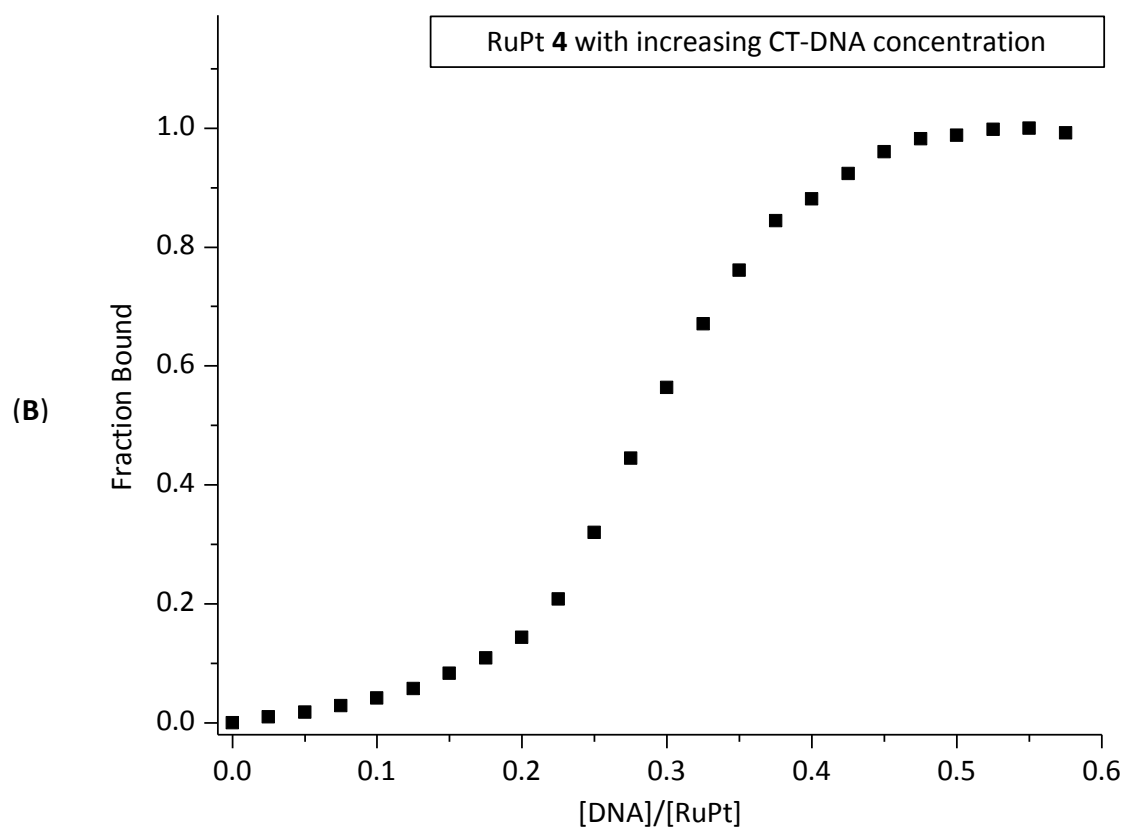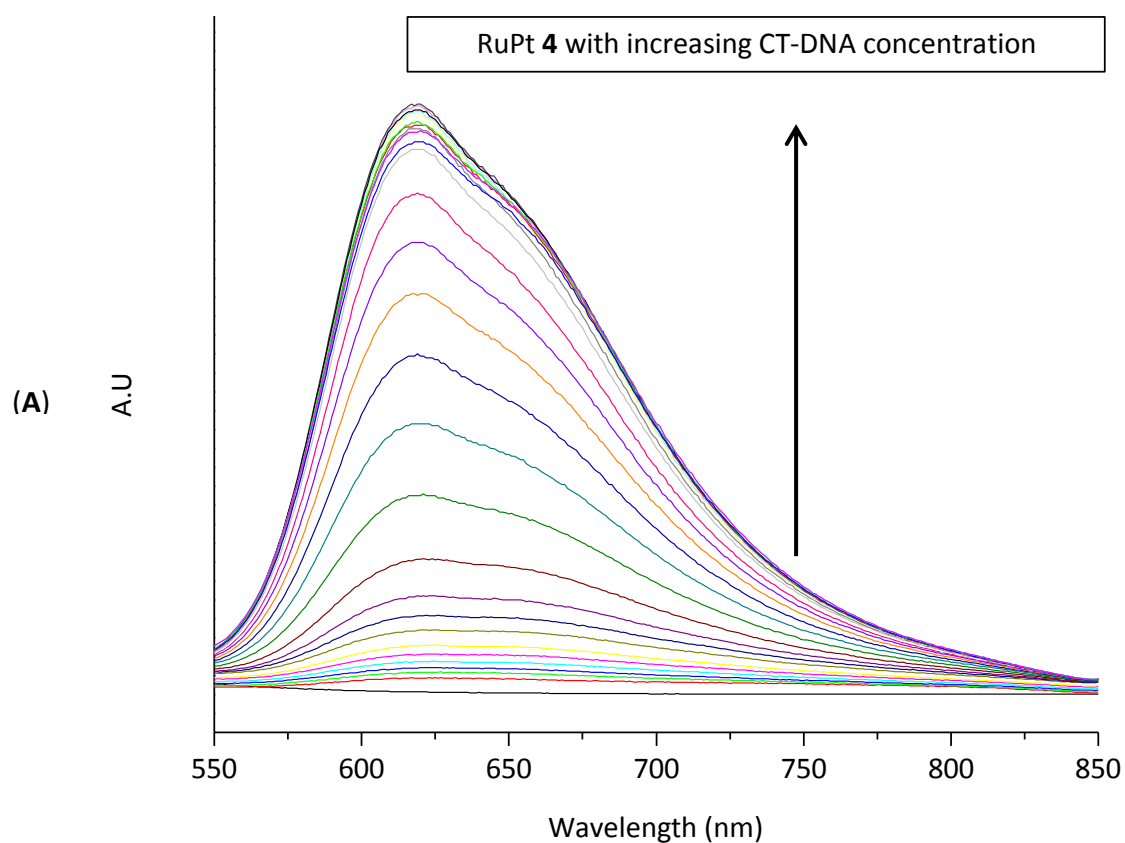
(A)

(B)
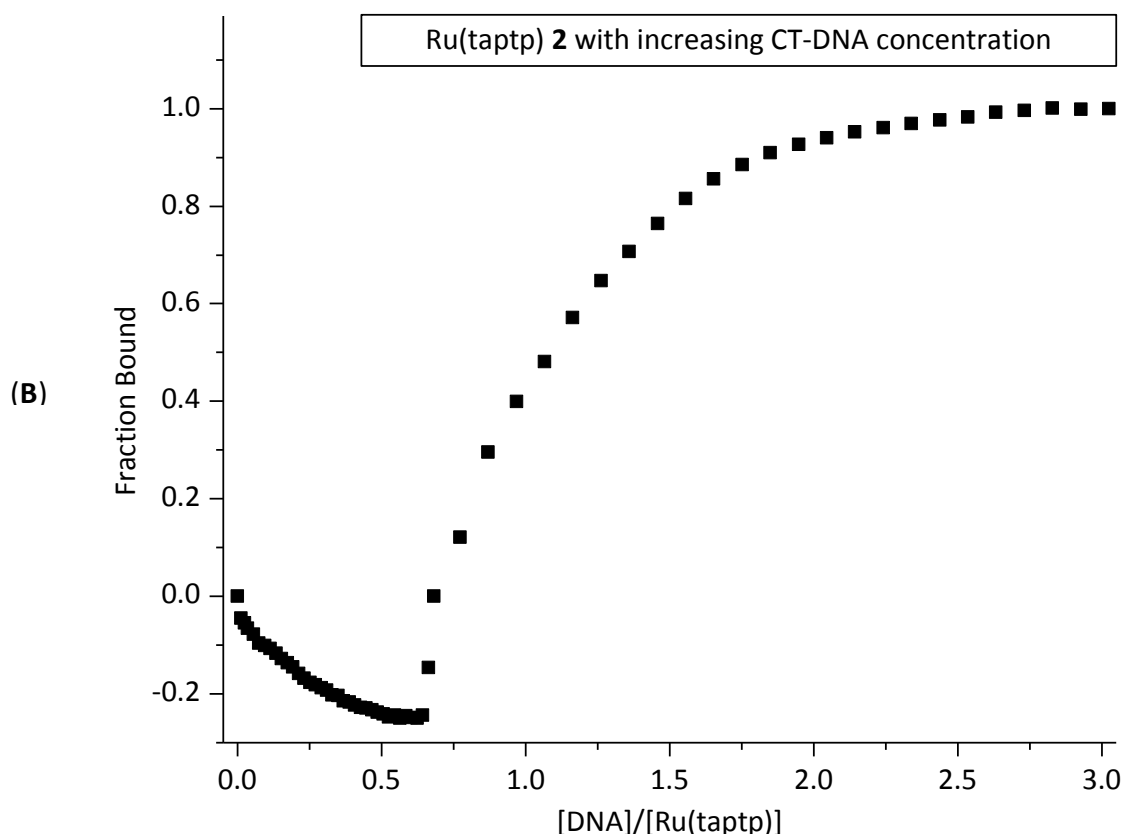
Figure 2.5 – (**A**) Luminescence titration of 10 μM [Ru(taptp)]Cl$_2$ in aqueous solution (25 mM NaCl, pH 7.4) with increasing additions of 1 mM CT-DNA (**B**) corresponding binding curve

Figure 2.6 – (**A**) Luminescence titration of 10 µM [RuRe]Cl$_2$ in aqueous solution (25 mM NaCl, pH 7.4) with increasing additions of 1 mM CT-DNA (**B**) corresponding binding curve

Figure 2.7 – (**A**) Luminescence titration of 10 μM [RuPt]Cl$_2$ in aqueous solution (25 mM NaCl, pH 7.4) with increasing additions of 1 mM CT-DNA (**B**) corresponding binding curve

For the complex Ru(tpphz) **1**, the maximum emission wavelength (λ_{max}) is 617 nm (giving a Stokes shift of 177 nm) and this emission increases with each addition of DNA. This complex has previously been shown, through viscosity measurements, to reversibly bind to DNA through intercalation of the flat planar ligand.[1] The binding constant, K_b, and site size, n, were calculated using the McGhee Von Hippel model as 4.5×10^5 M^{-1} and 1.8 respectively.

For the complex Ru(taptp) **2**, the luminescence titration still demonstrated an overall DNA light switch effect, with the λ_{max} being 608 and 604 nm before and after saturated binding, and therefore a Stokes shift of 164 nm upon DNA binding. This is a slightly shorter wavelength emission and Stokes shift compared to complex Ru(tpphz) **1**, and it also possesses an interesting binding profile. In DNA-free aqueous buffer, emission from the complex is still quite apparent, and upon small additions of DNA, the emission initially decreases before further DNA addition induces the expected enhanced emission of the light switch effect. The reason for the distinctive profile is hypothesised as follows: firstly in the aqueous buffer solution the excited state may not be as effectively quenched non-radiatively by hydrogen bonding as there are only the central two nitrogen atoms on the ligand (where tpphz has two terminal nitrogen atoms the taptp ligand has aryl C-H units in that position). The two contrasting effects in the emission appears to be due to biphasic binding where – upon addition of small amounts of DNA – the first binding mode allows direct redox quenching of the excited state through the DNA base pairs. Above a critical concentration of DNA, a second binding mode occurs in which redox quenching is reduced or absent. The two binding phases could be an initial intercalation phase followed by groove binding, or vice versa. Whilst the taptp ligand is very similar to tpphz, further experimentation would be required to verify which singular or multiple binding mode was occurring. The binding constant, for the main light switch phase, has been calculated as 2.1×10^8 M^{-1}, which is relatively strong and much closer to the that of the groove binders RuRe **3** and RuRu-bipy (a dinuclear groove binder included for comparative purposes, see *Experimental 6.2.17*) than the intercalator Ru(tpphz) **1**; and following on from the above hypothesis groove binding could be the second phase, after intercalation at low DNA concentrations.

Complex RuRe **3** also demonstrated the DNA light switch effect. In this case there was a larger Stokes shift of 220 nm with the λ_{max} at a longer wavelength of 660 nm. Through

viscosity measurements it was revealed that RuRe **3** is a groove binder as it showed similar properties to the positive groove binding control, Hoechst 33342 (See *Appendix 7.2*). This is in agreement with the hypothesis that the steric bulk of the $Re(CO)_5Cl$ unit would prevent intercalation between the base pairs. Interestingly, the binding constant, K_b, for this complex was calculated to be 1.6×10^7 M^{-1} which is two orders of magnitude greater than the mononuclear Ru(tpphz) **1**. The dinuclear groove binder RuRu-bipy gave a K_b value of 4.5×10^7 M^{-1} which is of the same order of magnitude as RuRe **3** (1.6×10^7 M^{-1}) and indicates the interaction with the groove is stronger than intercalation via the tpphz ligand.

Finally, the complex RuPt **4** also demonstrated the DNA light switch effect and had a λ_{max} of 619 nm (Stokes shift of 179 nm) which was slightly higher than Ru (tpphz) **1** but not significantly so. In contrast, to the other complexes, RuPt **4** displays a relatively prominent low energy shoulder. Interestingly, the binding curve differs as it is sigmoidal rather than a linear gradient, before still plateauing off at the point of saturation. The binding constant has been calculated as 8.0×10^7 M^{-1}, which is very similar to the groove binding of RuRe **3** and RuRu although the mode of binding could in theory be one of three options – groove binding, intercalation or irreversible binding through the chloride ligand(s) of platinum.

Complex	λ_{max} (nm) (aqueous)	λ_{max} (nm) with CT-DNA	Binding constant, K_b (10^6 M^{-1})	Site size, n (base pairs)
Ru(tpphz) **1**	621	617	0.45 ± 0.1	1.8 ± 0.029
Ru(taptp) **2**	608	604	7.2 ± 1.1	1.69 ± 0.025
RuRe **3**	621	660	1.6 ± 0.2	0.77 ± 0.033
RuPt **4**	618	619	80 ± 5.5	0.75 ± 0.004
RuRu-bipy	621	670	45 ± 3.9	2.20 ± 0.105

Figure 2.8 – Table of emission λ_{max} values, and from a MVH fit of binding data, K_b and n

In summary, all four complexes associate to DNA in cell free conditions. However binding to genomic CT-DNA in saline buffer at approximately 22°C is different to physiological cellular conditions, so it cannot be an assumed DNA is the intracellular target.

2.4 References

1. Gill, M. R., Derrat, H., Smythe, C. G. W., Battaglia, G. & Thomas, J. a. Ruthenium(II) metallo-intercalators: DNA imaging and cytotoxicity. *Chembiochem* **12,** 877–80 (2011).

2. Bolger, J., Gourdon, A., Ishow, E. & Launay, J. Mononuclear and Binuclear Tetrapyrido phenazine (tpphz) Ruthenium and Osmium Complexes. *Inorg. Chem.* **1669,** 2937–2944 (1996).

3. Zheng, R. H. *et al.* A new and convenient synthesis of phendiones oxidated by $KBrO_3/H_2SO_4$ at room temperature. *Chinese Chem. Lett.* **21,** 1270–1272 (2010).

4. Bodige, S. & MacDonnell, F. M. Synthesis of Free and Ruthenium Coordinated 5,6-Diamino-1,10-phenanthroline. *Tetrahedron Lett.* **38,** 8159–8160 (1997).

5. Zhen, Q. X. *et al.* Synthesis, characterization and the effect of ligand planarity of $[Ru(bpy)_2L]^{2+}$ on DNA binding affinity. *J. Inorg. Biochem.* **76,** 47–53 (1999).

6. Friedman, A., Chambron, J., Sauvage, J., Turro, N. & Barton, J. A molecular light switch for DNA: $[Ru(bpy)_2(dppz)]^{2+}$. *J. Am. Chem. Soc.* **112,** 4960–4962 (1990).

7. Gill, M. R. & Thomas, J. A. Ruthenium(II) polypyridyl complexes and DNA--from structural probes to cellular imaging and therapeutics. *Chem. Soc. Rev.* **41,** 3179–92 (2012).

8. Coogan, M. P. & Fernández-Moreira, V. Progress with, and prospects for, metal complexes in cell imaging. *Chem. Commun.* **50,** 384–99 (2014).

9. Scatchard, G. the Attractions of Proteins for Small Molecules and Ions. *Ann. N. Y. Acad. Sci.* **51,** 660–672 (1949).

Chapter 3

Cytotoxicity

3.1   Background

Following the synthesis of complexes **1 – 4**, and cell-free DNA binding studies that confirmed the complexes displayed DNA light switch effects, attention was turned to cellular studies.

Whilst platinum-based drugs are still widely used in the clinic as successful anti-cancer treatments, one major drawback is intrinsic or acquired resistance.[1] New metallodrugs could result in improved first- or second-line treatment options if they are able to overcome common cisplatin resistance mechanisms. Ruthenium complexes are attracting increasing attention as metallodrug leads, with several reaching clinical trials such as imidazolium *trans*-imidazoledimethylsulfoxidetetrachlororuthenate (NAMI-A)[2,3] and *trans*-[tetrachlorobis(1*H*-indazole)ruthenate(III)] (KP1019)[4] (*Figure 3.1*).
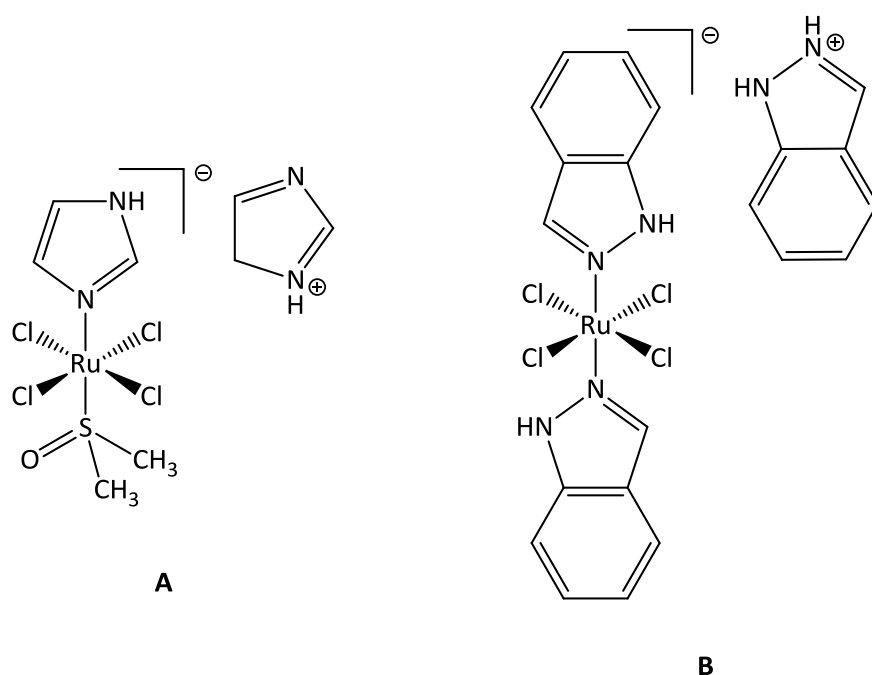
Figure 3.1 – Structures of NAMI-A (**A**) and KP1019 (**B**)

In this study, the cell lines investigated were A2780 and A2780cis, which are two variants of a human ovarian carcinoma line. A2780 is sensitive to cisplatin treatment, whereas A2780cis shows an approximately 10-fold increase in therapeutic resistance. The A2780cis cell line was originally generated by subjecting A2780 to chronic cisplatin exposure of increasing

concentrations (with the resistance maintained in subculture by periodic low level exposure - details of cell culture protocol found in *Experimental Section 6.4.1*). This protocol generates cells with several reported resistance mechanisms to cisplatin, including the loss of proficiency of the mismatch repair (MMR) pathway due to methylation and silencing of the *hMLH1* gene, resulting in an increased ability to repair DNA damage.[5,6] Other mechanisms implicated are the accumulation of the inactive mutant form of the p53 tumour suppressor gene,[7] and/or raised cellular content of glutathione (GSH) and an associated increase in Multi Drug Resistant Protein 2 (MRP2) expression.[8] Further changes in DNA damage recognition, cellular signalling and DNA damage repair in this cell line have also been reported and could be associated with resistance mechanisms.[9]

The cytotoxic response induced in cells by complexes **1** - **4** was first investigated by the widely used MTT assay - a colorimetric assessment of cellular metabolic activity. This technique utilises 3-(4,5-dimethylthiazol-2-yl)-2,5-diphenyletrazolium bromide (MTT), which is yellow in colour but is converted by active enzymes to an insoluble, purple formazan product (*Figure 3.2*) (Protocol found in *Experimental Section 6.4.2*).

$$\text{MTT} \xrightarrow{\text{mitochondrial reductase enzymes}} \text{Formazan}$$
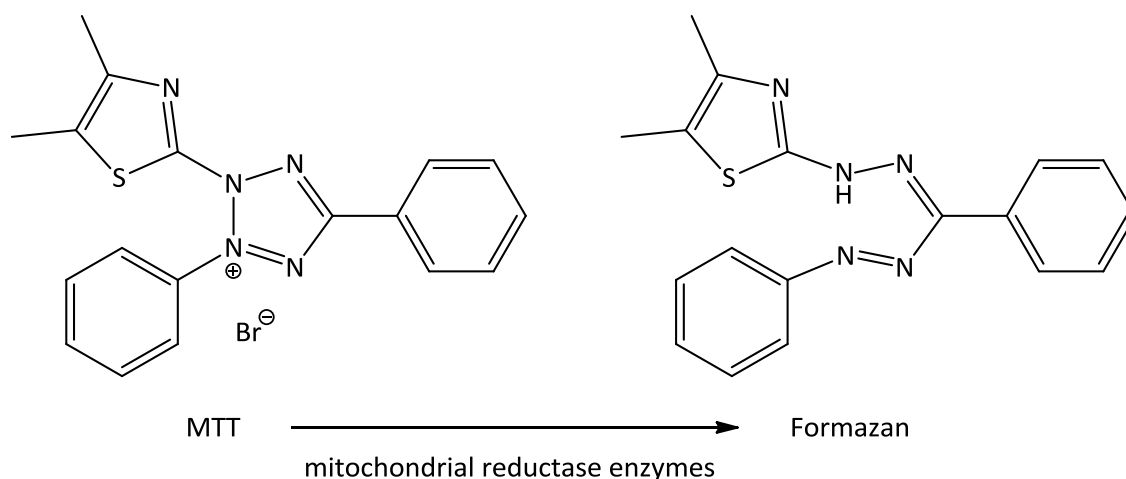
Figure 3.2 – Conversion of MTT to formazan product

3.2   IC$_{50}$ Determination

A commonly used reference for cytotoxicity is the half maximal inhibitory concentration, the IC$_{50}$ value, which is the concentration of a complex required to inhibit cellular processes in half of the treated population (protocol found in *Experimental Section 6.4.3*). Biological testing to determine the IC$_{50}$ value was carried out on complexes **1** - **4** (*Figure 3.3*).
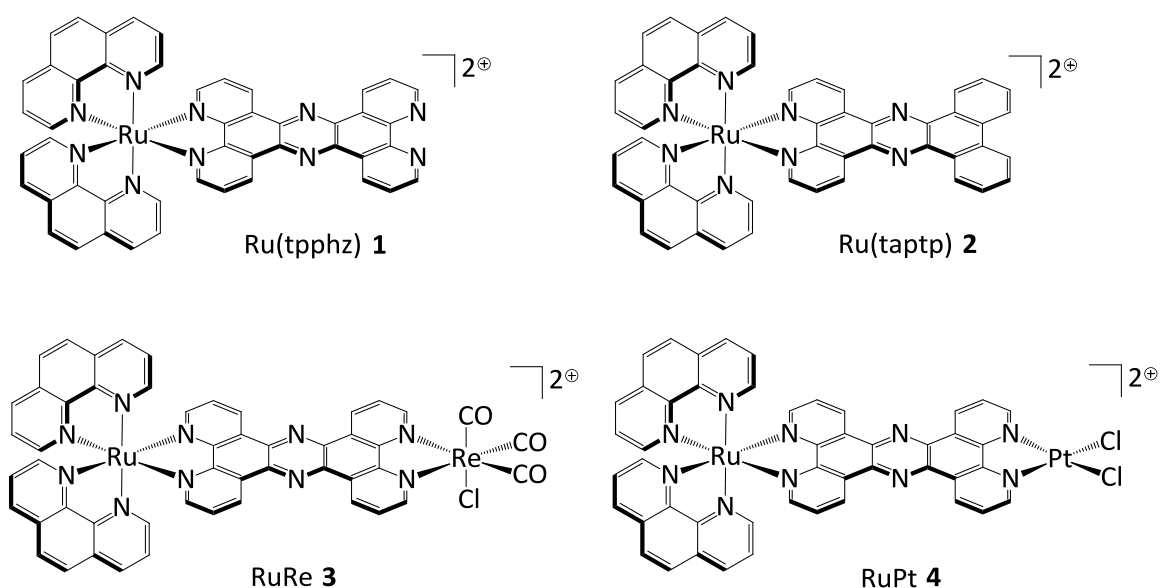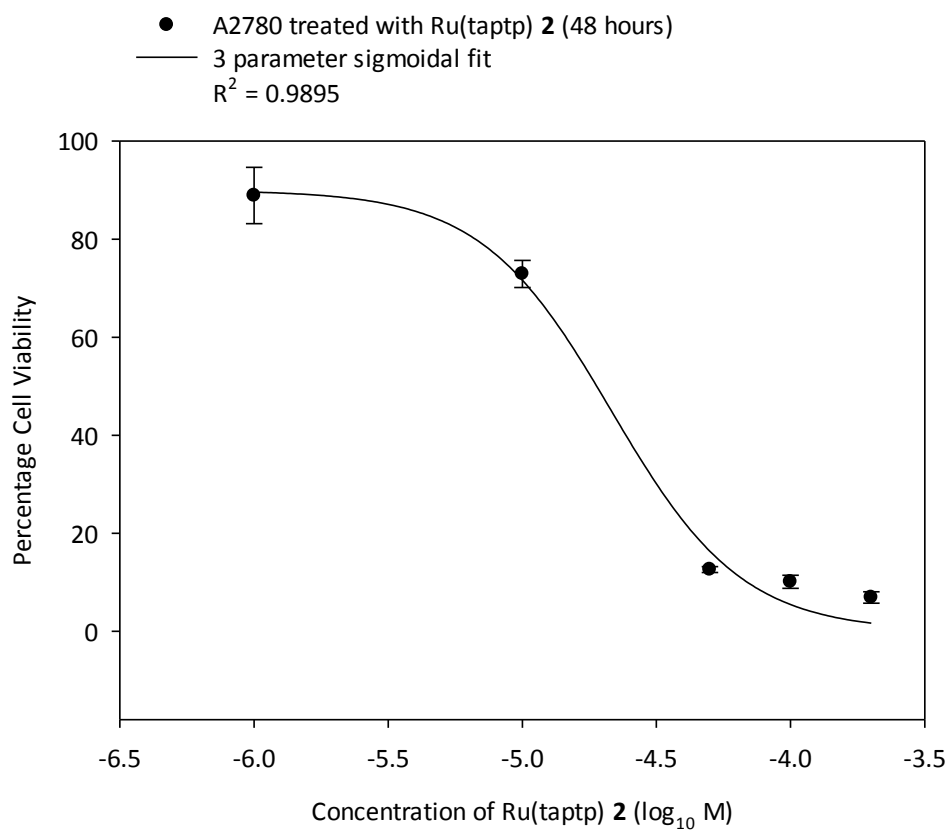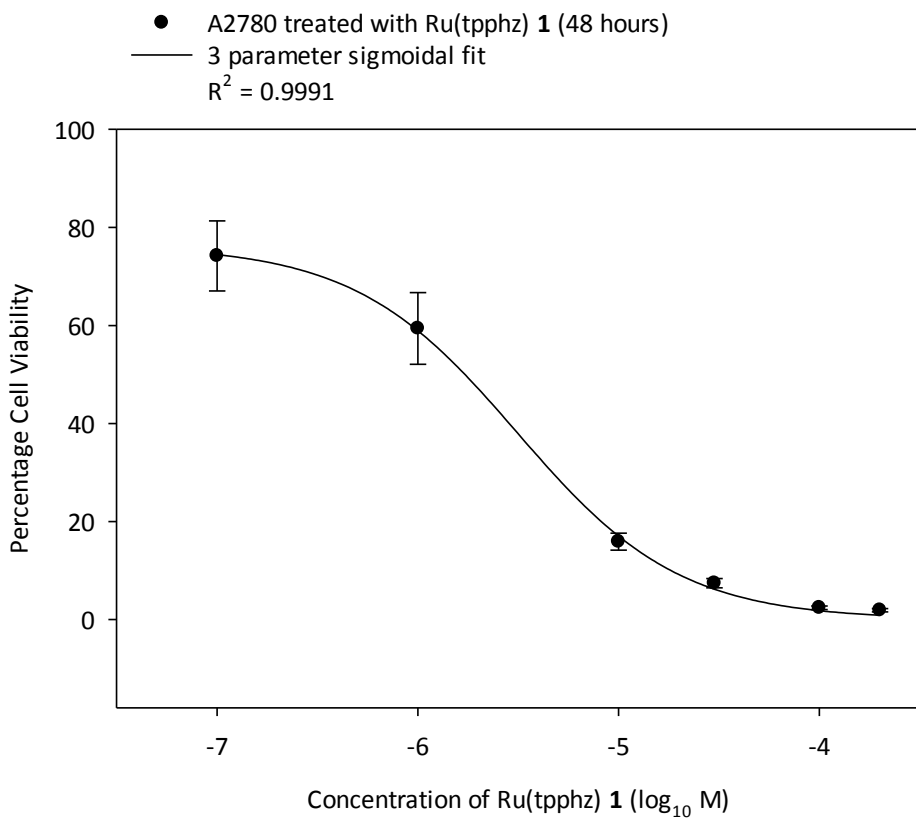

Figure 3.3 – Complexes **1** − **4**

To ensure experimental techniques were in line with literature methods cisplatin was employed as a positive control with the chosen A2780 and A2780cis cell lines, with the results from following these procedures shown below (*Figure 3.4*). The IC$_{50}$ value for cisplatin against A2780 was calculated, via interpolation of the curve, as 2 μM, and for A2780cis as 18 μM, which is in line with the 10 fold resistance literature value between the two cell lines.[10]
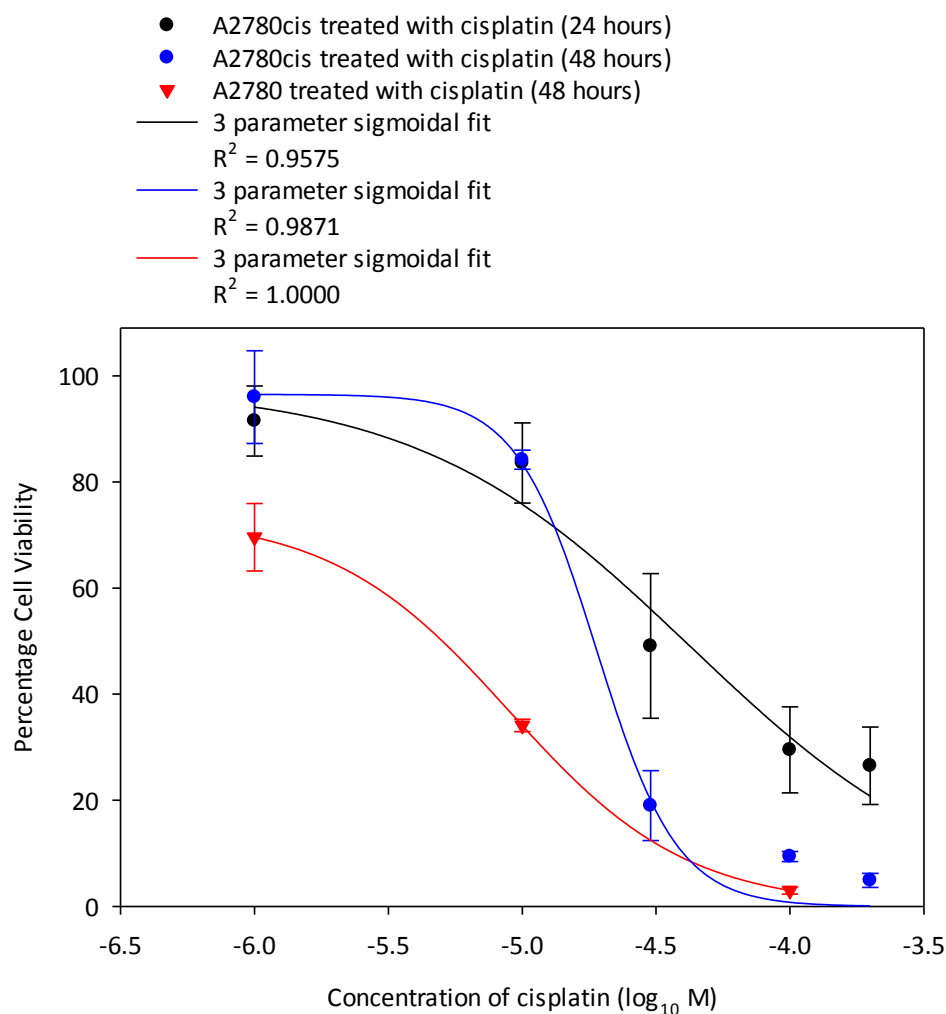
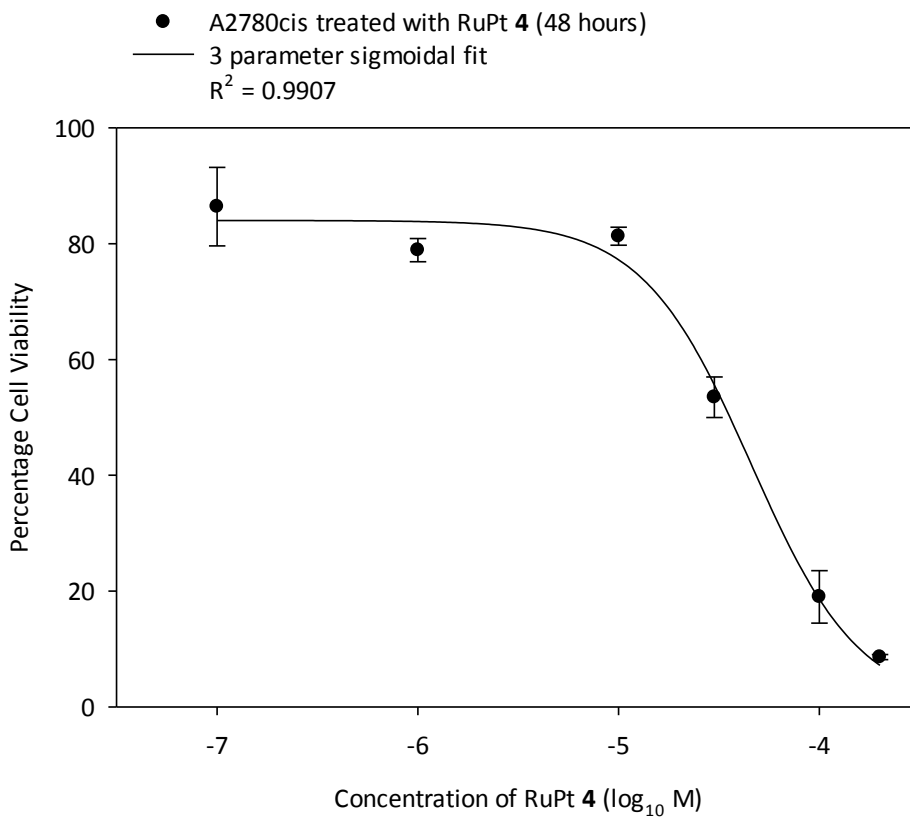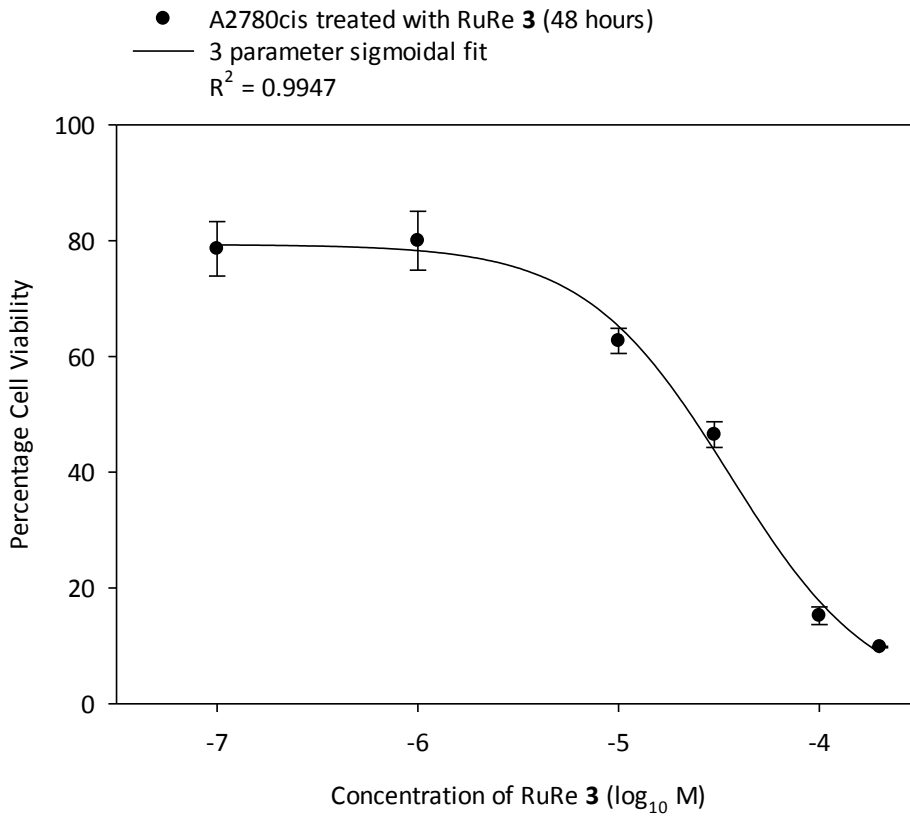| Cell line	Exposure time (hours)	IC$_{50}$ (μM)
A2780cis	24	30
A2780cis	48	18
A2780	48	2

Figure 3.4 – A2780 and A2780cis cell viability data for cisplatin

With this protocol experimentally verified, the cell lines A2780 and A2780cis were subjected to treatment by complexes **1 – 4**. An example of a viability curve, measuring cell viability versus increasing concentration of each complex for each cell line, can be seen below. This IC$_{50}$ data is summarised in *Figure 3.5*.

A2780 treated with Ru(tpphz) **1** (48 hours)
3 parameter sigmoidal fit
$R^2 = 0.9991$

Percentage Cell Viability

Concentration of Ru(tpphz) **1** ($\log_{10}$ M)

A2780 treated with Ru(taptp) **2** (48 hours)
3 parameter sigmoidal fit
$R^2 = 0.9895$

Percentage Cell Viability

Concentration of Ru(taptp) **2** ($\log_{10}$ M)

A2780cis treated with Ru(tpphz) **1** (48 hours)

3 parameter sigmoidal fit

$R^2 = 0.9839$

Percentage Cell Viability

Concentration of Ru(tpphz) **1** ($\log_{10}$ M)

A2780cis treated with Ru(taptp) **2** (48 hours)

3 parameter sigmoidal fit

$R^2 = 0.9969$

Percantage Cell Viability

Concentration of Ru(taptp) **2** ($\log_{10}$ M)

A2780cis treated with RuRe **3** (48 hours)
3 parameter sigmoidal fit
$R^2 = 0.9947$

Concentration of RuRe **3** ($\log_{10}$ M)

A2780cis treated with RuPt **4** (48 hours)
3 parameter sigmoidal fit
$R^2 = 0.9907$

Concentration of RuPt **4** ($\log_{10}$ M)

By obtaining IC$_{50}$ values for each permutation of complex and cell line, the relative toxicity of each complex to the two cell lines can be compared (*Figure 3.5*). Such an analysis reveals the presence or absence of any cross-resistance – in which tolerance to a usually toxic substance occurs through exposure to a similarly acting substance.[11] From each independent experiment an IC$_{50}$ was obtained, by interpolation of the generated curve, and these were averaged for the mean value shown in *Figure 3.5*. The error could then be calculated as the standard deviation of these independent repeats (except for A2780 and Ru(taptp) **2** where only one experiment was ran).

Cell Line	Complex IC$_{50}$ (μM mean value ± 1 standard deviation of independent values)				
	cisplatin	Ru(tpphz) **1**	Ru(taptp) **2**	RuRe **3**	RuPt **4**
A2780	2 ± 1 ***	2 ± 1 **	18 *	9 ± 4 **	44 ± 5 **
A2780cis	22 ± 4 ***	4 ± 2 ***	13 ± 5 ***	27 ± 10 ***	36 ± 3 **

Figure 3.5 – Table of IC$_{50}$ values (asterisks indicate independent repeats e.g. ** for n=2)

As can be seen from the estimated IC$_{50}$ values for the new complexes, there is a range in activities and cross-resistance profiles to cisplatin. The resistance factor for cisplatin between A2780 and A2780cis recorded in these experiments (approximately 10 fold from 2 to 22 μM) is in agreement with the literature values. Interestingly, none of the new Ru^{II} complexes demonstrate such high cross resistance factors.

The most toxic complex, with the same potency to cisplatin against A2780cis, was mononuclear ruthenium Ru(tpphz) **1**. In line with the previous reports from the group, this compound was not only highly cytotoxic against A2780 (IC$_{50}$ 2.1 μM) but also showed appreciable lack of cross-resistance by maintaining a similar level of cytotoxicity against A2780cis (IC$_{50}$ 4.4 μM).

The other mononuclear ruthenium complex Ru(taptp) **2** is not as potent as Ru(tpphz) **1** but still shows significant cytotoxicity against A2780 (IC$_{50}$ 18.0 μM) with no cross-resistance to A2780cis (IC$_{50}$ 13.2 μM).

In contrast to the two mononuclear complexes, the ruthenium-rhenium complex RuRe **3** displays a relatively high toxicity against A2780 (IC_{50} 8.6 µM) but cross-resistance against A2780cis cells (IC_{50} 27.3 µM) is observed - albeit to a lower degree than cisplatin (approximately 3 fold versus 10 fold).

The other heterometallic ruthenium-platinum complex RuPt **4** was notably less cytotoxic against A2780 (IC_{50} 44.3 µM) yet, like Ru(taptp) **2**, showed an *increase* in toxicity against A2780cis (IC_{50} 36.0 µM).

These results show that the mononuclear species have good intrinsic cytotoxicity and lack cross-resistance with cisplatin. This observation could be as a result of two mechanisms – either the potency is an effect of uptake efficiency in both cell lines with the same intracellular mechanism for all complexes, or there are differing intracellular mechanisms between the complexes that provoke cell death, i.e. a varying response in DNA damage repair. A third possibility involves a combination of both factors.

To investigate the intracellular characteristics of cell death microscopy experiments were utilised.

3.3   Microscopy Studies

Microscopy studies were used to investigate the intracellular mechanism responsible for cell death, primarily whether the general mode of cell death fitted with one of the three broad categories – apoptosis, oncosis or autophagy – described in more detail in *Section 1.4*. To recap, apoptosis and oncosis are the cellular reactions prior to cell death, whereas necrosis is the term used for the degradative reactions that constitute the postmortem cellular changes to restore an equilibrium with the environment.[12] Apoptosis is indicated by cell shrinkage, cytoplasmic blebbing, nuclear fragmentation and marked chromatin condensation which all lead to cell fragmentation and formation of apoptotic bodies.[13] Generally, oncosis produces broadly opposite morphological changes, with cell swelling accompanied by clearing of the cytosol, dilation of the endoplasmic reticulum (ER) and golgi, mitochondrial condensation then swelling, nuclear chromatin clumping and formation of cytoplasmic blebs that are organelle free.[13]

First, the optimum level of seeding for microscopy experiments was established with the appropriate vessel of a 35 mm diameter glass bottomed dish. To target the observation of cell death in a short time period of 3 hours, a complex concentration of 50 μM was chosen, which is greater than all the previously determined IC_{50} values, and remained the same for all treatments to obtain a basic qualitative comparison of cellular uptake. Images were recorded at 2 minute intervals over ten different coordinates within the sample, with observations started immediately after treatment in a live cell confocal microscopy chamber at 37 °C with a flow of CO_2 present (further detail in *Experimental Section 6.5*). For each 3 hour experiment, an equally seeded control dish was included in the chamber and imaged at the end to ensure the conditions of the chamber were having no detrimental effect on the morphology of the cell population. Also, an equally seeded but untreated dish was subjected to the same 3 hour cycle of 2 minute multi-coordinate image acquisition to control for light exposure. This protocol was carried out in a succession of experiments for complexes **1 – 4** on both A2780 and A2780cis cell lines (*Figures 3.6 – 3.14*).

The general observation with all of the complex treatments is that the cell death occurs via possible oncosis, as indicated by cell swelling being the typical cellular response.
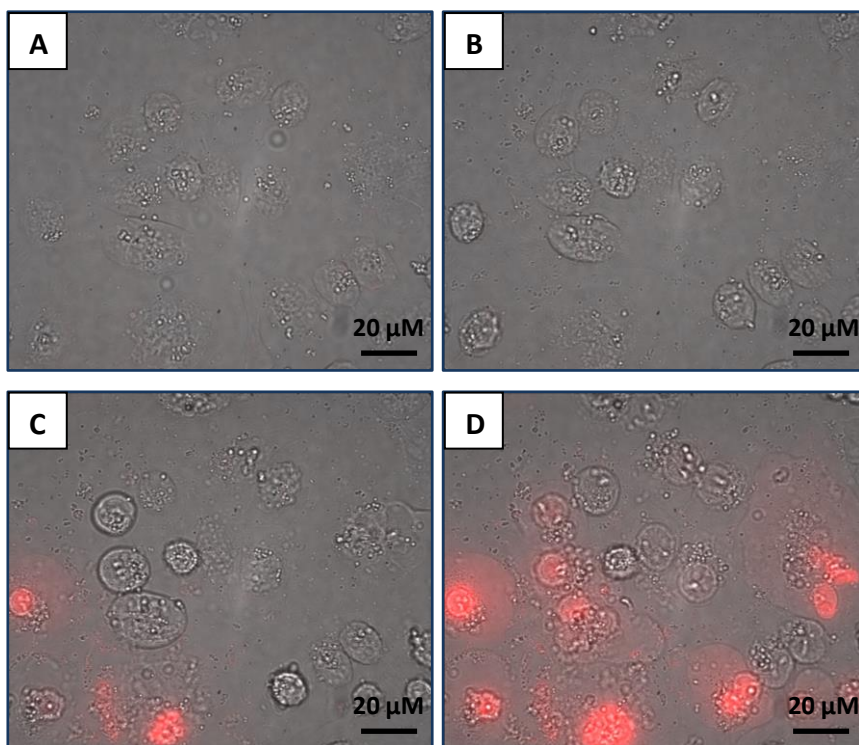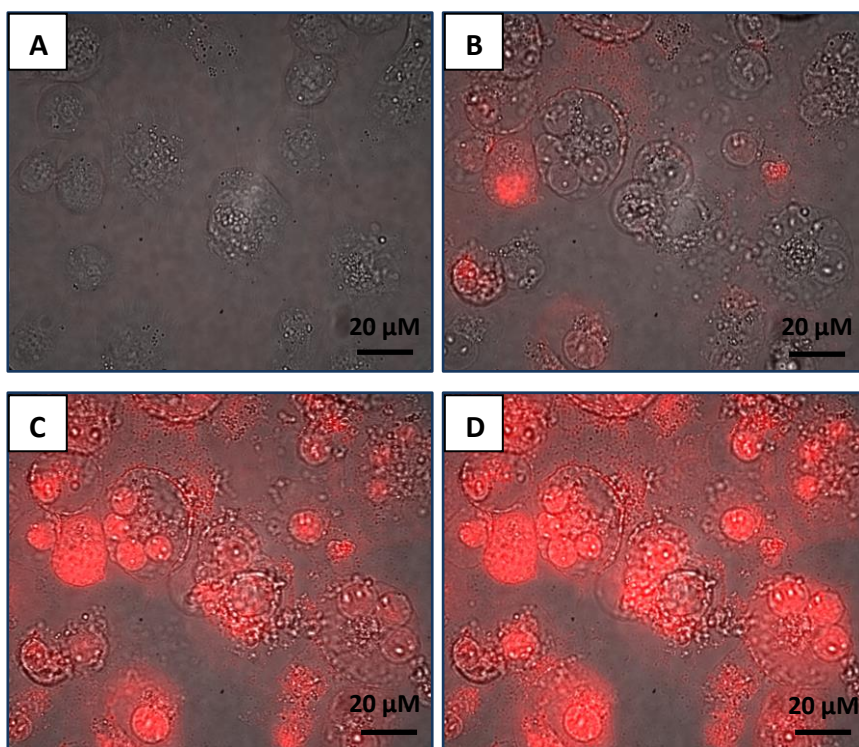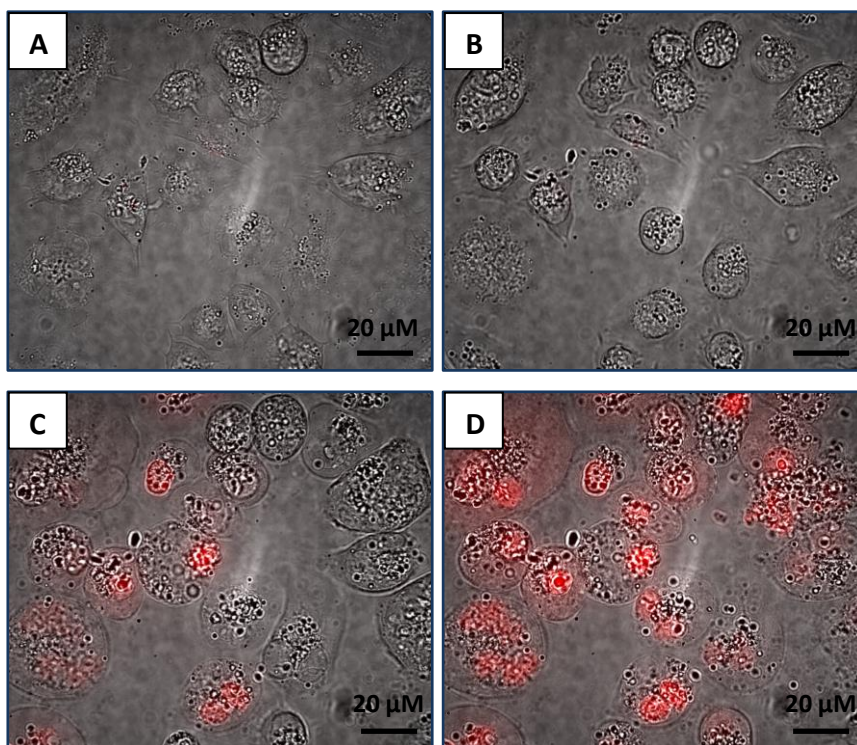
Figure 3.6 – A2780 cells treated with 50 µM Ru(tpphz) **1** in a live cell microscopy experiment as an overlay of phase contrast and epifluorescence (470 nm excitation and >520 nm emission collected) at time points of (**A**) 0 hours (**B**) 1 hours (**C**) 2 hours (**D**) 3 hours
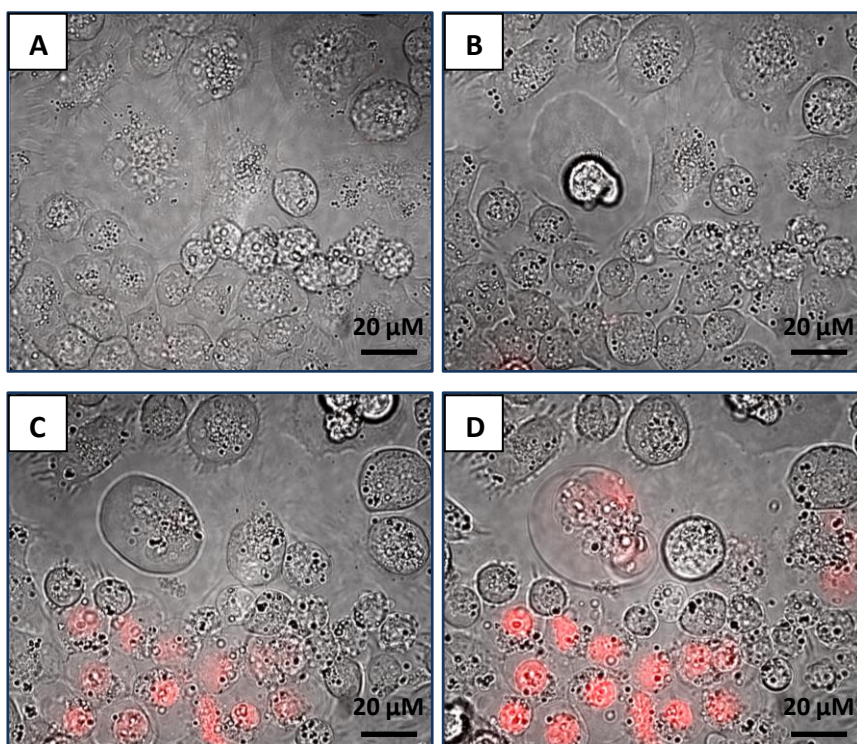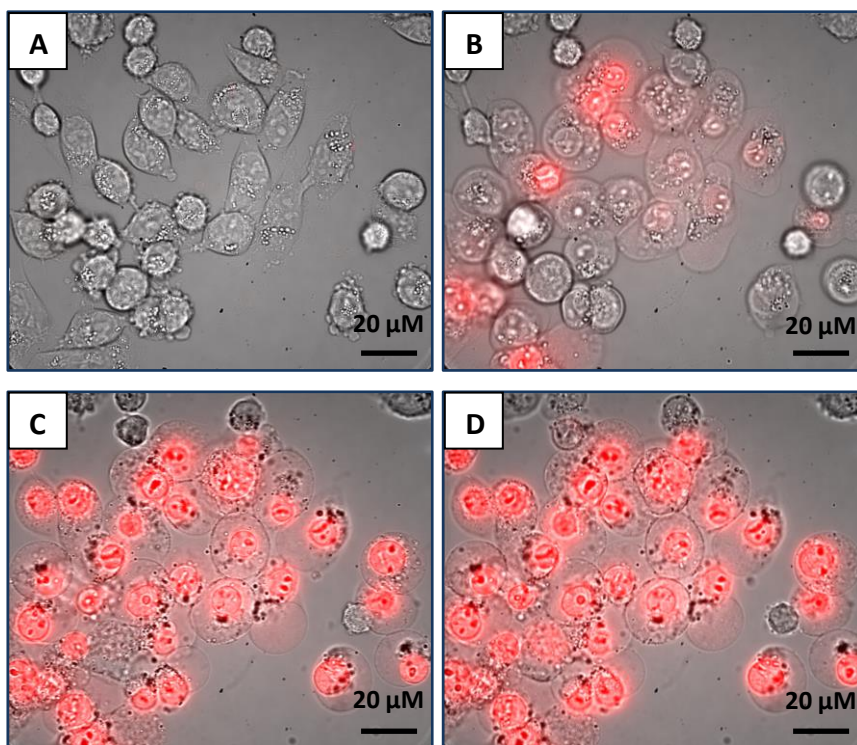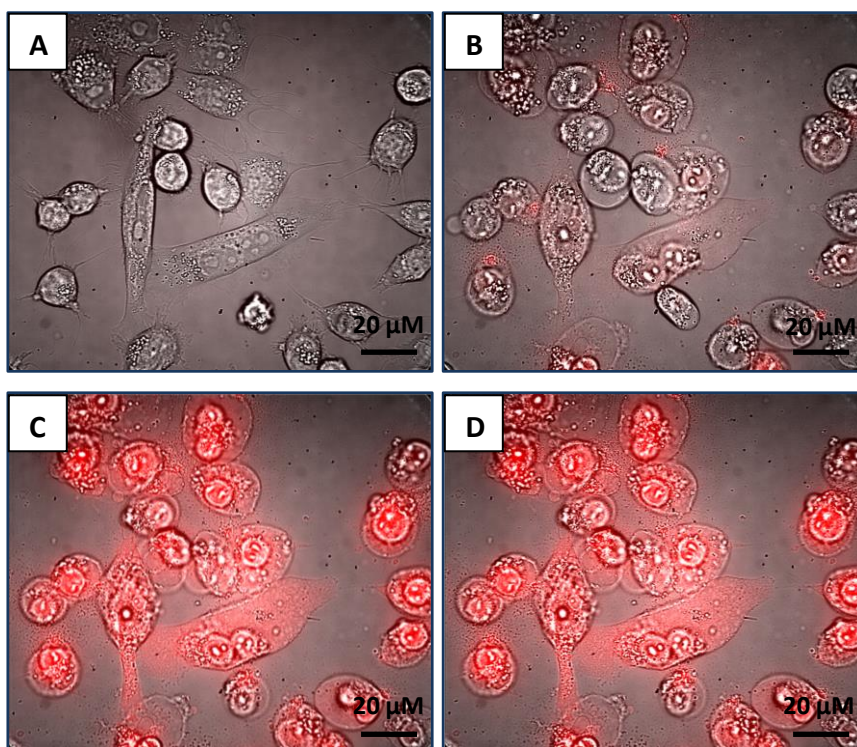

Figure 3.7 – A2780 cells treated with 50 µM Ru(taptp) **2** in a live cell microscopy experiment as an overlay of phase contrast and epifluorescence (470 nm excitation and >520 nm emission collected) at time points of (**A**) 0 hours (**B**) 1 hours (**C**) 2 hours (**D**) 3 hours
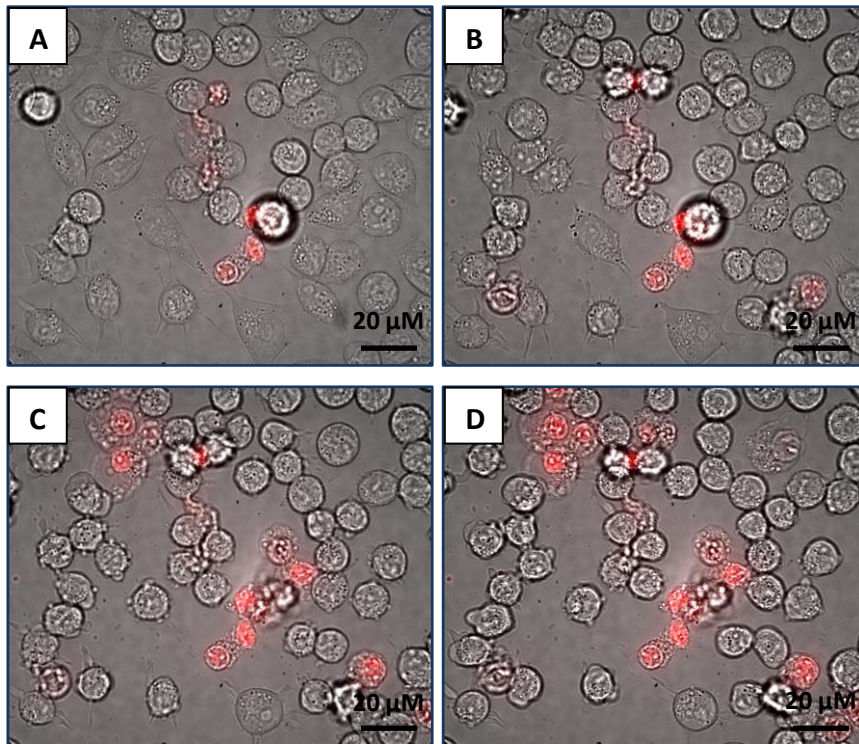
Figure 3.8 – A2780 cells treated with 50 µM RuRe **3** in a live cell microscopy experiment as an overlay of phase contrast and epifluorescence (470 nm excitation and >520 nm emission collected) at time points of (**A**) 0 hours (**B**) 1 hours (**C**) 2 hours (**D**) 3 hours
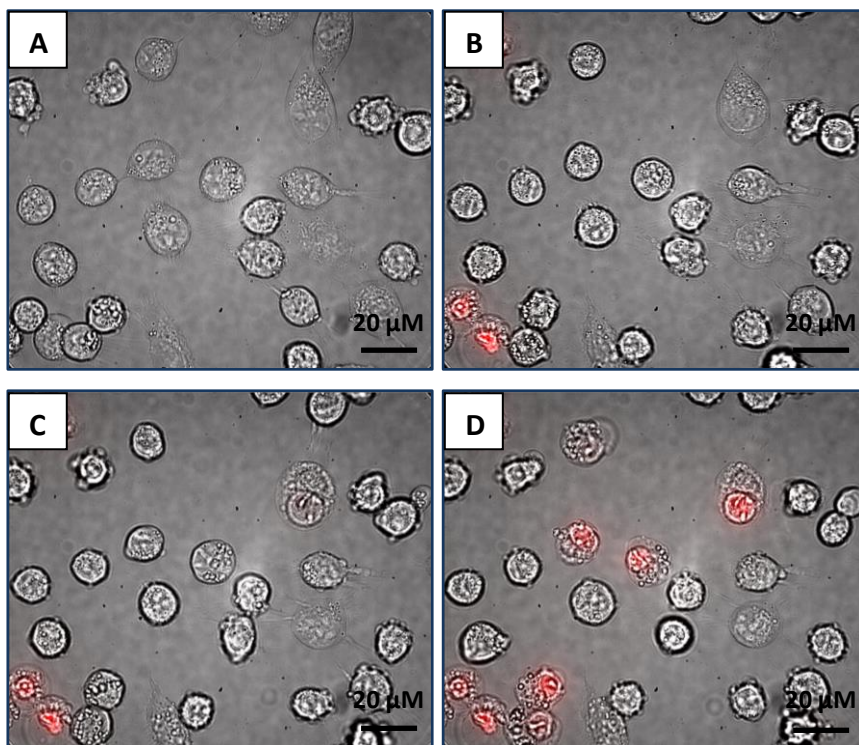

Figure 3.9 – A2780 cells treated with 50 µM RuPt **4** in a live cell microscopy experiment as an overlay of phase contrast and epifluorescence (470 nm excitation and >520 nm emission collected) at time points of (**A**) 0 hours (**B**) 1 hours (**C**) 2 hours (**D**) 3 hours

Figure 3.10 – A2780cis cells treated with 50 µM Ru(tpphz) **1** in a live cell microscopy experiment as an overlay of phase contrast and epifluorescence (470 nm excitation and >520 nm emission collected) at time points of (**A**) 0 hours (**B**) 1 hours (**C**) 2 hours (**D**) 3 hours
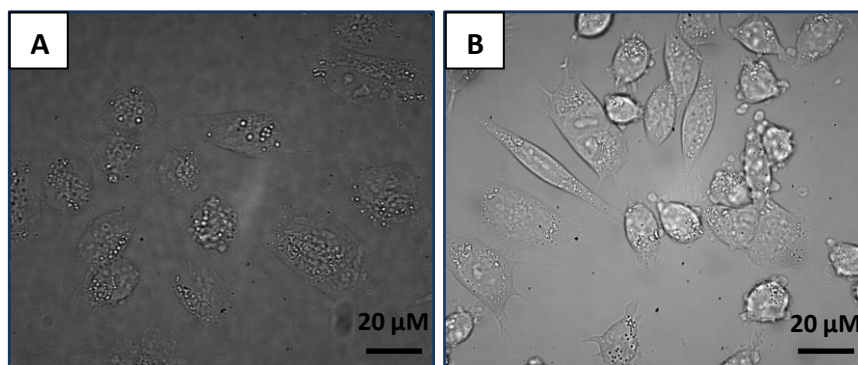

Figure 3.11 – A2780cis cells treated with 50 µM Ru(taptp) **2** in a live cell microscopy experiment as an overlay of phase contrast and epifluorescence (470 nm excitation and >520 nm emission collected) at time points of (**A**) 0 hours (**B**) 1 hours (**C**) 2 hours (**D**) 3 hours

Figure 3.12 – A2780cis cells treated with 50 µM RuRe **3** in a live cell microscopy experiment as an overlay of phase contrast and epifluorescence (470 nm excitation and >520 nm emission collected) at time points of (**A**) 0 hours (**B**) 1 hours (**C**) 2 hours (**D**) 3 hours

Figure 3.13 – A2780cis cells treated with 50 µM RuPt **4** in a live cell microscopy experiment as an overlay of phase contrast and epifluorescence (470 nm excitation and >520 nm emission collected) at time points of (**A**) 0 hours (**B**) 1 hours (**C**) 2 hours (**D**) 3 hours

Figure 3.14 – control dishes of untreated cells as an overlay of phase contrast and epifluorescence (470 nm excitation and >520 nm emission collected) following the same seeding and 3 hour experimental exposure as treated dishes for (**A**) A2780 (**B**) A2780cis

To interpret the data further, some quantification was carried out on. Firstly, a fluorescence intensity profile was obtained for each experiment, which can be seen plotted together on the same graph (*Figure 3.15*). The data generated from this analysis must be treated with care though – it is difficult to directly compare each curve because they are independent experiments so there are three areas of variance of particular note. One possible variable factor is present due to the intensity of light measured being proportional to that delivered to the subject, so discrepancies in laser performance will affect the output. Also, each complex will have different photophysical properties, particularly the quantum yield. Finally, between samples there are fluctuations in the net number of cells present regardless of treatment. Nonetheless, bearing this caution in mind, it can be seen that the samples treated with Ru(taptp) **2** complex are considerably more intense than the other complexes in both cell lines – this supports the observation of staining of the mass majority of cells in these samples, providing a high net fluorescence output. For A2780 treated with Ru(tpphz) **1** there is also a high fluorescence output, although less than that for Ru(taptp) **2** which could be postulated as a difference in the selectivity of staining – Ru(taptp) **2** appears to have more indiscriminate whole cell staining whereas Ru(tpphz) **1** is *more* confined to the nuclear regions. Interestingly, the fluorescence from samples of A2780cis treated with Ru(tpphz) **1** is much lower than from the A2780 samples, but postulation on this would require more experimentation. For the remaining cases of A2780 and A2780cis treated with RuRe **3** and RuPt **4** the fluorescence output is lower than the mononuclear complex treatment, which is in agreement with the observation of much less cell death and staining; and correlates with their lower cytotoxic activity.
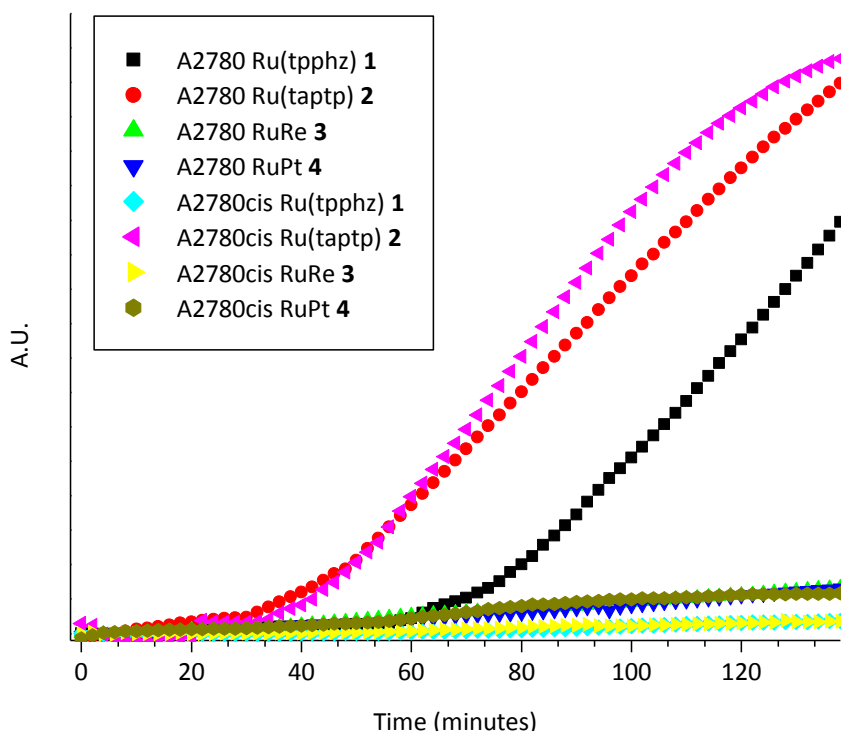
Figure 3.15 – fluorescence intensity profiles of each cell line and complex permutation

By looking at each of the fluorescence profiles in turn, interesting observations can be made with regard to the timing of when the fluorescence markedly increases as an indicator of cellular accumulation and death (*Figure 3.16*). From the fluorescence profile of A2780 cells treated with Ru(tpphz) **1** it can be seen to have a noticeable increase in intensity from approximately 60 minutes onwards, which is indicative of the cellular accumulation and death observed qualitatively. In slight contrast, the fluorescence for A2780 cells treated with Ru(taptp) **2** shows a similar sharp increase in intensity from approximately 40 minutes onwards. If the complex is entering the cell by passive diffusion then this subtle difference could be assigned as a result of the increased lipophilicity of the Ru(taptp) **2** complex due to loss of 2 hydrogen bonding donor sites; where the taptp ligand features aryl C-H units in place of the terminal nitrogen terminal nitrogen atoms on Ru(tpphz) **1**. For the samples treated with RuRe **3** and RuPt **4** there is a much lower magnitude of fluorescence intensity seen and this is represented in the qualitative observation of low cytotoxic activity and cellular staining compared to the mononuclear complexes. This fluorescence data could be indicative of the relationship between the cellular accumulation of the complexes – Ru(taptp) **2** has the fastest comparative uptake, closely followed by Ru(tpphz) **1**, whereas RuRe **3** and RuPt **4** are much slower to accumulate in cells; in this specific experimental

setup. To fully assess the cellular accumulation there will be a future study to investigate the intra-cellular metal content by inductively coupled plasma mass spectrometry (ICP-MS).
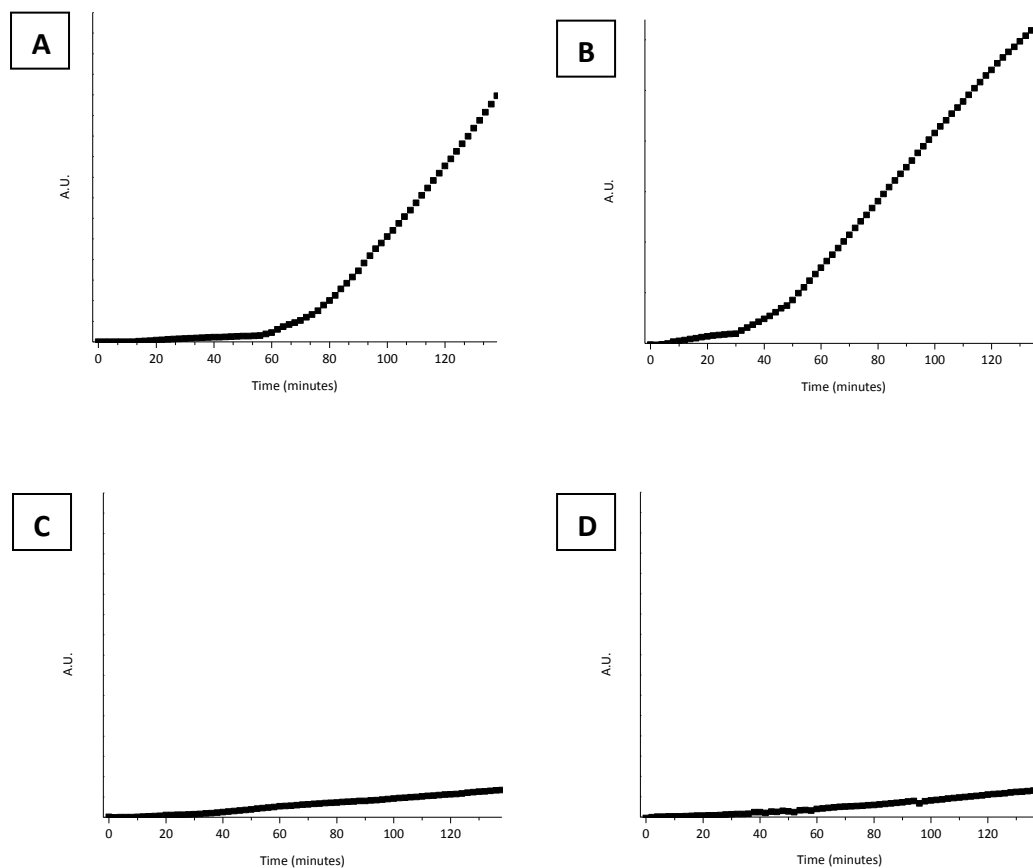

Figure 3.16 – Fluorescence profiles over time (obtained as an average of 5 sample areas) for A2780 cells treated with 50 µM (**A**) Ru(tpphz) **1** (**B**) Ru(taptp) **2** (**C**) RuRe **3** (**D**) RuPt **4**

For the mode of cell death, a similar pattern of observations can be seen in each treatment leading to the characteristics most similar to an oncosis – clearly distinguished swelling before compromised membranes result in the some of the intracellular matter leaking out. The fluorescent staining of the cells is often only seen a significant way down the cell death pathway as seen in the example below (*Figure 3.17*).
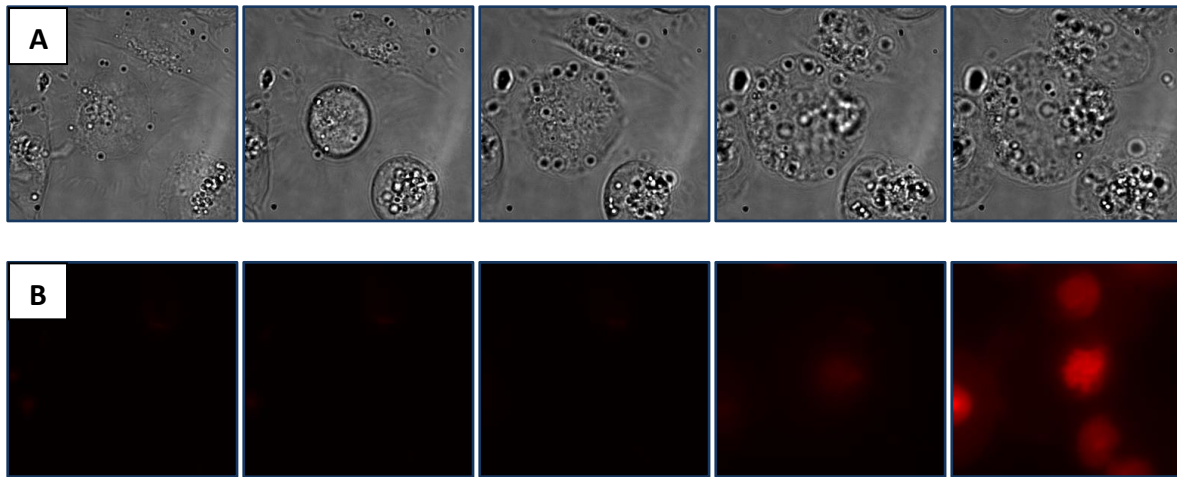
Figure 3.17 – Typically observed cell death pathway after A2780 cells were treated with RuRe **3** (50 µM, 0-3 hours) (**A**) phase contrast (**B**) epifluorescence (ex. 470 nm, em. >520 nm)

These observations were quantified by manual cell measurement using tools found in the FIJI imageJ software. The subjects chosen were those cells which at the final time point were dead (as judged by previously expansion of cell area to the point of no more cellular movement) and comprehensively stained. The perimeter of the cell was recorded for these subjects at the first and final time point, which subsequently gave the area of the cell. This was repeated for each affected cell in a field of view for 5 different coordinates of each cell line and complex permutation. This raw data was used to calculate a difference in area for each viable to dead cell as a percentage of the initial area. Looking at samples of individual cells this revealed a more subtle observation that the cells underwent a greater range of cell size differentiation than first thought, with the majority of dead cells having increased in size but to a varying magnitude and with some cases of cell shrinkage too. To ensure the mean increase in size was not skewed by those cases of cells that did in fact decrease in size, the data for each variable was partitioned into subsets of increasing and decreasing area prior to the calculation of respective mean and standard error of the mean values. The mean difference in cell size after the cytotoxic response, as a percentage of initial viable cell size, with the corresponding standard error of the mean (only positive direction of error bars shown for clarity) is plotted below (*Figure 3.18*).
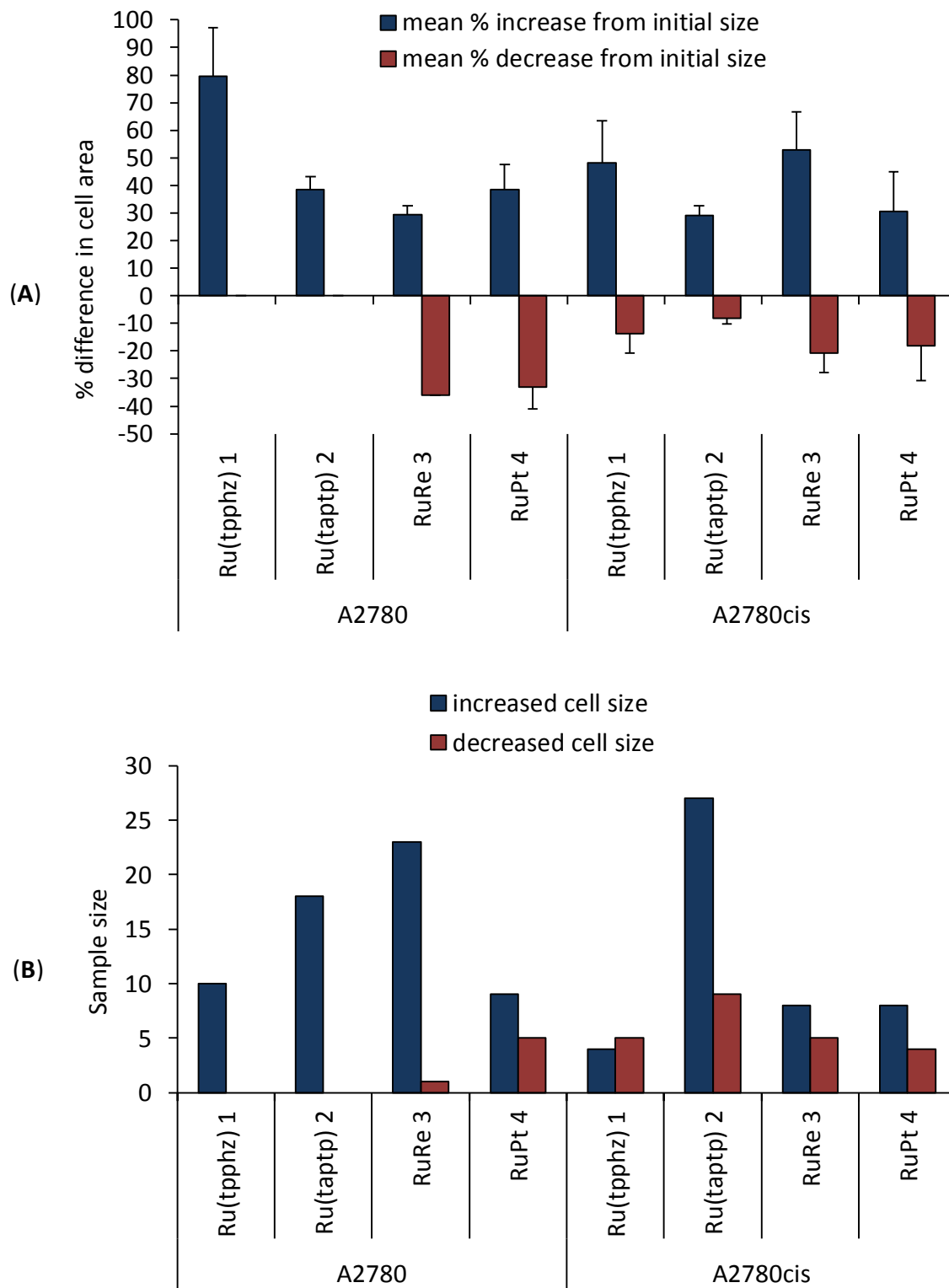
Figure 3.18 – (**A**) Mean difference in cell size for A2780 and A2780cis between initial viable cells and final dead cells after treatment with the corresponding complex, separated into subsets cells with an increase or decrease in size (**B**) Sample size of each cell line and complex permutation and the distribution of cells that increase or decrease in size

This data reveals a complex variability in the overall morphology of the cells as they undergo a cytotoxic response to the complex treatment. It appears the strongest agreement with the typical characteristics of oncosis is for Ru(tpphz) **1** treatment on A2780 cells, with an average increase in cell size of approximately 80%, with complexes **2 – 4** increasing in size to a lower magnitude of typically around 30-40%. For the A2780 cells which decreased in size, there was only one case for RuRe **3**, but it was approaching an even split between cell swelling and shrinkage after treatment with RuPt **4**. For the A2780cis samples treated with complexes **1** and **2** there was a smaller mean increase in size than the A2780 analogue's (50% and 30% respectively), but a more notable contrast to A2780 is the cases of cell shrinkage, albeit to a small magnitude of 14% and 8% respectively. For the cases of RuRe **3** and RuPt **4** there is still a prominent mean increase in cell size but for the cases of cell shrinkage an increasing magnitude of this effect. The magnitude of the standard error of the mean sufficiently validates an appreciable difference in characteristics between variables, but as there is some small overlap of ranges the trends should be taken as a general comparative oversight. Nevertheless, the difference in profiles between cell swelling and shrinkage are apparent and if postulated as a correlation to cases of oncosis and apoptosis, there appears to be a trend whereby, following treatment with complexes **1 – 4**, the A2780cis cell line is more prone to death by apoptosis than the A2780 cell line. Furthermore, looking at potential trends between the complexes, the only complex with a significant frequency of cell shrinkage in A2780 cells as well as A2780cis is RuPt **4**.

Interestingly, the fluorescence is sometimes seen only after a cell has significantly progressed along the cell death pathway – when it is already swollen or displays compromised membranes (*Figure 3.17*). One hypothesis that explains these observations is that an extracellular stimulus causes a proportion of the cell death, possibly in the form of cell signalling from the minority of cells that are initially affected, before compromised membranes remove any barrier to the rapid influx of complex which binds with intracellular targets. Another hypothesis is that the complex does immediately enter the cell but in such a relatively low concentration the fluorescence is not seen until the membrane is compromised in cell death and there is a large influx of complex that facilitates widespread binding to those intracellular targets capable of an observable light switch effect.

In addition, for the mononuclear complex Ru(tpphz) **1** a further experiment was run with 4',6-diamidino-2-phenylindole (DAPI) as a co-stain. DAPI is a known nuclear stain that has an excitation/emission profile of 358/461 nm, so its emission was collected from a 405 nm excitation. Ru(tpphz) **1** has a profile of 440/521 nm, but has a broad excitation so 470 nm was used for two distinct channels. Sample preparation was replicated from the previous protocol, but the complex treatment potency was reduced to 25 µM for 2 hours to avoid mass cell death with few intact membranes in place. The complex solution was removed and cells thoroughly washed with PBS before and after 15 minutes DAPI incubation, prior to imaging of the two channels (*Figure 3.19*).
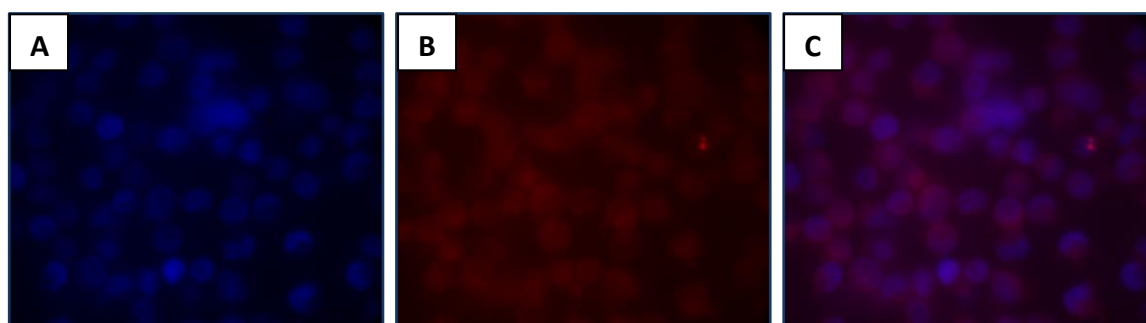
Figure 3.19 – (**A**) DAPI nuclear staining (blue) (**B**) Ru(tpphz) **1** staining (red) (**C**) overlay

Whilst there is mainly nuclear staining from DAPI, as intended, it can be seen from the overlap that Ru(tpphz) **1** does stain the nucleus but is not as exclusive as general cytoplasmic fluorescence is also observed.

The occurrence of the contrasting characteristics of cell death within single experiments shows the complexity of assigning only one mode of cell death, but oncosis seems the most likely cause for the majority of cell death. To gain a more detailed insight into the mechanistic characteristics, a proteomic approach was employed.

3.4   Proteomic Studies

To investigate the mechanism of cell death in more detail, a comparison of the protein expression levels between treated and untreated cells was carried out. Rather than analyse the presence of specific proteins through immunoblotting techniques, a whole proteome approach was adopted. This was carried out using the Stable Isotope Labelling by Amino Acids in Cell Culture (SILAC) methodology to analyse the ratio of peptides from untreated and treated samples (full protocol found in *Experimental Section 6.6*).

The basis of this technique involves running two parallel cell cultures in identical conditions, with one culture having cells labelled with heavy amino acids incorporated from specially formulated media in subculture (RPMI 1640 R10K8 containing L-Arginine $^{13}C_6$, $^{15}N_4$ hydrochloride and L-lysine-$^{13}C_6$,$^{15}N_2$ hydrochloride, sourced from Dundee Cell Products with full formulation in *Experimental Section 6.6.1*), and the other culture continuing in media without any labelling. After subjecting the two cultures to different experimental conditions, two cell lysates can be generated and combined in a 1:1 ratio before purification by SDS-PAGE. A series of steps are then employed to digest the peptides before a mass spectrometry analysis in which pairs of signals can be detected when they have the correct difference in mass between regular and labelled peptides. Since the same peptide structure is responsible for both signals but originates from the differing cell cultures, the ratio of specific [labelled/unlabelled] peptide concentrations in the two populations can be determined. In this case the two populations were untreated and treated cultures, so individual peptide ratios reveal, up- or down-regulation of specific proteins after treatment with a complex.

One valuable resource on the key analytical technique behind this approach – that is peptide sequencing by mass spectrometry – is a recent review by Steen and Mann, which includes a summary of the SILAC methodology and a schematic illustrating the process which can be seen below (*Figure 3.20*).[14]
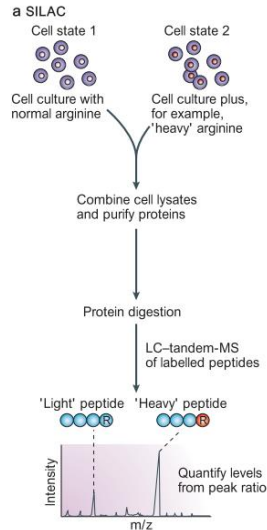
Figure 3.20 – Schematic of SILAC peptide sequencing from the review by Steen and Mann[14]

Many options are available in the processing of raw data, but the search engine software Mascot was used to assign to protein structures using the latest databases. The list of proteins, complete with light-heavy ratio, was then filtered through specific criteria using the Pegasus program to reveal statistically significant hits (*Experimental Section 6.6.6*).

First, the mononuclear complex Ru(tpphz) **1** was investigated, after treatment with the previously determined specific complex/cell line IC$_{50}$ concentration of 4.4 µM for 48 hours, provoking approximately half of the cell population to respond to the toxic effects of the complex. After cell lysis, protein content determination, normalisation, purification, in gel digest, analysis and data processing, the list of generated proteins and their corresponding up-regulation factors (that is the ratio of expression between untreated and treated populations) is shown below, with the summary included from the open access resource for protein sequence and function - UniProt[15] (*Figure 3.21*).

Protein (Accession number)	Up-reg. factor	UniProt Summary
Alpha-2-HS-glycoprotein (P02765)	3.6	Promotes endocytosis, possesses opsonic properties and influences the mineral phase of bone. Shows affinity for calcium and barium ions.
Insulin-like growth factor 2 mRNA-binding protein (Q9NZI8)	2.8	RNA-binding factor that recruits target transcripts to cytoplasmic protein-RNA complexes (mRNPs). This transcript 'caging' into mRNPs allows mRNA transport and transient storage. It also modulates the rate and location at which target transcripts encounter the translational apparatus and shields them from endonuclease attacks or microRNA-mediated degradation.
Beta-actin-like protein 2 (Q562R1)	2.7	Actins are highly conserved proteins that are involved in various types of cell motility and are ubiquitously expressed in all eukaryotic cells.
Microtubule-associated protein 1S (Q66K74)	2.4	Microtubule-associated protein that mediates aggregation of mitochondria resulting in cell death and genomic destruction (MAGD). Plays a role in anchoring the microtubule organizing center to the centrosomes. Binds to DNA. Plays a role in apoptosis. Involved in the formation of microtubule bundles (By similarity).
Heme oxygenase 1 (P09601)	2.4	Heme oxygenase cleaves the heme ring at the alpha methene bridge to form biliverdin. Biliverdin is subsequently converted to bilirubin by biliverdin reductase. Exhibits cytoprotective effects since excess of free heme sensitizes cells to undergo apoptosis.
Vimentin (P08670)	2.3	Vimentins are class-III intermediate filaments found in various non-epithelial cells, especially mesenchymal cells. Vimentin is attached to the nucleus, endoplasmic reticulum, and mitochondria, either laterally or terminally.
AP-3 complex subunit delta-1 (O14617)	2.3	Part of the AP-3 complex, an adaptor-related complex which is not clathrin-associated. The complex is associated with the Golgi region as well as more peripheral structures. It facilitates the budding of vesicles from the Golgi membrane and may be directly involved in trafficking to lysosomes. In concert with the BLOC-1 complex, AP-3 is required to target cargos into vesicles assembled at cell bodies for delivery into neurites and nerve terminals.
AP2-associated protein kinase 1 (Q2M2I8)	2.2	Regulates clathrin-mediated endocytosis by phosphorylating the AP2M1/mu2 subunit of the adaptor protein complex 2 (AP-2) which ensures high affinity binding of AP-2 to cargo membrane proteins during the initial stages of endocytosis. Isoform 1 and 2 display similar levels of kinase activity towards AP2M1. Regulates phosphorylation of other AP-2 subunits, AP-2 localization and AP-2-mediated internalization of ligand complexes. Phosphorylates NUMB and regulates its cellular localization, promoting NUMB localization to endosomes. Binds to/stabilizes activated form of NOTCH1, increasing localization in endosomes and regulating transcriptional activity.
Regulator of chromosome condensation (P18754)	2.2	Guanine-nucleotide releasing factor that promotes the exchange of Ran-bound GDP by GTP. Involved in the regulation of onset of chromosome condensation in the S phase. Binds both to the nucleosomes and double-stranded DNA. RCC1-Ran complex (together with other proteins) acts as a component of a signal

		transmission pathway that detects unreplicated DNA. Plays a key role in nucleo-cytoplasmic transport, mitosis and nuclear-envelope assembly.
Protein transport protein Sec16A (O15027)	2.2	Defines endoplasmic reticulum exit sites (ERES) and is required for secretory cargo traffic from the endoplasmic reticulum to the Golgi apparatus. SAR1A-GTP-dependent assembly of SEC16A on the ER membrane forms an organized scaffold defining an ERES. Required for normal transitional endoplasmic reticulum (tER) organization.
Lamina-associated polypeptide 2, isoforms beta/gamma (P42167)	2.1	May help direct the assembly of the nuclear lamina and thereby help maintain the structural organization of the nuclear envelope. Possible receptor for attachment of lamin filaments to the inner nuclear membrane. May be involved in the control of initiation of DNA replication through its interaction with NAKAP95. Thymopoietin (TP) and Thymopentin (TP5) may play a role in T-cell development and function. TP5 is an immunomodulating pentapeptide.
PC4 and SFRS1-interacting protein (O75475)	2.1	Transcriptional coactivator involved in neuroepithelial stem cell differentiation and neurogenesis. Involved in particular in lens epithelial cell gene regulation and stress responses. May play an important role in lens epithelial to fiber cell terminal differentiation. May play a protective role during stress-induced apoptosis. Isoform 2 is a more general and stronger transcriptional coactivator. Isoform 2 may also act as an adapter to coordinate pre-mRNA splicing. Cellular cofactor for lentiviral integration.
Transferrin receptor protein 1 (P02786)	2.0	Cellular uptake of iron occurs via receptor-mediated endocytosis of ligand-occupied transferrin receptor into specialized endosomes. Endosomal acidification leads to iron release. The apotransferrin-receptor complex is then recycled to the cell surface with a return to neutral pH and the concomitant loss of affinity of apotransferrin for its receptor. Transferrin receptor is necessary for development of erythrocytes and the nervous system (By similarity). A second ligand, the heditary hemochromatosis protein HFE, competes for binding with transferrin for an overlapping C-terminal binding site.
Zinc finger CCCH domain-containing protein 4 (Q9UPT8)	2.0	n/a
Protein transport protein Sec24C (P53992)	1.9	Component of the COPII coat, that covers ER-derived vesicles involved in transport from the endoplasmic reticulum to the Golgi apparatus. COPII acts in the cytoplasm to promote the transport of secretory, plasma membrane, and vacuolar proteins from the endoplasmic reticulum to the Golgi complex.
Plasminogen activator inhibitor 1 RNA-binding protein (Q8NC51)	1.9	May play a role in the regulation of mRNA stability. Binds to the 3'-most 134 nt of the SERPINE1/PAI1 mRNA, a region which confers cyclic nucleotide regulation of message decay.
Eukaryotic translation initiation factor 4B (P23588)	1.9	Required for the binding of mRNA to ribosomes. Functions in close association with EIF4-F and EIF4-A. Binds near the 5'-terminal cap of mRNA in presence of EIF-4F and ATP. Promotes the ATPase activity and the ATP-dependent RNA unwinding activity of both EIF4-A and EIF4-F.

Histone H2AX (P16104)	1.9	Variant histone H2A which replaces conventional H2A in a subset of nucleosomes. Nucleosomes wrap and compact DNA into chromatin, limiting DNA accessibility to the cellular machineries which require DNA as a template. Histones thereby play a central role in transcription regulation, DNA repair, DNA replication and chromosomal stability. DNA accessibility is regulated via a complex set of post-translational modifications of histones, and nucleosome remodelling. Required for checkpoint-mediated arrest of cell cycle progression in response to low doses of ionizing radiation and for efficient repair of DNA double strand breaks (DSBs) specifically when modified by C-terminal phosphorylation.
Brefeldin A-inhibited guanine nucleotide-exchange protein 1 (Q9Y6D6)	1.9	Promotes guanine-nucleotide exchange on ARF1 and ARF3. Promotes the activation of ARF1/ARF3 through replacement of GDP with GTP. Involved in vesicular trafficking. Required for the maintenance of Golgi structure; the function may be independent of its GEF activity. Required for the maturation of integrin beta-1 in the Golgi. Involved in the establishment and persistence of cell polarity during directed cell movement in wound healing. Proposed to act as A kinase-anchoring protein (AKAP) and may mediate crosstalk between Arf and PKA pathways. Inhibits GAP activity of MYO9B probably through competitive RhoA binding. The function in the nucleus remains to be determined.
DNA-directed RNA polymerase I subunit RPA1 (O95602)	1.9	DNA-dependent RNA polymerase catalyzes the transcription of DNA into RNA using the four ribonucleoside triphosphates as substrates. Largest and catalytic core component of RNA polymerase I. Forms the polymerase active center together with the second largest subunit. A single stranded DNA template strand of the promoter is positioned within the central active site cleft of Pol I. A bridging helix emanates from RPA1 and crosses the cleft near the catalytic site and is thought to promote translocation of Pol I by acting as a ratchet that moves the RNA-DNA hybrid through the active site by switching from straight to bent conformations at each step of nucleotide addition (By similarity).
Histone-binding protein RBBP4 (Q09028)	1.9	Core histone-binding subunit that may target chromatin assembly factors, chromatin remodelling factors and histone deacetylases to their histone substrates in a manner that is regulated by nucleosomal DNA. Component of several complexes which regulate chromatin metabolism. These include the chromatin assembly factor 1 (CAF-1) complex, which is required for chromatin assembly following DNA replication and DNA repair; the core histone deacetylase (HDAC) complex, which promotes histone deacetylation and consequent transcriptional repression; the nucleosome remodelling and histone deacetylase complex (the NuRD complex), which promotes transcriptional repression by histone deacetylation and nucleosome remodelling; the PRC2/EED-EZH2 complex, which promotes repression of homeotic genes during development; and the NURF (nucleosome remodelling factor) complex.
Ubiquitin-associated protein 2 (Q5T6F2)	1.8	n/a

Ras GTPase-activating protein-binding protein 2 (Q9UN86)	1.8	Probable scaffold protein that may be involved in mRNA transport.
Tripeptidyl-peptidase 2 (P29144)	1.8	Component of the proteolytic cascade acting downstream of the 26S proteasome in the ubiquitin-proteasome pathway. May be able to complement the 26S proteasome function to some extent under conditions in which the latter is inhibited. Stimulates adipogenesis (By similarity).
DNA replication licensing factor MCM4 (P33991)	1.8	Acts as component of the MCM2-7 complex (MCM complex) which is the putative replicative helicase essential for 'once per cell cycle' DNA replication initiation and elongation in eukaryotic cells. The active ATPase sites in the MCM2-7 ring are formed through the interaction surfaces of two neighbouring subunits such that a critical structure of a conserved arginine finger motif is provided in trans relative to the ATP-binding site of the Walker A box of the adjacent subunit. The six ATPase active sites, however, are likely to contribute differentially to the complex helicase activity.

Figure 3.21 – Table of up-regulated proteins upon treatment with Ru(tpphz) **1**

This approach generated a considerable amount of data and the 25 hits above are a result of the following criteria: light/heavy ratio >1.8, number of detected peptides >1, light/heavy pair count >1, light/heavy variability between separate pairs <30%. This excluded the majority of the data set which contained many instances of peptides appearing only once, which may be relevant but cannot be relied upon. It is very difficult to analyse each up-regulated protein in isolation as everything is part of a vastly complex system intrinsically linked, but instead general observations of the types of proteins affected can be made.

After treatment with the complex Ru(tpphz) **1**, there are several proteins being up-regulated that are associated with cytoskeletal components - Beta-actin-like protein 2 (2.7), Microtubule-associated protein 1S (2.4), Vimentin (2.3) and Lamina-associated polypeptide 2 (2.1). Also there is a response from several proteins with membrane functions, in particular a common theme of endocytic relations – Alpha-2-HS-glycoprotein (3.6), AP-3 complex subunit delta-1 (2.3), AP2-associated protein kinase 1 (2.2), Protein transport protein Sec16A (2.2), Transferrin receptor protein 1 (2.0) and Protein transport protein Sec24C (1.9). Another cluster is proteins with nuclear or RNA function – Insulin-like growth factor 2 mRNA-binding protein (2.8), Regulator of chromosome condensation (2.2), DNA-directed RNA polymerase I (1.9), Plasminogen activator inhibitor 1 RNA-binding protein (1.9)

and Eukaryotic translation initiation factor 4B (1.9). These findings imply that three of the key cellular functions affected upon treatment are the cells motility, membrane trafficking and transcriptional processes.

One interesting hit not grouped into the generalisations above is the up-regulation of the enzyme heme oxygenase 1 (2.4) which is responsible for the degradation of heme to form biliverdin, iron and carbon monoxide.[16] There are three isoforms and expression of this form appears to be induced as a protective response to oxidative stress as biliverdin and bilirubin have antioxidant properties.[16] An excess of free heme is also a sensitizer for apoptosis so up-regulation of this protein could also be a preventative measure against this effect.

Histone H2AX – a marker for DNA double strand breaks – is up-regulated by a factor of 1.9, indicating that this specific type of DNA damage is involved in the cytotoxicity of Ru(tpphz) **1**; this observation indicates DNA is indeed one of the intracellular targets of the complex. Histone-binding protein RBBP4 is also up-regulated and this could be due to the increased need for chromatin assembly following DNA repair attempts.

As well as the positive results of what is directly observed, any key omissions of conceivable proteins should also be considered and here there is a distinct lack of apoptosis associated caspase proteins. Whilst wary of drawing conclusions from possible false negative results, there is statistical reassurance in this case as there are numerous members in this family of proteins and none show up, which supports the observations from microscopy that oncosis is the dominant mode of cell death.

A pictorial overview of the general observations of which cell processes are affected can be obtained from a pie chart whereby the 25 up-regulated proteins have been grouped into broad categories of association with nucleic acid, cytoskeletal, membrane or other functions (*Figure 3.22*).
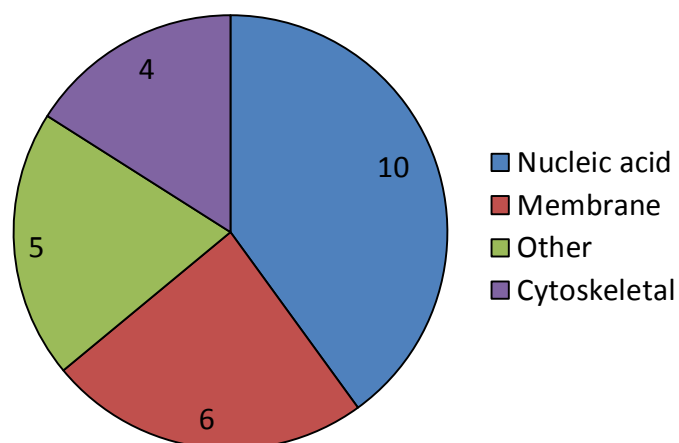
Figure 3.22 – Pie chart showing the associations of the up-regulated proteins with cellular function upon treatment with Ru(tpphz) **1** (4.4 µM, 48 hours)

These are still, however, relatively broad conclusions and more specific outcomes that were originally envisioned have not been realised from one experimental run – repeating the procedure would offer validation.

With the aim of gaining insight from comparing and contrasting the data of another complex treatment, Ru(taptp) was analysed using the same protocol for peptide sequencing. The lysate had been previously generated in the same SILAC experiment as Ru(tpphz) **1**, after treatment with the previously determined IC_{50} concentration specific to Ru(taptp) **2** (13.2 µM) for 48 hours; and the purification by SDS-PAGE had also been run simultaneously. The results, after processing of the raw data by Mascot and filtering by the previously used criteria on Perseus, gave the following hits with UniProt[15] summaries (*Figure 3.23*).

Protein (Accession number)	Up-reg. factor	UniProt Summary
Pigment epithelium-derived factor (P36955)	35.7	Neurotrophic protein; induces extensive neuronal differentiation in retinoblastoma cells. Potent inhibitor of angiogenesis.
High mobility group protein B2 (P26583)	3.3	DNA binding proteins that associates with chromatin and has the ability to bend DNA. Binds preferentially single-stranded DNA. Involved in V(D)J recombination by acting as a cofactor of the RAG complex.
NHL repeat-containing protein 2 (Q8NBF2)	2.6	n/a

PC4 and SFRS1-interacting protein (O75475)	2.3	Transcriptional coactivator involved in neuroepithelial stem cell differentiation and neurogenesis. Involved in particular in lens epithelial cell gene regulation and stress responses. May play an important role in lens epithelial to fiber cell terminal differentiation. May play a protective role during stress-induced apoptosis.
Vimentin (P08670)	2.2	Vimentins are class-III intermediate filaments found in various non-epithelial cells, especially mesenchymal cells. Vimentin is attached to the nucleus, endoplasmic reticulum, and mitochondria, either laterally or terminally.
Lamina-associated polypeptide 2, isoform alpha (P42166)	2.0	May be involved in the structural organization of the nucleus and in the post-mitotic nuclear assembly. Plays an important role, together with LMNA, in the nuclear anchorage of RB1.
6-phosphoglucono-lactonase (O95336)	2.0	Hydrolysis of 6-phosphogluconolactone to 6-phosphogluconate.
NADPH:adrenodoxin oxidoreductase, mitochondrial (P22570)	1.9	Serves as the first electron transfer protein in all the mitochondrial P450 systems.
Cell division control protein 42 homolog (P60953)	1.9	Plasma membrane-associated small GTPase which cycles between an active GTP-bound and an inactive GDP-bound state. In active state binds to a variety of effector proteins to regulate cellular responses. Regulates bipolar attachment of spindle microtubules to kinetochores before metaphase chromosome congression. Plays a role in extension and maintenance of the formation of the thin, actin-rich surface projections filopodia. Mediates CDC42-dependent cell migration.
Insulin-like growth factor 2 mRNA-binding protein 3 (O00425)	1.9	RNA-binding factor that may recruits target transcripts to cytoplasmic protein-RNA complexes (mRNPs). This transcript 'caging' into mRNPs allows mRNA transport and transient storage. It also modulates the rate and location at which target transcripts encounter the translational apparatus and shields them from endonuclease attacks or microRNA-mediated degradation. Binds to the 3'-UTR of CD44 mRNA and stabilizes it, promoting cell adhesion and invadopodia formation in cancer cells. Binds to beta-actin/ACTB and MYC transcripts. Binds to the 5'-UTR of the insulin-like growth factor 2 (IGF2) mRNAs.
Poly [ADP-ribose] polymerase 1 (P09874)	1.9	Involved in the base excision repair (BER) pathway, by catalyzing the poly(ADP-ribosyl)ation of a limited number of acceptor proteins involved in chromatin architecture and in DNA metabolism. This modification follows DNA damages and appears as an obligatory step in a detection/signalling pathway leading to the reparation of DNA strand breaks. Mediates the poly(ADP-ribosyl)ation of APLF and CHFR. Positively regulates the transcription of MTUS1 and negatively regulates the transcription of MTUS2/TIP150. With EEF1A1 and TXK, forms a complex that acts as a T-helper 1 (Th1) cell-specific transcription factor and binds the promoter of IFN-gamma to directly regulate its transcription, and is thus involved importantly in Th1 cytokine production. Required for PARP9 and

		DTX3L recruitment to DNA damage sites. PARP1-dependent PARP9-DTX3L-mediated ubiquitination promotes the rapid and specific recruitment of 53BP1/TP53BP1, UIMC1/RAP80, and BRCA1 to DNA damage sites.
Prelamin-A/C (P02545)	1.8	Prelamin-A/C can accelerate smooth muscle cell senescence. It acts to disrupt mitosis and induce DNA damage in vascular smooth muscle cells (VSMCs), leading to mitotic failure, genomic instability, and premature senescence.
Very long-chain specific acyl-CoA dehydrogenase, mitochondrial (P49748)	1.8	This protein is involved in the pathway mitochondrial fatty acid beta-oxidation, which is part of Lipid metabolism.

Figure 3.23 – Table of up-regulated proteins upon treatment with Ru(taptp) **2**

Again the generated proteins form an interesting set of results, with some up-regulated proteins common to both Ru(tpphz) **1** and Ru(taptp) **2** treatments, albeit having fewer reliable hits from this experiment (13 versus 25).

There are fewer up-regulated proteins associated with cytoskeletal functions, but vimentin still features at a similar factor of increased expression (2.2). Out of the proteins associated with membrane functions in the previous data set, none are seen here, but there was an up-regulation of the membrane-based cell division control protein 42 homolog (1.9) detected. Most of the up-regulated proteins are related to nuclear or RNA functions, with several common to the Ru(tpphz) **1** analysis - high mobility group protein B2 (3.3), PC4 and SFRS1-interacting protein (2.3), lamina-associated polypeptide 2 isoform alpha (2.0), Insulin-like growth factor 2 mRNA-binding protein 3 (1.9), Poly [ADP-ribose] polymerase 1 (1.9) and Prelamin-A/C (1.8). Of particular interest is Poly [ADP-ribose] polymerase 1. This enzyme is involved in base excision repair particularly of small, non-helix distorting lesions (rather than the related nucleotide excision repair pathway which is activated by large helix distorting lesions),[17] indicating intracellular DNA binding is involved in the cytotoxicity of Ru(taptp) **2**.

The remaining hits consist of two proteins related to mitochondrial function - NADPH:adrenodoxin oxidoreductase, mitochondrial (1.9) and very long-chain specific acyl-CoA dehydrogenase, mitochondrial (1.8) – and several ambiguous results that do not draw on a specific function. The greatest up-regulation by far in this data set is for the pigment

epithelium-derived factor(35.7), but information on this protein relates to physiological rather than cellular functions.

Once again, there is no instance of caspase up-regulation, which indicates a lack of apoptosis occurring and is in agreement with the microscopy studies conducted.

The grouping of protein function implies the localisation and effects of the complex are nuclear, with cellular functions such as mitochondrial processes and cell motility affected to a degree but not in a widespread profile such as Ru(tpphz) **1**; which is more toxic.

The general observation of which cell processes are affected can be summarised in the following pie chart featuring the 13 up-regulated proteins grouped into broad categories of association with nucleic acid, cytoskeletal, membrane or other functions (*Figure 3.24*).
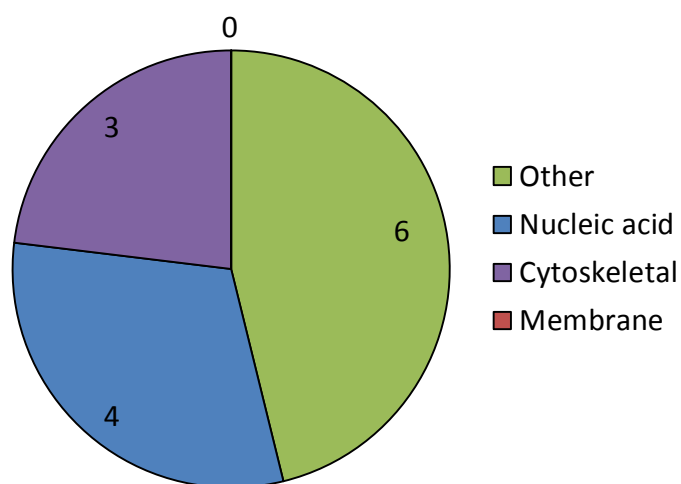
Figure 3.24 – Pie chart showing the associations of the up-regulated proteins with cellular function upon treatment with Ru(tpphz) **2** (13.2 µM, 48 hours)

3.5 Summary

In conclusion, complexes **1 – 4** display a range of toxicities and furthermore cross-resistance profiles for the two A2780 and A2780cis cell lines vary for each complex. The most cytotoxic was the mononuclear complex Ru(tpphz) **1** which is as potent as cisplatin but displays minimal cross-resistance. Ru(taptp) **2** is not as toxic against A2780 but interestingly shows an *increase* in toxicity against A2780cis. In contrast RuRe **3** is relatively potent against A2780 cells but exhibits a resistance profile similar to cisplatin. The relatively low cytotoxicity of RuRe **3** and RuPt **4** against A2780cis, suggests that the addition of a second metal centre offers no improvement in cytotoxic activity.

Microscopy experiments revealed that the mode of cell death after treatment with all complexes is via possible oncosis but with a varying magnitude of cell swelling for each complex treatment and also, in addition, a notable minority of cells dying with a net decrease in size. The staining occurs throughout the cell and nucleus and the majority of fluorescence is seen in the later stages of cell death.

Proteomic analysis of cells treated with complexes Ru(tpphz) **1** and Ru(taptp) **2** provided a wide array of information. Although it is difficult to narrow down any direct relationship between changes in the proteome and the complexes' action, cell processes that appear to be affected include cytoskeletal and membrane function and in particular DNA processing. Furthermore, indications of direct DNA strand damage, along with the absence of apoptosis associated expression, are in agreement with the microscopy observations of likely oncosis.

3.6 References

1. Wheate, N. J., Walker, S., Craig, G. E. & Oun, R. The status of platinum anticancer drugs in the clinic and in clinical trials. *Dalton Trans.* **39,** 8113–27 (2010).

2. Sava, G. *et al.* Influence of chemical stability on the activity of the antimetastasis ruthenium compound NAMI-A. *Eur. J. Cancer* **38,** 427–35 (2002).

3. Sava, G. *et al.* Dual Action of NAMI-A in Inhibition of Solid Tumor Metastasis Selective Targeting of Metastatic Cells and Binding to Collagen. *Clin. Cancer Res.* **9,** 1898–1905 (2003).

4. Hartinger, C. G. *et al.* From bench to bedside--preclinical and early clinical development of the anticancer agent indazolium trans-[tetrachlorobis(1H-indazole)ruthenate(III)] (KP1019 or FFC14A). *J. Inorg. Biochem.* **100,** 891–904 (2006).

5. Brown, R. *et al.* hMLH1 expression and cellular responses of ovarian tumour cells to treatment with cytotoxic anticancer agents. *Oncogene* **15,** 45–52 (1997).

6. Plumb, J. a, Strathdee, G., Sludden, J., Kaye, S. B. & Brown, R. Reversal of Drug Resistance in Human Tumor Xenografts by 2'-Deoxy-5-azacytidine-induced Demethylation of the hMLH1 Gene Promoter Reversal of Drug Resistance in Human Tumor Xenografts by 2 -Deoxy-5- azacytidine-induced Demethylation of the hMLH1 Gene Promo. *Cancer Res.* **60,** 6039–6044 (2000).

7. Brown, R. *et al.* Increased accumulation of p53 protein in cisplatin-resistant ovarian cell lines. *Int. J. Cancer* **55,** 678–684 (1993).

8. Kool, M. *et al.* of the Multidrug Resistance-associated Protein Gene (MRP1), in Human Cancer Cell Lines1. *Cancer Res.* **57,** 3537–3547 (1997).

9. Roy, G. *et al.* Acquired alkylating drug resistance of a human ovarian carcinoma cell line is unaffected by altered levels of pro- and anti-apoptotic proteins. *Oncogene* **19,** 141–150 (2000).

10. Aird, R., Cummings, J. & Ritchie, A. In vitro and in vivo activity and cross resistance profiles of novel ruthenium (II) organometallic arene complexes in human ovarian cancer. *Br. J. Cancer* **86,** 1652–1657 (2002).

11. Liu, H.-K. & Sadler, P. J. Metal complexes as DNA intercalators. *Acc. Chem. Res.* **44,** 349–59 (2011).

12. Weerasinghe, P. & Buja, L. M. Oncosis: An important non-apoptotic mode of cell death. *Exp. Mol. Pathol.* **93,** 302–308 (2012).

13. Majno, G. & Joris, I. Apoptosis, oncosis, and necrosis. An overview of cell death. *Am. J. Pathol.* **146,** 3–15 (1995).

14. Steen, H. & Mann, M. The ABC's (and XYZ's) of peptide sequencing. *Nat. Rev. Mol. Cell Biol.* **5,** 699–711 (2004).

15. Consortium, T. U. UniProt: a hub for protein information. *Nucleic Acids Res.* **43,** D204–D212 (2015).

16. Kikuchi, G., Yoshida, T. & Noguchi, M. Heme oxygenase and heme degradation. *Biochem. Biophys. Res. Commun.* **338,** 558–567 (2005).

17. Liu, Y. *et al.* Coordination of Steps in Single-nucleotide Base Excision Repair Mediated by Apurinic/Apyrimidinic Endonuclease 1 and DNA Polymerase beta. *J. Biol. Chem.* **282,** 13532–13541 (2007).

Chapter 4

Phototoxicity

4.1   Introduction

4.1.1   Background

Previous work on rhenium-based complexes has shown that they can produce photo-activated DNA damage; a notable example being a Re(dppz) "DNA scissor" system with the formula [Re(CO)$_3$(py)(L)](OTf) (py = pyridine, OTf = trifluoromethanesulfonate counterion) where L is one of the planar aromatic ligands dipyridophenazine (dppz) or benzodipryridophenazine (dppn) (*Figure 4.1*).[1,2]
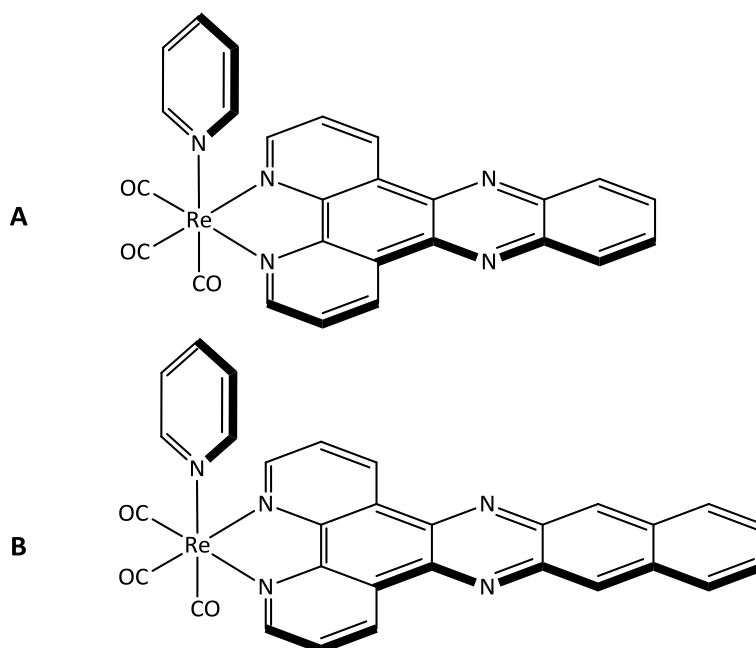

Figure 4.1 – DNA scissor molecule Re(CO)$_3$(py)(L) (py = pyridine, **A**: L = dppz, **B**: L = dppn)

Emission-based titration studies by Yam, *et al.* on the Re(dppz) and Re(dppn) complexes (*Figure 4.1*) showed they associate with CT-DNA through intercalation.[1] Irradiation of the complexes in the presence of the plasmid DNA pBR322 resulted in cleavage of the supercoiled form (I) to the nicked form (II). Surprisingly, these studies indicated that for both of the complexes, singlet oxygen was not involved in the cleavage process. For the dppz

species **A**, direct oxidation of DNA plasmid by the excited state of the molecule was implicated. For the dppn species **B**, inhibition of cleavage in a degassed solution or through the presence of an appropriate quencher indicated that the superoxide radical ($O_2^{\bullet-}$) was involved in this process; although the hydroxyl radical ($^{\bullet}OH$) was likewise implicated as decreased cleavage activity was also observed in the presence of hydroxyl scavengers.[2]

At the same time, studies carried out by Stoeffler, *et al.* with a methylpyridine derivative of Re(dppz) **A** investigated the photophysics with and without DNA.[3] They concluded that the lowest excited state was an intraligand triplet state of dppz, $^3IL_{dppz}$, with luminescence quenched in aqueous solution but present when protected by intercalation in DNA. The difference between this species and Ru(II) or Os(II) analogues is a result of the metal to ligand charge transfer states, $d\pi$ (M) $\rightarrow$ π^* (dppz) ^{3}MLCT, being higher in energy in the Re(I) species which allows the low lying intraligand $^3IL_{dppz}$ excited state to dominate the system.

Given the activity of these rhenium-based complexes, the ruthenium-rhenium complex RuRe **3** was investigated to see if it too displayed similar properties. The long-term aim of investigating the phototoxic activity of such complexes is towards identifying photosensitizers for photodynamic therapy (PDT) applications. PDT is a non-invasive therapy regime that can selectively damage diseased tissue through the generation of singlet oxygen. This is often achieved by the prodrug sensitizer generating cytotoxic singlet oxygen *in situ* upon photoexcitation through an energy transfer mechanism. The selectivity originates from carefully targeted irradiation and offers improvements over orthodox therapeutic regimes by reducing side-effects in unaffected tissue.[4]

Photosensitisers currently most commonly used in the clinic are tetrapyrrolic structures, but - as extended aromatic systems - they can have low water solubility and are often hard to synthesise and purify.[5] In contrast, the chloride salts of ruthenium polypyridyl complexes frequently exhibit very high water solubility and are relatively easy to synthesize, so offering an improvement over conventional systems if other characteristics are suitable for this application.

A comparative measure of phototoxic activity for a molecule is the phototoxic index (PI) which can be calculated from the dark IC_{50} divided by the light IC_{50} – giving a score of the increased toxicity under the action of light. An example of the use of this Figure of Merit is

given in the study by Howerton, *et al.*, which involves strained ruthenium complexes as photo-chemotherapeutics that show PI values ranging from 3 to 208 (*Figure 4.2*).[6]
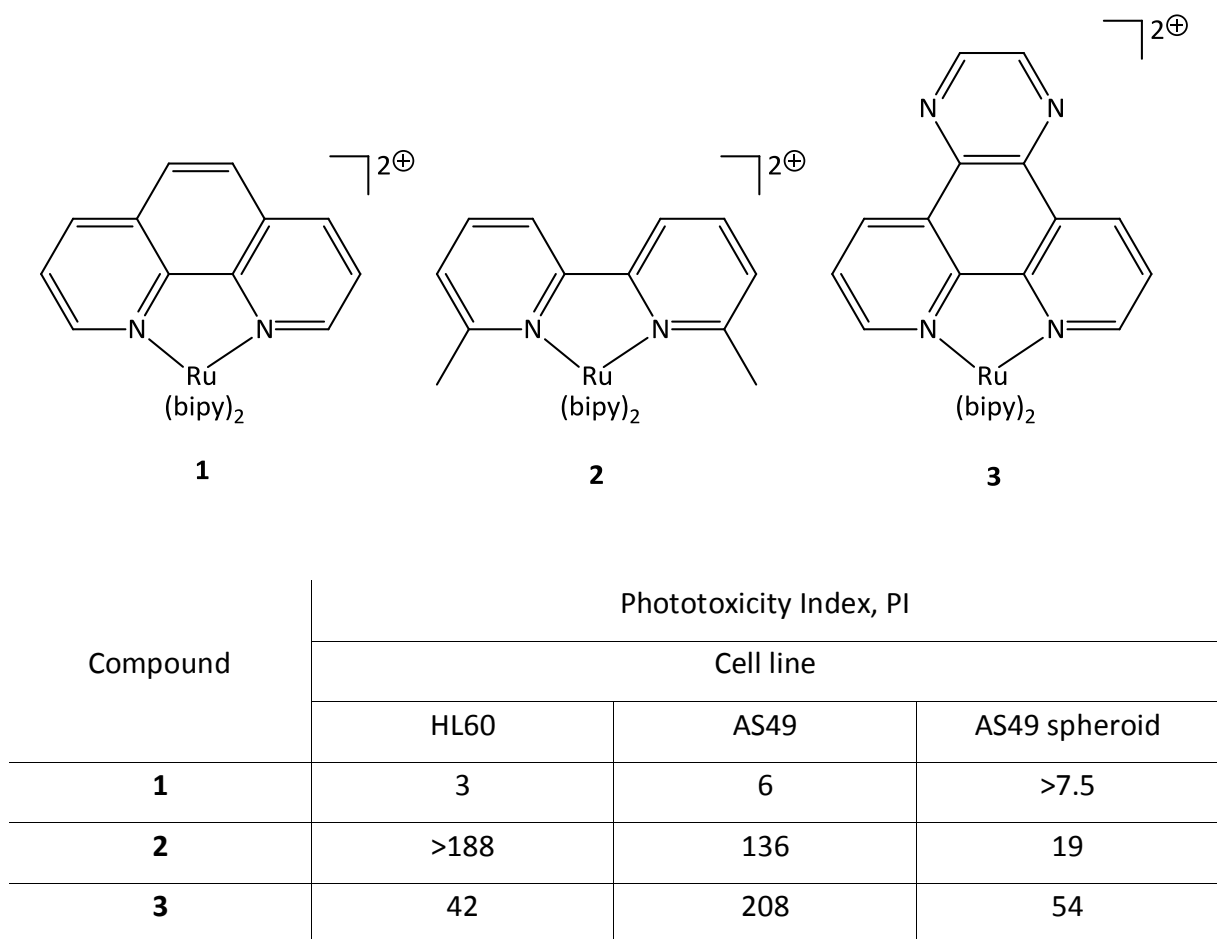

Compound	Phototoxicity Index, PI		
	Cell line		
	HL60	AS49	AS49 spheroid
1	3	6	>7.5
2	>188	136	19
3	42	208	54

Figure 4.2 – Data collected by Howerton *et al.* on strained ruthenium complex phototoxicity[6]

4.1.2   Light Irradiation Source Apparatus

The apparatus used to irradiate the sample was a custom made device featuring a broadband illumination source (technical specification in *Experimental 6.x*), fully contained in an empty computer base unit, which is referred to as the Light Irradiation Source Apparatus (LISA).

To quantify the power output of this light source, an experiment was carried out with the running conditions replicated whilst being monitoring by a power meter. The setup utilised was a THORLABS *S175C sensor* coupled to a *PM100USB Power and Energy Meter* with the readout displayed and stored on a connected netbook. Running three timed periods of irradiation in succession within experimental conditions (for three separate samples) accurately determined the power output to which the cells were exposed (*Figure 4.3*).

Stage	Stabilisation	5 minutes ON	Sample change	15 minutes ON	Sample Change	30 minutes ON
Time (minutes)	2	5	2	15	2	30
Average Power (W)	0.000	0.075	0.035	0.121	0.040	0.126
Corrected Power (W)	-	0.075	-	0.085	-	0.086
Energy (J)	-	22.6	-	76.9	-	155.7
Fluence (J cm^{-2})	-	8	-	24	-	48

Figure 4.3 – Table summarising the fluence calculations from timed irradiations

4.1.3   Protocol Optimisation

The same protocol as that for the 48 hour IC_{50} determination was initially used (*Experimental Section 6.5.4*) but four separate plates were employed, and after 24 hours, each was irradiated for a varying length of time. Three plates underwent timed exposures in the LISA while a dark control remained in the incubator throughout. The dark control was essential to provide a comparison in assessing any phototoxicity upon irradiation. Untreated control wells served the usual purpose of delineating maximum cell viability. Furthermore, not only could they be used to construct curves indicating any effect of increasing compound concentration on cell viability, but - through inclusion in each plate independently - they also acted as a control for any damaging effects of the radiation alone. This ensured the experiment was internally controlled for each variable and avoided any false positive results in which increased exposure to the irradiation increased toxicity regardless of compound treatment.

The compound used first was RuRe **3** which had been predicted to exhibit activity, with a broad concentration range of 1-200 µM - spanning either side of the previously determined IC_{50} value (28 µM). Early experimentation used only a 20 minute exposure with no dark control, but this protocol showed no significant difference in potency, with an IC_{50} value of 33 µM being comparable to the previous dark average within error.

Following this result, experimentation with a macrocyclic molecule which had previously shown phototoxic activity resulted in optimisation of the protocol – *vide infra*. This procedure involved a dark control plus three independent plates exposed to light intervals of 1, 2.5 and 5 minutes.

In the initial procedure, after irradiation, the cells were exposed to the complex for 24 hours. To discount the possible deleterious effect of long term exposure to the complex in the dark a different sequence was carried out in which, prior to irradiation, the complex containing solution was replaced by media alone followed by 24 hour incubation between irradiation and workup by MTT assay. This step was incorporated with the aim of clarifying the effects of irradiation upon cells that *already contained* the compound. This experiment, however, still did not reveal significant differences in cell viability on increasing irradiation.

Therefore the experiment was run again with an extended periods of light exposure of 5, 15 and 30 minutes respectively. In these conditions toxicity that correlated with increasing irradiation *was* observed, i.e. there is some phototoxic effect.

In this successful phototoxicity assay two further observations were made. Under the updated conditions, as might be expected, the cells showed a slightly increased susceptibility to radiative damage over the 3 timed exposures, however this factor was internally controlled through the use of separate plates. The susceptibility to radiative damage is quantified by calculating the relative viability of untreated exposed wells against the untreated dark control, using a standard MTT assay. An example is provided by the first 5-15-30 minute experiment. In this case, the 5, 15 and 30 minute control well viabilities show a somewhat surprising trend, as they are equal to 133%, 109% and 89% of the dark control respectively. The fact that the 5 and 15 minute exposures actually exhibit an increase in viability can probably be attributed to the slight increase in temperature that the cells are subjected to in the LISA, resulting in increased metabolic activity in the cells, as detected by the MTT assay, before the separate deleterious effect of radiative damage becomes detrimental overall (as seen by the 30 minute exposure having a relative viability of 89%). Again, the effect of this factor on the overall data is mitigated through the experiment being internally controlled within each separately exposed plate. This optimised protocol was then used to re-examine RuRe **3** and successfully delineate any observable phototoxic effect.

4.2 RuRe and RuPt molecules

Using the optimized phototoxicity protocol (described above and in *Experimental Section 6.5.5*), the activity of RuRe **3** against the cell line A2780cis was investigated using a concentration range of 1 – 200 μM, resulting in a phototoxic effect shown in *Figure 4.4*.
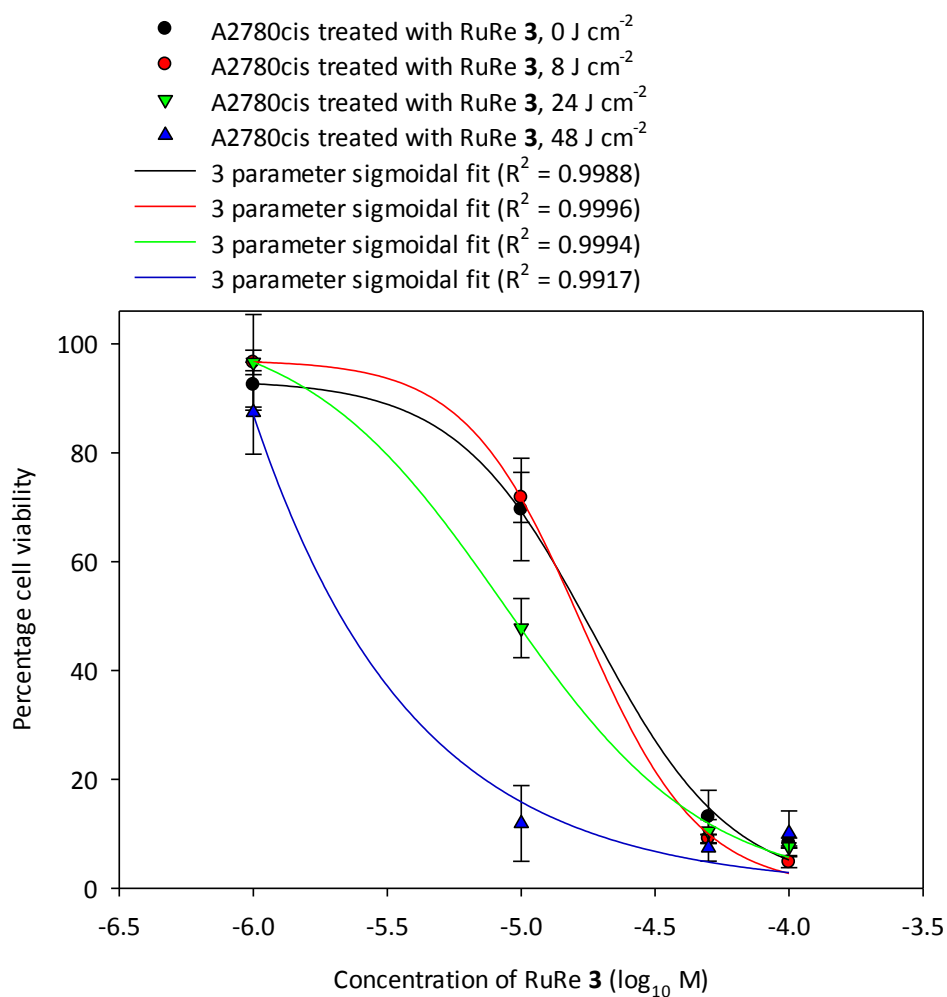
Fluence (J cm^{-2})	IC$_{50}$ concentration (μM)	Percentage Viability at 10 μM RuRe (% cells metabolising MTT +/- 1 SD)
0	18	70 +/- 9
8	18	72 +/- 5
24	9	48 +/- 6
48	3	12 +/- 7

Figure 4.4 – A2780cis cell viability data for RuRe **3** upon irradiation

Using the same protocol, the activity of RuPt **4** against A2780cis was also investigated using a 1 – 200 µM concentration range (*Figure 4.5*). This produced contrasting results, as there was a smaller phototoxic effect: an observed PI of 2 compared to the RuRe **3** PI of 6. Taking the general trend from these experiments, it seems clear that the rhenium centre does have an effect on the phototoxic activity of the final system.
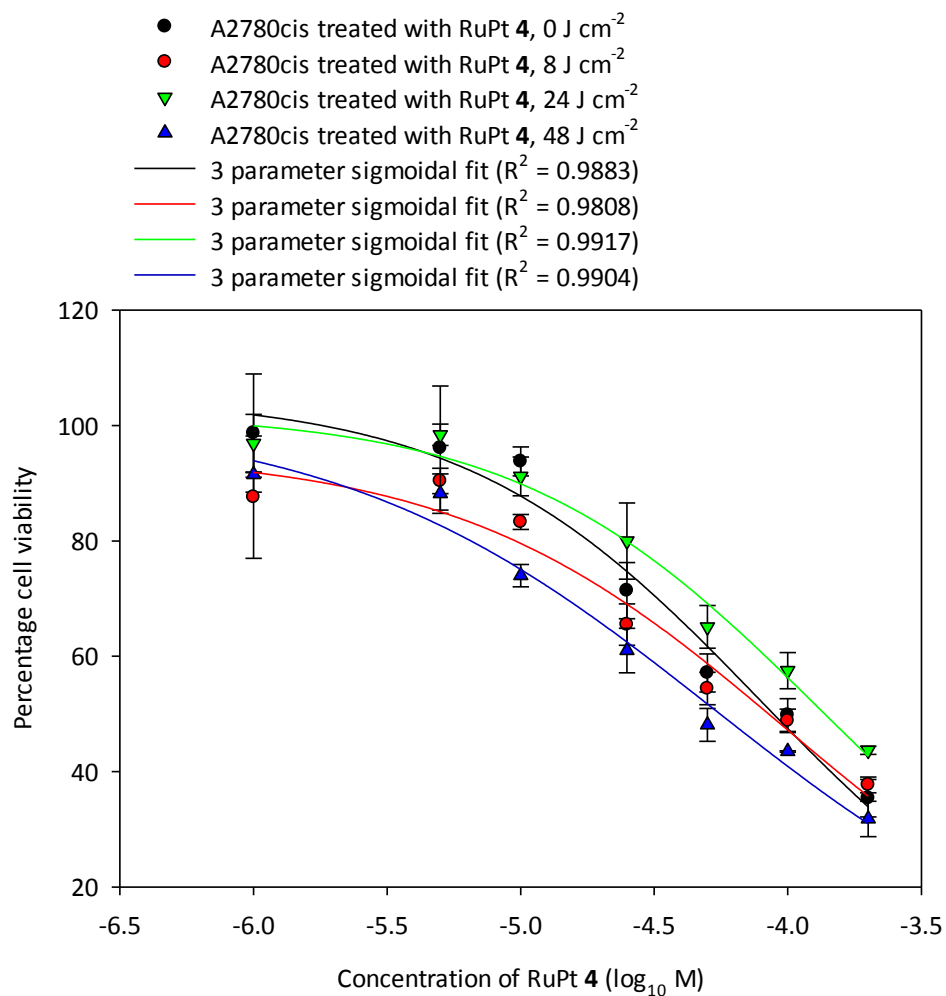
Fluence (J cm^{-2})	IC$_{50}$ (µM)	Percentage Viability at 100 µM RuPt (% cells metabolising MTT +/- 1 SD)
0	100	50 +/- 3
8	86	49 +/- 2
24	148	58 +/- 3
48	46	44 +/- 0.1

Figure 4.5 – A2780cis cell viability data for RuPt **4** upon irradiation

4.3   RuRe bis-intercalator

To further explore the phototoxicity of ruthenium-rhenium systems an alternative complex synthesized by Mr Hiwa Saeed, a fellow member of the Thomas group, was studied. The structure of this potential bis-intercalator is shown below (*Figure 4.6*).
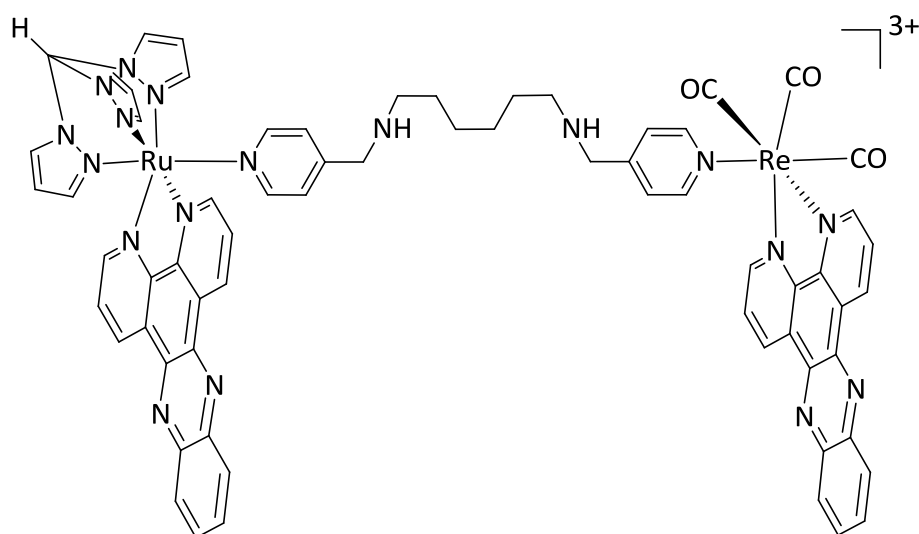
Figure 4.6 – Structure of RuRe bis-intercalator **5**

The DNA binding properties of this complex have previously been investigated and it is known to demonstrate a high DNA binding affinity to CT-DNA in cell-free conditions.[7]

First, using a concentration range of 0.1 – 200 μM, the 48 hour IC_{50} value of the complex was determined to assess its potency against the A2780 and A2780cis cell lines (*Figure 4.7*). Against the A2780 cell line, the IC_{50} was determined as 11 μM, which is not as potent as cisplatin (ca. 2 μM) but still relatively active in therapeutic terms and compared to the series of compounds **1 – 4**. Against A2780cis, the IC_{50} of 21 μM shows a two-fold reduction in potency versus A2780, but this is still at a similar level of cytotoxicity as cisplatin against this cell line (ca. 22 μM).
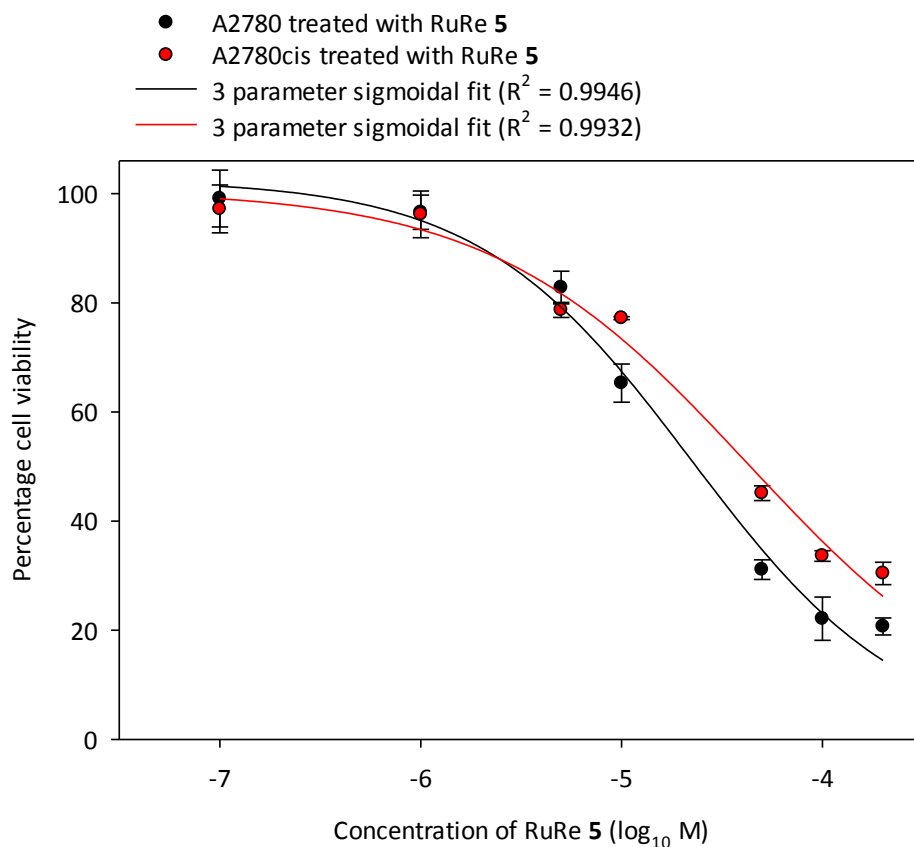
Cell Line	IC_{50} (μM)
A2780	11
A2780cis	21

Figure 4.7 – Cell viability data for RuRe bis-intercalator **5**

The same phototoxicity protocol used for RuRe **3** and RuPt **4** and the A2780cis cell line was then carried out with RuRe **5** using a concentration range of 1 – 200 µM (*Figure 4.8*). Complex RuRe **5** demonstrates some phototoxicity against A2780cis but to a much lesser degree than RuRe **3** (PI = 2).
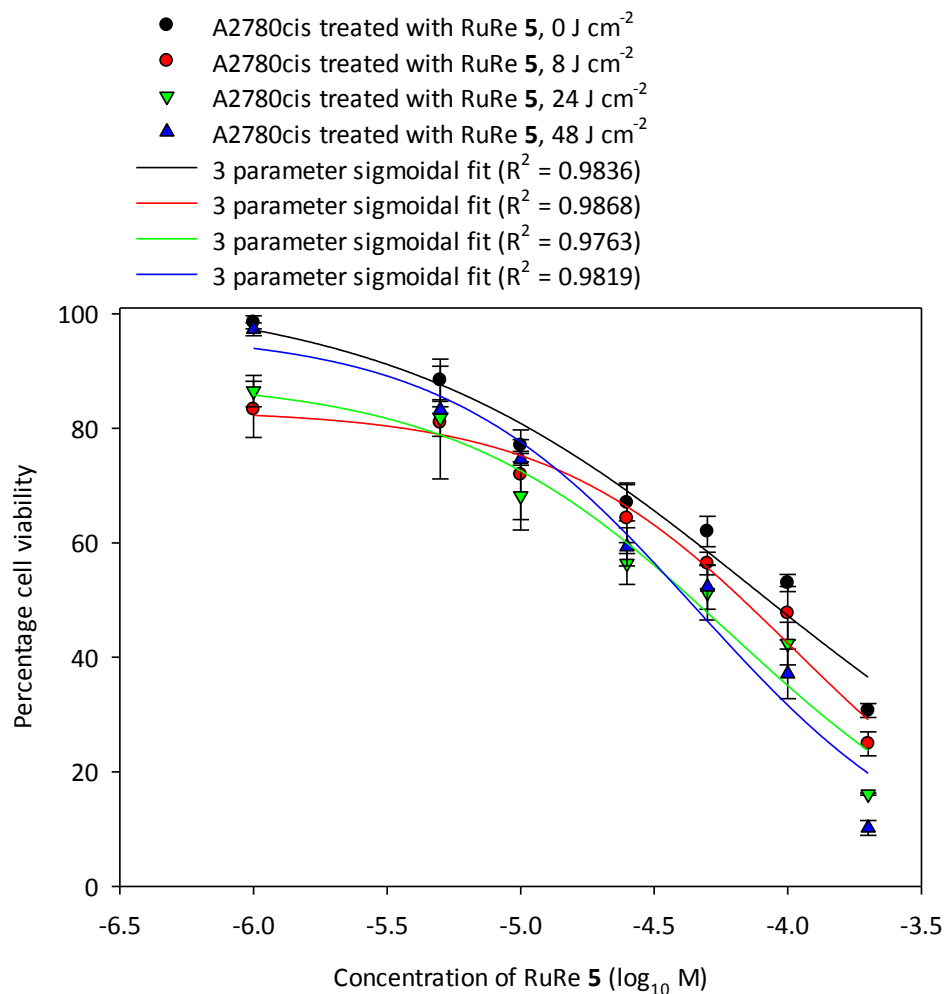
Fluence (J cm^{-2})	IC$_{50}$ concentration (µM)	Percentage Viability at 100 µM [M] (% cells metabolising MTT +/- 1 SD)
0	110	53 +/- 2
8	83	48 +/- 5
24	56	42 +/- 4
48	56	37 +/- 4

Figure 4.8 – A2780cis cell viability data for RuRe **5** upon irradiation

Therefore, with a modest phototoxic index, RuRe **5** is not a favourable lead for applications based on this characteristic. This could be due to lower oxygen sensitisation or due to poor cellular uptake; with this complex not being taken up so well as RuRe **3**, resulting in a low intra-cellular concentration. Further substantial experimentation would be required to determine this issue further.

4.4 Macrocycle Investigation

A further investigation of ruthenium-rhenium systems was facilitated through a study on the self-assembled macrocyclic molecule RuRe macrocycle **6A**, and its corresponding ruthenium monomer "building block" **6B**, synthesized by Dr. Mike Walker (*Figure 4.9*). The singlet oxygen quantum yield $\phi(^1O_2)$ of these two molecules had previously been determined by a collaborator Luke McKenzie in Weinstein group (protocol in *Experimental 6.8*). This data gave $\phi(^1O_2)$ estimates of 54 ±5% for RuRe macrocycle **6A** and 75 ±2% for Ru monomer **6B**, giving promise for singlet oxygen related phototoxic activity, depending on cellular uptake.
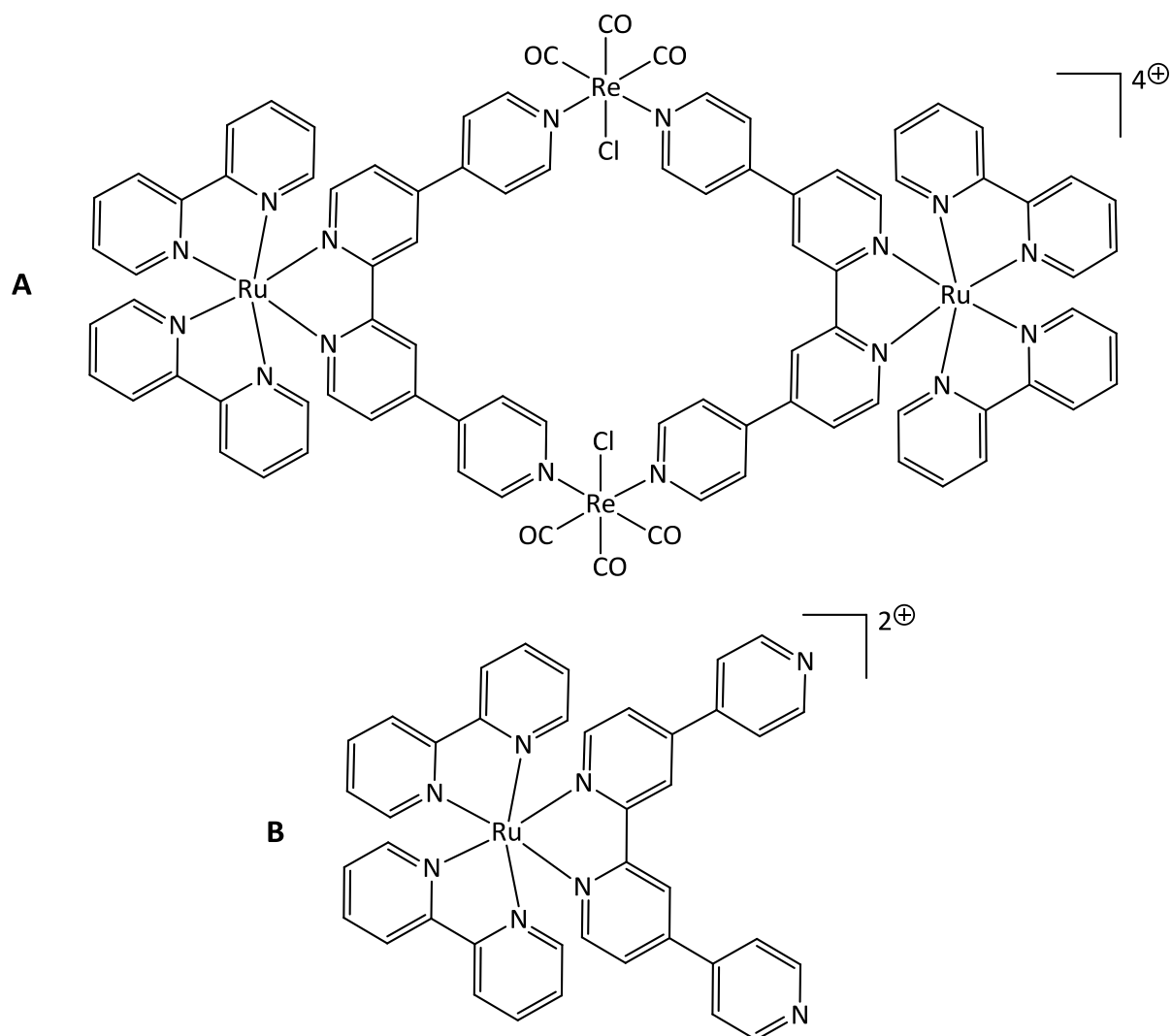
Figure 4.9 – Structure of RuRe macrocycle **6A**, and corresponding Ru monomer unit **6B**

First, to determine the level of cytotoxicity relative to the other compounds studied, a 48 hour IC_{50} protocol on both the A2780 and A2780cis cell lines was carried out in dark conditions using a macrocycle concentration range of $1 - 200$ μM (*Figure 4.10*). Against the A2780 cell line, an IC_{50} of 2 μM was determined - a relatively high potency around the same magnitude as cisplatin. Interestingly, against the A2780cis cell line there was a considerable decrease in potency with an IC_{50} of 59 μM being observed.

- ●   A2780 treated with RuRe **6A**
- ●   A2780cis treated with RuRe **6A**
- ──   3 parameter sigmoidal fit ($R^2 = 0.9751$)
- ──   3 parameter sigmoidal fit ($R^2 = 0.9799$)
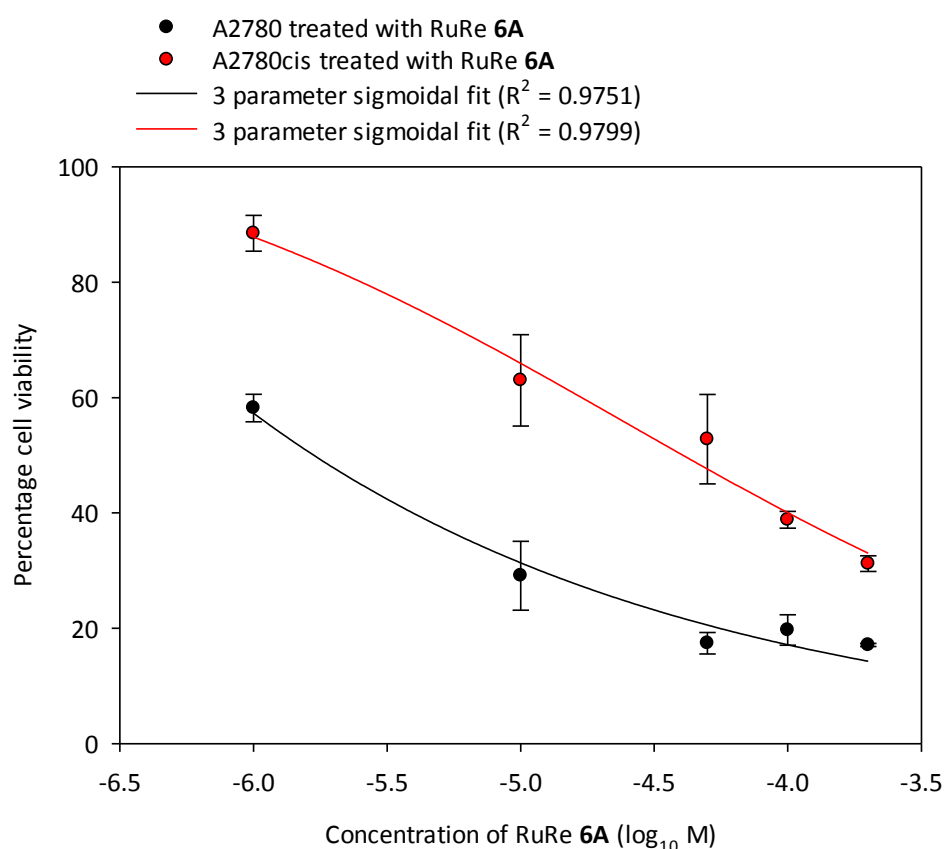
Cell Line	RuRe macrocycle **6A** IC_{50} (μM)
A2780	2
A2780cis	59

Figure 4.10 – Cell viability data for RuRe macrocycle **6A**

Using a macrocycle concentration range of 0.1 - 50 µM, its phototoxicity against the A2780 cell line was assessed (*Figure 4.11*). In these conditions the macrocycle did show phototoxic activity but, with treatment in the dark already producing a potent cyctotoxicity response, the increase in toxicity was modest. Despite this small degree of change in the IC_{50} value, at 5 µM there is a distinct phototoxic effect as seen at $\log_{10}(-5.3)$ in the graph below.
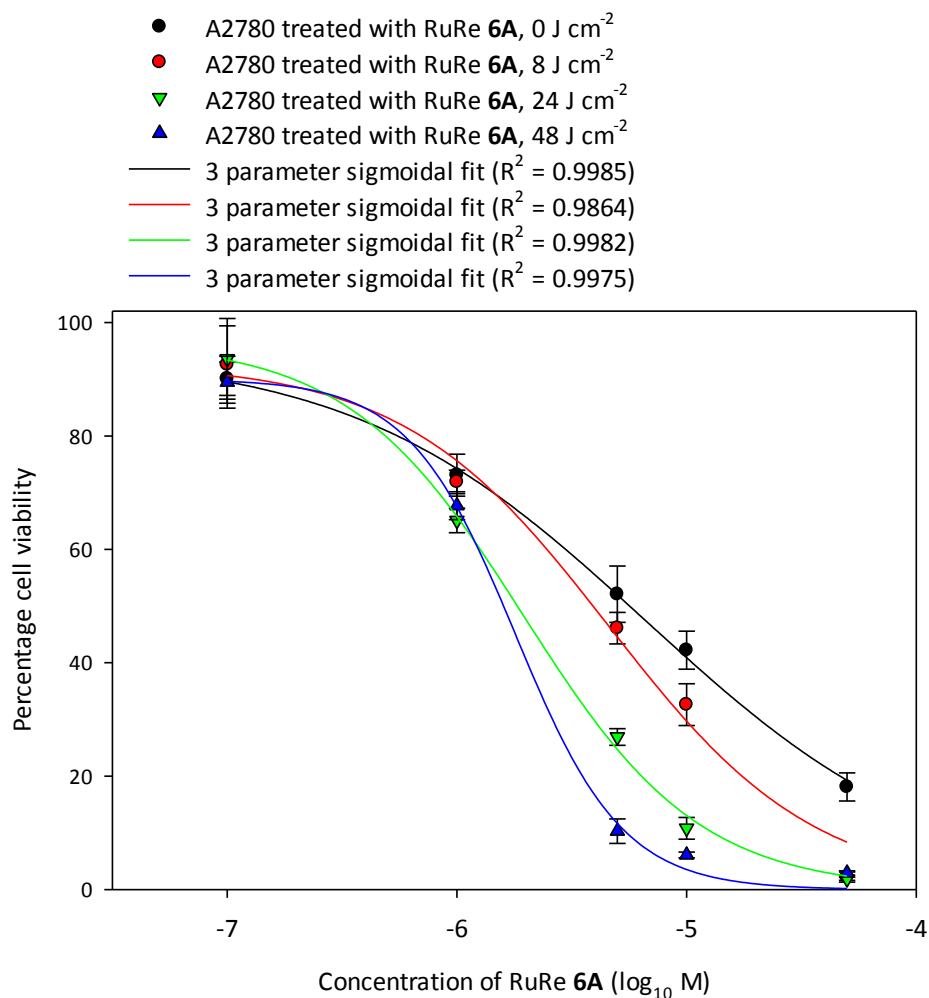
Fluence (J cm^{-2})	RuRe macrocycle 6A IC_{50} (µM)	Percentage Viability at 5 µM RuRe 6A (% metabolising MTT +/- 1 SD)
0	6	52 +/- 5
8	4	46 +/- 3
24	2	27 +/- 1
48	2	10 +/- 2

Figure 4.11 – A2780 cell viability data for RuRe macrocycle 6A upon irradiation

Apart from the promising phototoxic properties of the macrocycle against the A2780 cell line, the low level of classical cytotoxicity against A2780cis in the dark actually gave more reason to investigate phototoxicity with this cell line, as there is a large "toxicity window" in which the dark properties of the macrocycle could be improved upon. A concentration range of 0.1 - 50 μM (plus 100 and 200 μM samples for the dark control) of the macrocycle was tested on A2780 using the now established phototoxicity protocol (*Figure 4.12*).
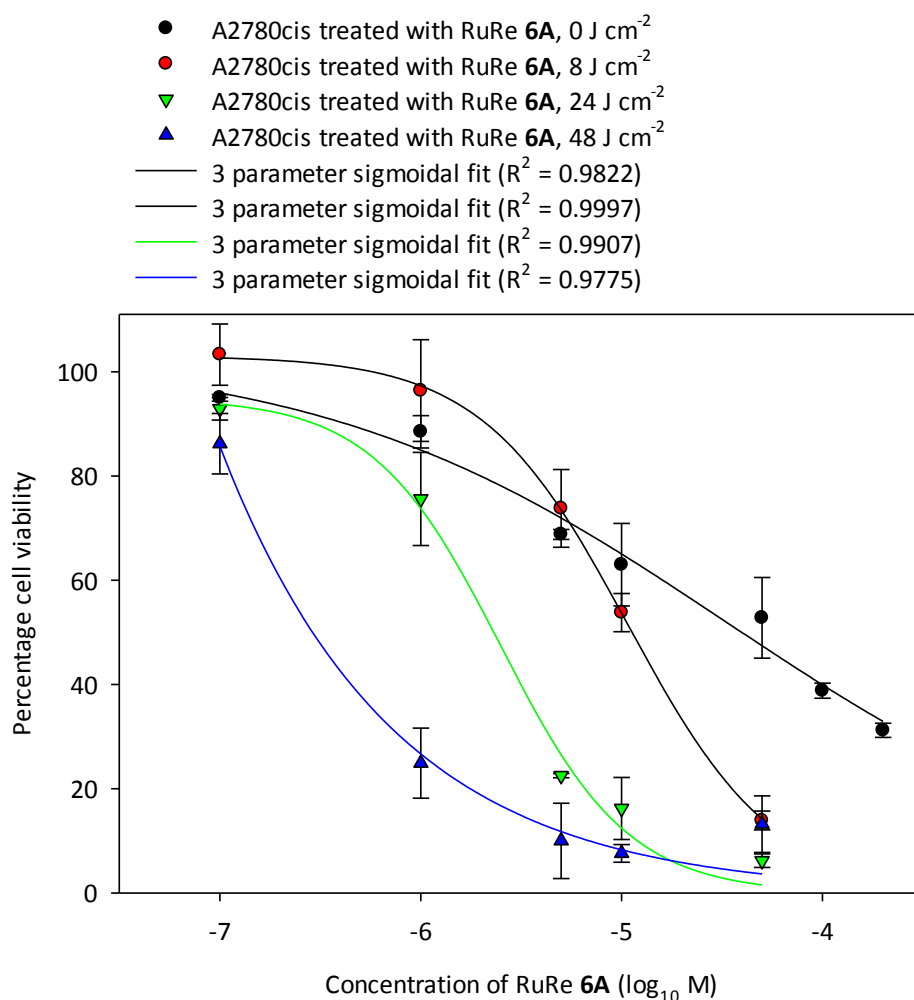
Fluence (J cm⁻²)	RuRe macrocycle 6A IC₅₀ (μM)	Percentage Viability at 10 μM RuRe 6A (% cells metabolising MTT +/- 1 SD)
0	58.9	63 +/- 8
8	12.0	54 +/- 4
24	2.2	16 +/- 6
48	0.4	8 +/- 2

Figure 4.12 – A2780cis cell viability data for RuRe macrocycle 6A upon irradiation

This cell line showed a much more notable phototoxic response with a decrease in IC_{50} values from 58.9 μM in the dark to 0.4 μM after an exposure of 48 J cm^{-2}. This experiment was then repeated, but with a concentration range of 0.1 – 100 μM for both the macrocycle and the ruthenium monomer unit side by side. This experiment showed a noticeable difference in the activity between monomer and macrocycle, with the macrocycle at the higher concentrations becoming markedly more cytotoxic upon irradiation than the monomer – clearly indicating that the macrocycle is more phototoxic than the monomer. In addition to the differing IC_{50} values, the full extent of the contrasting phototoxicity can be seen by cell viability bar charts of macrocycle and monomer data side by side (*Figure 4.13*).
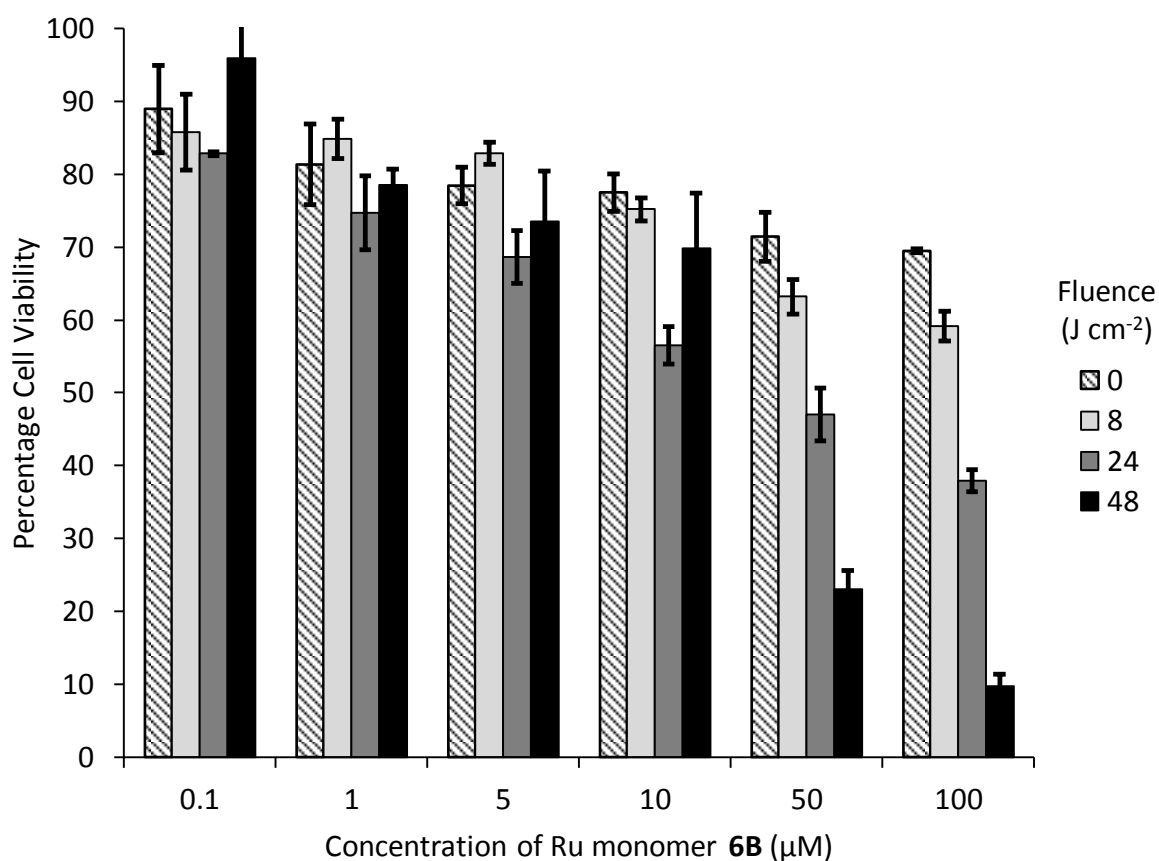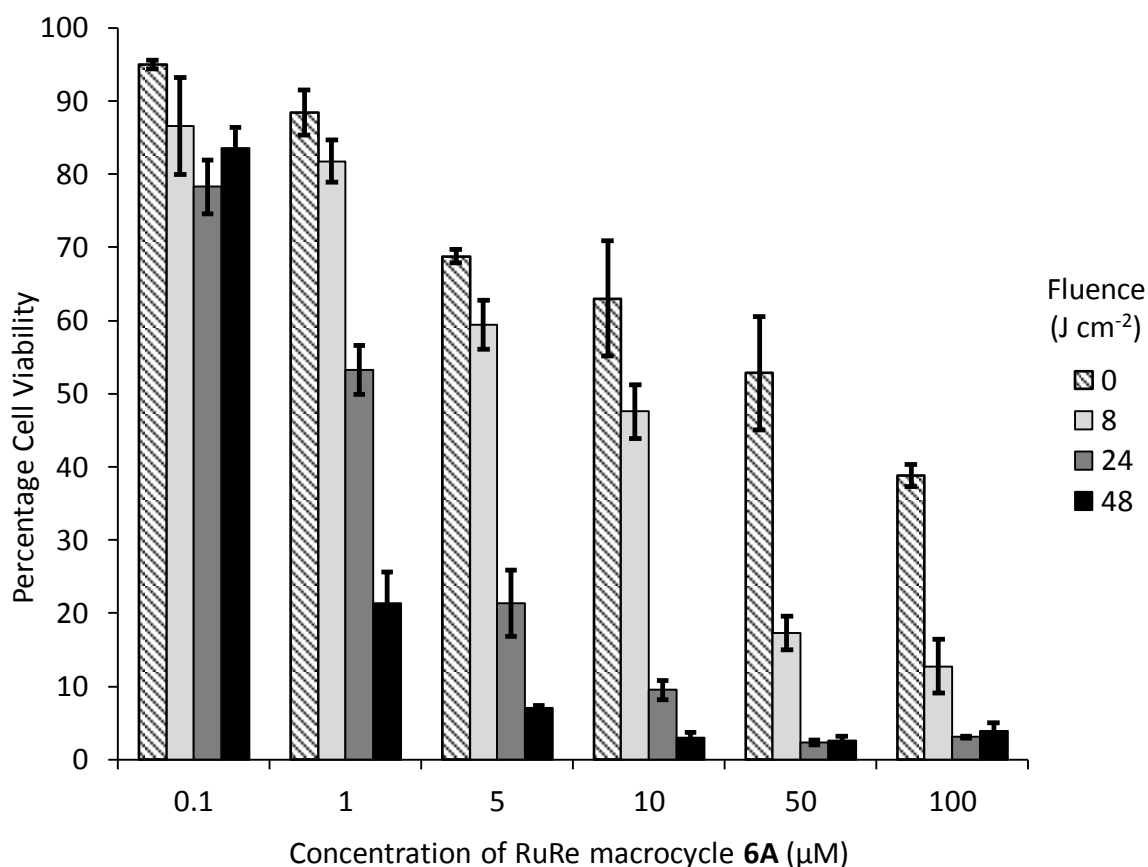
Fluence (J cm^{-2})	RuRe macrocycle 6A IC$_{50}$ (μM)	Ru monomer 6B IC$_{50}$ (μM)
0	58.7	>50
8	8.7	>50
24	1.2	30.2
48	0.3	19.5

Figure 4.13 – A2780cis cell viability data for RuRe **6A** and Ru **6B** upon irradiation

This photoactivation by a low light dose indicates a promising photophysical profile for potential PDT applications. Metal directed self-assembly is a very active field of research and the interactions of various architectures with biomolecules have been investigated, for example the cage systems of the Therrien group have been used as delivery vectors for DNA probes and therapeutics including PDT sensitizers,[8,9] and although the mechanisms are unknown, some metallocages have proven to be independently cytotoxic.[10] That said, the RuRe macrocycle **6A** is the first intrinsically phototoxic example of such architecture. Previously it has been shown to bind to biomolecules with high affinity, and similar Ru[II] and

Re^I mononuclear units are known to have rich photochemistry, but this is the first example of a PDT agent constructed by metal-directed self-assembly.

To compare the intracellular accumulation between Ru macrocycle **6A** and Ru monomer **6B**, inductively coupled mass spectrometry (ICP-MS) analysis of metal content was used after treatment with 50 and 100 µM complex concentrations for 12 hours (*Figure 4.14*).
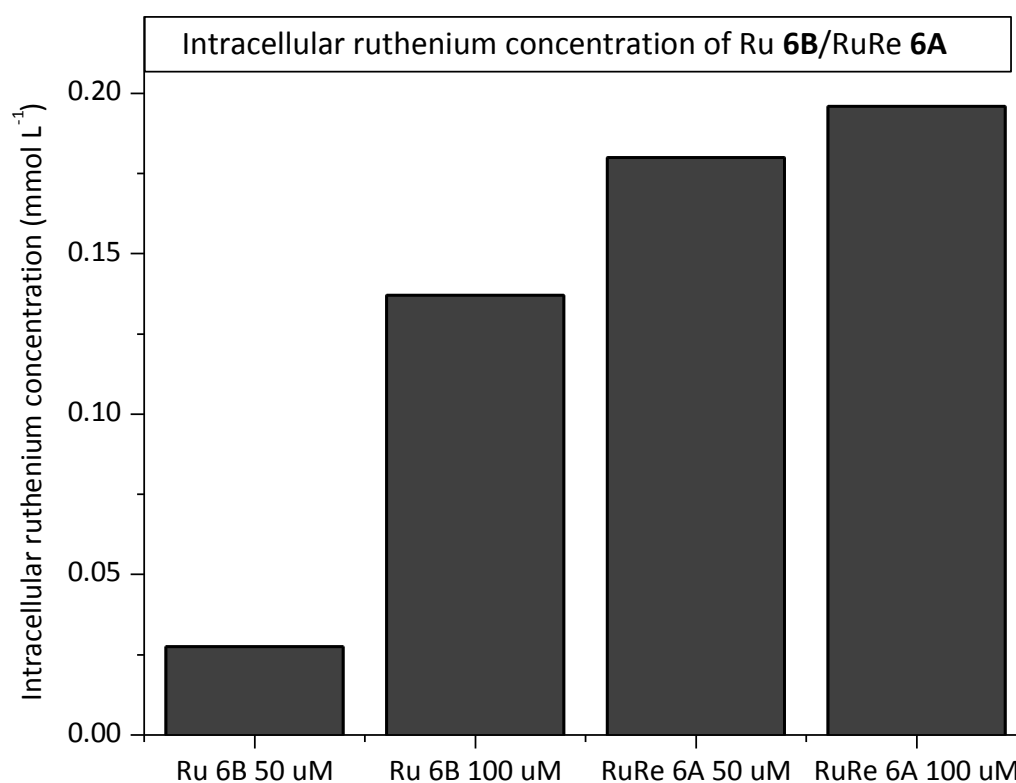
Complex	Intracellular metal concentration (mmol L^{-1})
50 µM Ru monomer **6B**	2.75E-02
100 µM Ru monomer **6B**	1.37E-01
50 µM RuRe macrocycle **6A**	1.80E-01
100 µM RuRe macrocycle **6A**	1.96E-01
Control	4.50E-03

Figure 4.14 - Intracellular metal content (ruthenium) data from ICP-MS analysis

This intracellular metal concentration was calculated by taking the initial concentration of ruthenium in µg L^{-1} from the submitted sample and converting it to total number of moles

of complex per sample; from the known volume, relative molecular mass of ruthenium and chemical structure of the complex. The number of moles could then be applied to the previously determined number of cells per sample and finally by using an estimated cell volume assumption of 2 $\times 10^{-12}$ L the intracellular metal concentration could be obtained; presented above in the units of mmol L^{-1}.

From these data two key observations can be made, the first being the clearly increased intracellular accumulation of RuRe macrocycle **6A** versus Ru monomer **6B** at equivalent treatment concentrations by comparing both the 50 µM mono v macro and the 100 µM mono v macro pairing. Comparing the ruthenium concentration after treatment with 100 µM Ru monomer **6B** and 50 µM RuRe macrocycle **6A** (the central 2 columns in *Figure 4.14*), reveals that even when the monomer concentration is double the treated concentration of the macrocycle it has still not reached the same intracellular accumulation.

The second observation is that the difference in intracellular accumulation between the two complexes is much less at the 100 µM concentration (discrepancy of 0.059 mmol L^{-1}, or the monomer accumulation is 70% that of the equivalent macrocycle) than the 50 µM concentration (discrepancy of 0.152 mmol L^{-1}, and in contrast the monomer accumulation is only 15% that of the macrocycle). This observation correlates with the trend in phototoxic activity where there is a greater contrast between monomer and macrocycle at 50 µM than 100 µM; indeed after a 100 µM treatment with Ru monomer **6B** appreciable phototoxic activity is observed (although this is seen at *much* lower concentrations for the macrocycle).

4.5 Summary

The molecules that have been investigated for phototoxicity show a varied response which can be seen in the table summarising the dark IC_{50}, light IC_{50} and phototoxic index (PI) of complexes **3**-**6** against the cell line A2780cis (*Figure 4.14*).

Complex	dark IC_{50} (µM)	light IC_{50} (µM)	PI
RuRe **3**	18	3	6
RuPt **4**	100	46	2
RuRe bis-intercalator **5**	110	56	2
RuRe macrocycle **6A**	59	0.3	197

Figure 4.15 – Table summarising the PI of complexes **3**-**6**

Although RuPt **4** and RuRe bis-intercalator **5** showed low light-dependant activity with a PI of 2, the ruthenium-rhenium complex RuRe **3** has a modest PI of 6, which nonetheless offers some promise as a lead for related compounds. The greatest phototoxicity with a PI of 197 was observed for the RuRe macrocycle **6A** which, at the highest dosage of light, far exceeds the toxicity of cisplatin against a cell line with increased resistance.

4.5 References

1. Yam, V. W.-W., Lo, K. K.-W., Cheung, K.-K. & Kong, R. Y.-C. Synthesis, photophysical properties and DNA binding studies of novel luminescent rhenium(I) complexes. X-Ray crystal structure of [Re(dppn)(CO)3(py)](OTf). *J. Chem. Soc. Chem. Commun.* **937,** 1191 (1995).

2. Wing-Wah Yam, V., Kam-Wing Lo, K., Cheung, K.-K. & Yuen-Chong Kong, R. Deoxyribonucleic acid binding and photocleavage studies of rhenium(I) dipyridophenazine complexes. *J. Chem. Soc. Dalt. Trans.* **14,** 2067–2072 (1997).

3. Stoeffler, H. D., Thornton, N. B., Temkin, S. L. & Schanze, K. S. Unusual photophysics of a rhenium (I) dipyridophenazine complex in homogeneous solution and bound to DNA. *J. Am. Chem. Soc.* **117,** 7119–7128 (1995).

4. Dougherty, T. J. *et al.* Photodynamic Therapy. *J. Natl. Cancer Inst.* **90,** 889–905 (1998).

5. Detty, M., Gibson, S. & Wagner, S. Current clinical and preclinical photosensitizers for use in photodynamic therapy. *J. Med. Chem.* **47,** 3897–3915 (2004).

6. Howerton, B. S., Heidary, D. K. & Glazer, E. C. Strained Ruthenium Complexes are Potent Light-Activated Anticancer Agents. *J. Am. Chem. Soc.* **134,** 8324–8327 (2012).

7. Foxon, S. P. *et al.* A multifunctional light switch: DNA binding and cleavage properties of a heterobimetallic ruthenium-rhenium dipyridophenazine complex. *Angew. Chemie - Int. Ed.* **46,** 3686–3688 (2007).

8. Therrien, B. Transporting and shielding photosensitisers by using water-soluble organometallic cages: A new strategy in drug delivery and photodynamic therapy. *Chem. - A Eur. J.* **19,** 8378–8386 (2013).

9. Schmitt, F. *et al.* Organometallic cages as vehicles for intracellular release of photosensitizers. *J. Am. Chem. Soc.* **134,** 754–757 (2012).

10. Therrien, B. Biologically relevant arene ruthenium metalla-assemblies. *CrystEngComm* **17,** 484–491 (2015).

Chapter 5

Conclusions and Future Work

5.1   Conclusions

By addressing the original aims of this project, the studies presented in this thesis have produced interesting results that span the interface of chemistry and cell biology. Originating in chemistry, the syntheses of complexes **1 – 4** were achieved and *in vitro* studies established that they were all capable of binding to DNA, which induced a light switch effect. This association occurs through different binding modes: Ru(tpphz) **1** intercalates between the base pairs whilst RuRe **3** is a groove binder; which is not surprising with the molecular shape of the rhenium unit deviating from a planar arrangement. These findings led to the hypothesis that DNA binding occurs in the cellular environment, although there could still be other intracellular targets in addition to or in place of DNA.

The interdisciplinary nature of the investigation resulted in assays being conducted for anticancer activity and it found all complexes induce a cytotoxic response in the cisplatin sensitive/resistant model A2780/A2780cis cell line. The potency and cross-resistance profiles of the four complexes varied, with a clear series from most toxic to least toxic of Ru(tpphz) **1** > Ru(taptp) **2** > RuRe **3** > RuPt **4**. The lack of cross-resistance between A2780 and A2780cis (which usually shows 10 fold resistance against cisplatin) was apparent for both mononuclear complexes Ru(tpphz) **1** and Ru(taptp) **2**. Time lapse microscopy experiments involving cells treated with the complexes revealed a likely oncotic mode of cell death. Notably widespread luminescence associated with DNA was only observed after this cell death pathway had significantly proceeded. A whole-proteome analysis employing SILAC techniques to investigate the expression response of the cell line A2780cis before and after treatment with complexes Ru(tpphz) **1** and Ru(taptp) **2** did not reveal any conclusive evidence of particular intracellular mechanisms although it did reveal a distinct lack of caspase up-regulation indicating that apoptosis can probably be ruled out.

Toxicity studies were extended to investigate the light dependence of toxicity for complexes RuRe **3**, RuPt **4**, and two separately synthesised compounds RuRe bis-intercalator **5** and RuRe macrocycle **6A**; after the protocol was optimised whilst examining the latter complex. This uncovered phototoxic activity in the complex RuRe **3**, which although only modest (PI = 6), was greater than that for RuPt **4** (PI = 2) and the potential bis-intercalator RuRe **5** (PI = 2).

In stark contrast the PI of macrocycle **6A** was very high with an approximate 200-fold increase in cytotoxicity under the highest dose of light, which places it in a similar bracket to current photodynamic therapy agents. Further to this, the corresponding mononuclear ruthenium monomer **6B** differed in activity and was much less potent, demonstrating an interesting contrast between monomer and macrocycle activity.

Further work, described below, will increase the impact of the main focus of this study by elucidating much more mechanistic detail for the cytotoxic action of Ru(tpphz) **1** and Ru(taptp) **2** in particular.

5.2 Future Work

Despite considerable progress in discovery and development of targeted agents exploiting the molecular basis of cancer, such agents are less effective in more common solid tumours. Cytotoxic agents continue to be of major importance in treatment of many cancers. Platinum(Pt)-based drugs are currently the most used cancer therapeutics in certain settings. It is estimated that 50-70% of all cancer patients have been treated with a Pt-based drug. The cellular target of these drugs is DNA, with the complex forming guanine adducts. Patients often have a high initial response to Pt-based chemotherapy, but subsequently become refractory, and many die with progressive chemo-resistant disease. Inherent and acquired drug resistance, involving changes in ion transporter expression and alterations in the DNA damage response, is very common and alternative therapies to address this issue are urgently required.

Metal coordination complexes can exhibit reactivity not possessed by either metal or organic ligands alone. Such reactivity may be fine-tuned by changes in properties of bound ligand or by variations in metal and oxidation state, and in the case of Ruthenium (Ru) which allows for more varied co-ordination geometries than Pt, provides a highly versatile platform offering significant potential for innovative drug discovery, design and development. My PhD studies have identified several potential leads with cytotoxicities

comparable to that of cisplatin but importantly, maintain this potency in cancer cells previously exposed to, and having an increased tolerance of, cisplatin.

Treatment with Pt-based drugs results in the evolution of tumour cell resistance. Mechanistic analysis of a new generation of Ru(II)-based compounds with cytotoxic activity comparable to cisplatin, but which show no cross-resistance in cisplatin-resistant cells will inform progression of this important, chemically tractable class of compounds for therapeutic development.

In the next steps on this project a range of cell biology approaches will be used to (i) understand the molecular basis for the variation in cytotoxic potency of complexes **1 – 4**, with the goal of understanding the structure-activity relationships and uptake mechanisms governing cytotoxicity of this series of compounds, (ii) identify molecular mechanisms by which complexes **1 – 4** induce cell death in cisplatin-resistant cancer model cells, and (iii) identify intracellular signalling pathways activated following exposure to complexes, as a means to identify the primary target of complexes Ru(tpphz) **1** and Ru(taptp) **2**, all of which are esssential to progress complexes into candidate leads for theraputic drug development. The experimental plan in more detail will be as follows.

i) The molecular basis for the variation in cytotoxic potency of complexes **1 – 4**:

(A) This will involve use of inductively coupled mass spectrometry (ICP-MS) to determine intracellular levels of each complex over time to establish whether alterations in uptake characteristics explain differences in cytotoxic potency of complexes **1 – 4**.

(B) To establish the identity of the transporter(s) responsible for the cytotoxic efficiency of Ru(tpphz) **1**, a siRNA screen of the human SLC transporter family will be undertaken, utilising the siRNA Screening Facility in the department of Biomedical Science. This technology determines extent of uptake in each case by analysis of the aggregate luminescence following each individual transporter knockdown. Once a specific transporter or subset of transporters has been identified, experiments will be designed to establish whether a single transporter is responsible for the variable uptake efficiency of complexes **1 – 4**, or whether complexes **2 – 4** are taken into cells by a different, or additional, sub-family of transporters.

ii) As outlined the initial studies presented in this thesis indicate induced cell death is through oncosis, full determination of the mechanism of cell death will require more extensive studies. Three major morphological types of cell death can be distinguished: apoptosis, autophagy and oncosis. Following treatment, these may be distinguished by microscopy and the use of key biochemical markers. In order to establish which pathway(s) complexes **1 – 4** act to induce cell death, complex-treated cells will be monitored for the timely appearance of key markers of apoptosis (activated caspase 3; appearance of DNA single-strand breaks, determined by Western blotting) autophagy, (immunofluorescence microscopical analysis of Beclin II and LC3-II) or oncosis (time-lapse microscopy of cell and mitochondrial membrane swelling).

iii) Identification of intracellular signalling pathways activated following exposure to complexes: To build upon the initial SILAC study and gain a more detailed insight into mechanisms by which complexes induce cell death, quantitative phosphoproteomics, a method of characterising proteins subject to post-translational modifications through phosphorylation (a reversible modification that determines protein function and localisation) will be employed. These data will provide insight into molecular signaling events preceding death revealing how complexes **1 – 4** exert their anti-cancer effect.

Chapter 6

Experimental

6.1 General

6.1.1 Techniques

All reactions were carried out under a nitrogen atmosphere unless otherwise stated. Reaction vessels containing solid starting materials underwent three cycles of alternating exposure to reduced pressure and nitrogen flow prior to solvent addition; as per Schlenk line techniques.

6.1.2 Chemicals

All chemicals were brought from commercial sources and used as supplied unless stated. Ruthenium complexes were treated as toxic.

6.1.3 Nuclear Magnetic Resonance Spectroscopy (NMR)

^{1}H NMR spectra were recorded on a Bruker AM250 machine working in Fourier transform mode. The following abbreviations are used in the annotation of 1H spectra: s = singlet, d = doublet, dd = doublet of doublets, t = triplet, tt = triplet of triplets, q = quintet and m = multiplet.

6.1.4 Mass Spectroscopy (MS)

Fast-atom bombardment (FAB) mass spectra (MS) were recorded on a Kratos MS80 mass spectrometer working in positive ion mode.

6.1.5 Elemental microanalysis

CHN analyses were acquired using a Perkin Elmer 2400 CHN elemental analyser.

6.2   Synthesis

6.2.1   1,10-phenanthroline-5,6-dione

(DPQ) [1]
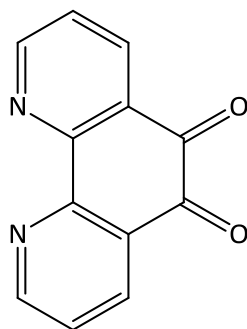
To a solution of 1,10-phenanthroline (2.73 g, 15.16 mmol) in 60% sulfuric acid, potassium bromate (2.75 g, 16.47 mmol) was added in batches over a period of 30 minutes and stirred at room temperature for 20 hours. The solution was poured over ice and carefully neutralised to pH 7 using a saturated solution of sodium hydroxide. The solution was then filtered, extracted with dichloromethane and evaporated to dryness. The crude product was recrystallised from methanol and dried *in vacuo* to yield a bright yellow solid (2.88 g, 13.71 mmol, 87.8 %).

^{1}H NMR (400 MHz, CDCl$_3$) δ 9.14 (dd, *J* = 1.8, 4.7 Hz, 2H), 8.53 (dd, *J* = 1.8, 7.9 Hz, 2H), 7.62 (dd, *J* = 4.7, 7.8 Hz, 2H).

6.2.2　1,10-phenanthroline-5,6-dioxime

(phen-dioxime) [2]
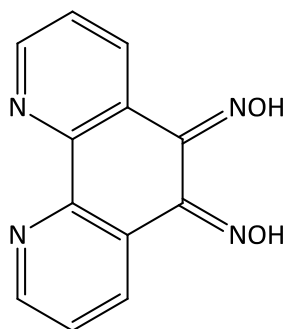
A mixture of 1,10-phenanthroline-5,6-dione (1.15 g, 5.50 mmol), hydroxylammonium chloride (1.35 g, 19.3 mmol) and barium carbonate (1.66 g, 8.25 mmol) were placed in ethanol and stirred under reflux for 12 hours. After removal of the solvent, the residue was treated with 40 mL of 0.2M HCl, stirred for 30 minutes, collected by filtration, washed with water and ethanol and dried *in vacuo* to give a pale green solid (1.32 g, 7.14 mmol, 77.0 %).

^{1}H NMR (400 MHz, DMSO-d[6]) δ 8.80 (m, 3H), 8.28 (dd, *J* = 1.7, 8.0 Hz, 1H), 8.22 (dd, *J* = 1.7, 7.9 Hz, 1H), 7.55 (m, 3H).

MS; m/z (%): 241 (100) [MH]$^+$.

6.2.3 1,10-phenanthroline-5,6-diamine

(phen-diamine) [2]
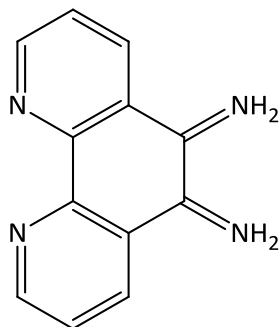
1,10-phenanthroline-5,6-dioxime (0.50 g, 2.090 mmol) and Pd/C (10%, 0.55 g) were added to ethanol (300 mL, anhydrous) and purged with N_2. The mixture was then heated to reflux under N_2 and a solution of hydrazine monohydrate (9 mL) in ethanol (36 mL, anhydrous) was added over a period of 1 hour, before allowing the reflux to continue for a further 12 hours. The solution was then filtered through a hot pad of celite and washed with boiling ethanol until the filtrate was colourless. The solvent was removed from the filtrate under reduced pressure and the residue triturated with water (30 mL) and left for 16 hours at 4°C. The solid was separated by filtration, washed with cold water and dried *in vacuo* to give a brown solid (0.291 g, 1.391 mmol, 66.6 %).

^{1}H NMR (400 MHz, DMSO-d[6]) δ 8.78 (dd, *J* = 1.4, 4.1 Hz, 2H), 8.49 (dd, *J* = 1.5, 8.4 Hz, 2H), 7.61 (dd, *J* = 4.2, 8.4 Hz, 2H), 5.25 (s, 4H).

MS; m/z (%): 211 (100) [MH][+].

6.2.4 tetrapyrido[3,2-a:2',3'-c:3'',2''-h:2''',3'''-j]phenazine (tpphz) [(3)]
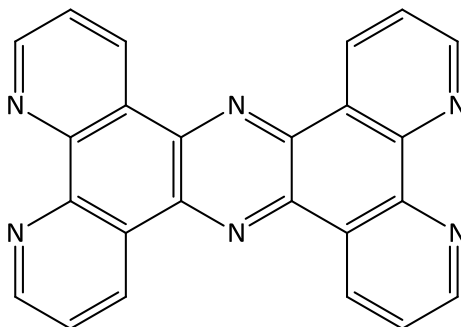
A mixture of 1,10-phenanthroline-5,6-dione (0.88 g, 4.19 mmol), ammonium acetate (4.56 g, 59.16 mmol) and sodium sulphite (0.091 g, 0.72 mmol) in ethanol (15 mL, anhydrous) was heated to reflux under N_2 for 2 hours. After cooling to room temperature water (20 mL) was added and the viscous precipitate collected by filtration, washed with water, methanol and acetone before being triturated in refluxing ethanol (100 mL), hot filtered, washed with ethanol and dried *in vacuo* to give a pale yellow solid (0.177 g, 0.46 mmol, 22.0 %).

^{1}H NMR (500 MHz, TFA-d) δ 10.34 (dd, *J* = 0.9, 8.2 Hz, 4H), 9.38 (dd, *J* = 0.8, 4.9 Hz, 4H), 8.44 (dd, *J* = 5.1, 8.2 Hz, 4H).

MS; m/z (%): 385 (100) [MH][+].

6.2.5   *4,5,9,18*-tetraazaphenanthrenotriphenylene

(taptp) [4]
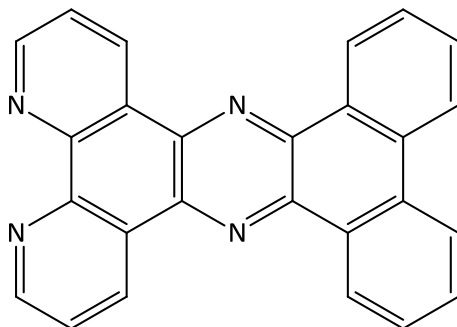
1,10-phenanthroline-5,6-diamine (0.21 g, 1.0 mmol) and 9-10-phenanthroquinone (0.21 g, 1.0 mmol) were purged with N_2, mixed in ethanol (160 mL, dry) and the solution heated to reflux for 3 hours. The precipitate was collected by hot filtration, washed with boiling ethanol, diethyl ether and dried *in vacuo* to give a light brown solid (0.091 g, 0.24 mmol, 23.7 %).

^{1}H NMR (400 MHz, TFA-d) δ 10.46 (dd, *J* = 1.1, 8.3 Hz, 2H), 9.90 (d, *J* = 8.0 Hz, 2H), 9.50 (d, *J* = 6.3 Hz, 2H), 9.29 (d, *J* = 4.9 Hz, 2H), 9.09 (d, *J* = 7.8 Hz, 2H), 8.55 (q, *J* = 4.5 Hz, 2H), 8.28 (m, *J* = 4.1 Hz, 2H), 7.71 (td, *J* = 7.4, 31.0 Hz, 2H).

MS; m/z (%): 383 (55) [MH][+].

6.2.6   [Ru(phen)₂Cl₂]

(Ru-phen) [5]
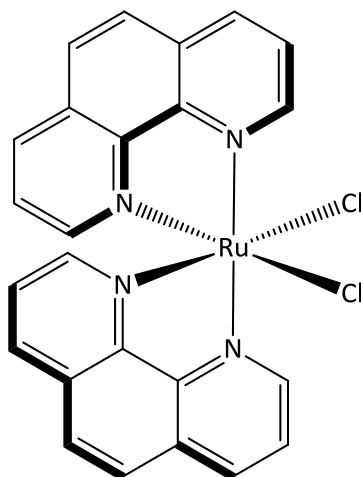
RuCl$_3$.xH$_2$O (0.500 g, 2.41 mmol), phenanthroline (O.687 g, 3.81 mmol) and LiCl (0.458 g, 10.80 mmol) were mixed in DMF (10 mL, anhydrous) and heated to reflux under N$_2$ for 8 hours [Ru(III)/Ru(II) reduction, DMF oxidation]. After cooling to room temperature acetone (50 mL) was added and the solution stored at 0°C for 12 hours. The precipitate was collected by filtration, washed with acetone, water, diethyl ether and dried *in vacuo* to give a black solid (1.258 g, 2.36 mmol, 97.9 %).

MS; m/z (%): 497 (50) [M]$^+$.

6.2.7   [Ru(bipy)₂Cl₂]

(Ru-bipy) [5]
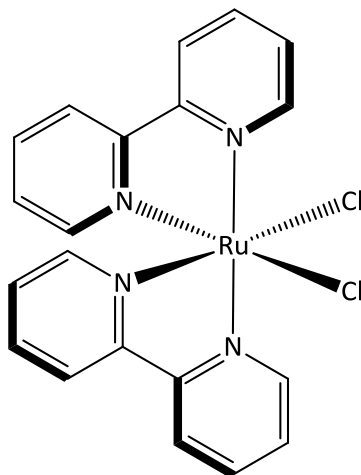
RuCl$_3$.xH$_2$O (1.000 g, 3.84 mmol), 2,2-bipyridine (1.200 g, 3.81 mmol) and LiCl (3.040 g, 24.60 mmol) were mixed in DMF (10 mL, anhydrous) and heated to reflux under N$_2$ for 8 hours [Ru(III)/Ru(II) reduction, DMF oxidation]. After cooling to room temperature acetone (70 mL) was added and the solution stored at 0°C for 12 hours. The precipitate was collected by filtration, washed with acetone, water, diethyl ether and dried *in vacuo* to give a black solid (0.937 g, 1.93 mmol, 50.3 %).

MS; m/z (%): 497 (60) [MH$^+$].

6.2.8   [Ru(phen)₂(DPQ)](PF₆)₂

(Ru-phen-DPQ) [3]
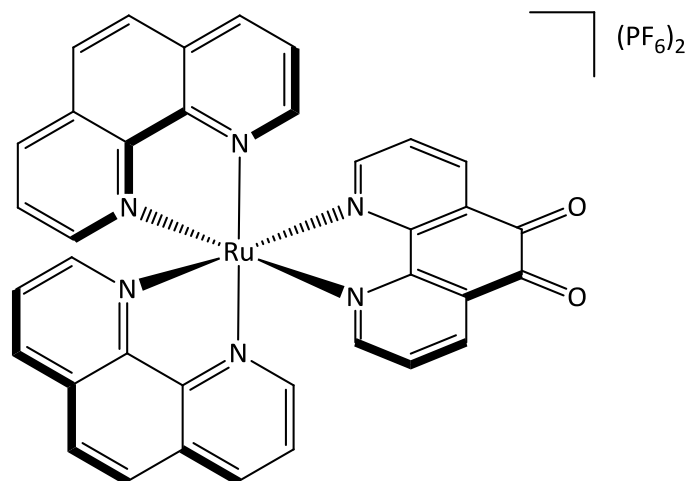
Ru(phen)$_2$Cl$_2$ (0.500 g, 0.94 mmol) and DPQ (0.254 g, 1.21 mmol) were purged with N$_2$, mixed in ethanol:water (1:1, 20 mL, N$_2$ flushed) and the solution heated to reflux under N$_2$ for 3 hours. After cooling to room temperature an aqueous solution of NH$_4$PF$_6$ was added and the resulting precipitate collected by filtration, washed with water, diethyl ether and dried *in vacuo* to give a brown solid (0.370 g, 0.38 mmol, 41.0 %).

^{1}H NMR (400 MHz, CD$_3$CN) δ 8.73 (dd, *J* = 1.1, 8.3 Hz, 2H), 8.61 (dd, *J* = 1.1, 8.3 Hz, 2H), 8.51 (dd, *J* = 1.2, 7.9 Hz, 2H), 8.27-8.35 (m, 6H), 7.93 (d, *J* = 5.2 Hz, 4H), 7.84 (dd, *J* = 5.3, 8.3 Hz, 2H), 7.62 (dd, *J* = 5.2, 8.3 Hz, 2H), 7.51 (dd, *J* = 5.6, 8.0 Hz, 2H).

MS; m/z (%): 817 (50) [M](PF$_6$)$^+$, 336 (100) [M]$^{2+}$.

6.2.9 [Ru(bipy)₂(DPQ)](PF₆)₂

(Ru-bipy-DPQ) [3]
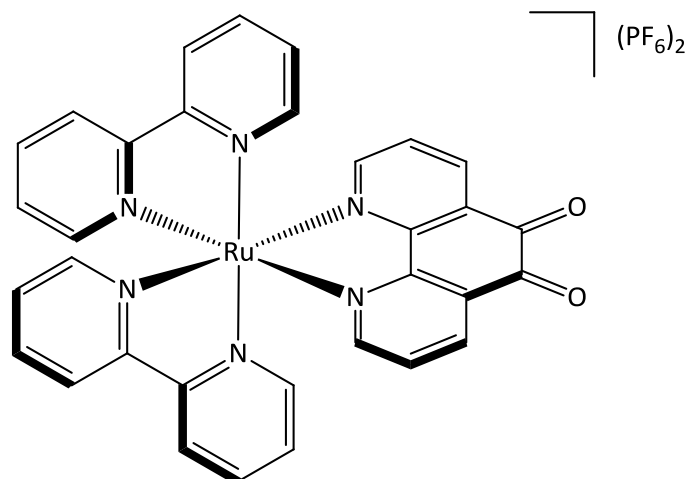
Ru(bipy)$_2$Cl$_2$ (0.400 g, 0.83 mmol) and DPQ (0.174 g, 0.83 mmol) were purged with N$_2$, mixed in ethanol:water (1:1, 20 mL, N$_2$ purged) and the solution heated to reflux under N$_2$ for 3 hours. After cooling to room temperature an aqueous solution of NH$_4$PF$_6$ was added and the resulting precipitate collected by filtration, washed with water, diethyl ether and dried *in vacuo* to give a brown solid (0.609 g, 0.67 mmol, 80.7 %).

^{1}H NMR (400 MHz, CD$_3$CN) δ 8.55 (d, *J* = 8.1 Hz, 3H), 8.11 (tt, *J* = 1.5, 7.9 Hz, 2H), 8.00 (d, *J* = 5.3 Hz, 1H), 7.86 (d, *J* = 5.6 Hz, 1H), 7.77 (d, *J* = 5.6 Hz, 1H), 7.63 (dd, *J* = 5.6, 8.0 Hz, 1H), 7.45 (tq, *J* = 1.4, 7.3 Hz, 2H).

MS; m/z (%): 769 (100) [M](PF$_6$)$^+$, 312 (90) [M]$^{2+}$.

6.2.10   [Ru(phen)₂(tpphz)](PF₆)₂
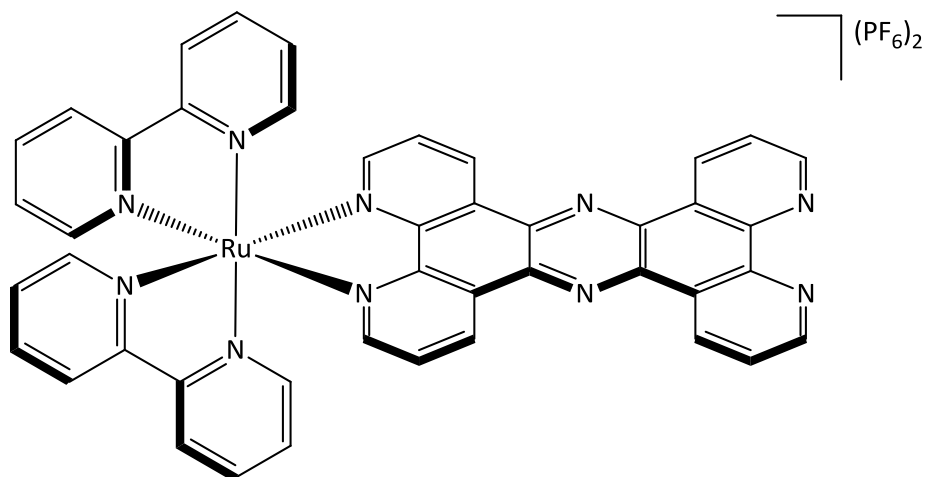
(Ru-phen-tpphz) [3]
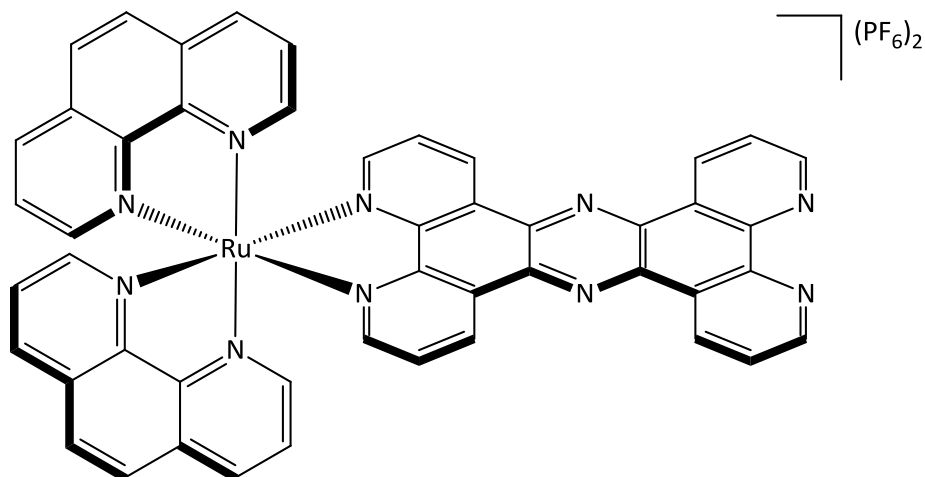
1,10-phenanthroline-5,6-diamine (0.103 g, 0.49 mmol) dissolved in hot methanol (40mL, anhydrous) was added to a boiling solution of [Ru(phen)₂(DPQ)](PF₆)₂ (0.200 g, 0.21 mmol) in acetonitrile (10mL, anhydrous) and heated to reflux under N_2 for 6 hours. After cooling to room temperature the solution was filtered, washed with acetonitrile and to the concentrated filtrate an aqueous NH_4PF_6 solution was added. The resulting precipitate was collected by filtration, washed with water, ethanol, diethyl ether and dried *in vacuo* to give an orange solid (0.171 g, 0.15 mmol, 72.4 %).

^{1}H NMR (400 MHz, CD₃CN) δ 9.65 (d, *J* = 8.0 Hz, 1H), 9.42 (d, *J* = 7.8 Hz, 1H), 8.67 (t, *J* = 8.3 Hz, 1H), 8.53 (s, 1H), 8.33 (s, 2H), 8.24 (d, *J* = 4.8 Hz, 1H), 8.13 (d, *J* = 4.8 Hz, 1H), 7.79 (q, *J* = 6.9 Hz, 3H), 7.71 (dd, *J* = 5.2, 8.3 Hz, 1H).

MS; m/z (%): 991 (100) [M](PF₆)⁺, 423 (100) [M]²⁺.

## 6.2.11 [Ru(bipy)$_2$(tpphz)](PF$_6$)$_2$

(Ru-bipy-tpphz) [3]

1,10-phenanthroline-5,6-diamine (0.266 g, 1.26 mmol) dissolved in hot methanol (135mL, anhydrous) was added to a boiling solution of [Ru(bipy)$_2$(DPQ)](PF$_6$)$_2$ (0.608 g, 0.67 mmol) in acetonitrile (30mL, anhydrous) and heated to reflux under N$_2$ for 6 hours. After cooling to room temperature the solution was filtered, washed with acetonitrile and to the concentrated filtrate an aqueous NH$_4$PF$_6$ solution was added. The resulting precipitate was collected by filtration, washed with water, ethanol, diethyl ether and dried *in vacuo* to give an orange solid (0.4296 g, 0.40 mmol, 59.3 %).

^{1}H NMR (400 MHz, CD$_3$CN) δ 9.62 (dd, *J* = 1.4, 8.1 Hz, 1H), 9.46 (d, *J* = 8.1 Hz, 1H), 8.63 − 8.57 (m, 3H), 8.29 (dd, *J* = 1.2, 5.3 Hz, 1H), 8.18 (td, *J* = 1.4, 8.0 Hz, 1H), 8.10 (d, *J* = 5.4 Hz, 1H), 8.06 (dd, *J* = 1.2, 7.8 Hz, 1H), 7.94 (d, *J* = 5.5 Hz, 1H), 7.90 (dd, *J* = 5.3, 8.1 Hz, 1H), 7.83 (dd, *J* = 4.4, 8.1 Hz, 1H), 7.54 (tt, *J* = 1.3, 7.7 Hz, 1H), 7.37 (tt, *J* = 1.4, 5.8 Hz, 1H).

MS; m/z (%): 943 (100) [M](PF$_6$)$^+$, 399 (100) [M]$^{2+}$.

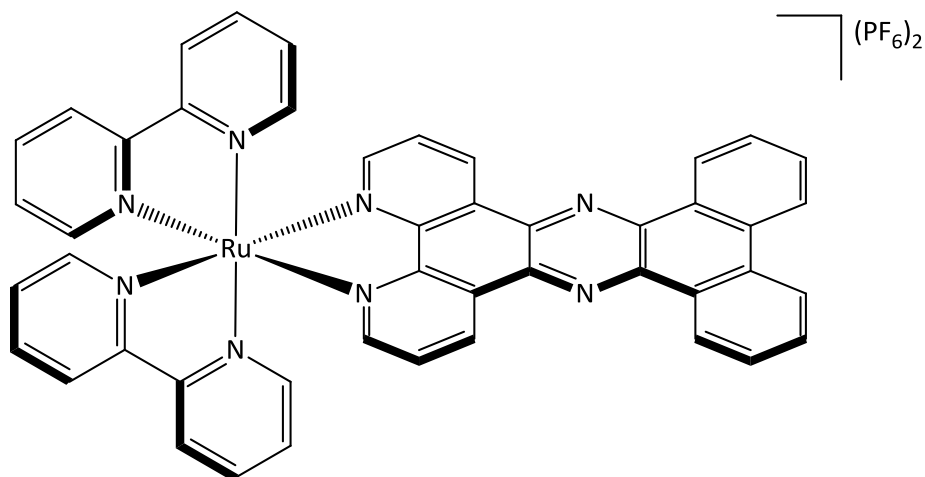## 6.2.12   [Ru(phen)₂(taptp)](PF₆)₂

(Ru-phen-taptp) [4]
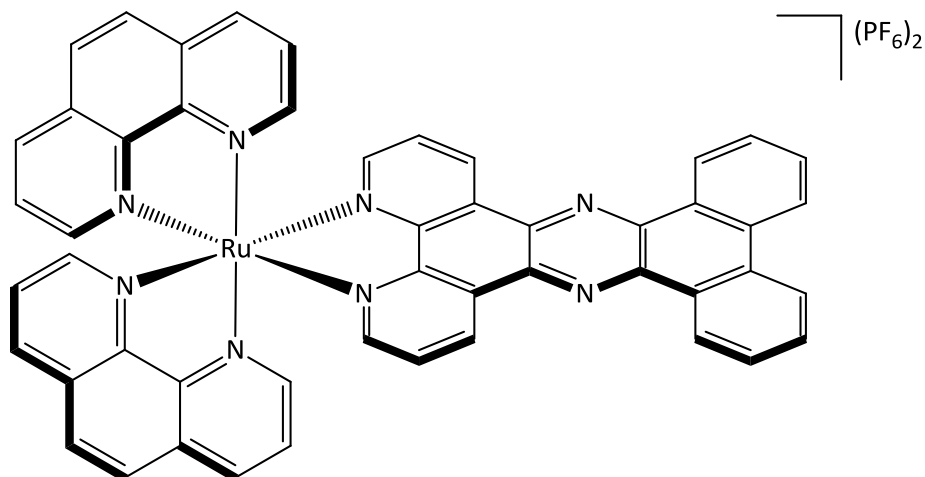
[Ru(phen)$_2$Cl$_2$] (0.26 g, 0.5 mmol) and taptp (0.191 g, 0.5 mmol) in ethylene glycol (100 mL) were heated to 150 °C under N$_2$ for 6 hours. After cooling to room temperature an equal volume of aqueous NH$_4$PF$_6$ solution was added. The resulting brown precipitate was collected by centrifugation, washed with water, ethanol and diethyl ether using the same technique and dried *in vacuo* to give a brown solid (0.362 g, 0.32 mmol, 63.8 %).

^{1}H NMR (400 MHz, CD$_3$CN) δ 9.90 (dd, J = 1.2, 8.2 Hz, 2H), 9.64 (dd, J = 1.3, 7.9 Hz, 2H), 8.83 (d, J = 7.9 Hz, 2H), 8.65 (d, J = 8.3 Hz, 4H), 8.31 (s, 4H), 8.26 (dd, J = 1.2, 5.3 Hz, 2H), 8.19 (dd, J = 1.2, 5.3 Hz, 2H), 8.08 (dd, J = 1.2, 5.2 Hz, 2H), 7.99 (t, J = 6.8, 2H), 7.94 (t, J = 7.1 Hz, 2H), 7.86 (d, J = 8.4 Hz, 1H), 7.85 (d, J = 8.3 Hz, 1H), 7.70 (t, J = 5.3 Hz, 2H), 7.68 (t, J = 5.3 Hz, 2H).

MS; m/z (%): 989 (50) [M](PF$_6$)$^+$, 422 (100) [M]$^{2+}$.

6.2.13 [Ru(bipy)₂(taptp)](PF₆)₂

(Ru-bipy-taptp) [4]

[Ru(bipy)$_2$Cl$_2$] (0.26 g, 0.5 mmol) and taptp (0.191 g, 0.5 mmol) in ethylene glycol (100 mL) were heated to 150 °C under N$_2$ for 6 hours. After cooling to room temperature an equal volume of aqueous NH$_4$PF$_6$ solution was added. The resulting brown precipitate was collected by centrifugation, washed with water, ethanol and diethyl ether using the same technique and dried *in vacuo* to give a brown solid (0.297 g, 0.27 mmol, 54.7 %).

^{1}H NMR (400 MHz, CD$_3$CN) δ 9.95 (dd, *J* = 1.3, 8.2 Hz, 2H), 9.67 (dd, *J* = 1.3, 8.0 Hz, 2H), 8.86 (d, *J* = 8.3 Hz, 2H), 8.58 (d, *J* = 15.2 Hz, 2H), 8.56 (d, *J* = 15.2 Hz, 2H), 8.25 (dd, *J* = 1.2, 5.3 Hz, 2H), 8.16 (dt, *J* = 1.4, 8.0 Hz, 2H), 8.00 (m, 8H), 7.91 (d, *J* = 5.4 Hz, 2H), 7.77 (d, *J* = 5.7 Hz, 2H), 7.51 (t, *J* = 7.2, 2H), 7.28 (t, *J* = 7.4, 2H).

MS; m/z (%): 941 (65) [M](PF$_6$)$^+$, 398 (100) [M]$^{2+}$.

## 6.2.14   [Ru(phen)₂(tpphz)PtCl₂](PF₆)₂

(Ru-Pt-phen)
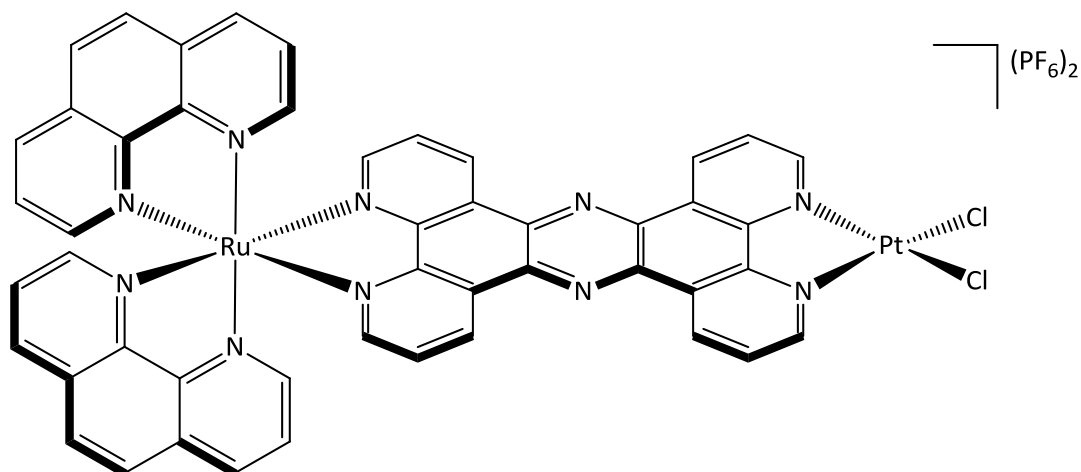
[Ru(phen)$_2$(tpphz)](PF$_6$)$_2$ (0.040 g, 0.035 mmol) and K$_2$[PtCl$_4$] (0.0146 g, 0.035 mmol) were mixed in methanol:water (1:1, 20mL, N$_2$ purged) and heated to reflux under N$_2$ for 12 hours. After cooling to room temperature the methanol was removed under reduced pressure, the precipitate collected by filtration, washed with ethanol, methanol and hexanes. The collected precipitate was dissolved in acetonitrile and re-precipitated by addition of diethyl ether, collected by filtration, washed with ether and dried *in vacuo* to give a brown solid (0.029 g, 0.024 mmol, 69.1 %).

^{1}H NMR (400 MHz, CD$_3$CN) δ 9.84 (d, *J* = 7.7 Hz, 2H), 9.58 (d, *J* = 8.7 Hz, 2H), 9.49 (s, 2H), 8.66 (t, *J* = 8.4 Hz, 6H), 8.52 (s, 2H), 8.32 (t, *J* = 5.6Hz, 8H), 8.21 (t, *J* = 7.8 Hz, 2H), 8.08 (d, *J* = 5.0 Hz, 2H), 7.97 (dd, *J* = 5.5, 8.0 Hz, 2H), 7.69 (dd, *J* = 5.2, 8.4 Hz, 6H).

MS; m/z (%): 1257 (100) [M](PF$_6$)[+], 556 (100) [M][2+].

6.2.15 [Ru(phen)₂(tpphz)Re(CO)₃Cl](PF₆)₂

(Ru-Re-phen)
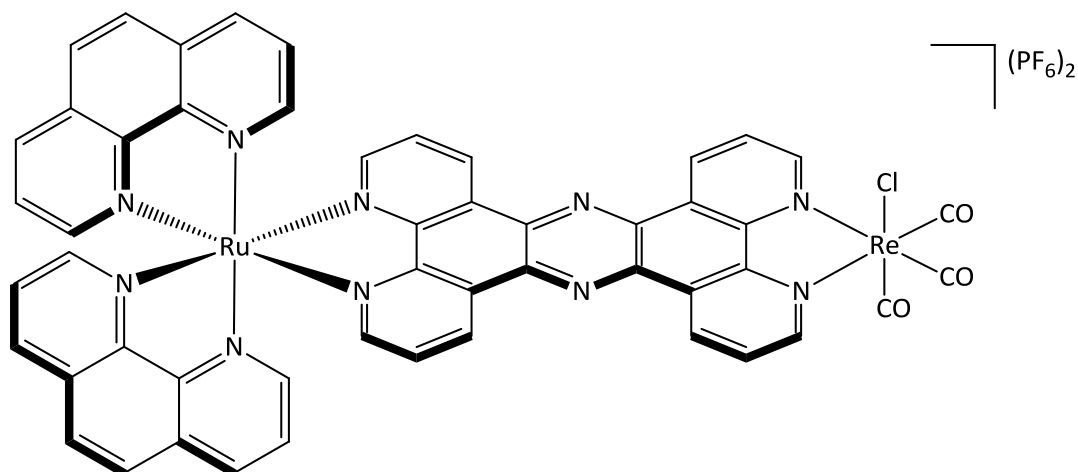
[Ru(phen)$_2$(tpphz)](PF$_6$)$_2$ (0.40 g, 0.35 mmol) and Re(CO)$_5$Cl (0.14 g, 0.39 mmol) were mixed in acetonitrile (100 mL, dry) and heated to reflux under N$_2$ for 16 hours. After cooling to room temperature the volume of acetonitrile was decreased under reduced pressure and the complex was precipitated by addition of diethyl ether. The precipitate was collected by centrifugation, washed with diethyl ether and dried *in vacuo* to give an orange solid (0.28 g, 0.19 mmol, 55.0 %).
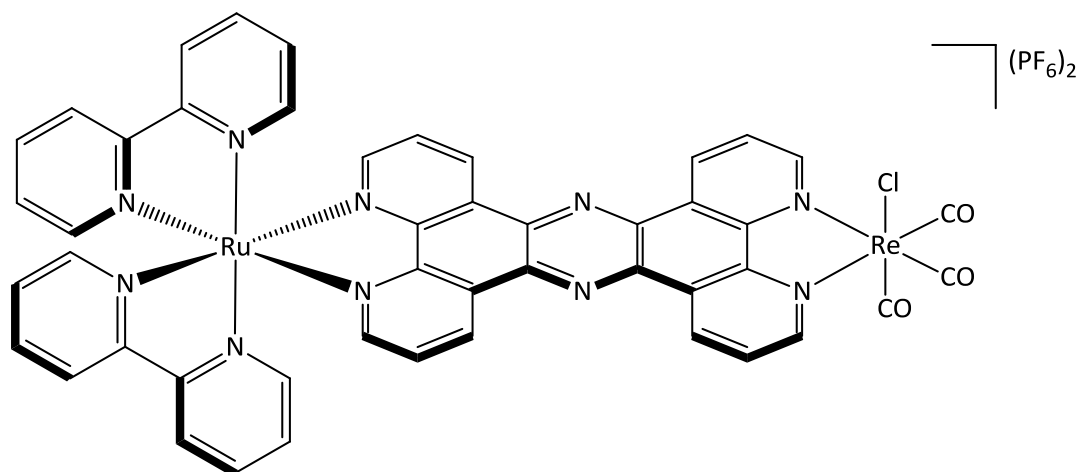
^{1}H NMR (400 MHz, CD$_3$CN): δ 10.12 (t, *J* = 7.5 Hz, 2H), 9.93 (d, *J* = 10.0 Hz, 2H), 9.60 (d, *J* = 5.0 Hz, 2H), 8.67 (d, *J* = 10.0 Hz, 4H), 8.34-8.17 (m, 10H), 8.08 (t, *J* = 5.0 Hz, 2H), 7.94-7.88 (m, 2H), 7.74-7.63 (m, 4H).

MS; m/z: 1297 [M](PF$_6$)[+]. Accurate Mass: Calc. for RuReC$_{51}$H$_{28}$N$_{10}$O$_3$F$_6$PCl [M](PF$_6$)[+]: 1297.0277, Observed: 1297.0260.

Elemental Analysis: Calc. for RuReC$_{51}$H$_{28}$N$_{10}$O$_3$ClP$_2$F$_{12}$: C 42.50; H 1.96; N 9.72. Observed: C 42.75; H 1.61; N 9.83.

6.2.16   [Ru(bipy)₂(tpphz)Re(CO)₃Cl](PF₆)₂

(Ru-Re-bipy)

[Ru(bipy)₂(tpphz)](PF₆)₂ (0.30 g, 0.28 mmol) and Re(CO)₅Cl (0.11 g, 0.30 mmol) were mixed in acetonitrile (80 mL, dry) and heated to reflux under N_2 for 16 hours. After cooling to room temperature the volume of acetonitrile was decreased under reduced pressure and the complex was precipitated by addition of diethyl ether. The precipitate was collected by centrifugation, washed with diethyl ether and dried *in vacuo* to give an orange solid (0.30 g, 21 mmol, 77.9 %).

^{1}H NMR (400MHz, CD₃CN): δ 10.09 (2H, t, *J* = 9.4 Hz), 9.92 (2H, dd, *J* = 6.2 Hz, 3.1 Hz), 9.56 (2H, t, *J* = 1.6 Hz), 8.55 (4H, dd, *J* = 18.8 Hz, 6.2 Hz), 8.28 (2H, t, *J* = 6.2 Hz), 8.18-8.25 (2H, m), 8.13 (2H, t, *J* = 9.4 Hz), 7.97-8.05 (4H, m), 7.86 (2H, t, *J* = 4.7 Hz), 7.77 (1H, d, *J* = 6.2 Hz), 7.71 (1H, d, *J* = 6.2 Hz), 7.49 (2H, t, *J* = 6.2 Hz), 7.23-7.30 (2H, m).

MS; m/z: 1249 [M](PF₆)[+]. Accurate Mass; Calc. for RuReC₄₇H₂₈N₁₀O₃F₆PCl [M](PF₆)[+]: 1249.0277. Observed: 1249.0217.

Elemental Analysis; Calc. for RuReC₄₇H₂₈N₁₀O₃ClP₂F₁₂: C 40.50; H 2.03; N 10.10. Observed: C 40.12; H 1.88; N 9.82.

6.2.17   [(Ru(bipy)₂)₂(tpphz)](PF₆)₄

$[(Ru(bipy)_2)_2(tpphz)](PF_6)_4$

(Ru-Ru-bipy) [3]
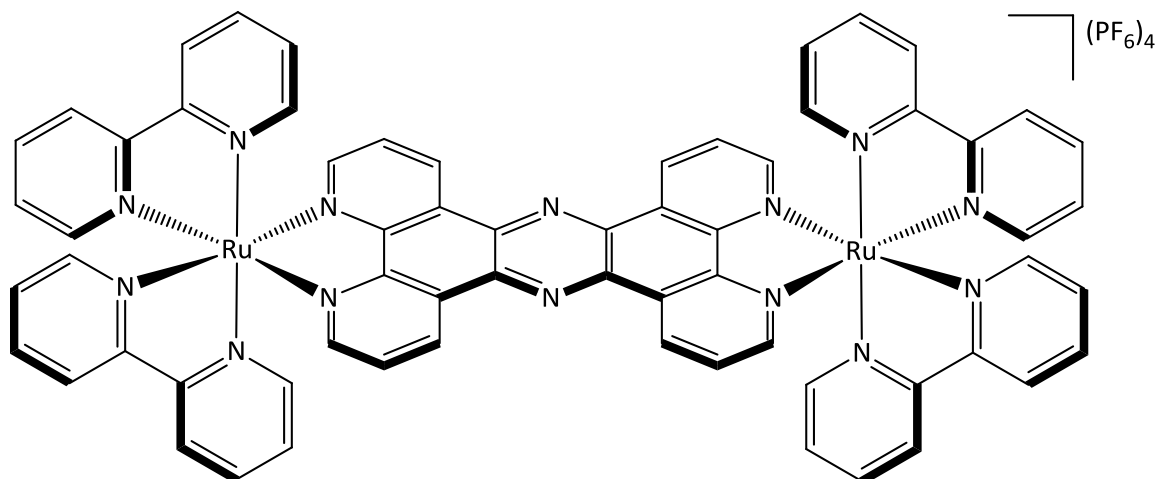
Ru(bipy)₂Cl₂ (0.535 g, 1.10 mmol) and tpphz (0.173 g, 0.449 mmol) were mixed in ethanol:water (1:1, 40mL, N₂ purged) and heated to reflux under N₂ for 12 hours. The solution was cooled to room temperature and stored at 4°C for 16 hours. The solution was filtered, ethanol removed under reduced pressure, filtered again and an aqueous solution of NH₄PF₆ was added to the filtrate. The resulting precipitate was collected by filtration, washed with water and dried *in vacuo*. The crude product was dissolved in acetonitrile and reprecipitated on addition of diethyl ether, collected by filtration, washed with diethyl ether and dried *in vacuo* to give a red solid (0.922 g, 0.51 mmol, 93.2 %).

^{1}H NMR (400 MHz, CD₃CN) δ 9.98 (dd, *J* = 1.2, 8.2 Hz, 2H), 8.58 (dd, *J* = 8.3, 15.5 Hz, 6H), 8.32 (dd, *J* = 1.2, 5.3 Hz, 2H), 8.17 (dt, *J* = 1.4, 7.9 Hz, 2H), 8.08 - 8.01 (m, 6H), 7.90 (d, *J* = 5.0 Hz, 3H), 7.77 (d, *J* = 5.1 Hz, 3H), 7.52 (tt, *J* = 1.3, 5.7 Hz, 2H), 7.29 (tt, *J* = 1.4, 5.9 Hz, 2H).

MS; m/z (%): 1647 [M-PF₆]⁺, 751 [M-2(PF₆)]²⁺, 452 [M-3(PF₆)]³⁺.

6.2.18   Anion Metathesis

For aqueous photochemistry, including DNA binding, and all cellular studies, the chloride complex ($[M]Cl_n$) corresponding to the initially synthesised hexafluorophosphate ($[M](PF_6)_n$) complex was used. The hexafluorophosphate salt of each complex was dissolved in the minimum volume of acetone and a saturated solution of ammonium chloride in acetone added. The resultant precipitated chloride salt was collected by filtration, washed with cold acetone and dried *in vacuo*.

6.3　DNA Binding Studies

6.3.1　DNA Preparation

Calf thymus DNA (CT-DNA) was dissolved in aqueous buffer (25 mM NaCl, 5 mM Tris, pH = 7) and broken into an average of 150-200 base pair fragments by sonication (2 × 15 minutes). The purity of the sample was determined by UV-vis spectroscopy, with $A^{260nm}/A^{290nm} > 1.9$ indicating a protein-free sample. The concentration of CT-DNA was determined by UV-vis spectroscopy ($\varepsilon 280nm = 13200$ M^{-1} cm^{-1}).

6.3.2　Luminescence Titration

A solution of the complex (concentration stated) was dissolved in aqueous buffer (25 mM NaCl, 5 mM Tris, pH = 7.4) and loaded into a quartz cuvette. This was allowed to equilibrate at 25°C for 30 minutes and the emission spectra recorded. $2 - 3$ μL of a concentrated stock CT-DNA solution in aqueous buffer (typically 200 μM) was added and the solution mixed by pipette. The emission spectrum was recorded and whilst showing an enhancement in emission this procedure was continued until the emission became constant.

The maxima of each emission spectrum were then carried forward to calculate the fraction bound. This could then be plotted against the concentration of DNA divided by the concentration of complex to generate a binding curve.

A Scatchard plot[6] could be generated using the McGhee and Von Hippel (MVH) model to account for non-linear deviation associated with the complex overlapping binding site system of DNA base pairs. The MVH equation used in the SigmaPlot 12.0 software was:

$$\frac{r}{C_f} = K \cdot (1 - nr) \left(\frac{1 - nr}{1 - (n-1)r} \right)^{n-1}$$

Data points between a bound ligand fraction of 0.3 and 0.9 were used as the model is inaccurate at high and low concentrations.

6.4 Cellular Studies

6.4.1 Complex preparation

Stock solutions were made up in a solution of one part phosphate buffered saline (PBS) to one part high purity milli-Q® water with sonication and gentle heating (60°C max) to aid dissolution at a high concentration, followed by sterile filtration with a 0.20 µm filter.

6.4.1 Cell Culture

A2780 and A2780cis cell lines were cultured in RPMI-1640 medium. All growth medium was supplemented by 2 mM L-Glutamine, 100 IU ml^{-1} penicillin, 100 µg ml^{-1} streptomycin and 10% v/v fetal bovine serum (FBS). Cultures were grown within the appropriate range of confluence at 37°C in 5% CO_2 / 95% air. Cultures were routinely subcultured using trypsin (0.1% v/v in PBS) at 80 – 90% confluence and used between passage numbers 6 – 60.

6.4.2 Cytotoxicity (MTT assay)

MTT (3-(4,5-dimethylthiazol-2-yl)-2,5-diphenyltetrazolium bromide) was used to determine the cell viability upon treatment with varying concentrations of complex. In the mitochondria of living cells MTT is reduced to a purple formazan product by reductase enzymes. This conversion can only occur in active mitochondria so the amount of formazan produced is directly proportional to the number of viable cells within the culture. The amount of formazan can be quantified by absorbance between 500 – 600nm and the toxicity of a treatment deduced by comparison of the formazan content for exposed cells against that of an untreated control. Different cell cultures can show different enzymatic activity so comparisons drawn are only valid within the assay.

6.4.3 IC$_{50}$ values

Cell cultures were grown on 48 well plates and allowed to grow for 24 hours before treatment with a complex of various concentrations (maintaining a ratio of 10% PBS/H$_2$O: 90% medium throughout all solutions) in triplicate for the given incubation time of 24 or 48 hours. Solutions were removed and the cells incubated with MTT (0.5 mg ml^{-1} dissolved in PBS) for 30 – 40 minutes. The MTT was removed and formazan product eluted using 110 μl/well acidified isopropanol, 100 μl/well of which was transferred to a 96 well plate for the absorbance to be quantified by spectrophotometer (540 nm, referenced at 640 nm). An average absorbance for each concentration was calculated and cell viability was determined as a percentage of the untreated negative control wells (10% PBS/water: 90% medium, average of triplicate). This data was plotted in a graph of concentration against cell viability to produce a curve from which the IC$_{50}$ could be estimated by interpolation.

6.4.4 Light Irradiation Source Apparatus (LISA)

The apparatus used to irradiate the samples was a custom made device featuring a broadband illumination source fully contained in an empty computer base unit, referred to as the Light Irradiation Source Apparatus (LISA). The technical specifications of the bulb contained within are as follows (*Table 1*).

Product Code	871691
International Model Number	HC01080i
Description	CFL 80W E40 Integrated Clusterlite
Watts	80W
Cap	E40
Operating Hours	15000
Colour Temp	4000K
Lumens	5400 lm
Dimming	No
Dimensions (length x diameter)	256mm x 80mm

Table 1 – Specification of the bulb contained within the irradiation apparatus

6.4.5   Photocytotoxicity (phototoxicity)

Cell cultures were grown on 48 well plates at a seeding density of 50,000 cells per well and allowed to grow for 24 hours. The cells were then treated with complex (solubilised in and maintained at 10% PBS/water: 90% medium throughout all solutions) of a 1 – 100 μM concentration range, in triplicate, and incubated for 24 hours. All complex solution (and control media) was removed from the cells and replaced with regular growth medium 30 minutes prior to irradiation. Of the four prepared well plates, one remained in the incubator whilst the other three were exposed to the LISA for the duration of 5, 15 or 30 minutes (corresponding to light doses of 8, 24 or 48 J cm^{-2}) before being incubated for a further 24 hours after culmination of light treatment. All media was then removed and cells incubated with MTT (0.5 mg ml^{-1} dissolved in PBS) for 30 – 40 minutes. The MTT was removed and formazan product eluted using 120 μl/well acidified isopropanol, 100 μl of which was transferred to a 96 well plate for the absorbance to be quantified by spectrophotometer (540 nm, referenced at 640 nm). An average absorbance for each concentration was calculated and cell viability was determined as a percentage of the untreated negative control wells (10% PBS/water: 90% medium, average of triplicate). Data were plotted in a graph of concentration against cell viability to produce a curve from which the IC$_{50}$ value could be derived by interpolation.

6.5   Microscopy

6.5.1   Sample preparation and treatment

Cell culture samples were prepared by first pre-coating 35 mm glass bottomed tissue culture dishes with poly-l-lysine (10 minutes on, aspirate and 5 x PBS wash to remove excess). Dishes were then seeded with cells at a density of 150,000 cells/dish and incubated for 24 hours to allow sufficient adherence.

For all of the experiments carried out in *Section 3.1* the cells had all medium removed, were washed with PBS and the complex added as a 50 µM solution composed of 10% PBS/H_2O:90% medium.

For the DAPI co-stain, the complex was removed after 2 hours, 1x PBS wash, 15 minutes dark incubation with 300 nM DAPI solution followed by 3x PBS wash prior to imaging in PBS.

6.5.2   Imaging

Following treatment with the complex, the cell samples were placed in the live cell microscopy chamber (37 °C and 5% CO_2) and immediately imaged using a 100x plan apochromat (1.4NA) objective lens on a Nikon Ti inverted microscope. Samples were illuminated at 405 nm using a Lumencor spectraX solid state light engine, and emission from the sample at 640–800 nm was collected using an Andor Zyla sCMOS camera. All images were taken using the Nikon Elements software in a programmed cycle of a multiple coordinate set every 2 minutes for 3 hours to construct each time lapse sequence.

A control dish of equally seeded cells having only 10% PBS/H_2O:90% medium replaced with fresh solution before the experiment remained alongside each treated sample experiment in the live cell chamber and was imaged after 3 hours to ensure there was no deterioration of cell morphology in the ambient conditions. In addition, a control experiment was run with an equally seeded dish imaged on the same cycle (multiple coordinate images every 2 minutes for 3 hours) to assess the effects of microscope light exposure.

6.6   SILAC Proteomics

6.6.1   Cell culture

An A2780cis cell line culture was first established in regular RPMI 1640 medium (supplemented by 2mM L-Glutamine, 100 IU ml^{-1} penicillin, 100 µg ml^{-1} streptomycin and 10% v/v dialysed FBS) before being split into two parallel populations which were identically sub-cultured but with one continuing to use the regular RPMI medium and one using SILAC RPMI medium containing labelled amino acids (supplemented with 2mM L-Glutamine, 100 IU ml^{-1} penicillin, 100 µg ml^{-1} streptomycin and 10% v/v dialysed FBS). Labelled SILAC media was used for 6 passages to ensure heavy amino acid incorporation by exceeding the suggested 10-12 cell cycle period. The type of labelling used was the heavy combination featuring both of the amino acid isotopes R10 (L-ARGININE $^{13}C_6$, $^{15}N_4$ HYDROCHLORIDE) and K8 (L-LYSINE-$^{13}C_6$,$^{15}N_2$ HYDROCHLORIDE). Dundee Cell Products was used to purchase all SILAC media and dialyzed FBS with the following catalogue entries and following media composition:

Catalogue Number: DS1002   Description: SILAC Dialysed calf serum (MWCO 10,000 Da)

Catalogue Number: LM021   Description: SILAC RPMI 1640 R10K8

CAS Number	Component	Molecular Weight	Concentration, g/L
AMINO ACIDS			
56-40-6	Glycine	75	0.010
74-79-3	L-Arginine free base (R10 LABELLED)	174	0.200
70-47-3	L-Asparagine anhydrous	132	0.050
56-84-8	L-Aspartic acid	133	0.020
30925-07-6	L-Cystine dihydrochloride	313	0.0652
56-86-0	L-Glutamic acid	147	0.020
70-00-1	L-Histidine	155	0.015
51-35-4	L-Hydroxy-L-Proline	131	0.020
73-32-5	L-Isoleucine	131	0.050
61-90-5	L-Leucine	131	0.050
657-27-2	L-Lysine hydrochloride (K8 LABELLED)	183	0.040
63-68-3	L-Methionine	149	0.015
63-91-2	L-Phenylalanine	165	0.015
147-85-3	L-Proline	115	0.020
56-45-1	L-Serine	105	0.030
72-19-5	L-Threonine	119	0.020
73-22-3	L-Tryptophan	204	0.005
69847-45-6	L-Tyrosine Disodium Salt Dihydrate	261	0.02883

72-18-4	L-Valine	117	0.020
VITAMINS			
67-48-1	Choline chloride	140	0.003
58-85-5	D-Biotin	244	0.0002
137-08-6	D-Ca Pantothenate	477	0.00025
59-30-3	Folic acid	441	0.001
87-89-8	Myo-Inositol	180	0.035
98-92-0	Nicotinamide	122	0.001
150-13-0	P-Aminobenzoic Acid (PABA)	137	0.001
58-56-0	Pyridoxine Hydrochloride	169	0.001
67-03-8	Thiamine Hydrochloride	337	0.001
83-88-5	Riboflavin	376	0.0002
127-47-9	Vitamin A Acetate	328	0.0001
68-19-9	Vitamin B12	1355	0.00001
INORGANIC SALTS			
13477-34-4	Calcium Nitrate Tetrahydrate		0.100
7487-88-9	Magnesium Sulfate Anhydrous	120	0.04884
7447-40-7	Potassium Chloride	75	0.400
7647-40-15	Sodium Chloride	58	6.000
144-55-8	Sodium Bicarbonate	84	2.000
7558-79-4	Sodium Phosphate Dibasic Anhydrous	142	0.8
OTHER COMPONENTS			
70-18-8	L-Glutathione reduced	370	0.001

6.6.2   Cell treatment and lysis

Cell cultures were prepared in 100 mm tissue culture dishes and incubated for 24 hours prior to complex treatment. The cells were treated with complex at the 48 hour IC_{50} concentration but only incubated for 24 hours before all complex solution was removed, samples washed with PBS x3 and treated with lysis buffer. The lysis buffer had the following composition:

6.6.3   Bradford protein assay

The cell lysates were subjected to a Bradford protein assay to determine the protein concentration in each sample. The protocol followed was that produced by Bio-Rad, and first involved generating a standard calibration curve using Bovine Serum Albumin (BSA) through the following steps:

1. Prepare dye reagent by diluting 1 part Dye Reagent Concentrate with 4 parts distilled, deionized (DDI) water.

2. Prepare five dilutions of BSA – 2.000, 1.000, 0.500, 0.250 and 0.125 mg/mL.

3. Pipet 100 μL of each standard solution into a clean, dry disposable polystyrene cuvette, and repeat to assay in triplicate.

4. Add 990 μL of diluted dye reagent to each tube and mix with reverse pipetting.

5. Incubate at room temperature for 5 minutes.

6. Measure absorbance at 595 nm in a spectrophotometer.

A graph was then produced by plotting concentration of BSA against absorbance, and an equation of the subsequent line could be calculated which could be used to determine a protein concentration given an absorbance in this linear range (see below). The protocol was subsequently repeated for the cell lysate samples, which were diluted and each protein concentration determined using a Microsoft Excel worksheet programmed with the equation of the standard calibration line and the appropriate formula calculations.

$y = 1.4939x + 0.0135$
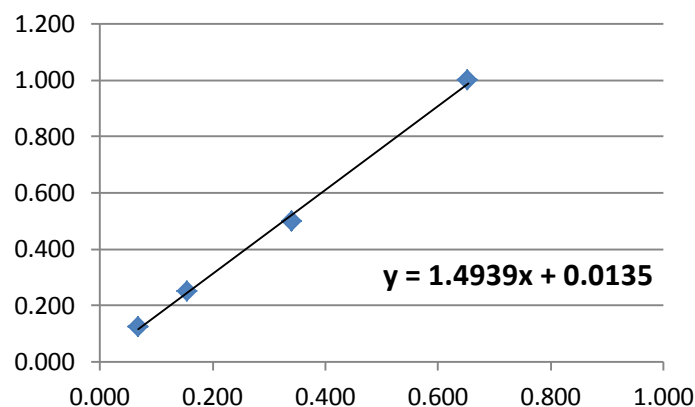
6.6.4   Protein purification (SDS-PAGE)

Cell lysates were subjected to purification by sodium dodecyl sulfate polyacrylamide gel electrophoresis.

Gel Casting

10% acrylamide gels were prepared by firstly creating the resolving gel using the following component quantities; with the ammonium persulfate (APS) and tetramethylethylenediamine (TEMED) added last to initiate gel polymerisation:

Resolving Gel						
Acr %	ddH$_2$O	30% Acrylamide/ Bisacrylamide	Buffer 1.5M TrisHCl, pH 8.8	10% SDS	10% APS	TEMED
10%	4.0 mL	3.3 mL	2.5 mL	100 µL	100 µL	4 µL
Stacking Gel						
Vol.	ddH$_2$O	30% Acrylamide/ Bisacrylamide	Buffer 1.5M TrisHCl, pH 6.8	10% SDS	10% APS	TEMED
5 mL	3.4 mL	0.83 mL	0.63 mL	50 µL	50 µL	5 µL

Polymerisation of the resolving gel was first initiated (with APS and TEMED) before being poured into the gel casting apparatus (5 mL per gel), ethanol added and left to set for 1 hour. The ethanol was then removed, stacking gel polymerisation was initiated (with APS and TEMED), the solution poured on top of the set resolving gel, well comb inserted and left to set for 45 minutes. The comb was then removed and the wells rinsed with running buffer.

Sample Preparation

Sample buffer was made according to the following concentrated formula, which was then diluted 5 fold with MQ H$_2$O and 50 µL β-mercapto ethanol added to 950 µL diluted sample buffer before application:

Concentration	ddH$_2$O	Buffer 0.5M TrisHCl, pH 6.8	Glycerol	SDS	Bromophenol Blue
5x	1.825 mL	3.125 mL	5 mL	1 g	50 µL

Using the pre-determined protein concentrations of the cell lysates and the sample volume to determine the mass of protein present in each sample, dilutions could be calculated to create new samples of normalised protein content between the complex treated lysate and untreated lysate which were then used to make a mixed sample, maintaining the same total protein content, of 1:1 treated : untreated lysates. All three samples (treated, untreated and mixed, corresponding to light, heavy and mixed amino acids) were then diluted 2:1 with 2x sample buffer and heated for 3 minutes at 95°C to ensure full protein denaturation.

Gel Electrophoresis

Running buffer was prepared as a 2L solution of 25 mM Tris, 192 mM and 0.1% SDS:

Concentration	ddH$_2$O	Tris base	Glycine	SDS
1x	Up to 2 L	6.04 g	28.8 g	2 g

The gels were secured in place on each side of the gel electrophoresis equipment, the inner chamber and the lower chamber of the tank were filled with running buffer and the samples loaded into the wells, along with a protein marker ladder each side, before being ran at 150 volts. When the protein marker had proceeded down the majority of the gel, the electrophoresis was stopped and the gel stained with collodial coomassie to visualise the sample protein bands and confirm a degree of separation had occurred.

6.6.5   In-gel digest of SDS-PAGE gel

The completed SDS-PAGE gels were subjected to the following in-gel digest protocol to prepare samples for proteomic analysis.

Solution preparation

Solution 1: 200 mM ammonium bicarbonate (ABC), 40% acetonitrile (ACN)

(1.58g ABC, 40 mL ACN, 60 mL MQ H₂O)

Solution 2: 50 mM ammonium bicarbonate

(0.395 g ABC, 100 mL MQ H₂O)

Solution 3: 50 mM ammonium bicarbonate, 50% acetonitrile

(0.395 g ABC, 50 mL ACN, 50 mL MQ H₂O)

Solution 4: 40 mM ammonium bicarbonate

(0.316 g ABC, 9 mL ACN, 91 mL MQ H₂O)

Solution 5: 100% acetonitrile

(100 mL ACN)

Solution 6: 5% formic acid (FA)

(5 mL FA, 95 mL MQ H₂O)

Solution 7: 50% acetonitrile, 5% formic acid

(50 mL ACN, 5 mL FA, 45 mL MQ H₂O)

Solution 8: 1 mM HCl

(25 μL 4M HCl up to 100 mL with MQ H₂O)

Reduction Buffer: 10 mM dithiothreitol (DTT), 50 mM ammonium bicarbonate

(0.0155g DTT, 10 mL Solution 2)

Alkylation Buffer: 55 mM iodoacetamide (IAA), 50 mM ammonium bicarbonate

(0.10172 g of IAA, 10 mL Solution 2)

Trypsin solution: 0.02 μg/μL

(1 vial of proteomic grade trypsin TPCK treated 20 μg, add 100 μL of Solution 8, then 900 μL of Solution 4)

Band excission and destain

1. Carefully wash the gel several times with MQ H_2O.

2. Within a fume hood, excise each gel lane into 10 equal width bands with a fresh scalpel blade and transfer into a fresh siliconized Eppendorf tube.

3. Cover each gel piece with 200 µL Solution 1, incubate at 37°C for 30 minutes.

4. Discard supernatant.

5. Repeat step 3 with fresh Solution 1.

6. Dry down gel pieces in vacuum concentrator for approximately 30 minutes.

Reduction and alkylation of proteins

1. Add 200 µL of Reduction buffer (prepared fresh) to each gel piece and incubate at 56°C for 1 hour.

2. Centrifuge gel pieces in Eppendorf tube at 13000 x g for 10 minutes.

3. Discard supernatant

4. Add 200 µL of Alkylation buffer (prepared fresh) to each gel piece and incubate at room temperature for 30 minutes _in the dark_.

5. Wash each gel piece with 200 µL of Solution 2 and leave at room temperature for 15 minutes.

6. Discard supernatant.

7. Repeat steps 5 and 6 once more.

8. Wash each gel piece with 200 µL of Solution 3 and incubate at 37°C for 15 minutes.

9. Centrifuge gel piece in Eppendorf tube at 13000 x g for 10 minutes.

10. Discard supernatant.

11. Dry down gel pieces in vacuum concentrator for approximately 30 minutes.

Enzymatic digestion

1. Add 20 µL of Trypsin solution (equivalent to 0.4 µg trypsin) to each gel piece.

2. Add 50 µL of Solution 4 to each gel piece, ensuring full coverage by fluid.

3. Incubate at 37°C overnight.

Peptide extraction

1. Centrifuge gel piece in Eppendorf tube at 13000 x g for 10 minutes

2. Collect supernatant to a fresh siliconized Eppendorf supernatant collection tube (SCT).

3. Add 20 μL of Solution 5 to each gel piece, briefly vortex and incubate at 37°C for 15 minutes.

4. Add 50 μL of Solution 6 to each gel piece, briefly vortex and incubate at 37°C for 15 minutes.

5. Vortex each tube briefly, centrifuge gel piece in Eppendorf tube at 13000 x g for 10 minutes, remove supernatant and add to the corresponding SCT.

6. Repeat steps 3 to 5 once more.

7. Add 50 μL of Solution 7 to each gel piece, briefly vortex and incubate at 37°C for 30 minutes.

8. Vortex each tube briefly, centrifuge gel piece in Eppendorf tube at 13000 x g for 10 minutes, remove supernatant and add to the corresponding SCT.

9. Discard gel piece.

10. Place supernatant collection tubes in vacuum concentrator and dry down extracted peptides overnight.

11. Store supernatant collection tubes at -20°C ready for analysis.

6.6.6   Data processing

After the samples were analysed by mass spectrometry, the data was processed to assign the detected peptide sequences to their corresponding proteins using the Mascot software search engine; which utilises several primary sequence databases.

The Perseus software suite was used to filter the entire data set for statistically significant information. The criteria applied to isolate up-regulated proteins were: Number of peptides > 1, Light/Heavy ratio > 1.8, Light/Heavy Count > 1, Light/Heavy Variability < 30%.

6.7   Intracellular metal content (ICP-MS)

The intracellular metal content was calculated using the following protocol for inductively coupled mass spectrometry (ICP-MS).

Cell culture

1. Seed cells in 60mm dishes
2. Incubate for 24 hours
3. Treat cells with complex at a set concentration and time
4. Remove complex solution
5. Wash with PBS
6. Add 500 μL serum free media and 1 mL trypsin solution
7. Incubate for 3 minutes and shake to detach some of the cells
8. Scrape to detach the remaining cells (some complexes can neutralise trypsin)
9. Harvest cells into Eppendorf tubes and centrifuge (4000 rpm, 3 minutes)
10. Remove supernatant and resuspend in 500 μL serum free media
11. Remove 20 μL to count cells and calculate the cell number in the remaining volume

ICP-MS Sample preparation

1. Transfer each sample completely to a glass vial with plastic lid (no metal or rubber insert) and add 2 mL 60% nitric acid
2. Heat at 60°C overnight to dissolve all of the sample into a colourless solution
3. Add approximately 8 mL MQ H_2O to each sample to make a total volume of 10 mL
4. Submit for ICP-MS analysis of appropriate metal nuclei

With the results in μg L^{-1}, and a known sample volume and cell number the total metal mass per cell could be calculated. This can be used to calculate moles of metal, and therefore the moles of compound, per cell. Finally, with the assumption of a cell volume of 2×10^{-12} L an estimate of intracellular concentration in mol L^{-1} could be deduced.

6.8   Singlet Oxygen Quantum Yield

Emission quenching was accompanied by singlet oxygen generation as shown by the O_2 $(^1\Delta g) \rightarrow {}^3O_2$ phosphorescence at $\lambda > 1100$ nm.[7] Singlet oxygen quantum yield, $\phi(^1O_2)$, was determined through measurement of phosphorescence intensity in dichloromethane employing 355 nm excitation and perinaphthenone as the standard.[8]

6.9   References

1.   Zheng, R. H. *et al.* A new and convenient synthesis of phendiones oxidated by $KBrO_3/H_2SO_4$ at room temperature. *Chinese Chem. Lett.* **21,** 1270–1272 (2010).

2.   Bodige, S. & MacDonnell, F. M. Synthesis of Free and Ruthenium Coordinated 5,6-Diamino-1,10-phenanthroline. *Tetrahedron Lett.* **38,** 8159–8160 (1997).

3.   Bolger, J., Gourdon, A., Ishow, E. & Launay, J. Mononuclear and Binuclear Tetrapyrido phenazine (tpphz) Ruthenium and Osmium Complexes. *Inorg. Chem.* **1669,** 2937–2944 (1996).

4.   Zhen, Q. X. *et al.* Synthesis, characterization and the effect of ligand planarity of $[Ru(bpy)_2L]^{2+}$ on DNA binding affinity. *J. Inorg. Biochem.* **76,** 47–53 (1999).

5.   Sullivan, B., Salmon, D. & Meyer, T. Mixed phosphine 2,2'-bipyridine complexes of ruthenium. *Inorg. Chem.* **17,** 3334–3341 (1978).

6.   Scatchard, G. the Attractions of Proteins for Small Molecules and Ions. *Ann. N. Y. Acad. Sci.* **51,** 660–672 (1949).

7.   Rodgers, M. a. J. & Snowden, P. T. Lifetime of oxygen $(O_2(^1\Delta_g))$ in liquid water as determined by time-resolved infrared luminescence measurements. *J. Am. Chem. Soc.* **104,** 5541–5543 (1982).

8.   Schmidt, R., Tanielian, C., Dunsbach, R. & Wolff, C. Phenalenone, a universal reference compound for the determination of quantum yields of singlet oxygen $O_2(^1\Delta_g)$ sensitization. *J. Photochem. Photobiol. A Chem.* **79,** 11–17 (1994).

Chapter 7

Appendices

Appendix I – Supporting information

Appendix II – Publications resulting from this thesis

Directly originating:

A self-assembled metallomacrocycle singlet oxygen sensitizer for photodynamic therapy

Indirectly originating:

A Cytostatic Ruthenium(II)-Platinum(II) Bis(terpyridyl) Anticancer Complex That Blocks Entry into S Phase by Up-regulating p27^{KIP1}

7.1   NMR Spectra

1,10-phenanthroline-5,6-dione   **[Exp. 6.2.1 pg. 132]**
(DPQ) in CD$_3$Cl
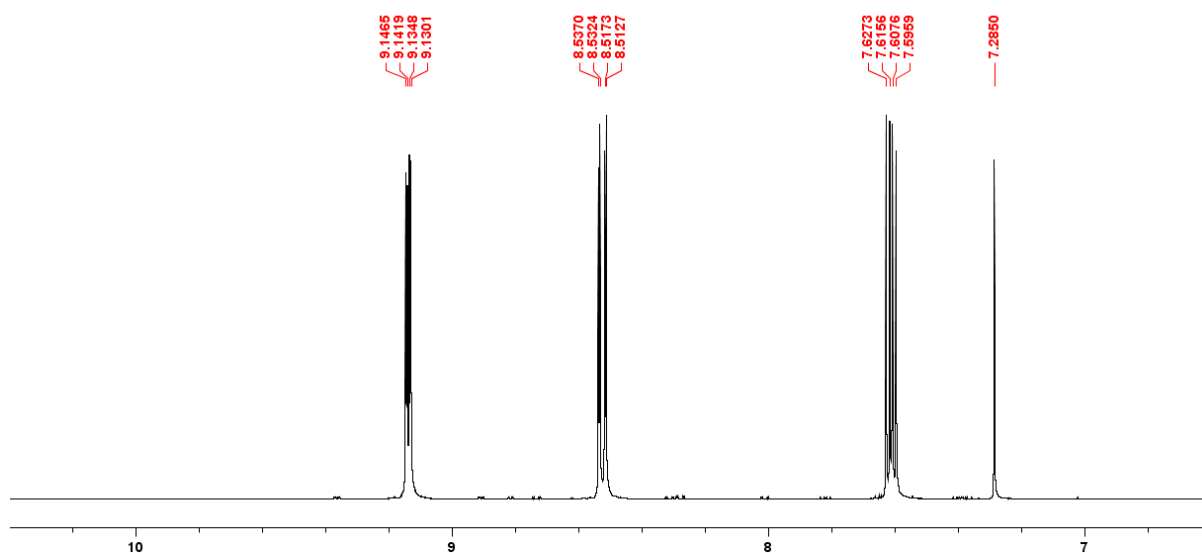
1,10-phenanthroline-5,6-dioxime   **[Exp. 6.2.2 pg. 133]**
(phen-dioxime) in (CD$_3$)$_2$SO
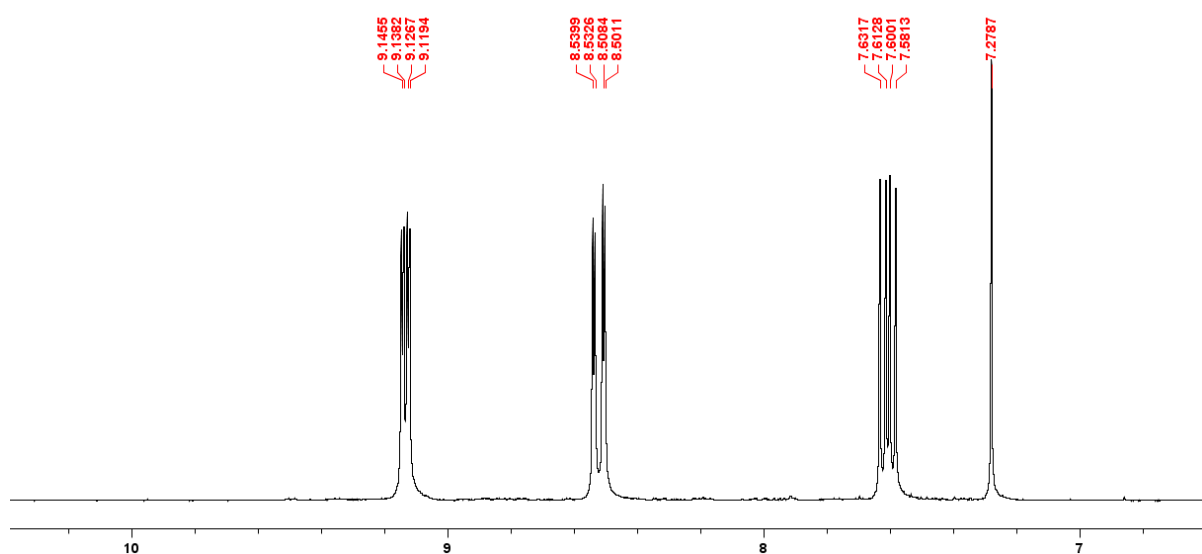
1,10-phenanthroline-5,6-diamine   **[Exp. 6.2.3 pg. 134]**

(phen-diamine) in (CD₃)₂SO
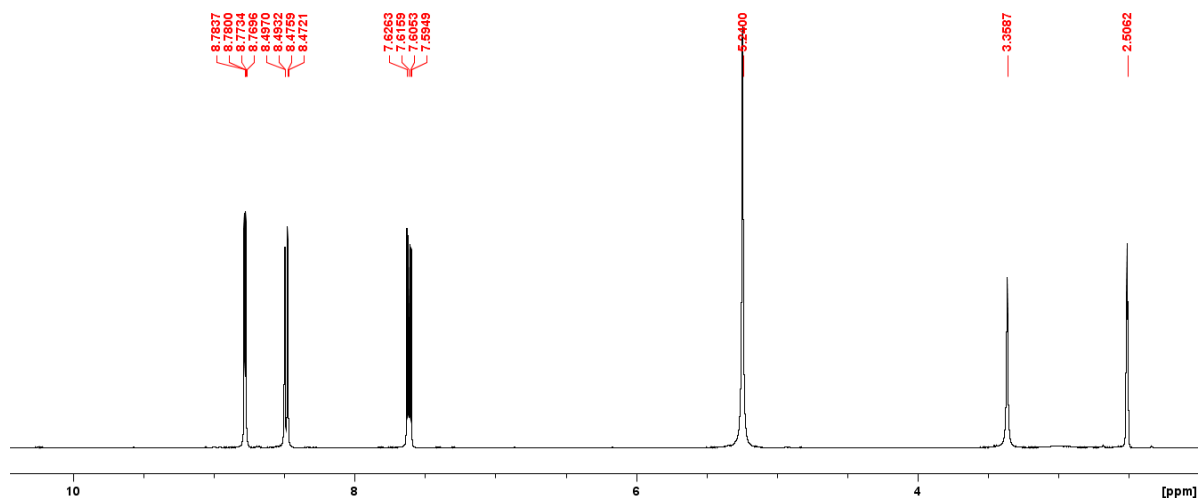
tetrapyridophenazine   **[Exp. 6.2.4 pg. 135]**

(tpphz) in CF₃COOD
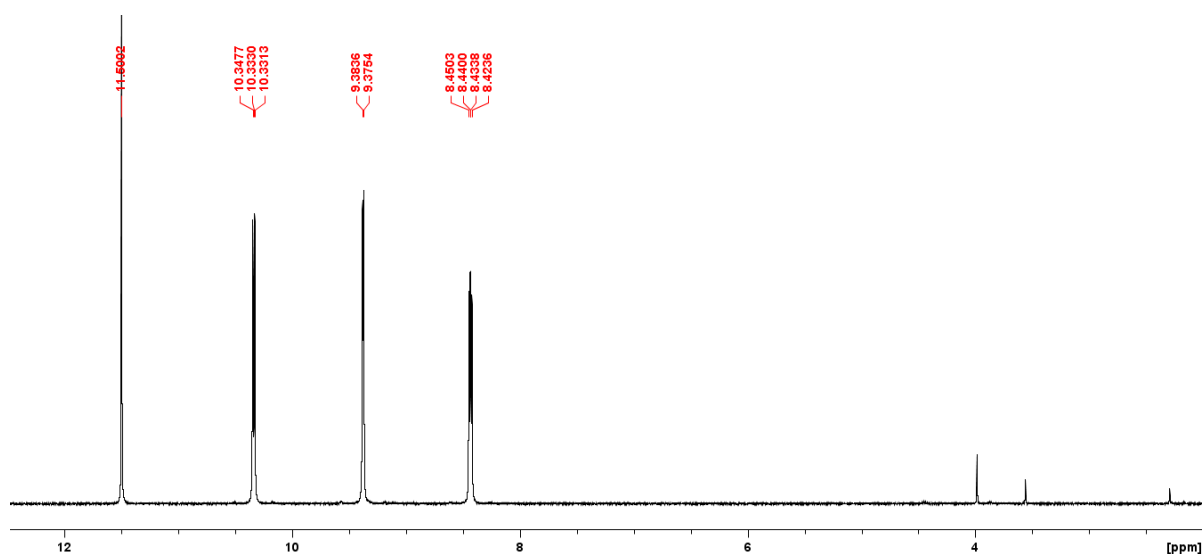
[Ru(phen)₂(DPQ)](PF₆)₂   **[Exp. 6.2.8 pg. 139]**

(Ru-phen-DPQ) in CD₃CN
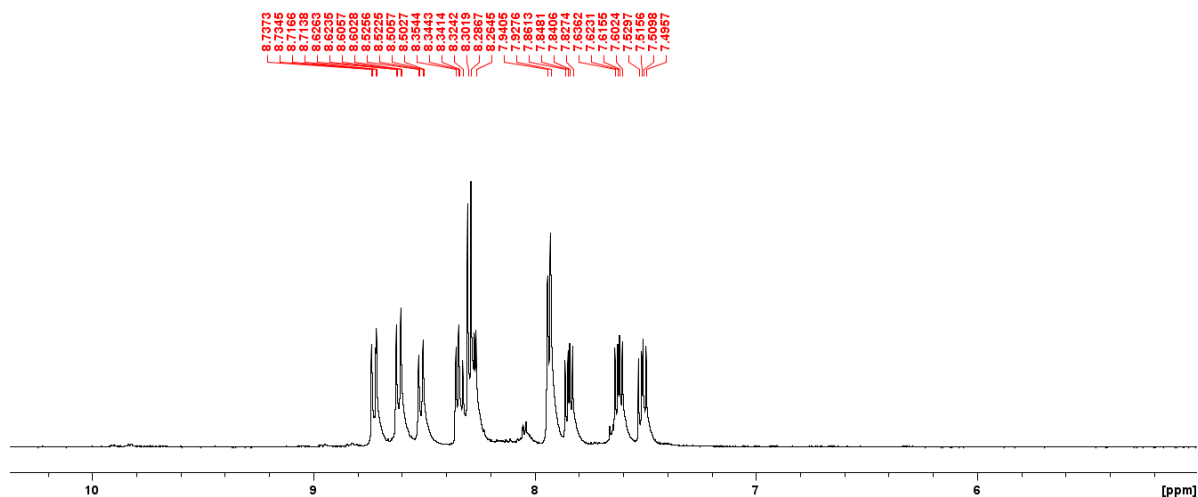
[Ru(bipy)₂(DPQ)](PF₆)₂

(Ru-bipy-DPQ) in CD₃CN

[Exp. 6.2.9 pg. 140]
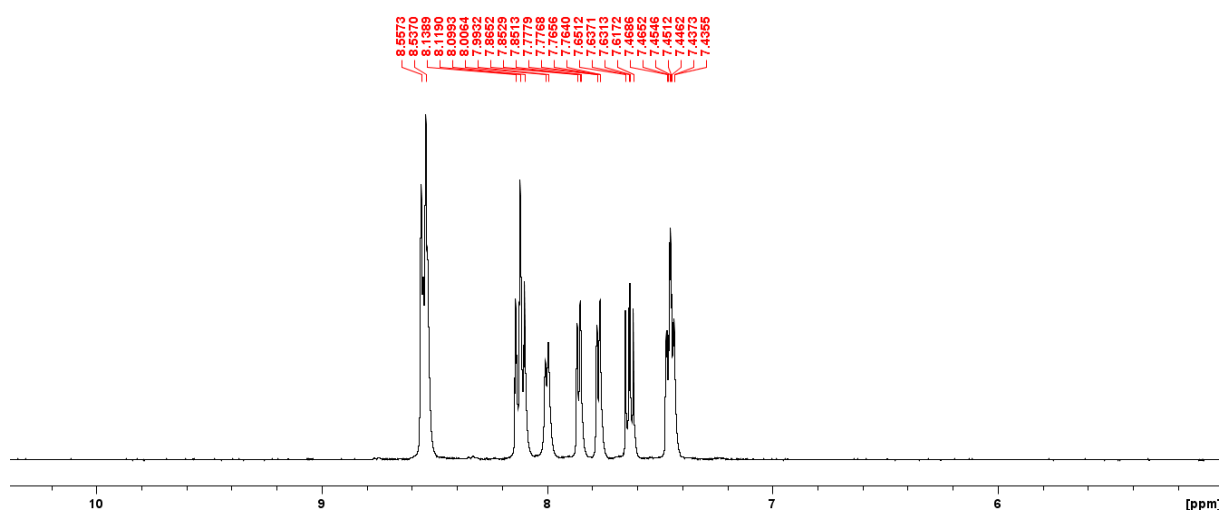
[Ru(phen)₂(tpphz)](PF₆)₂

(Ru-phen-tpphz) in CD₃CN

[Exp. 6.2.10 pg. 141]
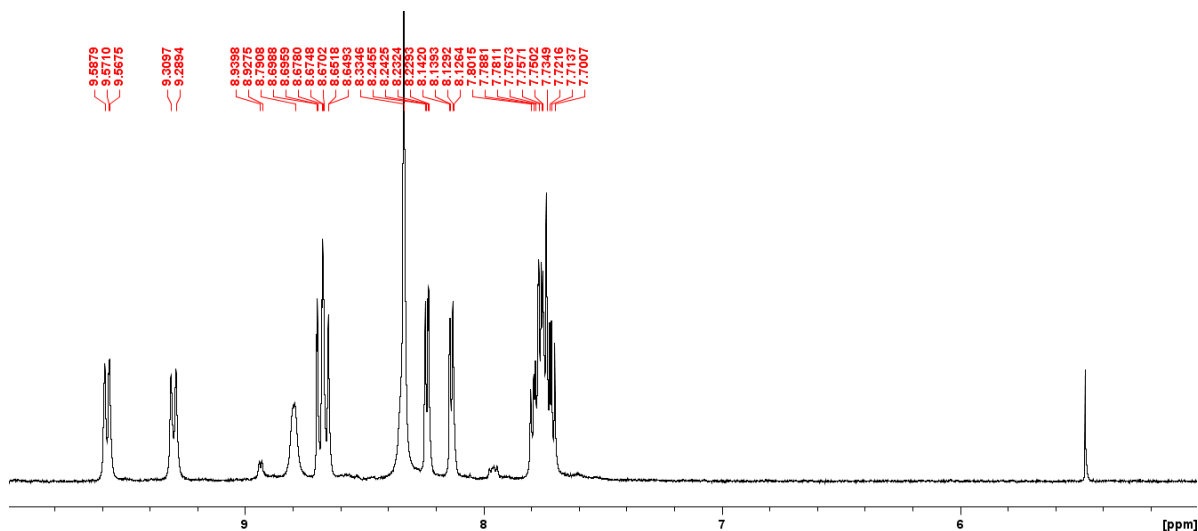
[Ru(bipy)₂(tpphz)](PF₆)₂

(Ru-bipy-tpphz) in CD₃CN

[Exp. 6.2.11 pg. 142]
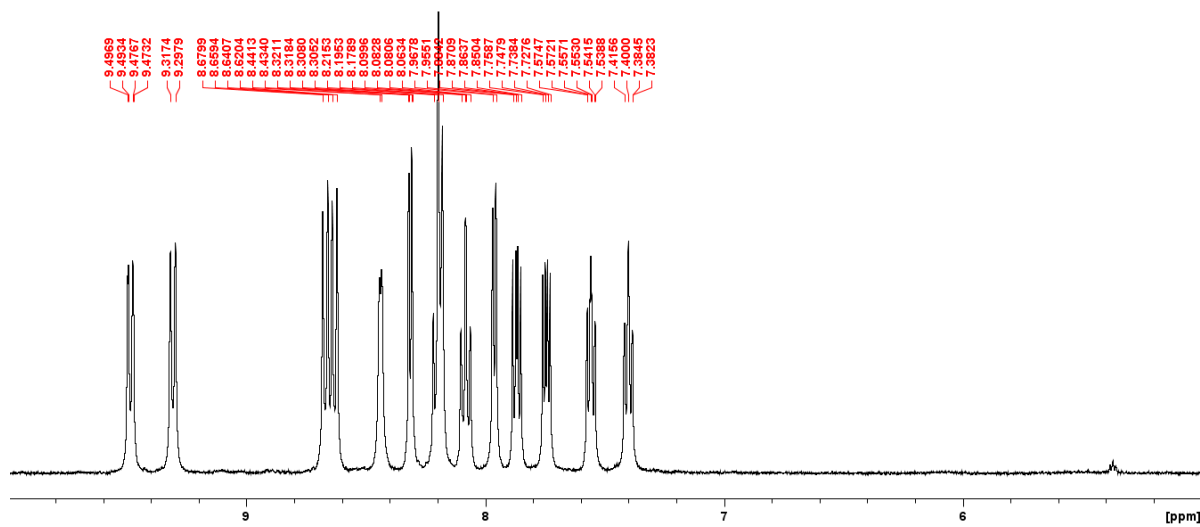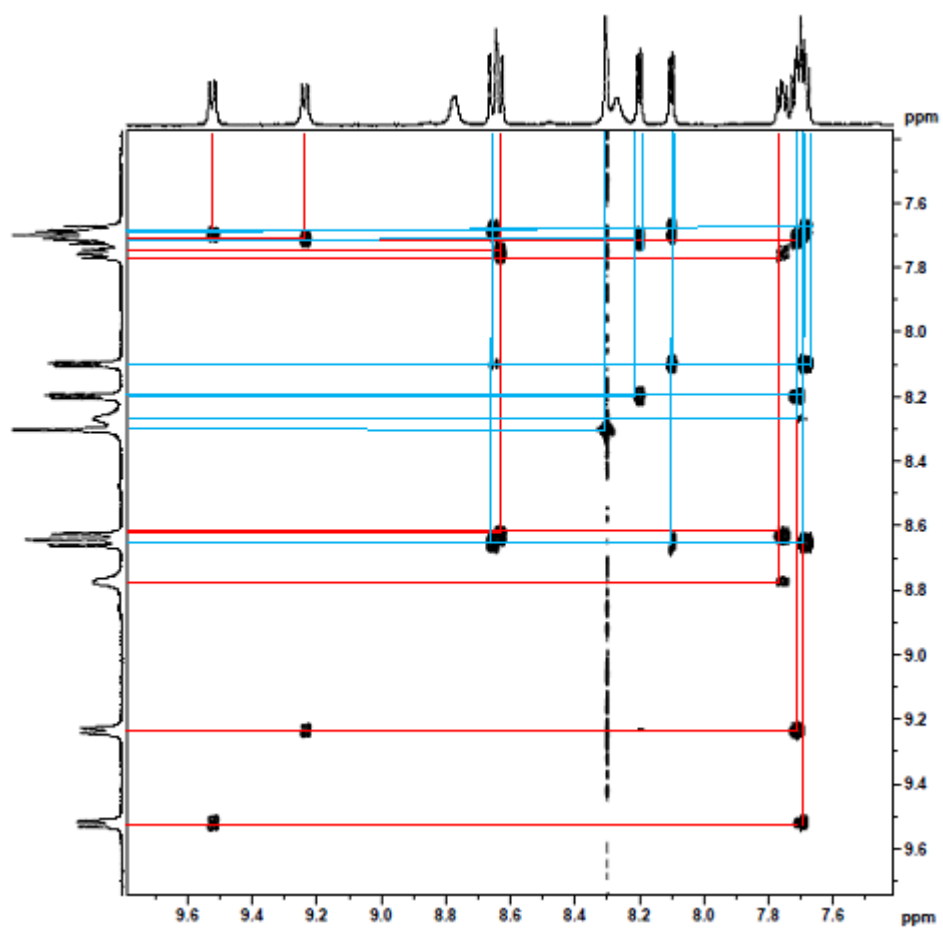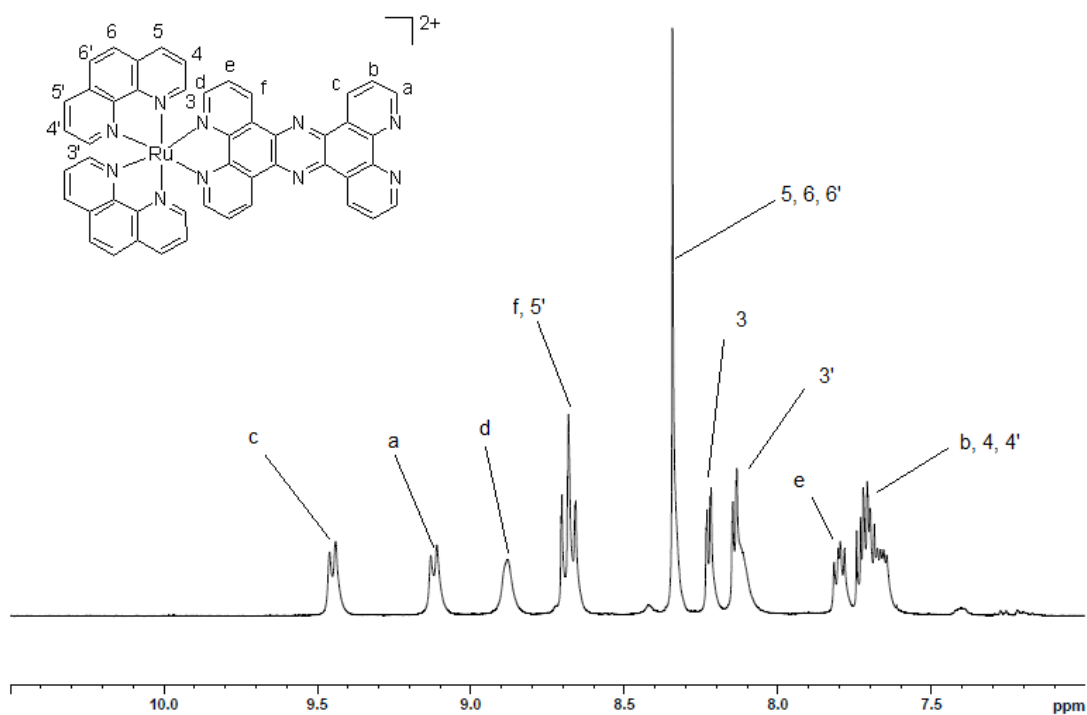
(Ru-phen-tpphz)

(Red lines = tpphz protons a,b,c,d,e,f and Blue lines = phen protons 3,4,5,6,3',4',5',6')

(Ru-bipy-tpphz)
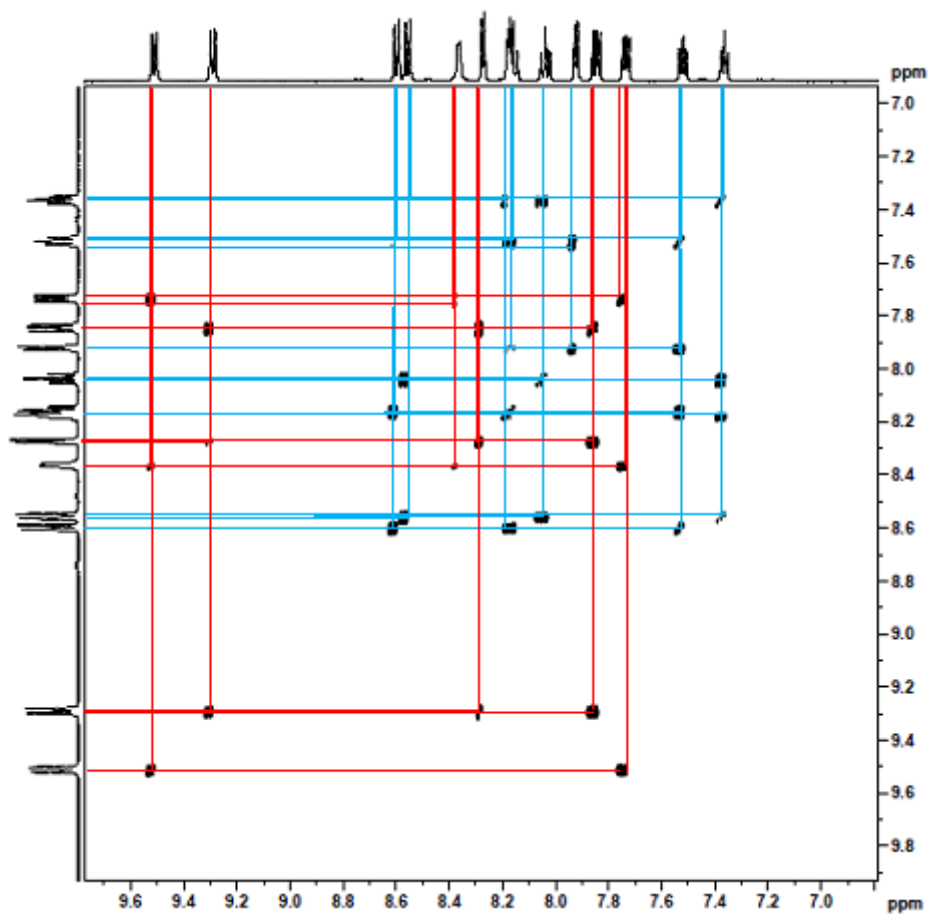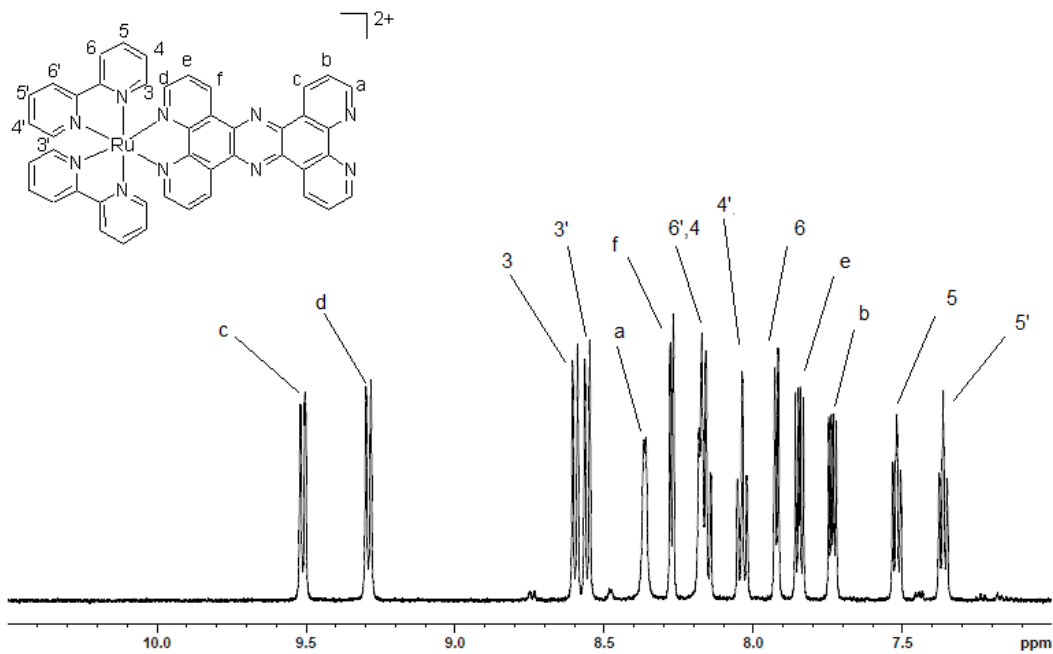
(Red lines = tpphz protons a,b,c,d,e,f and Blue lines = phen protons 3,4,5,6,3',4',5',6')

tetraazaphenanthrenotriphenylene   **[Exp. 6.2.5 pg. 136]**
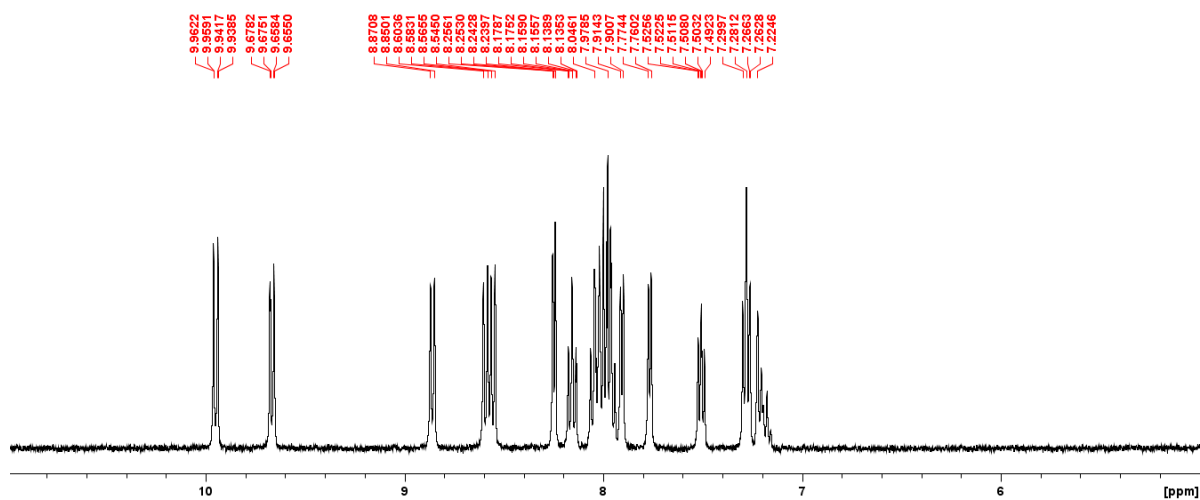
(taptp) in CF₃COOD
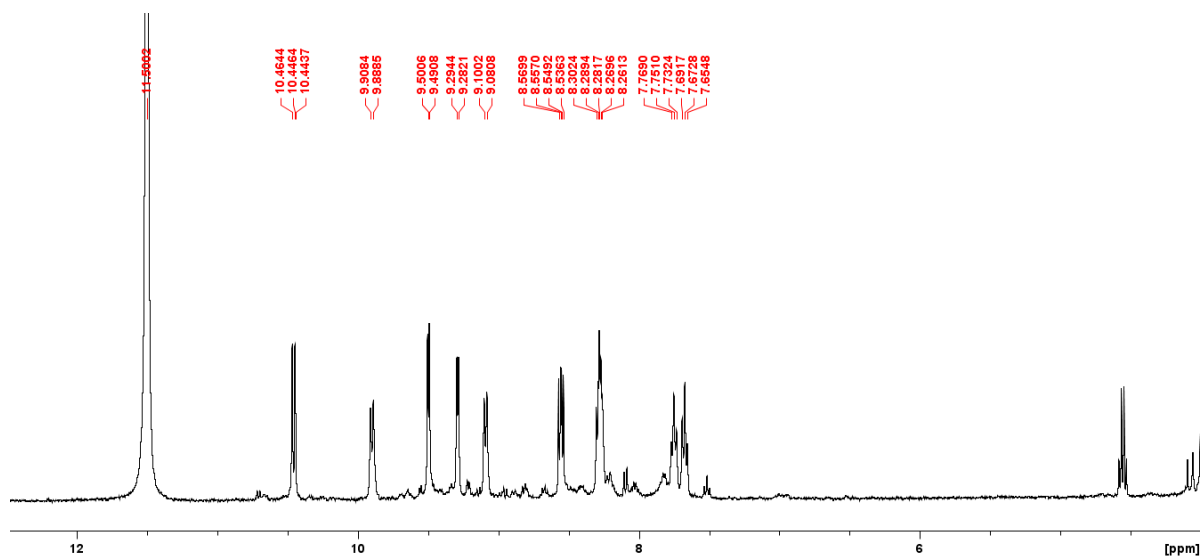
[Ru(phen)₂(taptp)](PF₆)₂ **[Exp. 6.2.12 pg. 143]**

(Ru-phen-taptp) in CD₃CN
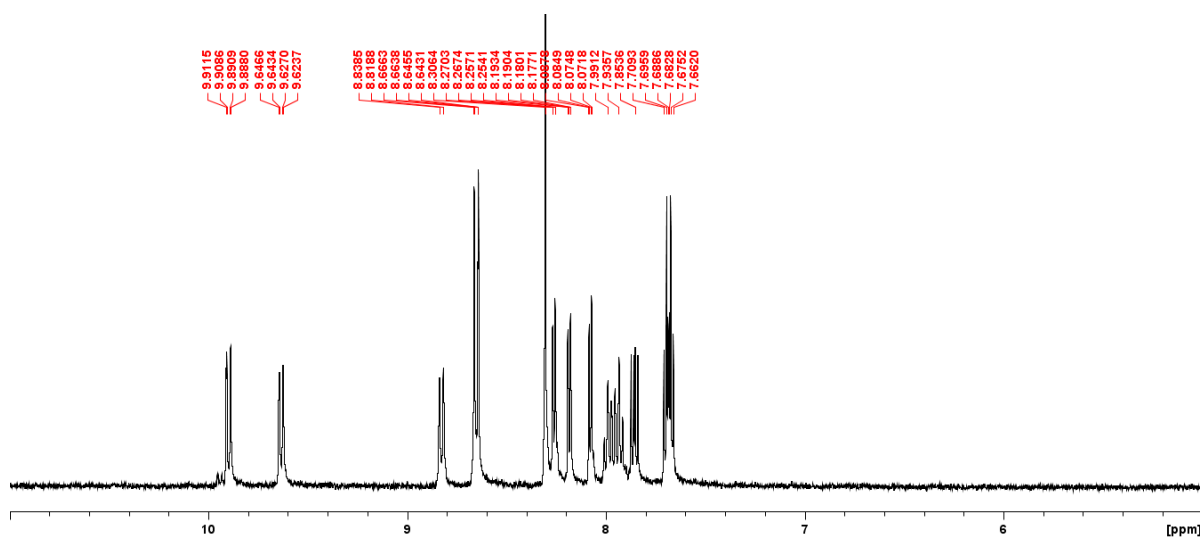
[Ru(bipy)₂(taptp)](PF₆)₂ **[Exp. 6.2.13 pg. 144]**

(Ru-bipy-taptp) in CD₃CN

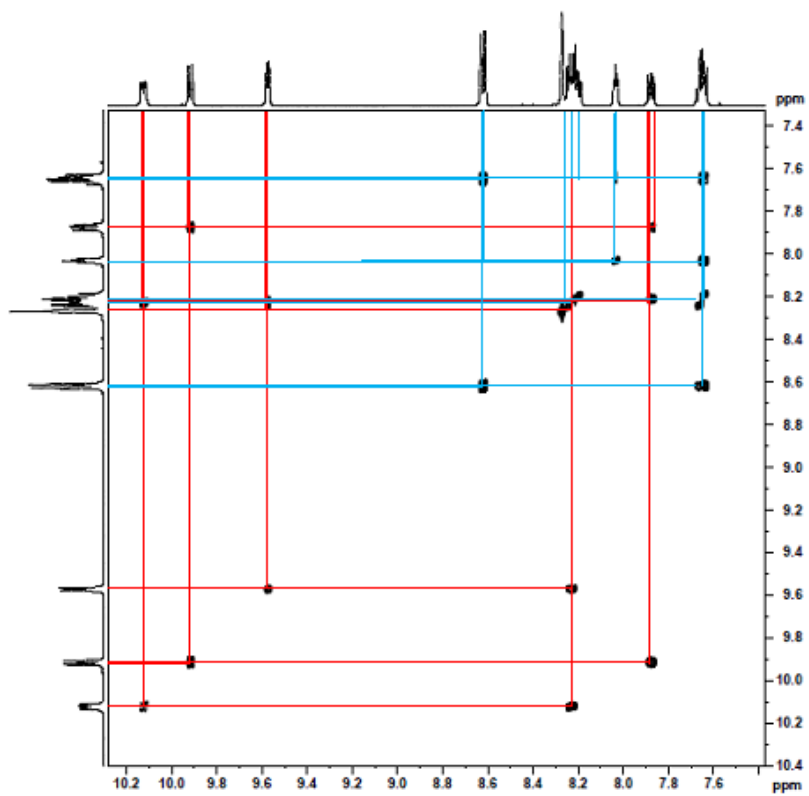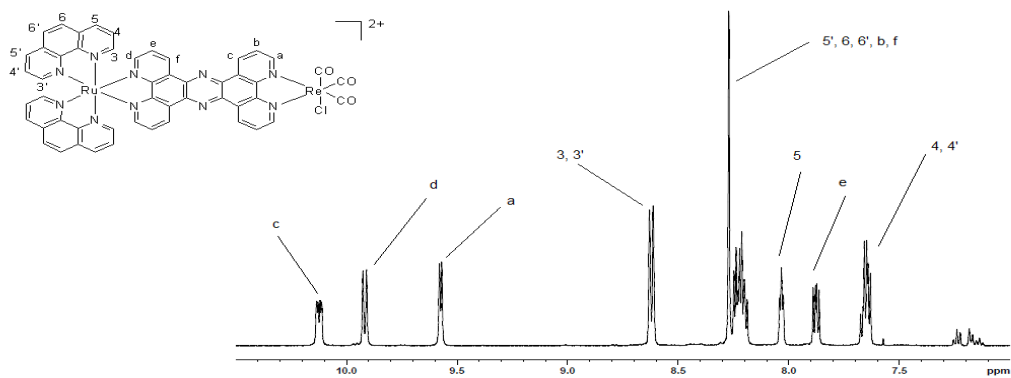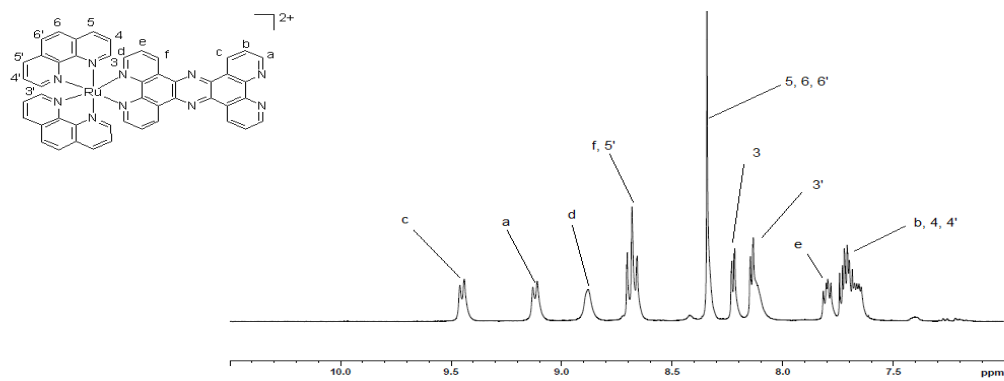**[Ru(phen)₂(tpphz)PtCl₂](PF₆)₂**   **[Exp. 6.2.14 pg. 145]**

(RuPt-phen) in CD₃CN
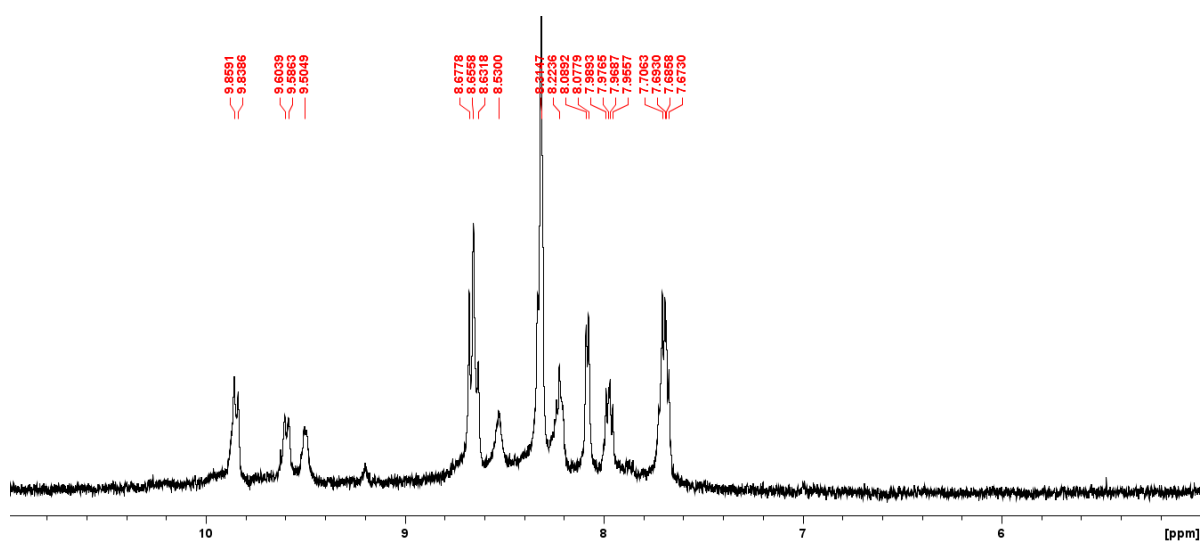
[Ru(phen)₂(tpphz)Re(CO)₃Cl](PF₆)₂   **[Exp. 6.2.15 pg. 146]**

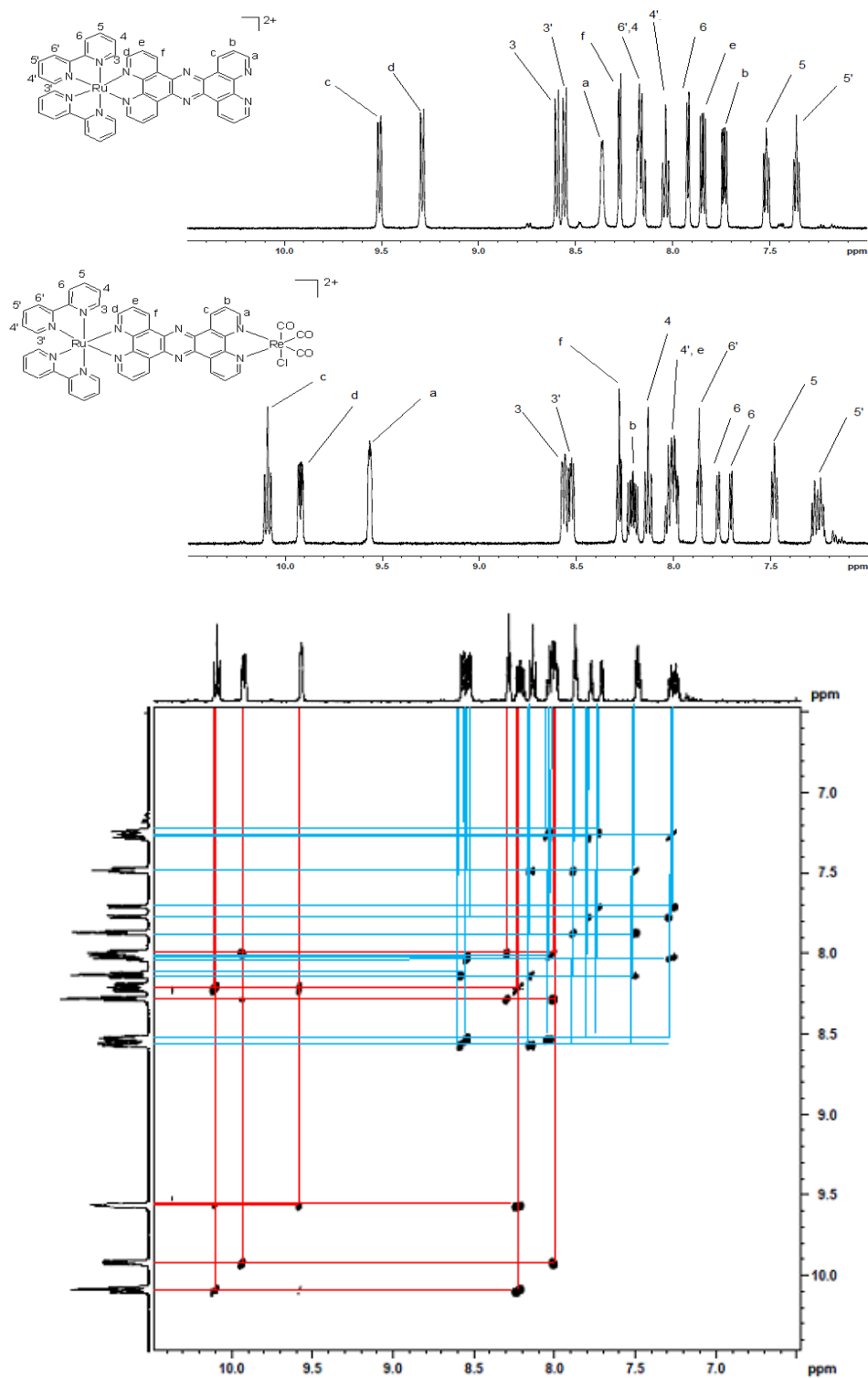**(RuRe-phen) in CD₃CN**

(red lines = tpphz protons a,b,c,d,e,f and blue lines = phen protons 3,4,5,6,3',4',5',6')

[Ru(bipy)₂(tpphz)Re(CO)₃Cl](PF₆)₂   **[Exp 6.2.16 pg. 147]**
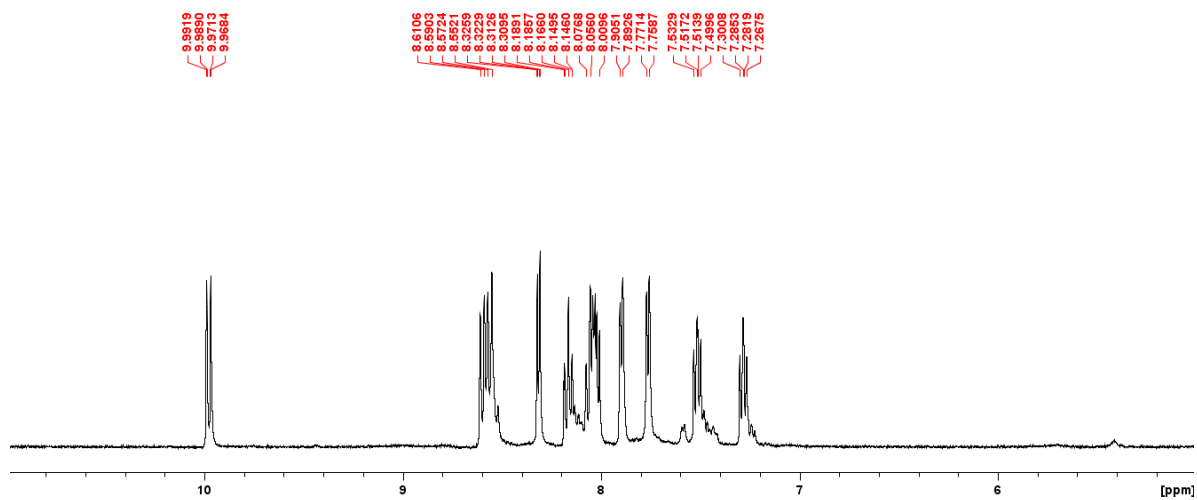
(RuRe-bipy) in CD₃CN

(red lines = tpphz protons a,b,c,d,e,f and blue lines = phen protons 3,4,5,6,3',4',5',6')

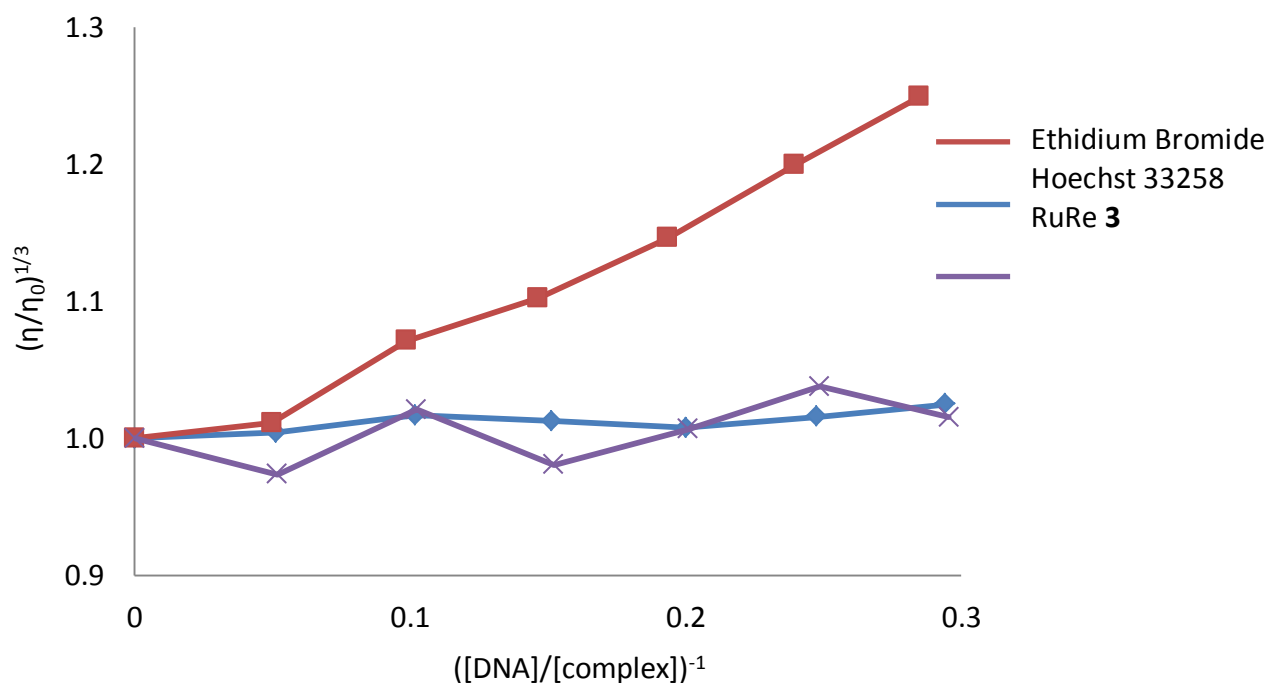**[(Ru(bipy)₂)₂(tpphz)](PF₆)₄**   **[Exp. 6.2.17 pg. 148]**

(RuRu-bipy) in CD₃CN

7.2   Viscometry

The following data was collected by Isabel Griffiths (Level 4 Masters student) using a Canon viscometer (size 50) immersed in a water bath maintained at 26 °C. For each solution the 1/R (R = ([DNA]/[complex]) value falls between 0 – 0.3 and 20 minutes equilibration was allowed after each complex addition. Capillary tube flow rates were ran in triplicate and an average value calculated. The figure below shows the relative viscosity $(\eta/\eta_0)^{1/3}$ of 50 μM CT-DNA upon an increasing concentration $([DNA]/[complex])^{-1}$ of RuRe **3**, the model intercalator ethidium bromide and the model groove binder Hoechst 33258.

7.3   UV-vis Spectra

The following data was collected by Isabel Griffiths (Level 4 Masters student) using a Varian Cary 50 Probe UV-vis spectrophotometer and Cary Win UV software, and shows the UV-vis absorption spectra and assignment of Ru(tpphz) **1**, RuRe **3**, and for the bipy derivatives Ru-bipy-tpphz and RuRe-bipy, all as a PF_6 salt in acetonitrile.

Complex	λmax / nm	ε / M^{-1} cm^{-1}	Assignment
	225	114334	π→π*
	245	105802	π→π*
	265	165529	π→π*
Ru(tpphz) **1**	315	63140	π→π*
	365	35836	π→π*
	380	51195	π→π*
	450	27304	MLCT
	265	154143	π→π*
	280	148362	π→π*
RuRe **3**	305	75145	π→π*
	370	34682	π→π*
	440	32755	MLCT

Complex	λmax (nm)	ε (M^{-1} cm^{-1})	Assignment
	245	92559	π→π*
	282	154265	π→π*
Ru-bipy-tpphz	315	63521	π→π*
	365	27223	π→π*
	380	43557	π→π*
	450	25408	MLCT
	245	66265	π→π*
	280	168675	π→π*
RuRe-bipy	325	48193	π→π*
	370	32129	π→π*
	440	30120	MLCT

Also obtained (below) were the UV-vis spectra for RuRe **3** as both a hexafluorophosphate salt in acetonitrile and chloride salt in H$_2$O, showing very little change and validating an assumption of the same photophysical properties before and after metathesis from hexafluorophosphate to chloride complex.

Complex	λmax (nm)	ε (M^{-1} cm^{-1})	Assignment
	220	63319	π→π*
	265	79694	π→π*
	280	84061	π→π*
RuRe **3**	305	40393	π→π*
	365	20742	π→π*
	380	24017	π→π*
	440	18559	MLCT

A self-assembled metallomacrocycle singlet oxygen sensitizer for photodynamic therapy

Michael G. Walker, ‡[a] Paul J. Jarman, ‡[a] Martin R. Gill,[b] Xiaohe Tian,[c] Haslina Ahmad,[d] Pattubala A. N. Reddy,[a] Luke McKenzie,[a] Julia A.Weinstein,[a] Anthony J . H. M. Meijer,[a] Giuseppe Battaglia,[c] Carl G. W. Smythe*[b], Jim A. Thomas*[a]

Abstract: Although metal ion directed self-assembly has been widely used to construct a vast number of macrocycles and cages, it is only recently that the biological properties of these systems have begun to be explored. However, up until now, none of these studies have involved intrinsically photo-excitable self-assembled structures. Herein we report the first metallomacrocycle that functions as an intracellular singlet oxygen sensitizer. Not only does this Ru_2Re_2 system possess potent photocytotoxicity at light fluences below those used for current medically employed systems, it offers an entirely new paradigm for the construction of sensitizers for photodynamic therapy.

Keywords: Self-assembly • singlet oxygen • ruthenium • PDT • luminescence

Introduction

Photodynamic therapy, PDT, is a non-invasive therapy regime in which light is used to selectively damage diseased tissue, usually through the *in situ* creation of reactive oxygen species (ROS).[1-5] Commonly, this is accomplished through a prodrug photosensitizer molecule that generates cytotoxic singlet oxygen *via* excited-state energy transfer. PDT has been successfully employed to treat a range of cancers[6] and other disease states.[7]

One advantage of PDT is that cell death can be targeted to specific locations through a carefully selected combination of sensitizer and light; minimising many of the undesired side-effects of conventional therapeutic regimes. The majority of photosensitizers in clinical use are tetrapyrrolic structures. [8,9] However, these structures have a number of disadvantages; for example, as extended aromatic systems they often display relatively low water solubility and they can be difficult to synthesize and purify. In recent years - due to their good water solubility, attractive optical properties, and high photostability - transition metal coordination compounds have been investigated as alternative photosensitizer leads.[10] In particular, Ru^{II} complexes have attracted much attention and one such complex is currently entering Phase I trials as a PDT sensitizer for bladder cancer.[11]

Meanwhile, over the last two decades, interest in metal directed self-assembly has exploded, leading to a huge variety of often very complex molecular architectures.[12-14] Many of these systems are hosts, and have been developed as devices such as sensors for ions and molecules or even catalysts.[15-17] Although the interaction of such architectures with biomolecules has been investigated; originally much of this work focused on helicate structures, producing several promising potential therapeutics. [18-20]

It is only more recently that the bioactivity of metallomacrocycles and cages has begun to be examined.[21,22] In this context, perhaps the most well-studied cage systems are those reported by the Therrien group; for example, these architectures
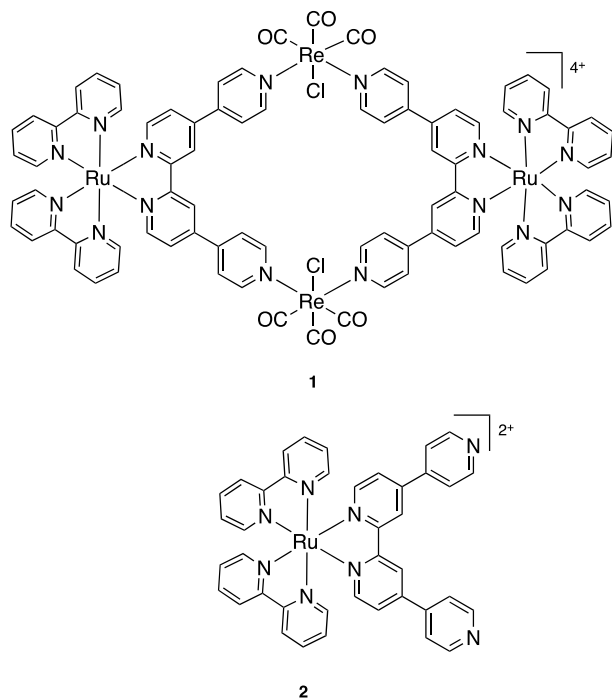
[a]   Dr M G Walker, Dr P J Jarman, Dr P A N Reddy, Mr L McKenzie, Prof J A Weinstein, Dr A J H M Meijer, Prof J A Thomas
       Department of Chemistry,
       University of Sheffield
       Sheffield, S10 3GZ, UK
       Fax: (+)44 (0)114 22 29436
       E-mail: james.thomas@sheffield.ac.uk

[b]   Dr M R Gill, Prof C G W Smythe.
       Department of Biomedical Science
       University of Sheffield
       Sheffield, UK
       Fax: (+)44 (0)114 22 2787
       E-mail: c.g.w.smythe@sheffield.ac.uk

[c]   Dr X Tian, Prof G Battaglia
       Department of Chemistry,
       University College London
       London, UK

[d]   Dr H Ahmad,
       Department of Chemistry,
       Universiti Putra Malaysia
       43400 UPM Serdang, Malaysia

have been successfully employed as *in cellulo* delivery vectors for a variety of "payloads" including cytotoxic therapeutics, [23,24] luminescent DNA probes,[25] and porphyrin-based sensitizers for PDT.[26] Furthermore, a number of metallocages have been identified as promising anticancer therapeutic leads in themselves, although the exact molecular basis of observed cytotoxicity in such systems is largely unidentified or poorly understood. [27,28]

1

2

Scheme 1 Structures discussed in this study.

Results and Discussion

In combination with light microscopy, the MLCT (metal to ligand charge-transfer) emissive properties of Ru(II) polypyridyl complexes provide a useful property by which to assess the cellular internalisation of a complex of interest;[36,37] a concept that may be extended to hetero bi-metallic systems.[38] As both macrocycle **1** and its "building block" mononuclear complex **2** display Ru^{II}→qtpy ^{3}MLCT-based luminescence on photoexcitation at 458 nm[30,31] we initially explored cellular localisation using confocal laser scanning microscopy (CLSM) and fixed MCF7 human breast cancer cells.

Surprisingly - even though **2** is emissive whether or not it is bound to biomolecules such as DNA and the barrier to transport across the plasma membrane has been removed by fixation - no intracellular emission from mononuclear complex **2** was observed. In contrast, macrocycle **1** *does* localise in fixed MCF7 cells. Although some non-specific nuclear staining is observed, the macrocycle particularly brightly stains the lipid rich regions of the cell, such as the nuclear membrane and endoplasmic reticulum (ER) – Figure 1 and SI.
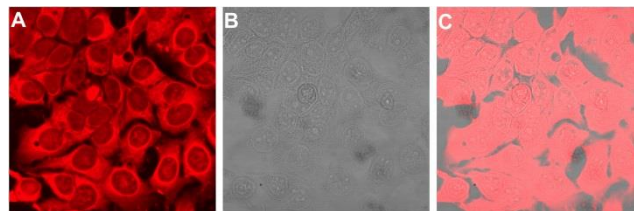

Figure 1. (**A**) CLSM images of fixed MCF7 cells stained with **1** for emission at 640-700 nm (^{3}MLCT emission of **1**). (**B**) Phase Contrast image at 485 nm (^{1}MLCT absorbance of **1**). (**C**) Merged image. [**1**] = 100 μM..

As expected from the fixed cell studies, live MCF7 cells shows no intracellular emission from **2**, indicating that live cells do not take up the complex; however addition of macrocycle **1** produced very different results – Fig 2. After 20 minutes incubation with 200 μM of the macrocycle, the media was removed. Following washing with PBS, the cells were placed in complex-free fresh media and imaged through CLSM using monochromated laser light exciting into the MLCT of **1** at 488 nm. Although initial images showed only plasma membrane staining over a period of <10 mins, cells began to display dramatic changes in both dye localisation and cellular morphology with prolonged light exposure - Fig 2A. During the first hour after exposure, **1** begins to localize within cells with evidence of nuclear accumulation and particularly intense emission being observed from nucleoli. After this period, general staining of the nuclear membrane and other membrane-enclosed structures in the cytoplasm such as endosomes, lysosomes, and the ER was increasingly observed. Gross cell swelling and the generation of growing amounts of apparently dead cells, along with complex-stained cell debris, accompanied the shifts in cellular localization of **1** - Fig 2 B.

These cellular responses, which are characteristic of oncosis/necrosis processes,[39,40] are often consequences of *in cellulo* $^1O_2$ generation.[41] Furthermore, these changes only occur after exposure of treated cells to light, clearly indicating a phototoxic response: if cells are treated with the same concentration of **1** but kept in the dark they still display normal morphology, even after two hours exposure – See SI.

It is notable that final localization in necrotic cells, where membranes have been disrupted, is very similar to that observed in fixed cells, indicating that the initial target of **1** in live cells is the plasma membrane. This hypothesis is consistent with the images in Fig 2 showing the complex accumulating at the plasma membrane at early time-points before it localizes within intracellular compartments, including the cell nucleus, as plasma membrane integrity is increasingly compromised. A similar effect has been reported to occur on cell treatment with lipophilic mononuclear Ru^{II}

In this context, we have previously reported on the synthesis[29,30] and structure[31] of self-assembled, kinetically inert, water-soluble metallomacrocycles, such as **1** (Scheme 1). These systems which – because they are based on inert d^6 metal ions - are high stable in aqueous solution possess highly structured, binding pockets composed of hydrophobic aromatic residues that bind to biomolecules with high affinity in biologically relevant conditions.[32-34] Since these macrocycles incorporate polypyridyl Ru^{II} and Re^I units that are related to systems being explored as PDT sensitizers, [10,11,35] we investigated the cellular internalisation properties and photocytotoxicy of **1** towards human cancer cells. Employing clinically relevant light doses, we find that metallomacrocycle **1** is successfully internalised by cells where it functions as a potent photosensitizer though ROS generation that results in plasma membrane damage.

complexes.[42] Given these striking results, the ability of **1** and **2** to generate singlet oxygen on photo-excitation was investigated.
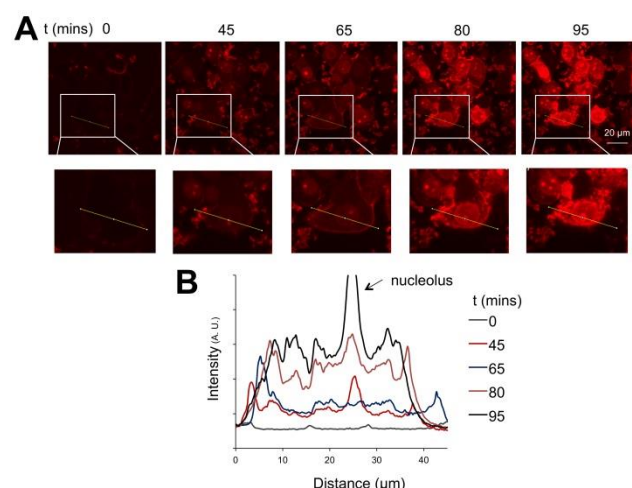
Figure 2. (**A**). Top panels: CLSM images of live MCF7 cells pre-treated with **1** ([**1**] = 200 μM, 20 mins) before exposure to 488 nm light over a 100 minute time course. MLCT emission (640-700 nm) Lower panels: detailed Image of the single cell shown in the white box in the upper panels (**B**). Time dependent emission profile of the same cell illustrating the increase in intensity and the appearance of strong nucleolus signal after initial plasma membrane staining.

Singlet oxygen quantum yields were directly measured by assessing luminescence at 1270 nm following photoexcitation of hexafluorophosphate salts of the complexes in acetonitrile. An optically matched solution of phenalenone was used as a reference sensitizer. This led to $\phi(^1O_2)$ estimates of 54 ± 5 % and 75 ± 2 % for **1** and **2** respectively. These figures probably reflect the lower energy, slightly shorter excited state lifetime of **1** in water (667 nm, 490 ns) compared to **2** (657 nm, 511 ns).

Since **1** binds to biomolecules such as DNA with high affinities >10^6 M^{-1} and has a $\phi(^1O_2)$ value comparable to previously reported sensitizers, it seems the biological action of **1** is through singlet oxygen sensitization. To test this hypothesis, DNA was selected as a representative biomolecule to examine the ability of **1** to induce singlet-oxygen mediated damage upon MLCT photoexcitation in cell-free experiments.

Figure 3. Photocleavage of supercoiled pBR322 DNA (3 μg) y **1** under illuminated condition (476 nm, 100 mW, 10 minutes exposure) in 50 mM Tris-HCL buffer. Forms **I** and **II** are supercoiled and nicked circular forms of DNA, respectively. (**A**) Lane 1, DNA control; lane 2, DNA + **1** (10 μM); lane 3, DNA + **1** (20 μM); lane 4, DNA + **1** (30 μM) ; lane 5, DNA + **1** (40 μM). (**B**) Lane 1, DNA control; lane 2, DNA + **1**; lane 3,

DNA + **1** + NaN$_3$ (200 μM) ; lane 4, DNA + **1** + DMSO (2 μL); lane 5, DNA + **1** in D$_2$O; lane 6, DNA + **1** in argon; lane 7, DNA + **1** in dark..
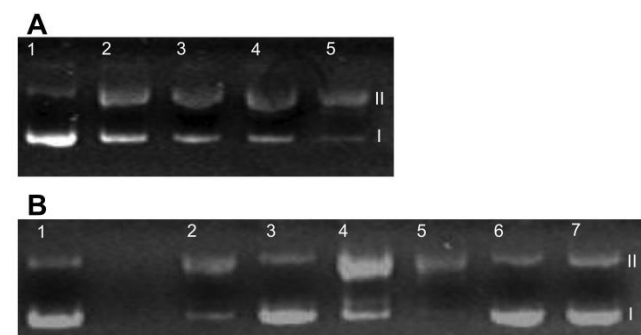
Treatment with 25 μM **1** followed by 10 minutes illumination at 480 nm produces significant cleavage of supercoiled (form I) pBR322 plasmid DNA in buffered aqueous solutions, Fig 3A.

Complete cleavage is observed at concentrations above 40 μM. The mechanism of photocleavage was explored through further experiments involving pBR322 and a range of different inhibitors – Fig 3B. In the dark no significant cleavage is observed, confirming light is necessary for nuclease activity. Since hydroxyl radical scavengers such as DMSO do not inhibit plasmid cleavage, it is unlikely that this radical is responsible for cleavage. In contrast, photocleavage is not observed under argon indicating the involvement of dioxygen. To confirm that photoinduced cleavage involves singlet oxygen, experiments were carried out in the presence of sodium azide and D$_2$O. Sodium azide is a very effective $^1O_2$ quencher and - since $^1O_2$ has a longer lifetime in D$_2$O compared to H$_2$O - the deuterated solvent potentiates the activity of singlet oxygen. As shown in Fig 3B (lanes 3 and 5), the cleavage of pBR322 is inhibited by the presence of sodium azide and enhanced in D$_2$O, confirming that $^1O_2$ is responsible for the cleavage reaction.

Having confirmed that macrocycle **1** is phototoxic to MCF7 cells and induces damage to biomolecules by singlet oxygen generation, we quantified its photo-cytotoxicity towards A2780cis ovarian cancer cells, we chose this second cell line as it is highly resistant to the commonly employed Pt^{II}-based therapeutic cisplatin. To aid comparisons, complex **2** was investigated in parallel studies.

Cells were pre-treated with concentration gradients of **1** or **2** for 24 h before complex removal and exposure to increasing fluences of white light. The impact of each treatment upon cell viability was determined through MTT assay (MTT = 3-(4,5-dimethylthiazol-2-yl)-2,5-diphenyltetrazolium bromide) 24 h after light treatment. Data were normalized against cells not exposed to the complexes but treated with the relevant light dose, yielding the half-inhibitory IC50 values summarized in Table 1 and Figure 4.

Table 1. IC$_{50}$ Values for **1** and **2** towards the cisplatin-resistant cell line A2780cis in the presence and absence of light.

Fluence (J cm^{-2})	IC$_{50}$ concentration (μM) for complexes.[a]	
	1	**2**
0	61.7	> 100
8	8.5	> 100
24	1.2	28.8
48	0.3	22.9

[a] In same conditions, the cytotoxicity of cisplatin is IC$_{50}$ = 22.9 μM.

These data show that in the dark both **1** and **2** display low cytotoxicity. Complex **2** is particularly inactive (IC50 > 100 μM) and, although **1** does demonstrates some potency, it is still approximately three-fold less toxic (IC$_{50}$ =61.7 μM) towards a

cisplatin resistant line than cisplatin itself. However, on exposure to light, **1** produces a dramatic impact upon cell viability.

As illustrated in Fig 4a, cell viabilities are sensitive to both the concentration of **1** and light dosage: even when exposed to low fluences of 8 or 24 Jcm^{-2}, **1** now demonstrates potent cytotoxicity, over an order of magnitude greater than its dark value. In fact at a higher light dose of 48 Jcm^{-2}, the IC$_{50}$ decreases to 0.3 μM; a value two orders of magnitude more potent than cisplatin.
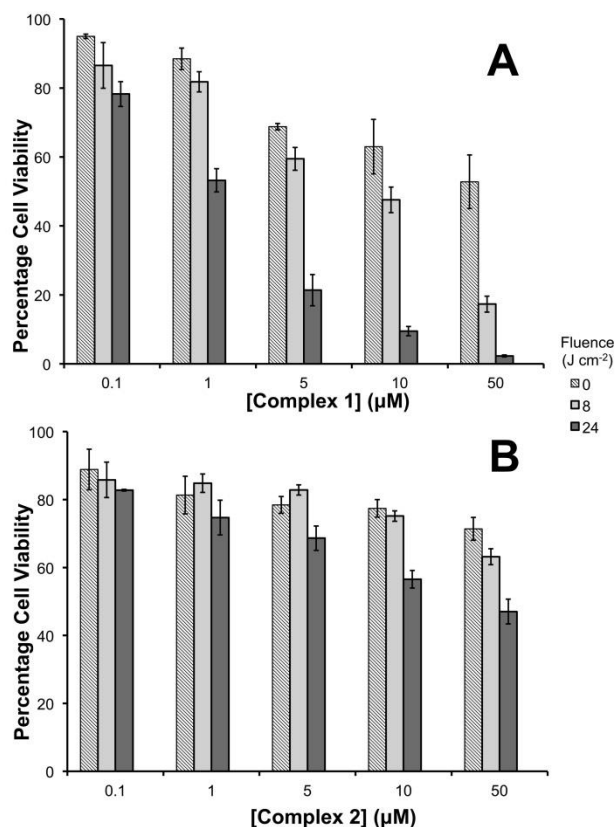

Figure 4. Light and dark cell viability figures on exposure to varying light fluences and different concentration of macrocycle **1** and mononuclear complex **2**.

In contrast, **2** produces only minimal phototoxic effects at high concentrations and light doses – Fig 4b. For example, at a fluence of 48 Jcm^{-2} (a fluence less than half of that used with the licenced PDT sensitizer photofrin) the photocytotoxicity (PI) index - where PI = IC50(light)/IC50(dark) – for the complexes showed that whilst PI(**2**) < 5, PI(**1**) = 206. Thus, on exposure to light, macrocycle **1** displays nanomolar cytotoxicity in cisplatin resistant cells at fluences that are lower than those required for a clinically approved sensitizer.

Given that **2** actually has a higher $\phi(^1O_2)$ than **1**, the dramatic differences in cytotoxicities and PI between the mononuclear complex and the macrocycle can be attributed to their contrasting cellular uptake properties; a well-established principle in the cell biology of ruthenium polypyridyl complexes.[43] To quantify this effect, relative cellular accumulation of both compounds in A2780CIS cells was determined using inductively coupled plasma mass spectrometry (ICP- MS). Cells were incubated for 12 hours with 50 μM concentrations of **1** or **2** - the highest concentration employed in the experiments summarized in Figure 4 – before intracellular Ru and Re content was determined. This analysis

confirmed that ruthenium intracellular concentrations are approximately seven times higher on treatment with **1** compared to **2** – see SI. Since the macrocycle contains two Ru centres, in terms of molarity, this corresponds to a 3.5-fold preferential increase in **1** over **2**. Further analyses of the ICP-MS experiments with **1** confirm that the intracellular ratio of [Ru]:[Re] is 1:1, providing further evidence of macrocycle uptake into cells. Furthermore, the fact that low levels of **2** enter cells explains why some phototoxicity is observed for this complex at higher exposure concentrations and fluences.

Conclusion

In summary, for the first time, a metal complex PDT sensitizer has been constructed through metal directed self-assembly of photo-excitable oligonuclear metallomacrocycles. The striking bioactivity of this system can be largely attributed to its more favourable cellular uptake properties compared to its mononuclear building block. Presumably, this observation is due to a previously reported effect, the overall charge density/lipophilicity of the macrocyclic assembly is lower than that of the corresponding mononuclear complex. Since the novel macrocyclic PDT sensitizer discussed in this study has been self-assembled from mononuclear complex "modules", architecturally complex systems with new properties and functions can be readily constructed from relatively simple, previously reported, building blocks. Through this new paradigm, systems with enhanced uptake and tuneable photo-redox properties can be targeted. For example, as our previous studies indicate, [32-34] by judicious selection of ancillary and bridging ligand, cellular and subcellular binding properties of these novel PDT sensitizers can be selectively modulated to produce highly targeted PDT regimes.

Furthermore, as recently demonstrated in a number of studies, it is possible to construct Ru^{II}-based systems that can be photo-excited within the therapeutic optical window.[44-47] For example, since oligonuclear Ru^{II} complexes often display high two-photon absorption, 2PA, cross-sections,[48-50] using this modular approach, the design of macrocyclic systems for 2PA-PDT can be readily envisioned. Such studies will provide the basis of future publications.

Experimental Section

See SI for experimental details.

[1]   T. J. Dougherty, C. J. Gomer, B. W. Henderson, G. Jori, D. Kessel, M. Korbelik, J. Moan, Q. Peng, *J. Natl. Cancer Inst.* **1998**, *90*, 889–905.

[2]   P. Agostinis, K. Berg, K. A. Cengel, T. H. Foster, A. W. Girotti, S. O. Gollnick, S. M. Hahn, M. R. Hamblin, A. Juzeniene, D. Kessel, et al., *CA: A Cancer Journal for Clinicians* **2011**, *61*, 250–281.

[3]   G. B. Kharkwal, S. K. Sharma, Y.-Y. Huang, T. Dai, M. R. Hamblin, *Lasers Surg Med* **2011**, *43*, 755–767.

[4]   R. Ackroyd, C. Kelty, N. Brown, M. Reed, *Photochem Photobiol* **2001**, *74*, 656–669.

[5]   D. E. J. G. J. Dolmans, D. Fukumura, R. K. Jain, *Nat Rev Cancer* **2003**, *3*, 380–387.

[6]   R. R. Allison, C. H. Sibata, *Photodiagnosis Photodyn Ther* **2010**, *7*, 61–75.

[7]   T. Dai, Y.-Y. Huang, M. R. Hamblin, *Photodiagnosis Photodyn Ther* **2009**, *6*, 170–188.

[8]   M. R. Detty, S. L. Gibson, S. J. Wagner, *J. Med. Chem.* **2004**, *47*, 3897–3915.

[9]   J. P. Celli, B. Q. Spring, I. Rizvi, C. L. Evans, K. S. Samkoe, S. Verma, B. W. Pogue, T. Hasan, *Chem. Rev.* **2010**, *110*, 2795–2838.

[10]   C. Mari, M. Kaur, S. Ladouceur, G. Gasser, *Chem. Sci.* **2015**, *6*, 2660–2686.

[11]   G. Shi, S. Monro, R. Hennigar, J. Colpitts, J. Fong, K. Kasimova, H. Yin, R. DeCoste, C. Spencer, L. Chamberlain, et al., *Coord. Chem. Rev.* **2015**, *282-283*, 127–138.

[12]   M. Fujita, M. Tominaga, A. Hori, B. Therrien, *Acc. Chem. Res.* **2005**, *38*, 369–378.

[13]   R. Chakrabarty, P. S. Mukherjee, P. J. Stang, *Chem. Rev.* **2011**, *111*, 6810–6918.

[14]   K. Harris, D. Fujita, M. Fujita, *Chem. Commun.* **2013**, *49*, 6703.

[15]   T. R. Cook, Y.-R. Zheng, P. J. Stang, *Chem. Rev.* **2013**, *113*, 734–777.

[16]   C. J. Brown, F. D. Toste, R. G. Bergman, K. N. Raymond, *Chem. Rev.* **2015**, *115*, 3012–3035.

[17]   J. A. Thomas, *Dalton Trans* **2011**, *40*, 12005–12016.

[18]   M. J. Hannon, *Chem Soc Rev* **2007**, *36*, 280–295.

[19]   A. D. Faulkner, R. A. Kaner, Q. M. A. Abdallah, G. Clarkson, D. J. Fox, P. Gurnani, S. E. Howson, R. M. Phillips, D. I. Roper, D. H. Simpson, et al., *Nat Chem* **2014**, *6*, 797–803.

[20]   M. Li, S. E. Howson, K. Dong, N. Gao, J. Ren, P. Scott, X. Qu, *J. Am. Chem. Soc.* **2014**, *136*, 11655–11663.

[21]   T. R. Cook, P. J. Stang, *Chem. Rev.* **2015**, *115*, 7001–7045.

[22]   T. R. Cook, V. Vajpayee, M. H. Lee, P. J. Stang, K.-W. Chi, *Acc. Chem. Res.* **2013**, *46*, 2464–2474.

[23]   B. Therrien, G. Süss-Fink, P. Govindaswamy, A. K. Renfrew, P. J. Dyson, *Angew. Chem. Int. Ed.* **2008**, *47*, 3773–3776.

[24]   A. Pitto-Barry, N. P. E. Barry, O. Zava, R. Deschenaux, P. J. Dyson, B. Therrien, *Chem. Eur. J.* **2011**, *17*, 1966–1971.

[25]   K. Suntharalingam, A. Łęczkowska, M. A. Furrer, Y. Wu, M. K. Kuimova, B. Therrien, A. J. P. White, R. Vilar, *Chem. Eur. J.* **2012**, *18*, 16277–16282.

[26]   F. Schmitt, J. Freudenreich, N. P. E. Barry, L. Juillerat-Jeanneret, G. Süss-Fink, B. Therrien, *J. Am. Chem. Soc.* **2012**, *134*, 754–757.

[27]   I. V. Grishagin, J. B. Pollock, S. Kushal, T. R. Cook, P. J. Stang, B. Z. Olenyuk, *Proc Natl Acad Sci USA* **2014**, *111*, 18448–18453.

[28]   B. Therrien, *CrystEngComm* **2015**, *17*, 484–491.

[29]   P. de Wolf, S. L. Heath, J. A. Thomas, *Chem. Commun.* **2002**, 2540–2541.

[30]   H. Ahmad, A. J. H. M. Meijer, J. A. Thomas, *Chem Asian J* **2011**, *6*, 2339–2351.

[31]   P. de Wolf, P. Waywell, M. Hanson, S. L. Heath, A. J. H. M. Meijer, S. J. Teat, J. A. Thomas, *Chem. Eur. J.* **2006**, *12*, 2188–2195.

[32]   D. Ghosh, H. Ahmad, J. A Thomas, *Chem. Commun.* **2009**, 2947–2949.

[33]   H. Ahmad, D. Ghosh, J. A. Thomas, *Chem. Commun.* **2014**, *50*, 3859–3861.

[34]   H. Ahmad, B. W. Hazel, A. J. H. M. Meijer, J. A. Thomas, K. A. Wilkinson, *Chem. Eur. J.* **2013**, *19*, 5081–5087.

[35]   K. K.-W. Lo, *Acc. Chem. Res.* **2015**, 150710135055006.

[36]   C. A. Puckett, J. K. Barton, *J. Am. Chem. Soc.* **2007**, *129*, 46–47.

[37]   M. R. Gill, J. Garcia-Lara, S. J. Foster, C. Smythe, G. Battaglia, J. A. Thomas, *Nat Chem* **2009**, *1*, 662–667.

[38]   A. Wragg, M. R. Gill, D. Turton, H. Adams, T. M. Roseveare, C. Smythe, X. Su, J. A. Thomas, *Chem. Eur. J.* **2014**, *20*, 14004–14011.

[39]   G. Majno, I. Joris, *Am. J. Pathol.* **1995**, *146*, 3–15.

[40]   S. Van Cruchten, W. Van den Broeck, *Anat Histol Embryol* **2002**, *31*, 214–223.

[41]   W. Fiers, R. Beyaert, W. Declercq, P. Vandenabeele, *Oncogene* **1999**, *18*, 7719–7730.

[42]   F. R. Svensson, M. Matson, M. Li, P. Lincoln, *Biophysical Chemistry* **2010**, *149*, 102–106.

[43]   M. R. Gill, J. A. Thomas, *Chem Soc Rev* **2012**, *41*, 3179–3192.

[44]   S. C. Boca, M. Four, A. Bonne, B. van der Sanden, S. Astilean, P. L. Baldeck, G. Lemercier, *Chem. Commun.* **2009**, 4590–4592.

[45]   E. Baggaley, M. R. Gill, N. H. Green, D. Turton, I. V. Sazanovich, S. W. Botchway, C. Smythe, J. W. Haycock, J. A. Weinstein, J. A. Thomas, *Angew. Chem. Int. Ed.* **2014**, *53*, 3367–3371.

[46]   H. Yin, M. Stephenson, J. Gibson, E. Sampson, G. Shi, T. Sainuddin, S. Monro, S. A. Mcfarland, *Inorg Chem* **2014**, *53*, 4548–4559.

[47]   H. Huang, B. Yu, P. Zhang, J. Huang, Y. Chen, G. Gasser, L. Ji, H. Chao, *Angew. Chem.* **2015**, *127*, 14255–14258.

[48]   O. Maury, H. Le Bozec, *Acc. Chem. Res.* **2005**, *38*, 691–704.

[49]   M. Samoc, J. P. Morrall, G. T. Dalton, M. P. Cifuentes, M. G. Humphrey, *Angew. Chem. Int. Ed. Engl.* **2007**, *46*, 731–733.

[50]   A. M. McDonagh, M. G. Humphrey, M. Samoc, B. Luther-Davies, *Organometallics* **1999**, *18*, 5195–5197.

A self-assembled metallomacrocycle singlet oxygen sensitizer for photodynamic therapy [Supporting Information]

Michael G. Walker, Paul J. Jarman, Martin R. Gill, Xiaohe Tian, Haslina Ahmad, Pattubala A. N. Reddy, Luke McKenzie, Julia A. Weinstein, Anthony J . H. M. Meijer, Giuseppe Battaglia, Carl G. W. Smythe*, Jim A. Thomas*.

Experimental details

All chemicals and solvents were purchased from Sigma unless otherwise stated. Complexes **1** and **2** were synthesised as previously reported.[1,2] ^{1}H NMR and mass spectra data were in agreement with previously-reported results.

DNA photocleavage

Photoinduced cleavage of supercoiled (SC) pBR322 DNA by the complexes was studied by agarose gel electrophoresis. The reactions were carried out under illuminated conditions using 476 nm CW laser (100 mW). The sample was prepared in a dark room at room temperature using SC DNA (3 μL, ~3 μg) in 50 mM Tris-HCl buffer (pH 7.2) containing 50 mM NaCl and varying concentrations of the complex. The solution path length used for illumination in the sample vial was 6 mm. After photoexposure, the sample was incubated for 1 h at 37 ℃, followed by the addition of the loading buffer containing 25% bromophenol blue, 0.25% xylene cyanol, and 30% glycerol (2 μL), and the solution was finally loaded on an 0.9% agarose gel containing 1.0 μg/mL ethidium bromide. Electrophoresis was carried out for 1 h at 60 V in TAE (Tris-acetate-EDTA) buffer. Bands were visualized by UV light and photographed.

Singlet Oxygen generation

Singlet oxygen quantum yield (φΔ) in dichloromethane was determined as previously described employing 355 nm excitation and perinaphthenone as the standard (φΔ perinaphthenone = 95%).[3]

Light Irradiation Source Apparatus

The apparatus used to irradiate the samples was a custom made device featuring a broadband illumination source fully contained in an empty computer base unit, referred to as the Light Irradiation Source Apparatus (LISA). The technical specifications of the bulb contained within are as follows (**Table 1**).

Product Code	871691
International Model Number	HC01080i
Description	CFL 80W E40 Integrated Clusterlite 4000K
Watts	80W
Cap	E40
Operating Hours	15000
Colour Temp	4000K
Lumens	5400 lm
Dimming	No
Dimensions (length x diameter)	256mm x 80mm

Table 1 – Specification of the bulb contained within the irradiation apparatus

Determination of Fluence

In order to quantify the power output of this light source, an experiment was carried out with the running conditions replicated whilst being monitoring by a power meter. The setup utilised was a THORLABS *S175C Sensor* coupled to a *PM100USB Power and Energy Meter* with the readout displayed and stored on a connected netbook. Running the three timed periods of irradiation in succession as under experimental conditions (for three separate samples) determined an accurate power output that the cells were exposed to (**Table 2**).

Stage	Stabilisation	5 minutes ON	Sample change	15 minutes ON	Sample Change	30 minutes ON
Time (minutes)	2	5	2	15	2	30
Average Power (W)	0.000	0.075	0.035	0.121	0.040	0.126
Corrected Power (W)	-	0.075	-	0.085	-	0.086
Energy (J)	-	22.6	-	76.9	-	155.7
Fluence (J cm^{-2})	-	**8**	-	**24**	-	**48**

Table 2 – Table summarising the fluence calculations from timed irradiations

Cell Culture

A2780 and A2780CIS cell lines were cultured in RPMI-1640 medium. All growth medium was supplemented by 2mM L-Glutamine, 100 IU ml^{-1} penicillin, 100 µg ml^{-1} streptomycin and 10% v/v fetal bovine serum (FBS). Cultures were grown within the appropriate range of confluence at 37°C in an atmosphere of 5 % CO_2 / 95% air. Cultures were routinely subcultured using trypsin (0.1% v/v in PBS) at 80 – 90% confluence. Cell lines were used between passage numbers 6 – 60.

Confocal microscopy

Cells were seeded in 6 well plates and luminescently imaged on a Zeiss LSM 510 META upright confocal laser microscope using 40x and 63x water immersion objectives. Where appropriate, cell fixation was achieved using 5% paraformaldehyde for ten minutes followed by permabilisation using 0.1 % Triton. **1** and **2** were excited with an Ar-ion laser at 458 nm and emission collected at 640-700 nm using a polychomric (META) detector. Live cell imaging experiments involved constant laser exposure 0 – 100 mins with images recorded every 5 min. Image data acquisition and processing was performed using Zeiss LSM Image Browser.

Photocytotoxicity (phototoxicity)

Cell cultures were grown on 48 well plates at a seeding density of 50,000 cells per well and allowed to grow for 24 hours. The cells were then treated with compound (solubilised in 10% PBS/water: 90% medium) of a 1 – 100 μM concentration range, in triplicate, and incubated for 24 hours. All compound solution (and control media) was removed from the cells and replaced with regular growth medium 30 minutes prior to irradiation. Of the four prepared well plates, one remained in the incubator whilst the other three were exposed to the LISA for the duration of 5, 15 or 30 minutes (corresponding to light doses of 8, 24 or 48 J cm^{-2}) before being incubated for a further 24 hours after culmination of light treatment. All media was then removed and cells incubated with MTT (0.5 mg ml^{-1} dissolved in PBS) for 30 – 40 minutes. The MTT was removed and formazan product eluted using 120 μl/well acidified isopropanol, 100 μl of which was transferred to a 96 well plate for the absorbance to be quantified by spectrophotometer (540 nm, referenced at 640 nm). An average absorbance for each concentration was calculated and cell viability was determined as a percentage of the untreated negative control wells (10% PBS/water: 90% medium, average of triplicate). Data were plotted in a graph of concentration against cell viability to produce a curve from which the IC$_{50}$ value (the concentration corresponding to a cell viability of 50%) could be derived by interpolation.
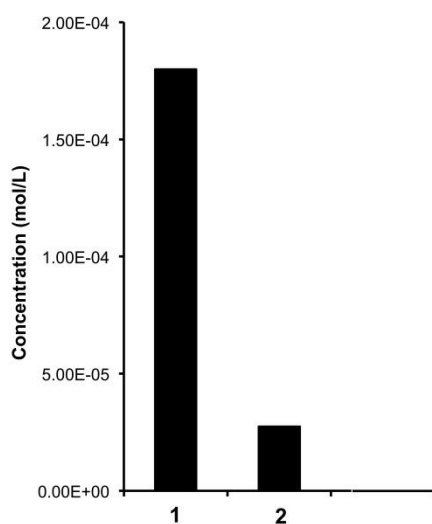
Supplementary Figures
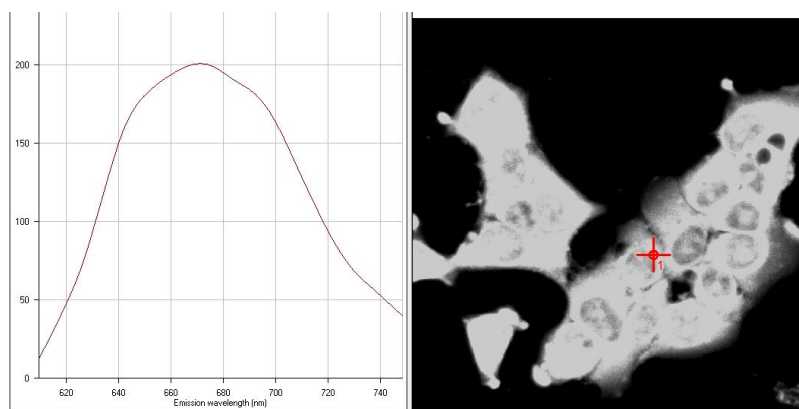
Supplementary Figure 1 - Emission spectra (left) of fixed MCF7 cells stained with **1** (right) (100 μM, 10 mins).
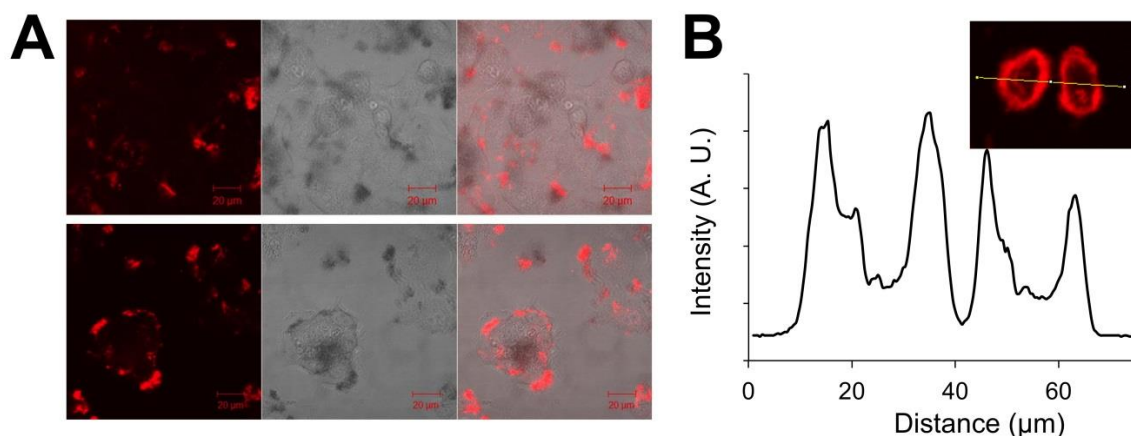
Supplementary Figure 2 - (**A**) Live MCF7 cells stained with **1** ([**1**] = 200 μM) but not exposed to continuous laser light. Cells imaged 100 min after complex addition. (**B**) Emission profile of cells (across white line) illustrating that the majority of staining is restricted to the plasma membrane.

Supplementary Figure 3 - cellular uptake levels of **1** and **2** in A2780CIS cells (50 μM, 12 hr), as quantified by ICP-MS analysis of Ru content.

References

1. (a) P. de Wolf, S. L. Heath and J. A. Thomas, *Chem. Commun.*, 2002, 2540–2541.(b) P. de Wolf, P. Waywell, M. Hanson, S. L. Heath, A. J. H. M. Meijer, S. J. Teat and J. A. Thomas, *Chem. Eur. J.*, 2006, **12**, 2188–2195.

2. H. Ahmad, A. J. H. M. Meijer and J. A. Thomas, *Chem Asian J*, 2011, **6**, 2339–2351.

3. N. M. Shavaleev, H. Adams, J. Best, R. Edge, S. Navaratnam, J. A. Weinstein, *Inorg. Chem.* **2006**, *45*, 9410-9415.